BNL 51443

ISABELLE

PROCEEDINGS OF THE 1981 SUMMER WORKSHOP

VOLUME 4

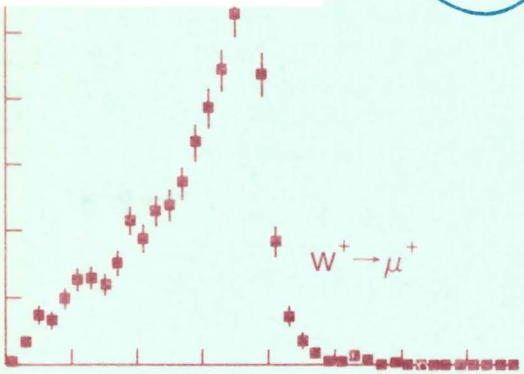

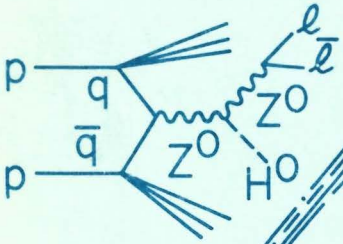

BROOKHAVEN NATIONAL LABORATORY
Upton, Long Island, New York, 11973

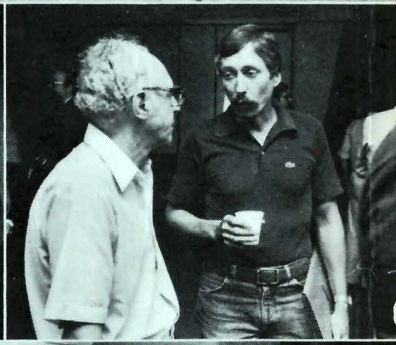

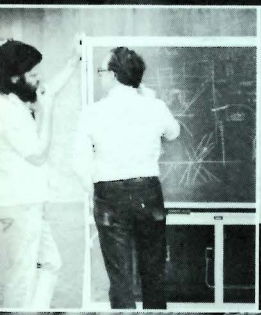

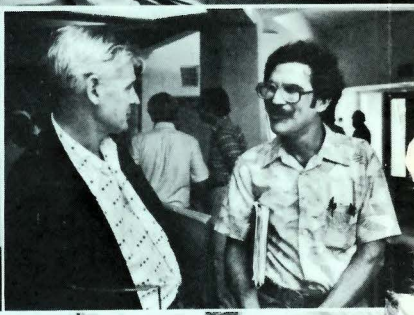

BNL 51443
UC-28
UC-34d
(Particle-Accelerators
and High-Voltage Machines;
Physics — Particles and Fields TIC-4500)

ISABELLE

PROCEEDINGS OF THE 1981 SUMMER WORKSHOP

JULY 20 — 31, 1981

VOLUME 4
DETECTOR R&D

BROOKHAVEN NATIONAL LABORATORY
ASSOCIATED UNIVERSITIES, INC.
UNDER CONTRACT NO. DE-AC02-76CH00016 WITH THE
UNITED STATES DEPARTMENT OF ENERGY

FOREWORD

The ISABELLE Summer Workshop, held at BNL from July 20 through July 31, was attended by 259 physicists representing 72 institutions. The discussions covered experimental areas, large detectors and detector technology, with a primary emphasis on physics opportunities, both with a phased and a full luminosity ISABELLE.

There was a consensus that physics with Phase I ($E_{cm} \approx 700$ GeV and $L \sim 2 \times 10^{31}/cm^2/sec$, with bunched beams) was feasible, important and exciting. It has been known for years that the orthodox gauge theories will be critically tested by studying the $W^{\pm}$, Z^0 and high $p_\perp$ phenomena. The Z^0 has a reasonable chance of being found at the $\bar{p}p$ colliders if luminosities reach $10^{30}/cm^2/sec$, but its properties will be difficult to decipher. Seeing the $W^{\pm}$'s or new heavy quarks is less probable and measuring their properties is even less likely. At ISABELLE these phenomena can all be studied with high precision. But the more exciting conclusion which emerged from the workshop was related to the question of what generates the $\sim$100 GeV masses of the W's and Z's. The answer could involve Higgs, technicolor, or other particles with masses ranging from 10.8 GeV to 1 TeV, with an intermediate mass scale of 200-300 GeV being a possible region of strong interest. Some of these models predict spectacular experimental signatures. It is clear that only ISABELLE with $L \sim 10^{32} - 10^{33}$, has an opportunity of addressing and resolving such questions.

The great interest in ISABELLE physics was also evidenced by the variety of large detectors (6 to date) that have evolved - characterized by magnetic field configurations ranging from solenoid through dipole and toroid to no field at all. The ability to extract the physics was re-examined, leptons and γ's being straightforward, with greater attention being paid to analyzing jet and multijet events and defining their properties, masses, $p_\perp$, etc. Many advances were also reported in detector R&D, for example, imaging Cerenkov counters, precision drift chambers, scintillating optical fibers. Although there were many problems to be solved, such as data handling and vertex detectors, there was

more confidence and less apprehension about our ability to solve them. Experimental areas look fine except for the rerouting of some trenches and exchanging areas #10 and #12 to more easily accomodate the ep option.

The question of options was discussed at length and in quite some depth. It seems natural to augment ISABELLE with an ep capability, especially with a separate ring. Electron energies of 10-20 GeV with luminosities of 10^{31} - 10^{32} look achievable and have stimulated great interest. The addition of a booster, Phase II, would also naturally allow for the study of heavy ion interactions for which enthusiasm seems to be growing, especially in the light of ISR results.

In summary, the Workshop was a very upbeat, enthusiastic, and successful meeting. With the opportunities for carrying out high energy experiments being limited at present and more so in the future, the community is beginning to reaffirm even more strongly the great physics potential of ISABELLE. The consensus is to get on with the project, get it done and perform the physics. A turn-on in '86 or '87 is what is desired.

N.P. Samios
S.C.C. Ting
Co-Chairmen

INTRODUCTION

The Workshop and these proceedings were organized into five parts:

	Organizers
1. Lectures	Ling-Lie Chau
2. Physics	M.A.B. Beg Ling-Lie Chau V. Fitch A. Mann
3. Experimental Areas	R. Lanou S. Aronson
4. Large Detectors	C. Baltay H. Gordon
5. Detector Research and Development	W. Carithers T. Ludlam

During the two weeks of the Workshop authors gave us their drafts and figures. These were put into final form by BNL typists and draftsmen. Under the extremely tight time constraints we could not guarantee that everything has come out perfectly - we did the best job we could.

The Workshop and Proceedings were truly a herculean job and could not have been accomplished without the gracious help of many people. Kit McNally and Joyce Ricciardelli coordinated the Workshop from its inception. During the Workshop, they were joined by Penny Baggett and Pat Tuttle at the conference desk. The various amenities were organized by Pat Glynn, Bill Love, Mike Schmidt, Tom Rizzo, Larry Trueman and Peter Yamin.

For the Proceedings, Ken Foley served as managing editor, organizing the entire production in less than a month. The sections were ordered and edited by Ling-Lie Chau, Bob Lanou, Sam Aronson, Tom Ludlam and Frank Paige. We had an army of hard-working typists: Donna Early, Judy Ferrero, Barbara Gaer, Rae Greenberg, Isabell Harrity, Pat Knisely, Pat Lebitski, Sharon Smith, Kathy Tuohy, Pat Valli, and Diana Votruba. Drafting the myriad of figures was skillfully accomplished by Randy Bowles, Rip Bowman, Kathy Brown, Bill Dieffenbach, Sal Morano, and Sue Norton. The enormous job of copy preparation was done by Fern Coyle, Liz Russell and Joyce Ricciardelli. None of this would have been possible without the complete support of the Technical Photography and Graphic Arts Division.

Neil Baggett deserves special mention for his incomparable efforts in making this Workshop successful.

Howard A. Gordon
Editor-in-Chief

21 August 1981

Table of Contents

VOLUME 1

Page No.

VOLUME 4

SECTION V - Detector Research and Development

Participants
ISABELLE Summer Workshop July 20-31, 1981

Participant's name	Institution
K. Abe	University of Pennsylvania
A. Ali	DESY
K. Amako	University of Pennsylvania
E. W. Anderson	Iowa State University
T. W. Appelquist	Yale University
S. Aronson	BNL
F. W. Ascolese	BNL
V. Ashford	BNL
M. Atac	Fermilab
M. Atiya	Columbia University
J. Babcock	Carnegie-Mellon University
T. Bacon	Imperial College
N. Baggett	BNL
P. Baggett	BNL
N. Baker	BNL
C. Baltay	Columbia University
A. J. Baltz	BNL
Z. J. Banas	BNL
Z. Bar-Yam	Southeastern Massachusetts University
A. Bassetto	University of Trento, Italy
L. Baumel	Yale University/BNL
U. Becker	Massachusetts Institute of Technology
M. A. B. Beg	Rockefeller University
E. W. Beier	University of Pennsylvania
S. Beingessner	Carleton University
O. Benary	University of Tel-Aviv
J. Bensinger	Brandeis University
D. Berley	National Science Foundation
M. Bernias	BNL
K. Black	Yale University
S. Blatt	Yale University/BNL
B. Blumenfeld	Johns Hopkins University
S. Borenstein	York College of the C.U.N.Y.
G. Bozoki	BNL
P. Braccini	INFN-Pisa/CERN
J. Branson	Massachusetts Institute of Technology
M. Bregman	Nevis Laboratory
G. Bunce	BNL
M. Capell	Massachusetts Institute of Technology
W. Carithers	Lawrence Berkeley Laboratory
L.-L. Chau	BNL
M. Chen	Massachusetts Institute of Technology

S.-P. Chen	Institute of Atomic Energy, Beijing/BNL
C.P. Cheng	Institute of High Energy Physics, Beijing
Y. Cho	Argonne National Laboratory
T. S. Chou	BNL
J.H. Christenson	New York University
S. U. Chung	BNL
P. Clarke	SUNY, Stony Brook/BNL
W. E. Cleland	University of Pittsburgh
D. Coon	University of Pittsburgh
J. W. Cooper	University of Pennsylvania
P. Coteus	Columbia University
S. Csorna	Vanderbilt University
E. D. Courant	BNL
G. T. Danby	BNL
J. F. Donoghue	University of Massachusetts
J. Dowd	Southeastern Massachusetts University
D. S. Du	Institute of High Energy Physics, Beijing
P. Duinker	NIKHEF/DESY
R. Edelstein	Carnegie-Mellon University
F. Eiseler	CUNY
J. Elias	Fermilab
R. Engelmann	BNL
A. Erwin	University of Wisconsin
G. Y. Fang	Massachusetts Institute of Technology
R. Fernow	BNL
R. Field	University of Florida
J. Fischer	BNL
K. J. Foley	BNL
S. Frankel	University of Pennsylvania
W. Frati	University of Pennsylvania
W. R. Frisken	York University
G. Gammel	BNL
G. Giacomelli	University of Bologna
B. G. Gibbard	BNL
M. Goldhaber	BNL
P. Gollon	BNL
H. Gordon	BNL
P. D. Grannis	SUNY, Stony Brook
R. Gustafson	University of Michigan
S. Hagopian	Florida State University
V. Hagopian	Florida State University
H. Hahn	BNL
C. Hargrove	National Research Council of Canada
J. C. Herrerra	BNL

J. Hettema	BNL
H. Hilke	CERN
S. Holmes	Columbia University
H.-C. Hseuh	BNL
K. Huang	Massachusetts Institue of Technology
J. W. Humphrey	BNL
V. W. Hughes	Yale University
Y. Inagaki	BNL
N. Isgur	University of Toronto
J. Jackson	BNL
K. Jaeger	BNL
D. Jensen	University of Massachusetts
H. Jensen	Fermilab
R. Johnson	BNL
S. Kabe	KEK-Japan
T. Kalogerpoulos	Syracuse University
S. Kahn	BNL
G. Kane	University of Michigan
A. Kanofsky	Lehigh University
G. Kantardjian	CERN
H. Kasha	Yale University
S. Katcoff	BNL
E. Keil	CERN
W.-Y. Keung	BNL
J. Kirz	SUNY, Stony Brook
B. Knapp	Nevis Laboratory
H. Kraner	BNL
P. Kunz	SLAC
B. P. Kwan	BNL
T. F. Kycia	BNL
R. E. Lanou	Brown University
K. W. Lai	BNL, University of Arizona
L. Lasker	BNL
W. Lee	Columbia University
Y.Y. Lee	BNL
L. B. Leipuner	BNL
K. Li	BNL
P. Limon	Fermilab
S. Lindenbaum	BNL/CCNY
L. Littenberg	BNL
R. S. Longacre	BNL
W. A. Love	BNL
D. I. Lowenstein	BNL
D. Luckey	Massachusetts Institute of Technology
T. Ludlam	BNL

D. Makowiechi	BNL
K. Manivannan	SUNY, Stony Brook
A. K. Mann	University of Pennsylvania
V. Manzella	BNL
W. Marciano	Northwestern University
J. Martin	University of Toronto
J. Marraffino	BNL/Vanderbilt University
J. Marx	Lawrence Berkeley Lab
M. Marx	SUNY, Stony Brook
G. Massaro	NIKHEF/Amsterdam
T. Matsuda	Osaka University/ MIT
D. Maurizio	BNL
M. May	BNL
R. McCarthy	SUNY, Stony Brook
K. McDonald	Princeton University
A. Melissinos	University of Rochester
A. Metz	BNL/Harvard University
T. Meussen	BNL
D. Miller	Northwestern University
T. Miyachi	INS - Tokyo
M. Month	Department of Energy
W. M. Morse	BNL
A. H. Mueller	Columbia University
M. J. Murtagh	BNL
S. Murtagh	BNL
K. Nakagawa	University of Naples
A. Nappi	University of Pisa
P. Nemethy	Lawrence Berkeley Laboratory
J. Niederer	BNL
S. Nussinov	Massachusetts Institute of Technology
T. O'Halloran	University of Illinois
J. Okamitsu	Columbia-Nevis
B. Ovryn	BNL/University of Rochester
H. Paar	Columbia University/NIKHEF
F. E. Paige	BNL
J. A. Paradiso	Massachusetts Institute of Technology
Z. Parsa	Northwestern University
E. A. Paschos	BNL/Universitat Dortmund
A. Pascolini	University of Padua
R.M. Patel	McGill University
R. Peierls	BNL
A. Pevsner	Johns Hopkins University
O. Piccioni	University of California
H. Piekarz	BNL
J. Piekarz	BNL
R. Plano	Rutgers University
E. Platner	BNL

B. Pope	Princeton University
A. Prodell	BNL
S. Protopopescu	BNL
M. Pusterla	BNL
G. Rabinowitz	BNL
S. Raby	SLAC
V. Radeka	BNL
D. Rahm	BNL
R. R. Rau	BNL
G. Reiter	BNL
T. G. Rizzo	BNL
J. Roberts	Rice University
N. Rofail	BNL
C. Roos	Vanderbilt University
J. Rosen	Northwestern University
E. Rosenberg	Iowa State University
L. Rosenson	Massachusetts Institute of Technology
J. A. Rubio	JEN-Madrid
R. Rückl	University of Munich
J. Russell	Southeastern Massachusetts University
M. Sakitt	BNL
J. Sanford	BNL
J. Sandweiss	Yale University
D. Schildknecht	University Bielefeld
M. Schmidt	Yale University
L. S. Schroeder	Lawrence Berkeley Laboratory
W. Selove	University of Pennsylvania
W. P. Sims	BNL
A. Sinha	SUNY, Stony Brook
W. Sippach	Columbia University
E. J. Siskind	BNL
J. Skelly	BNL
P. Skybic	University of Oklahoma
S.D. Smith	BNL
G. Snow	University of Maryland
J. Spiro	BNL
R. M. Sternheimer	BNL
A. Stevens	BNL
H. Sticker	Rockefeller University
R. Strand	BNL
K. Strauch	Harvard University
I. Stumer	BNL
L. Sulak	University of Michigan
S. Sumorok	University of Birmingham/CERN
Y. Suzuki	Brown University
M. Tanaka	BNL
X. W. Tang	Institute of High Energy Physics, Beijing

M. J. Tannenbaum	BNL
S. Terada	BNL
G. Theodosiou	University of Pennsylvania
D. Theriot	Fermilab
J. Thompson	University of Pittsburg
S.C.C. Ting	Massachusetts Institute of Technology
F. G. Tinta	BNL
A. Tollestrup	Fermilab
M. Tran	University of California, Los Angeles
T. L. Trueman	BNL
M. Valdata-Nappi	INFN-Pisa
G. Voss	DESY
A. Walenta	BNL
W. G. Walker	BNL
W. Wallenmeyer	Department of Energy
P. Wanderer	BNL
J. Warnock	Massachusetts Institute of Technology
W. Weisberger	SUNY, Stony Brook
D. Wheeler	BNL
D. H. White	BNL
S. White	Rockefeller University
B. Wiik	DESY
A. Wijangco	BNL
B. F. Wilczek	University of California, Santa Barbara
H. H. Williams	University of Pennsylvania
W. Willis	CERN
R. R. Wilson	Columbia University
Y. S. Wu	Institute of Theoretical Physics, Beijing/ Institute for Advanced Study
P. Xue	Beijing/MIT
T. Yamanouchi	Fermilab
P. Yamin	BNL
C. N. Yang	SUNY, Stony Brook
T. Ypsilantis	Ecole Polytechnique
J. Zingman	Yale University; BNL

SECTION V

DETECTOR R+D

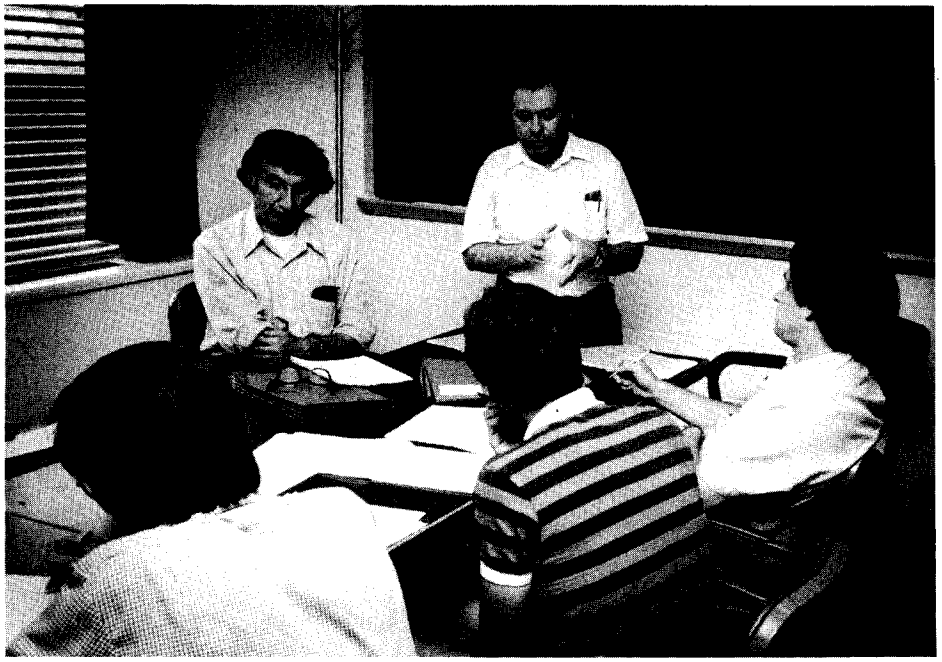

DETECTOR R&D
WORKSHOP SUMMARY

T. Ludlam, Brookhaven National Laboratory
W. Carithers, Lawrence Berkeley Laboratory

Workshop participants were asked to assess the current status of detector R&D in terms of the specific needs for ISABELLE experiments: the demands of high particle rates, extremely selective triggers on complex and rare events, and the economics of large detector systems. The detailed results of working groups convened to consider specific areas of detector development are presented on the pages which follow. The key points of this assessment, as regards the continuing R&D program for ISABELLE are summarized here.

The rate tolerance of a particular detector element is determined not only by its ability to withstand high luminosities, but also by the rate at which its data can usefully be recorded. Sophisticated trigger processors are necessary to reduce the initial interaction rate of up to 50 MHz (at $L = 10^{33}$ $cm^{-2}sec^{-1}$) down to a tolerable rate of 10 Hz for mass storage. Several technologies are being developed, and with a reasonable investment flexible trigger processors could reduce an input of 10^4 Hz down to 10 Hz. Even with a 10 Hz output, a large detector would require the effective computing power of five CDC 7600's for the off-line analysis to keep pace with the recorded data. Efforts to improve selectivity at the detector/processor level are clearly important.

Calorimeters, as a central element of most envisioned ISABELLE detectors, must have good spatial resolution (segmentation) as well as energy resolution to be effective in this environment. Considerable effort is going into the development of gas sampling calorimeters as means of achieving highly segmented devices at relatively low cost. An interesting new development, for gas detectors in general but particularly for calorimeters, is the realization of well-localized self-quenching streamers at anode wires. A great deal of attention at this workshop was given to parameterizing the theoretical

limitations of performance for gas sampling calorimeters in terms of gas gain, charge collection and signal shaping time, detector capacitance, and multiple event pile-up.

The implementation of wire chambers as tracking devices at ISABELLE poses many special problems. In large measure the solutions lie with the development of fast, low-noise, low-cost electronics. For instance, an important recent advance is the development of a 256 bit shift register with $> 10^8$ MHz clock rate which now allows sampling of gas multiplication devices at a speed that is limited only by the gas physics.

The ultimate resolution of drift chambers is presently limited by fluctuations in the deposition of ionization energy and by the angular dispersion of tracks. With improved electronics, new strategies for attacking these limits are being pursued.

Very large tracking detectors present extraordinary challenges in calibrating the devices and in controlling mechanical tolerances. Recent tests have shown that 150 μm spatial resolution can be obtained with 5 meter long wires in a 15 kG magnetic field. A computer-controlled servo system with optical coupling has demonstrated that a heavy frame carrying such wires can be positioned and maintained with respect to a stable reference surface to within 25 μm over long times. The development of laser beams to produce ionizing "tracks" in drift chambers for accurate monitoring of wire positions and pulse height calibration has given very encouraging results.

One of the most difficult problems of instrumentation for ISABELLE is that of particle identification for high momentum charged tracks over large solid angles. Two techniques have recently reached a stage of development to be considered candidates for a relatively compact device, optimized for particle identification and capable of sustaining high rates, which could successfully be integrated into a large detector system. One of these is the ring-imaging Cerenkov counter, which has recently gotten a boost through the development of photoionizing gas mixtures sensitive in a spectral range which permits the use of quartz windows. The other new technique involves an improved method of relativistic rise dE/dx measurement based on longitudinal drift and fast-sampling electronics.

Particle identification of another sort, which is seen to have potentially great importance for ISABELLE experiments, involves a high precision tracking chamber placed very close to the interaction region with the capability of resolving the decay vertices of charmed particles. Space resolutions of the order of 10-30 μm are required. Multi-electrode semiconductor detectors offer promise in this respect. Small prototype devices have demonstrated the required precision and may soon be used in fixed target experiments at CERN and FNAL, but devices of the size and complexity required for colliding beam experiments will require a substantial R&D effort.

Other "new" technologies with the potential for expanding the physics capabilities of ISABELLE experiments include fine grain scintillating fiber hodoscopes with avalanche photodiode readout and the continued development of microchannel plate devices for applications in high energy physics instrumentation.

THE WORKING GROUP ON CALORIMETERS: GENERAL COMMENTS

T. Ludlam, BNL

A great deal of the discussion of calorimeters at this workshop focussed on their implementation in large detector systems to meet the requirements of a range of physics goals. The results of these discussions will be found mainly in Section IV of these proceedings.

The working group on R&D for calorimeters concentrated on the limitations of gas-sampling devices in the Isabelle environment. The premise being that the relative immunity of calorimeters to multiple event pile-up may allow the use of slower detector technologies, even at high rates, without compromising the physics goals. This is an important consideration in view of the very high cost of providing 4π coverage of hadron calorimetry, and the need for a high degree of segmentation.

The members of the working group were:

E.W. Anderson, Iowa State
M. Atac, Fermilab
*W. Carithers, Berkeley
J. Fischer, BNL
V. Radeka, BNL
S.D. Smith, BNL
H.W. Tang, M.I.T.
H.H. Williams, U. Penn

*Chairman

COUNTING RATES FOR PHASE II ISABELLE

S.D. Smith, BNL

In this short note I would like to address the issue of the singles counting rates in large solid angle hadron calorimeters at luminosities of 10^{33} $cm^{-2}sec^{-1}$. By means of comparison I will demonstrate the difference the physical configuration makes in these background counting rates. In addition a sobering calculation of the total calorimeter mass is made. Effects of an analyzing magnetic field are not considered here.

For the purposes of this argument it is assumed that a calorimeter covering the full azimuth as well as the entire pseudo-rapidity interval between $y = \pm 4$ $\left[\text{or } 2.1^\circ \leq \theta \leq 177.9^\circ \text{ since } y = \ln(\cot\theta/2)\right]$ is desired. Figure 1 shows two different possible configurations one of which is called spherical and the other cylindrical based on the shape of the internal area available for tracking in the region $\sin\theta \gtrsim .35$. Both designs imagine θ,ϕ segmentation and have a calorimeter thickness along the particle trajectory that is independent of θ. In all comparisons to be made between the two, we take the inner cylindrical radius to be three quarters of the spherical radius. For this choice, the two configurations have roughly similar total masses. In addition, if we have a dipole or toroidal magnetic analyzing field, this ratio affords the cylindrical geometry with greater analyzing power for $\sin\theta < .73$ where it is needed while the spherical configuration has greater analyzing power only near $\theta = 90^\circ$ where typical particle energies are lower.

Figure 2 gives the total mass estimates for the two calorimeter configurations as a function of the inner spherical radius. Their thickness was taken as five nuclear absorption lengths of uranium. If the final density of the calorimeter is 5 g/cm^3 (10 g/cm^3), this corresponds to a thickness of 2.28m (1.14m). Note the considerable advantage to be gained by maintaining a high density device, particularly at the smaller radii. Figure 3 gives the mass calculation as a function of total thickness in nuclear absorption lengths for the spherical design with a 2 meter inner radius. The total mass escalates rapidly with thickness, particularly at low density. Note the vertical scale. If the cost of these detectors really does run to \$10/lb, the price of such

calorimeters will be considerable.

If the lateral segmentation is chosen to be approximately equal to the average hadronic shower size, we can calculate the rapidity and ϕ intervals covered by each tower. This granularity is shown qualitatively in Fig. 4. In the spherical case the $\Delta\phi$ and Δy bites of each tower increase with decreasing $\sin\theta$, necessitating the abrupt increase in radius at $\theta = 20^{o}$. For the cylindrical case this segmentation is more nearly uniform until the forward end cone is reached at $\sin\theta = .2$. This has the consequence that, since singles rates are uniform in ϕ and nearly so in y, the counting rate in each tower is proportional to its $\Delta y \Delta\phi$ bite. This makes the uniform $\Delta\phi\Delta y$ granularity of the cylindrical geometry attractive from this point of view, as well as from that of single event analysis. In the latter case, jet events deposit particles over a limited range of ϕ and y, and it would seem advantageous that detector properties not vary rapidly with θ. As a final remark, note that the typical shower width varies inversely with density. Increased density affords the possibility of increased segmentation. The resulting decreased $\Delta\phi\Delta y$ bite per tower will result in lower singles rates per tower at a given radius.

To put the counting rate discussion on a slightly more quantitative basis, I use the semi-empirical cross-sections of Wang[1] (See F. Paige, p. 202, 1977 Isabelle Summer Study) for charged pion production to estimate the singles rates in 20 x 20 cm^2 towers at a spherical (cylindrical) radius of 2 m.(1.5 m.), for $L = 10^{33}\ cm^{-2}sec^{-1}$. Comparison with more recent monte carloed particle production data by Paige suggests these rates to be underestimates by approximately a factor of two. The results of these calculations are presented in Figs. 5 and 6. Although the counting rates are quite high, it should be remarked that the average energy of these particles is low, being slightly more than 500 MeV at $\theta = 90^{o}$ and increasing like $1/\sin\theta$ in the forward regions. Clearly, the effects of an analyzing field will be important to the low energy particles that dominate the counting rate.

REFERENCES

1. C.L. Wang, Phys. Rev. D10, 3876 (1974).

FIGURE CAPTIONS

Fig. 1. This is a cutaway side view comparing two differeing configurations for a large solid angle calorimeter. The beams are running left and right in the plane of the page. Full 2π azimuthal coverage is assumed for these discussions. The "spherical" (1a) and "cylindrical" (1b) configurations experience very different counting rates as a function of the polar angle θ, while requiring very nearly the same tonnage of material to construct.

Fig. 2. This is a comparison of the total mass (metric tons) of 5 nuclear absorption length thick uranium calorimeters as a function of the inner radius, r, of the spherical version (solid curves) for two different average densities. The dashed curves show the mass of a cylindrical calorimeter of the same thickness and densities but with cylindrical inner radius, p, equal to 3/4 r.

Fig. 3. Compares the mass required for calorimeters of a fixed inner radius (r = 2 meters or p = 1.5 m) as a function of calorimeter thickness for two differing calorimeter densities.

Fig. 4. This is a schematic comparison of the calorimeter granularity in the ϕ - y plane. The calorimeter is assumed to be segmented transversely into elements approximately equal to the hadronic shower size. Each box represents the $\Delta\phi$, Δy area covered by one of the elements for the spherical (4a) and cylindrical (4b) configurations.

Fig. 5. The counting rate (in megacycles) vs. polar angle experienced by the calorimeter elements at a luminosity of 10^{33} $cm^{-2}sec^{-1}$, is shown for the spherical (5a) and cylindrical (5b) configurations.

Fig. 6. These curves make the same comparison as Fig. 5 but this time as a function of rapidity: 6a) spherical; 6b) cylindrical.

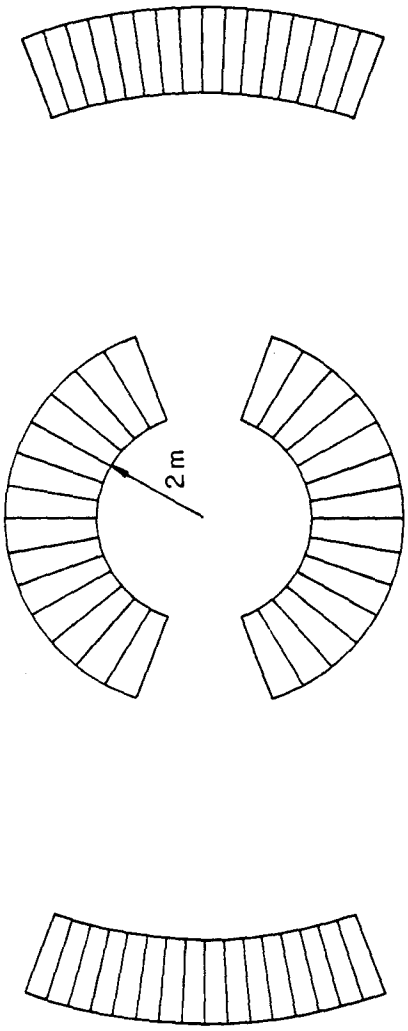

Fig. 1a

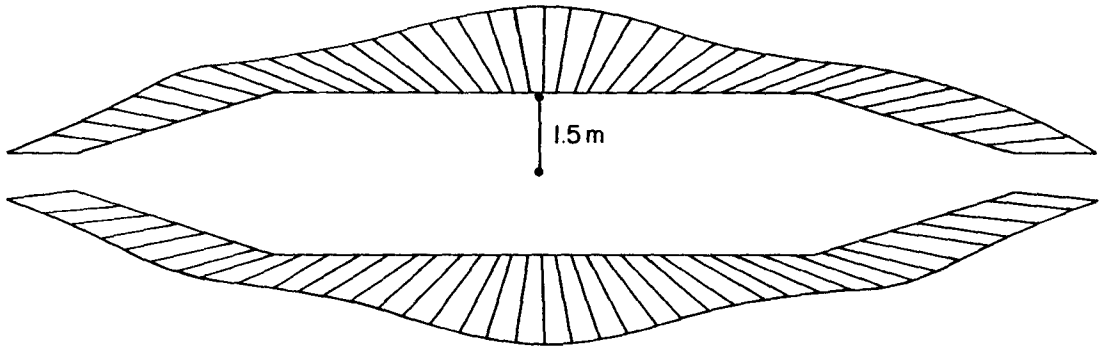

FIG. 1b

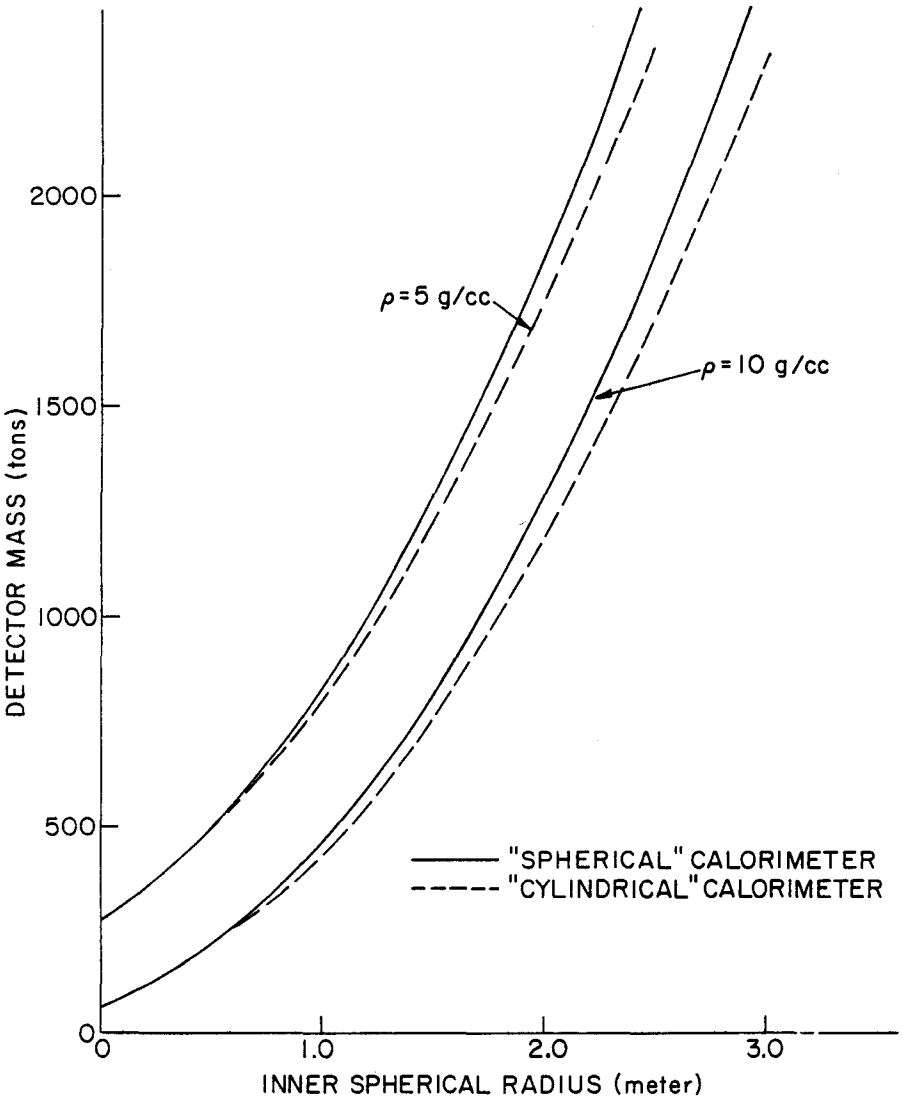
2000
1500
1000
500
0
DETECTOR MASS (tons)
ρ=5 g/cc
ρ=10 g/cc
"SPHERICAL" CALORIMETER
"CYLINDRICAL" CALORIMETER
0
1.0
2.0
3.0
INNER SPHERICAL RADIUS (meter)

Fig. 2

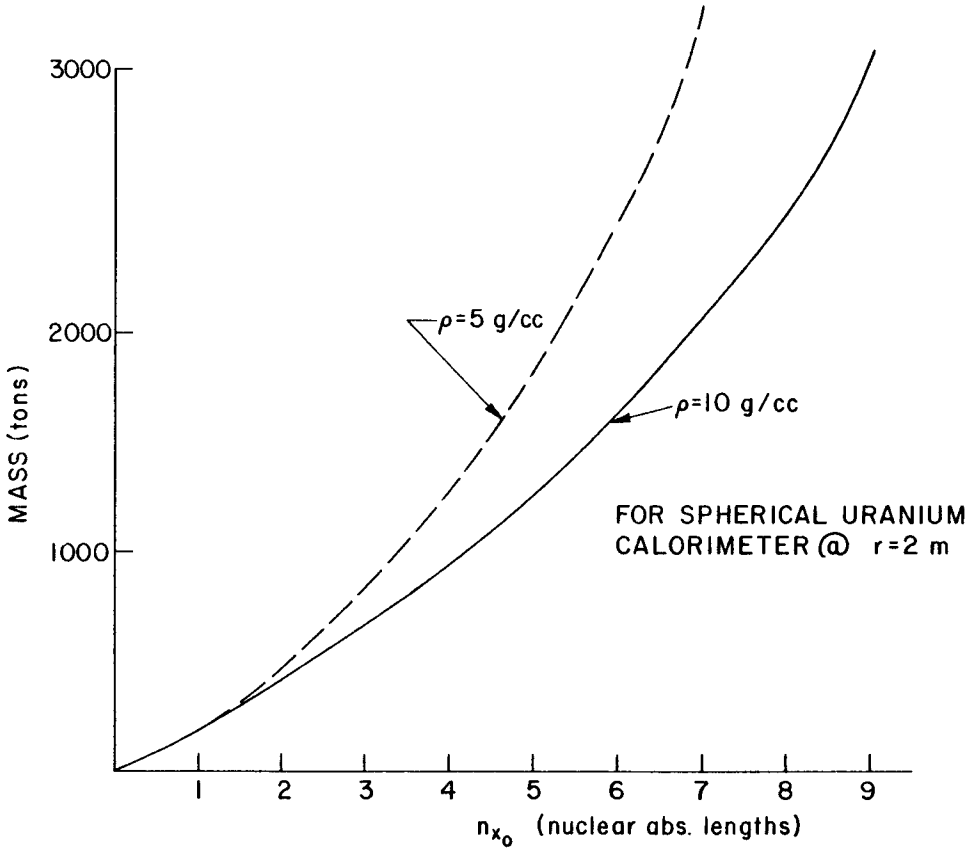
3000
2000
1000
MASS (tons)
ρ=5 g/cc
ρ=10 g/cc
FOR SPHERICAL URANIUM
CALORIMETER @ r=2 m
1
2
3
4
5
6
7
8
9
n_{x_0} (nuclear abs. lengths)

Fig. 3

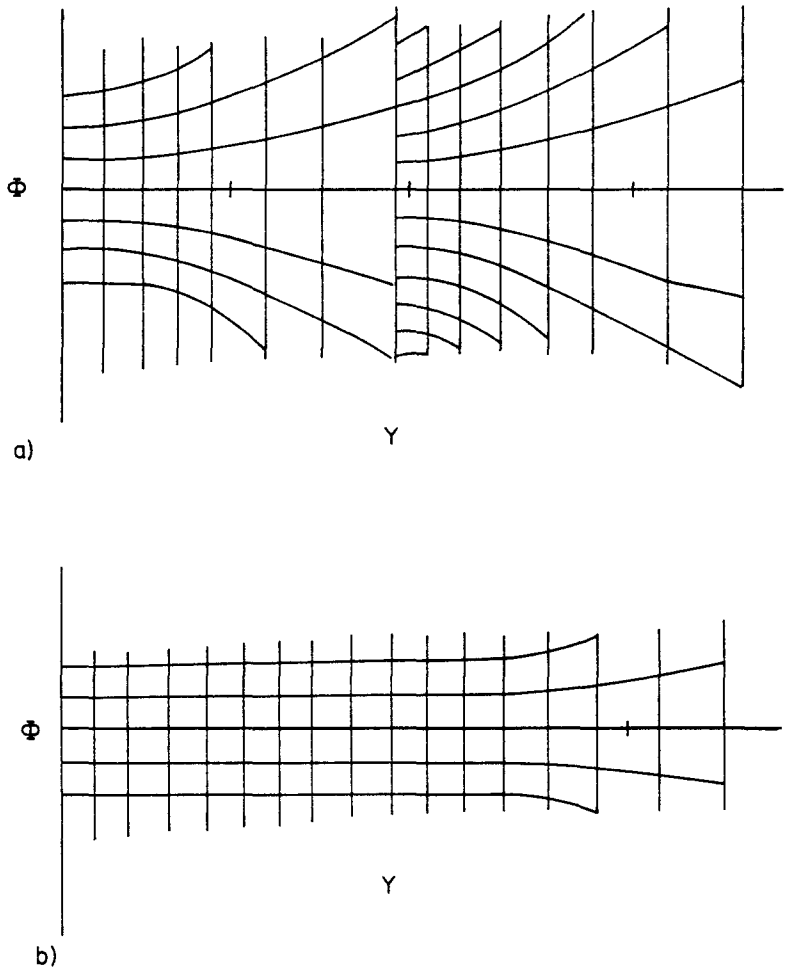

FIG. 4

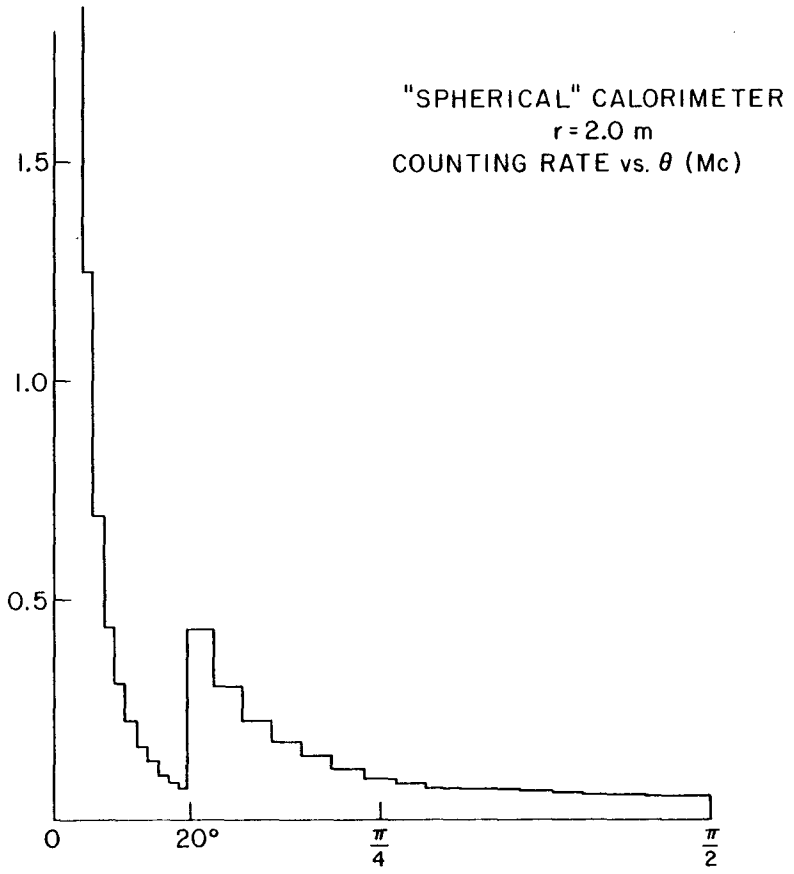
"SPHERICAL" CALORIMETER
r = 2.0 m
COUNTING RATE vs. θ (Mc)
1.5
1.0
0.5
0
20°
π/4
π/2

Fig. 5a

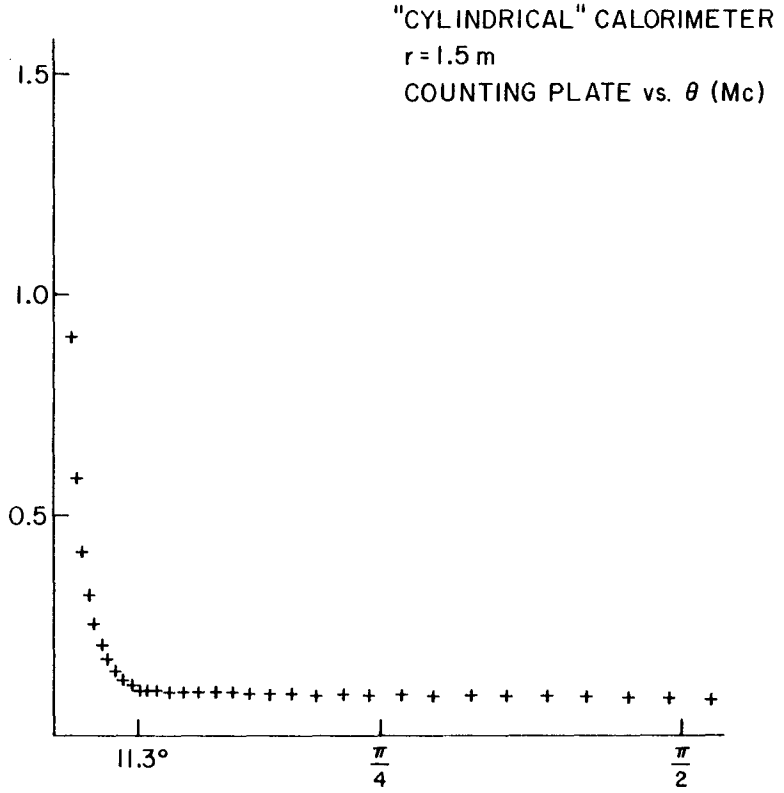
"CYLINDRICAL" CALORIMETER
r = 1.5 m
COUNTING PLATE vs. θ (Mc)
1.5
1.0
0.5
11.3°
π/4
π/2

Fig. 5b

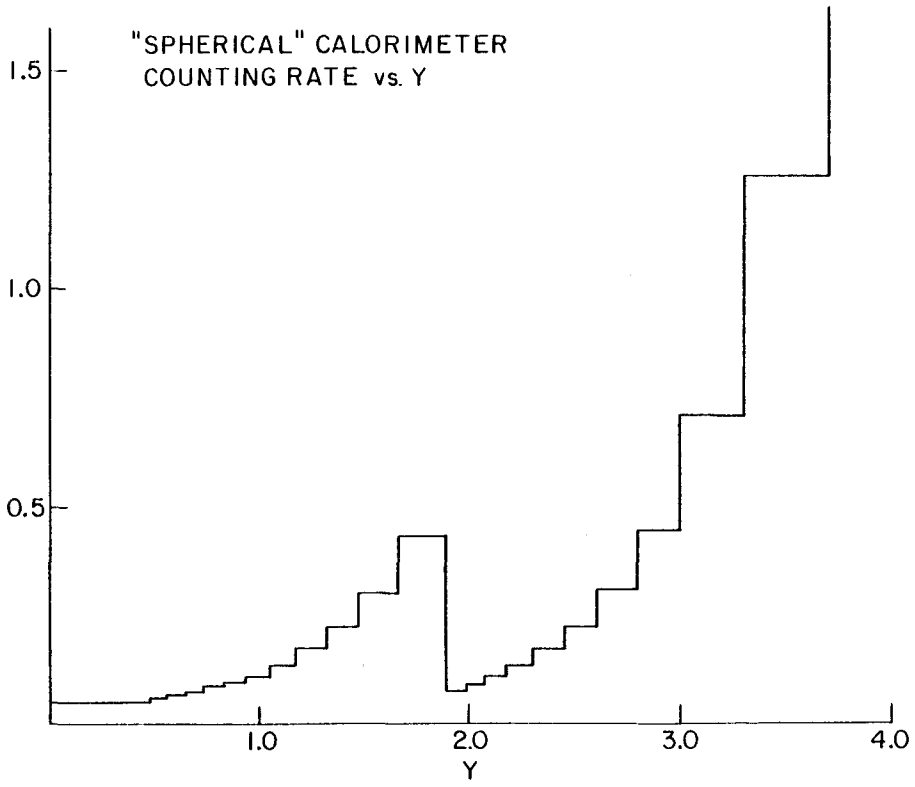
"SPHERICAL" CALORIMETER
COUNTING RATE vs. Y
1.5
1.0
0.5
1.0
2.0
3.0
4.0
Y

Fig. 6a

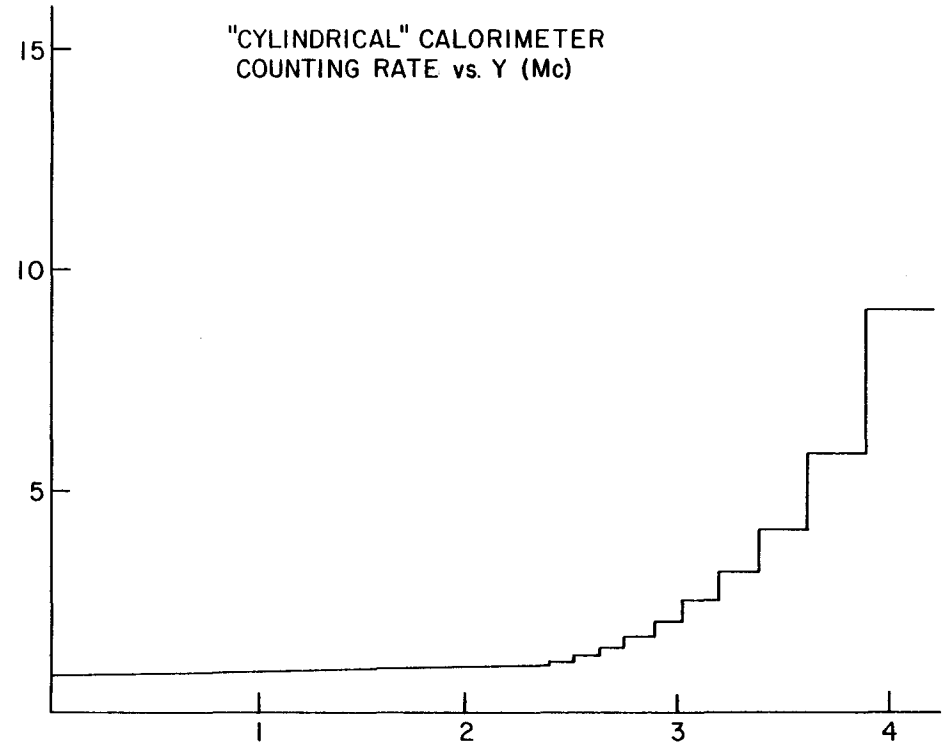

FIG. 6b

ELECTRONIC NOISE AND RESOLVING TIME IN LARGE WIRE CHAMBER CALORIMETERS

V. Radeka and H. H. Williams, BNL

Wire chamber or proportional tube sampling in large calorimeters, such as those to be used in colliding beams experiments at ISABELLE, offer several important features. Foremost among these are capability to operate in a magnetic field, ease of segmentation (particularly if the induced signals on cathode pads are read out), and reasonably short resolving time. The capacitance of such detectors is quite large, however, and at very short shaping times, electronic noise becomes significant.

There exist many different types of wire sampling including: 1) multi-wire proportional chambers (MWPC) with anode readout, 2) proportional tubes with anode readout, 3) MWPC and proportional tubes with cathode pad readout, and 4) geiger-mode and limited streamer chambers with or without cathode pads. The latter types 4) result in very large avalanches and presumably are not suitable for high rate environments due to space charge effects and chamber lifetime considerations. We concentrate on 2) since the relative ease of construction and ruggedness of proportional tubes has already resulted in their being used in large calorimeter systems. The results of this analysis are applicable to 1) and 3).

For purposes of discussion, we hypothesize a more-or-less "conventional" 4π calorimeter detector for colliding beam physics (Figure 1). It consists of a cylindrical calorimeter, with inner radius r = 1.5 m, and length L = 4.5 m. Two end caps with a diameter equal to the outer diameter of the cylindrical calorimeter are employed at each end. The total thickness of the calorimeter is six absorption lengths, and the first twenty radiation lengths are sampled at 1/2 radiation length intervals. While this model calorimeter is clearly not optimized, it is rather similar in size and scope to calorimeters currently proposed or under construction. Within these general characteristics, two different types of calorimeters are considered: 1) a "conventional" one with 40 2.8 mm Pb plates and 46 2 cm Fe plates for the electromagnetic and hadronic sections of the calorimeter and 2) a "fine-sampling" calorimeter with 40 1.5 mm U plates and 16 5 mm U plates for

the electromagnetic and hadronic portions respectively.

We first calculate the noise for sampling with proportional tubes of gap thickness t_g = b and width t_w = b.

The total area of sampling for the model calorimeter is given by

$$A_T = A^{em}_{central} + A^{em}_{end} + A^{h}_{central} + A^{h}_{end}$$

where

$$A^{em}_{central} = 2\pi L \left(kr + \frac{k(k-1)}{2} t_{em}\right)$$

$$A^{h}_{central} = 2\pi L \left(\ell r_1 + \frac{\ell(\ell-1)}{2} t_h\right)$$

$$A^{em}_{end} = 2\pi R^2 k$$

$$A^{h}_{end} = 2\pi R^2 \ell$$

are the sampling areas of the electromagnetic and hadronic portion of the central and end cap regions of the detector and

$$r_1 = r + kt_{em}$$

$$t_{em} = t^{e}_{pl} + t_g$$

$$t_h = t^{h}_{pl} + t_g$$

with t^{em}_{pl} (t^{h}_{pl}) the thickness of each of the k(ℓ) electromagnetic (hadronic) absorber plates. We approximate the capacitance/unit length of the proportional tubes by the result for a cylindrical tube of diameter b:

$$c \text{ (capacitance/meter)} = \frac{2\pi\varepsilon_o}{\ln b/a}$$

where a is the wire diameter. The capacitance/m^2 is then c/b. Table 1 lists the sampling areas, A^{Fe}_{cent}, A^{Fe}_{end}, A^{U}_{cent}, A^{U}_{end}, the total length of wire, and the total capacitance for the Pb-Fe and U calorimeters.

TABLE 1

Sampling areas (for central and end cap regions), total wire length, and total capacitance for Fe and U calorimeters as a function of proportional tube width, b

b (mm)	A^{Fe}_{cent} (m^2)	A^{Fe}_{end} (m^2)	A^{U}_{cent} (m^2)	A^{U}_{end} (m^2)	L^{Fe}_{wire} (km)	L^{U}_{wire} (km)	C_T^{Fe} (μF)	C_T^{U} (μF)
6	5058	5027	14084	15331	1680	4902	18	53
4	4851	4480	12902	11904	2332	6201	27	73
2	4644	3939	11720	8905	4291	10312	59	142

Signal

To determine the signal to noise, consider a minimum ionizing particle traversing a single plane of proportional tubes of total area A followed by a single absorber plate of thickness t_{pl} and density ρ. If the tube width is b, and the number of ionization electrons/m in the gas is n, then the total capacitance is

$$C = A \frac{2\pi\varepsilon_o}{b \ln b/a} , \qquad (1)$$

the number of ionized electrons in the gas is

$$bn$$

and the energy lost in the plate is

$$t_{pl} \rho \frac{dE}{dx} . \qquad (2)$$

Assuming a gas gain G, the total induced charge on the anode is Gbn; however, only a fraction of this charge is collected sufficiently rapidly to be useful. The amount of charge collected within a time t_c is

$$Q(t_c) = \frac{Gnb}{2 \ln b/a} \ln \left(1 + \frac{t_c}{t_o}\right) \qquad t < t_o \left(\frac{b}{a}\right)^2 \qquad (3)$$

where

$t_o = \frac{a^2}{4} \frac{\ln b/a}{\mu_+ V_o}$

a = anode wire diameter

V_o = anode voltage

μ_+ = positive ion mobility ~ 2×10^{-4} m^2/Vsec

For a = 35μ, b = 4 mm, and V_o = 1500 volts, t_o = 4.8 nsec. Then the fraction of charge collected after time t is

t	$Q(t)/Q_T$
t_o	.073
10 ns	.119
20 ns	.173
40 ns	.236
100 ns	.325

The number of electrons, collected within time t_c, per GeV of energy deposition in the calorimeter is then

$$S(e/GeV) = \frac{Gnb \ln (1 + t_c/t_o)}{2 \ln(b/a) t_{pl} \rho \, dE/dx} \tag{4}$$

Noise

A typical detector-amplifier circuit configuration is shown in Figure 2 and the corresponding equivalent circuit for noise analysis is shown in Figure 3a.(1)

A bipolar trapezoidal filter weighting function is asumed as shown in Figure 3b. The noise filter time is t_{nf} and the flattop width is taken to be $t_c + t_D^{max}$ where t_c is the charge collection time for a single avalanche and t_D^{max} is the maximum drift time, $t_D^{max} = 10^4 b$, (where b is the full cell width in meters and t_D^{max} is in nanoseconds). The resolving time is assumed to be equal to the full width of the shaping signal plus the width, $t_c + t_D^{max}$, of the input signal.

For short resolving times, the parallel noise contribution may be made negligible; in this case the optimum series equivalent-noise-charge is

$$ENC_{s\ opt} = 4\sqrt{2} e_n \left[C_d C_A \left(1 + \frac{C_d}{C_b}\right) \right]^{1/2} \frac{1}{[t_{nf}]^{1/2}} \tag{5}$$

obtained for a transformer with n:1 turns ratio where

$$n = \left[\frac{C_d}{C_A \left[1 + C_d/C_b\right]} \right]^{1/2},$$

We shall take as typical values

$C_A \sim 30$ pF

$e_n \sim 1$ nV/Hz$^{1/2}$

$C_b \gg C_d$

Then

$$ENC_{s,opt} \sim 5.9 \times 10^6 \left[\frac{C_d\ (\mu f)}{t_{nf}(\text{nsec})}\right]^{1/2} \text{ electrons} \qquad (6)$$

Combining equations (4) and (6), the ENC in GeV for a sampling plane of area A and capacitance C_d is

$$ENC\ (\text{GeV}) = \frac{5.9 \times 10^6 \cdot 2 \ln(b/a)\ t_{pl}\ \rho\ dE/dx}{Gnb\ \ln\ (1 + t_c/t_o)} \left[\frac{C_d\ (\mu F)}{t_{nf}(\text{nsec})}\right]^{1/2}$$

$$= \text{const}\ \frac{2\ \ln\ b/a}{b\ \ln\ (1 + t_c/t_o)} \left[\frac{A}{2b\ \ln(b/a)\, t_{nf}}\right]^{1/2}$$

To determine the noise for a given resolving time t_R, it is necessary to optimize the maximum drift time t_d^{max} (nsec) $\sim$ 104 b (m), the collection time t_c, and the noise filtering time t_{nf} subject to the constraint $t_R = 3(t_c + t_D^{max}) + t_{nf}$.

Ignoring the $[\ell n\ (b/a)]^{1/2}$ factor, and the dependence of t_o on b (since it contributes as $\ell n\ \ell n$ b), the primary tradeoffs result from the fact that 1) the primary ionization increases as b 2) the capacitance increases as b^{-1} (and hence the noise as $b^{-1/2}$), and 3) the noise increases as $\ell n\ t_{nf}^{-1/2}$ and 4) the signal decreases $\alpha\ \ell n\ (1 + t_c/t_o)$. In the crude approximation that b t_{nf} decreased proportional to a decrease in t_R (with t_c held fixed), the noise in GeV would increase proportional to t_R^{-2}. Figures 4 and 5 show the actual change in the noise as a function of t_R, where for each value of t_R, b, t_c and t_{nF} have been optimized to achieve the minimum noise. Since the minimum noise is in some cases a slowly varying function with respect to any one of the parameters, there exists some flexibility in choosing the most appropriate values of b, t_c and t_{nF} while still obtaining noise near the true minimum. One set of parameters corresponding to t_R = 160 nsec, 260 nsec, and t_R = 360 nsec is shown in Table 2.

TABLE 2

A set of detector and shaping parameters producing (nearly) minimum noise as a function of t_R

t_R (nsec)	t_c (nsec)	t_{nf} (nsec)	b (cm)
360	40	60	.6
260	20	80	.4
160	15	25	.3

Figure 4 shows the noise for a total energy trigger, i.e., one in which all calorimeter elements are summed. The noise contributions from the electromagnetic and hadronic portions of the calorimeter are shown separately. Figure 5 shows the noise for a limited trigger, such as one searching for "jets" for example, in which elements over $\Delta\theta = \pi$, and $\Delta z = 1$ m are summed (.07 of 4π steradians).

In each case, the (total) gas gain was assumed to be 1000. It may in fact be possible to operate with gas gains as large as 1000, but the limits imposed by chamber lifetime and, in particular, space charge limits are reasonably stringent and need to be further investigated. It should be noted that the parameters listed in Table 2 for $t_R = 160$ nsec are probably not obtainable, so that the actual noise for that point is likely to be larger than shown.

References

1. W.J. Willis, V. Radeka, NIM 120 (1974) 221.

2. V. Radeka, IEEE Trans. Nucl. Sci. NS-21, No. 1 (Feb. 1974) 51.

Fig. 1 Model calorimeter for noise calculations. The sampling thickness of hadron calorimeter is discussed in the text.

Fig. 2 Detector-Preamplifier circuit configuration.

Fig. 3 (a) Equivalent circuit for detector plus preamplifier. (b) Pulse shaping following preamplifier. t_c = charge collection time for single avalanche, t_D^{max} = maximum drift time, t_{nF} = noise filtering time, t_R - resolving time.

Fig. 4 Electronic noise in GeV assuming a total energy trigger (summing the entire calorimeter) and a gas gain = 1000. The noise is shown separately for the hadronic and electromagnetic portions of the calorimeter. t_R is the resolving time.

Fig. 5 Electronic noise in GeV for a limited solid angle trigger (summing 0.07 of 4π) assuming the gas gain = 1000. The noise is shown separately for the hadronic and electromagnetic portions of the calorimeter. t_R is the resolving time.

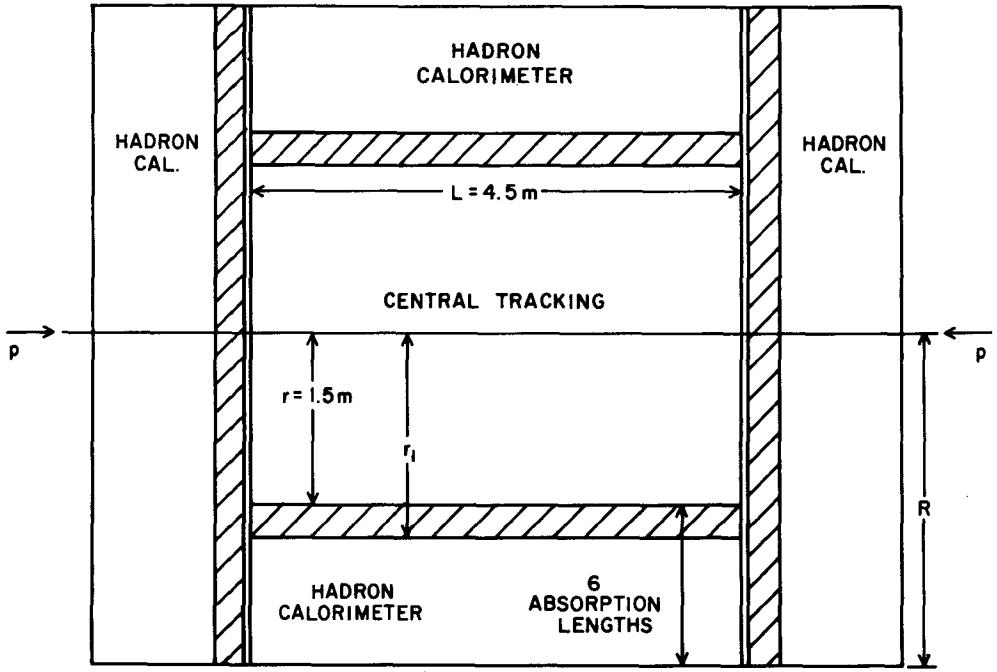
HADRON
CALORIMETER
HADRON
CAL.
HADRON
CAL.
L = 4.5 m
CENTRAL TRACKING
p
p
r = 1.5m
r_1
R
HADRON
CALORIMETER
6
ABSORPTION
LENGTHS
ELECTROMAGNETIC CALORIMETER
20 RADIATION LENGTHS, 1/2 R.L. SAMPLING

Fig. 1

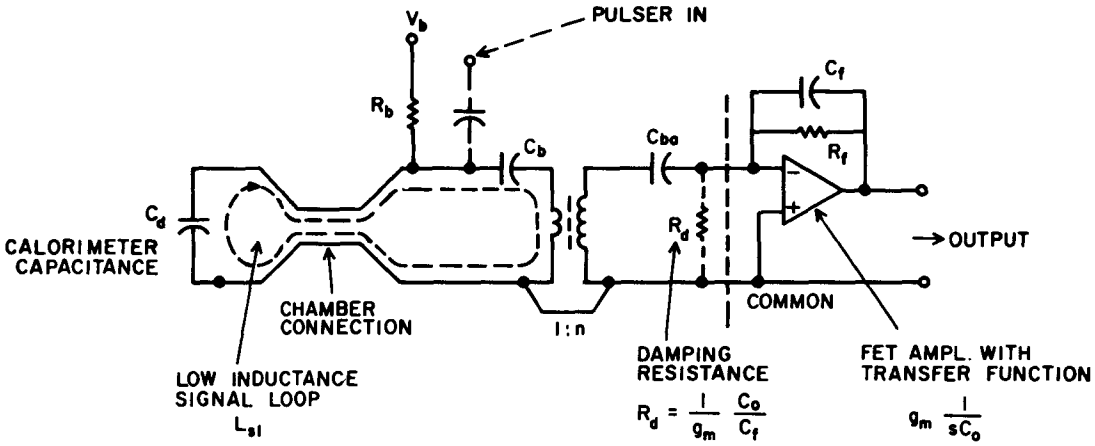
V_b
PULSER IN
R_b
C_b
C_{ba}
C_f
R_f
C_d
CALORIMETER CAPACITANCE
R_d
→OUTPUT
CHAMBER CONNECTION
1:n
COMMON
LOW INDUCTANCE SIGNAL LOOP
L_{sl}
DAMPING RESISTANCE
$R_d = \frac{1}{g_m}\frac{C_o}{C_f}$
FET AMPL. WITH TRANSFER FUNCTION
$g_m \frac{1}{sC_o}$

Fig. 2

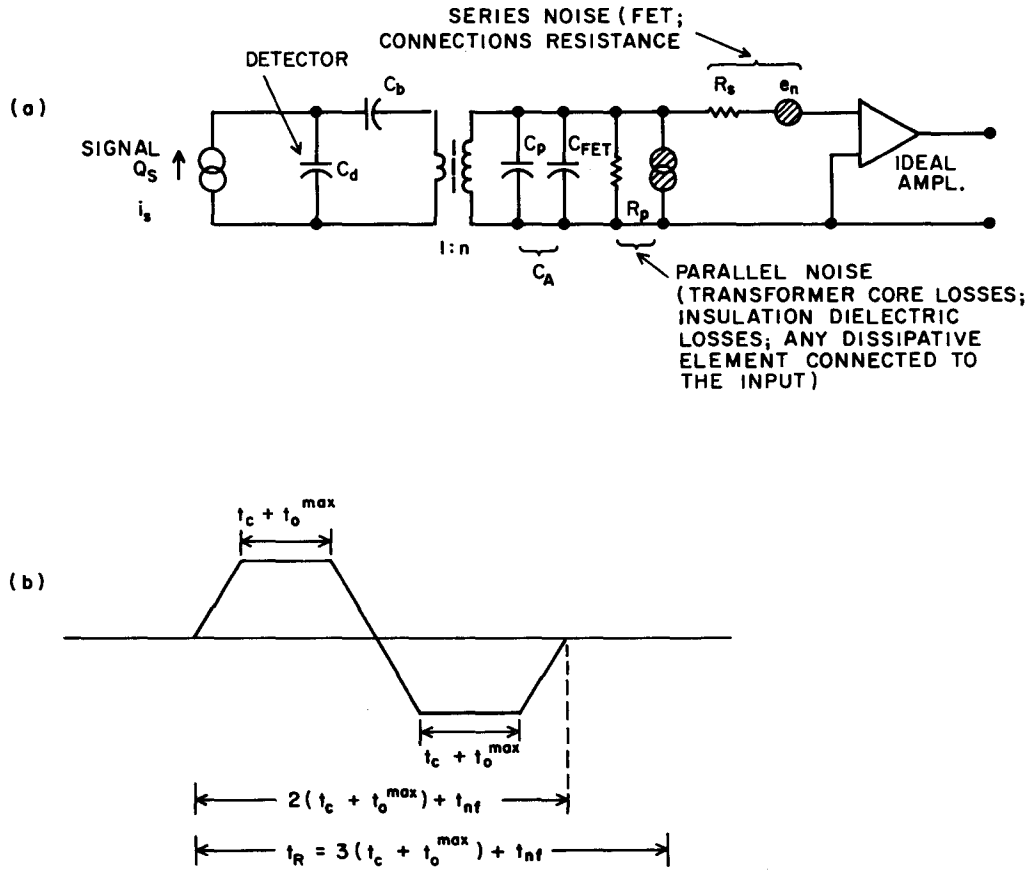
(a)
SERIES NOISE (FET; CONNECTIONS RESISTANCE
DETECTOR
C_b
R_s
e_n
SIGNAL
Q_s
i_s
C_d
C_p
C_{FET}
R_p
IDEAL AMPL.
1:n
C_A
PARALLEL NOISE (TRANSFORMER CORE LOSSES; INSULATION DIELECTRIC LOSSES; ANY DISSIPATIVE ELEMENT CONNECTED TO THE INPUT)
(b)
$t_c + t_o^{max}$
$t_c + t_o^{max}$
$2(t_c + t_o^{max}) + t_{nf}$
$t_R = 3(t_c + t_o^{max}) + t_{nf}$

Fig. 3

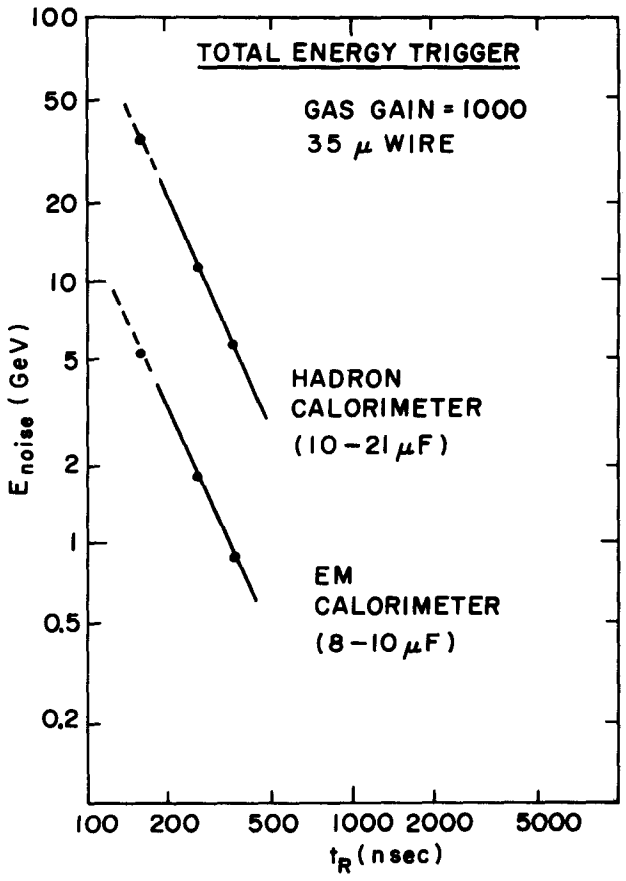
TOTAL ENERGY TRIGGER
GAS GAIN = 1000
35 μ WIRE
HADRON
CALORIMETER
(10 – 21 μF)
EM
CALORIMETER
(8 – 10 μF)
E noise (GeV)
100
50
20
10
5
2
1
0.5
0.2
100
200
500
1000
2000
5000
t_R (nsec)

Fig. 4

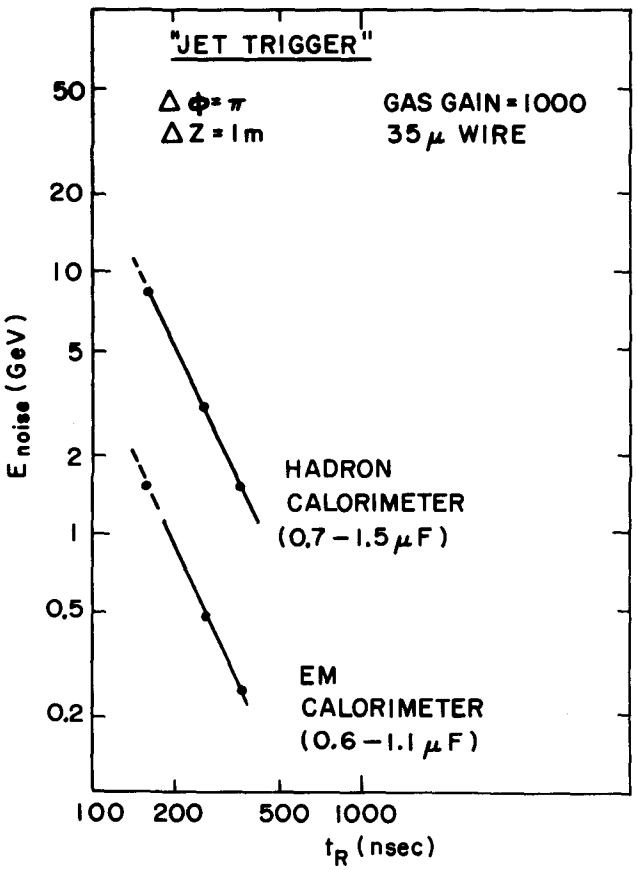
"JET TRIGGER"
Δφ=π
ΔZ=1m
GAS GAIN=1000
35μ WIRE
50
20
10
5
2
1
0.5
0.2
E noise (GeV)
HADRON
CALORIMETER
(0.7 – 1.5 μF)
EM
CALORIMETER
(0.6 – 1.1 μF)
100
200
500
1000
t_R (nsec)

Fig. 5

RATE ESTIMATE FOR A SELF-QUENCHING STREAMER HADRON CALORIMETER AT ISABELLE

M. Atac, Fermilab

We consider a hadron calorimeter composed of 35 one-inch iron plates and 35 extruded aluminum chambers

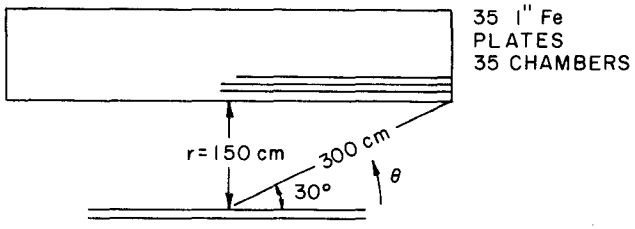

The chamber specifications are as follows:

Wire spacing: 1 cm

Chamber gap: 1 cm

Wire diameter: 50 μm

Gas: 50% A - 50% C_2H_6 flowing through CH_3CH_2OH at 0°C.

Pressure: 1.6 atm

Total number of electrons per streamer[1]: $10^8 e^-$

A large part of the contribution to the rates will be from π^0's. This can be estimated from the calculations of F. Paige[2] by taking 1/2 of the $\pi^{\pm}$ cross section approximately[3]

$$\frac{d\sigma}{d\Omega} \simeq 7 \times 10^{-27}\ \theta^{-1/2}$$

for $0.5 \leq \theta \leq \pi/2$, $\sqrt{s} = 800$ GeV.

Then the rate per $\Delta\Omega$ for a given luminosity L is given by

$$n = L \frac{d\sigma}{d\Omega} \Delta\Omega \text{ (particles sec}^{-1}\text{)}.$$

For the region $30 \leq \theta \leq 150$ covered by the calorimeter (see Ref. 3, p.140):

$$n = L \frac{d\sigma}{d\Omega} \frac{1}{r} \frac{2\pi}{N} \sin^3\theta \text{ (particles cm}^{-1}\text{sec}^{-1}\text{)}.$$

Thus, maximum n for $\theta = 30°$, $L = 10^{33}$, $r = 150$ cm, $N = 2\pi r = 940$ cm.

$$n \equiv \frac{7 \times 10^{-27}}{0.25} \times 10^{33} \times \frac{1}{150}\,\frac{2\pi}{940} \times 0.125 \text{ (number of } \pi^{\circ}\text{'s per cm}^2 \text{ per second at } 30°$$

$$n = \frac{5.5 \times 10^{6}}{0.25 \times 1.4 \times 10^{5}} = 157\ \pi^{\circ}\text{'s of all energies.}$$

The majority of π°'s fall inbetween 0.5 to 2 GeV energies. Take an average energy of 1 GeV. 1 GeV γ will produce less than 10 tracks at the shower maximum. Maximum total number of tracks at the shower maximum per cm wire per second at $r = 150$ cm at $\theta = 30°$ angle for $L = 10^{33}$,

$$n' = 1570 \text{ (tracks} \equiv \text{streamers cm}^{-1}\text{sec}^{-1})$$

Then the total number of electrons

$$q = 1.6 \times 10^{11}\ e^{-}\text{cm}^{-1}\text{sec}^{-1}$$

Take the critical number of electrons per centimeter to be a lifetime given by Walenta[3] for Argon/isobutane + methylal: 3.3×10^{19} electrons (this mixture is closest A - C_2H_6 + CH_3CH_2OH in nature).

Thus a lifetime estimate would be

$$t_{\text{seconds}} = \frac{3.3 \times 10^{19}}{1.6 \times 10^{11}} = 2 \times 10^{8} \text{ seconds}$$

$$t_{\text{years}} \simeq 7 \text{ years.}$$

REFERENCES

1. M. Atac, Fermilab Note FN-339, July 1981.
2. F.E. Paige, Proc. 1977 ISABELLE Summer Workshop, Brookhaven, BNL 50721, p.202
3. H. Okuno et al., Proc. 1978 ISABELLE Summer Workshop, Brookhaven, BNL 50885, p.139.

THE WORKING GROUP ON WIRE CHAMBERS: GENERAL COMMENTS

T. Ludlam

The primary questions confronting this group were i) how can wire chamber systems cope with the high rates at Isabelle? and ii) how can we achieve and maintain the inherent resolution of drift chambers in very large detector arrays?

Experience with existing large central track detectors was reviewed, as well as proposals for future detectors. Possible scenarios for implementing wire chambers at Isabelle were considered, taking advantage of new advances in electronics, small drift cells, and special geometries for streamlined pattern recognition in order to handle the rates. New results were presented on chamber lifetime under particle loading at high luminosities.

The use of laser beams to produce ionization tracks in drift chambers for accurate correction of systemmatic errors due to magnetic fields, mechanical tolerances, gravitational and electrostatic deflections of wires, etc. was described. This appears to be a sound technology whose development will be very important for fully exploiting drift chamber precision in large detectors. Also described - another wave of the future for large detector systems - was a computer-controlled servo system with optical coupling which can maintain the position of large chamber structures with respect to a stable reference surface to within $\sim$25 μm over long periods of time.

The members of the working group were:

K. Amako, U. Penn.
M. Atac, Fermilab
*U. Becker, MIT
M. Capell, MIT
P. Duinker, NIKHEF
H.J. Hilke, CERN
J. Paradiso, MIT
E. Platner, BNL
R.J. Wu, MIT/Peking

*Chairman

VERY LARGE AND ACCURATE DRIFT CHAMBER

U. Becker, M. Chen, Y. H. Chen[1], G. Y. Fang, J. Li[1],
D. Luckey, D. A. Ma[1], C. M. Ma, X. R. Wang[1], J. W. Wu[1],
R. J. Wu[1], C. H. Ye[2].

Massachusetts Institute of Technology

[1]On leave from Institute of High Energy Physics, Peking

[2]On leave from University of Nanking

D. Lowenstein, A. H. Walenta

Brookhaven National Laboratory

P. Duinker, J. C. Guo, F. Hartjes, B. Hertzberger

NIKHEF

Presented at the ISA 1981 Summer Study

by

Ulrich Becker

I. EXPERIMENTAL APPLICATION

The energies of colliders have increased from the SPEAR/DORIS ~ 2 x 5 GeV to PETRA/PEP ~ 2 x 20 GeV and are now approaching 2 x 270 GeV at the CERN collider. The energy increase was by no means matched by the analyzing powers of the detectors remaining within factors two at the original configuration of $B \cdot \ell = 5 \cdot 1$ kgauss-meter.

We recall that new particles in fact can and have been detected from hadronic reactions; however, excellent mass resolution was necessary:

In 1974 at BNL[1)] $pp \to J\,X$, $\quad J \to m_{ee}$ measured with $\frac{\Delta m}{m} = 0.3\%$

In 1977 at FNAL $pp \to T\,X$, $\quad T \to m_{\mu\mu}$ measured with $\frac{\Delta m}{m} = 2\%$

which was just barely enough to establish the multiple states T, T', T". Therefore we must ask the question whether $\Delta m/m = 1\%$ at, say, 100 GeV is indeed feasible as to have a detector with the potential of resolving multiple states and measuring the width of Z^0 accurately enough to determine the number of neutrino channels it may decay into. Such a detector is shown in Fig. 1a in the side view and in Fig. 1b in an end view. A 15 kgauss solenoidal field was chosen and a central drift chamber samples the track over $\ell \simeq 2$ m in order to maximize the resolution, which is proportional to $B\ell^2$. Hadrons are measured in the inner calorimeter, shielding the chamber from high multiplicity confusion. Muons will penetrate the calorimeter, be momentum analyzed in the chamber, and be identified by penetration into the outer chamber through the iron yoke. All these components are recognizable in Figs. 1 and 2--the hadron calorimeter, the trigger counters, and the external muon chambers. The dimensions of various elements starting at the intersection point are as follows:

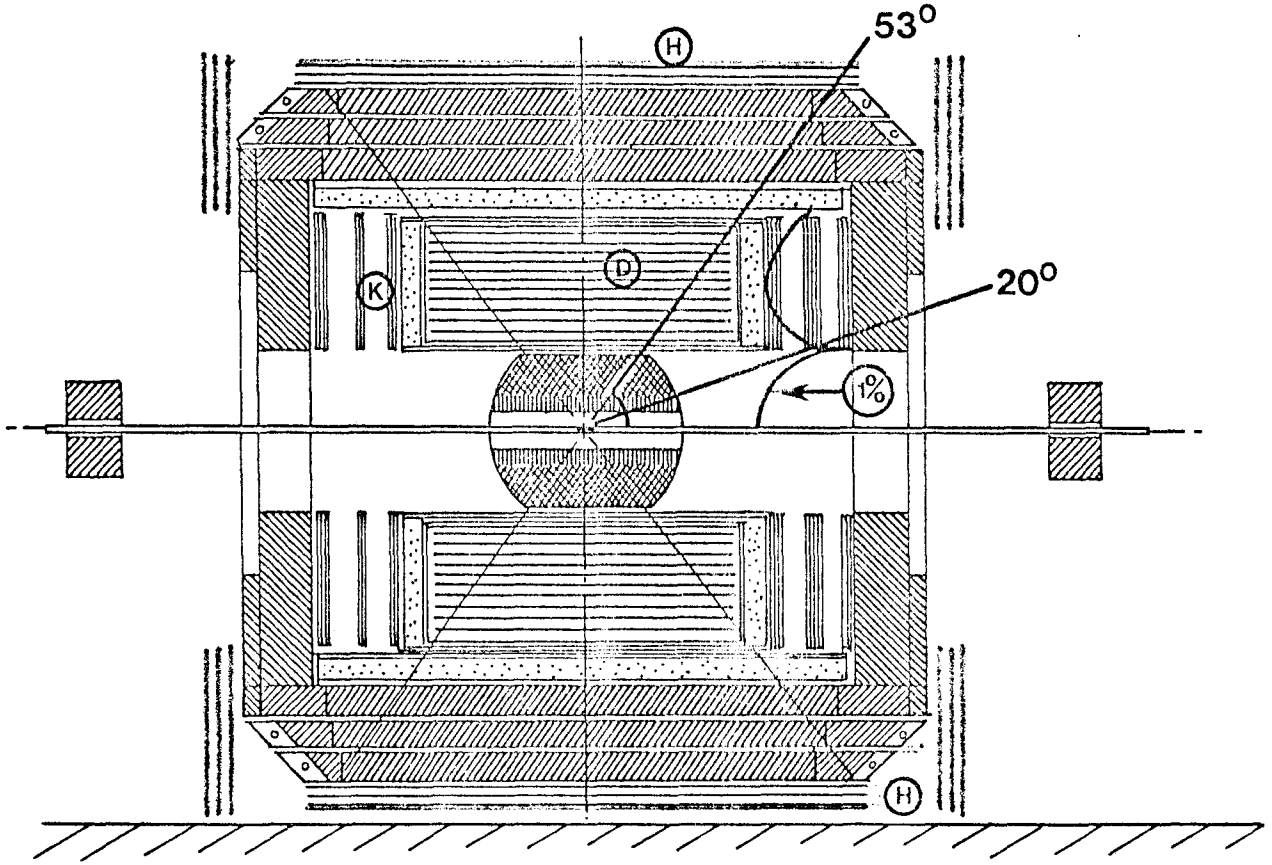

Fig. 1a

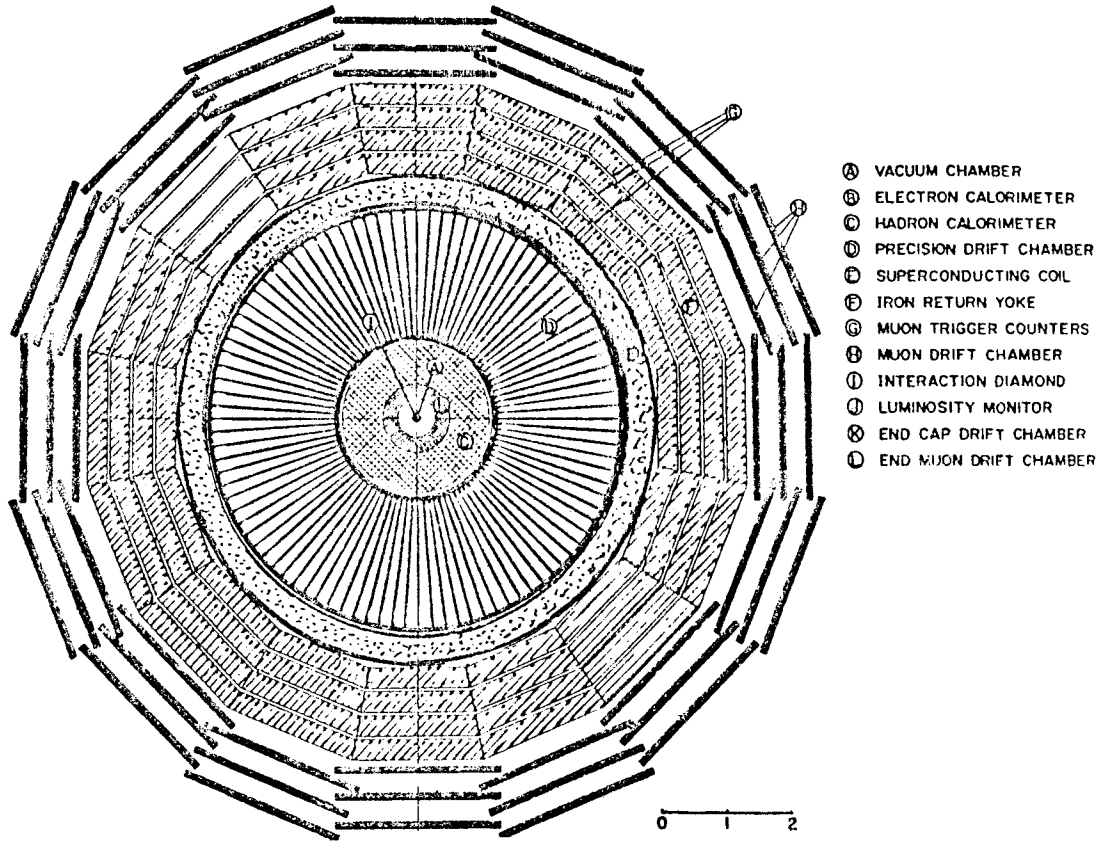
Ⓐ VACUUM CHAMBER
Ⓑ ELECTRON CALORIMETER
Ⓒ HADRON CALORIMETER
Ⓓ PRECISION DRIFT CHAMBER
Ⓔ SUPERCONDUCTING COIL
Ⓕ IRON RETURN YOKE
Ⓖ MUON TRIGGER COUNTERS
Ⓗ MUON DRIFT CHAMBER
Ⓘ INTERACTION DIAMOND
Ⓙ LUMINOSITY MONITOR
Ⓚ END CAP DRIFT CHAMBER
Ⓛ END MUON DRIFT CHAMBER
0
1
2

Figure 1b

TABLE 1

Element	Radial Distance	Length
Beam pipe	0.000 - 0.050 m	5.0 cm
Calorimeter	0.050 - 1.195	114.5
Inner pressure tank wall	1.195 - 1.270	7.5
Carrier ring central chamber	1.270 - 1.320	5.0
Adjustment gadgets	1.320 - 1.335	1.5
Drift tubes	1.335 - 1.390	5.5
Length of cell with 160 wires	1.390 - 3.030	164.0
Drift Tubes	3.030 - 3.085	5.5
Adjustment gadgets	3.085 - 3.100	1.5
Space for outside carrier	3.100 - 3.150	5.0
Pressure tank	3.150 - 3.225	7.5
Space for coil	3.225 - 3.765	54.0
Iron	3.765 - 5.125	136.0
Outside chambers	5.125 - 5.825	70.0

The side view of the detector in Figure la shows in the central region a huge cylindrical drift chamber which determines the muon momenta with high precision over the range $53^{o} < \theta < 143^{o}$ covering 60% of the solid angle. In the forward direction and down to 20^{o} from the beam axis the muons are measured by three clusters of toroidal chambers with wires orthogonal to the beam.

THE CENTRAL DRIFT CHAMBER

It is designed to provide a mass resolution $\Delta m/m \leq 1\%$. Once a very high mass resonance is observed, such resolution is necessary to prove that the width is in fact the one demanded from the coupling strength of Z^{o}.

For example, in the G.W.S. hypothesis with one Z^{o} and $\sin^{2}\theta_{w} = .23$, one expects $\Gamma\ (Z \rightarrow \text{all}) = 2.50$ GeV with partial contributions of 150 MeV from each sort of $\nu\bar{\nu}$ pairs and 262 MeV from $t\bar{t}$. Uncertainties in these values from $\sin^{2}\theta_{w}$ will be eliminated from knowledge of $m(Z)$. Low statistics experiments are not useful in this realm since the statistical error on the measured width is too big. For 140 observed events, which approximates the yearly yield of the CERN collider, one is limited by statistics rather than resolution:

$$\Gamma \pm \frac{\sqrt{2}\sigma}{N} \simeq 2.5 \pm 0.25 \text{ GeV},$$

which does not consider errors from background subtraction. The luminosity of ISABELLE allows us to obtain $N = 10^{3}$ events, thus removing such limitation.

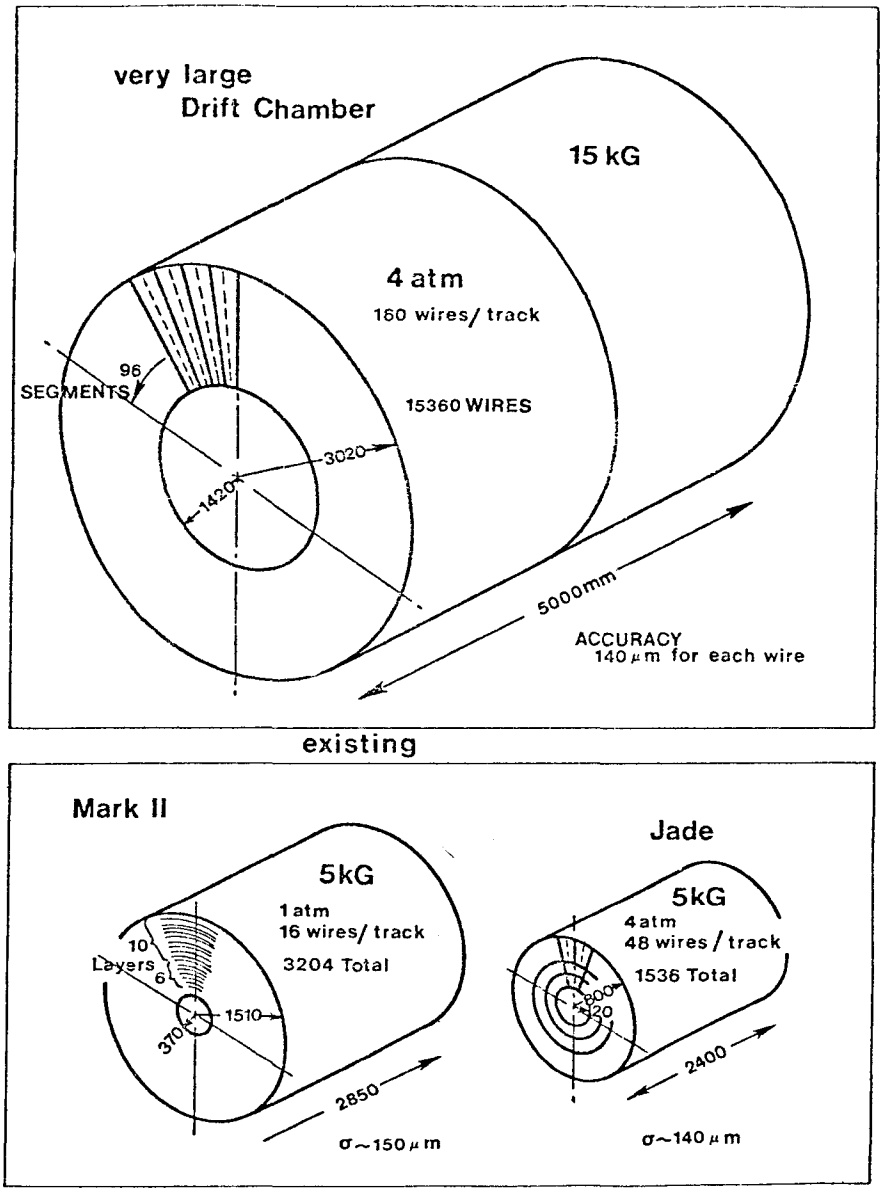
very large
Drift Chamber
15 kG
4 atm
160 wires/ track
96
SEGMENTS
15360 WIRES
3020
1420
5000mm
ACCURACY
140 μm for each wire
existing
Mark II
5kG
1 atm
16 wires/ track
3204 Total
10
Layers
6
1510
370
2850
σ~150 μm
Jade
5kG
4 atm
48 wires / track
1536 Total
800
320
2400
σ~140 μm

Figure 2

DESIGN

The chamber has 5 m long signal wires parallel to the beam and also to the magnetic field of the solenoid. They are supported in the middle so that the momentum determination of muons emitted in either hemisphere is unobstructed. Figure 2 shows this chamber in comparison to the size of existing operational chambers.* The chamber is assembled of 96 segments of 160 wires each, 15360 total. The wire spacing of 1 cm is sufficient to make 160 independent[2] measurements of the curved tracks over a projected radial distance of 142-302 cm. By measuring the track N times an improvement of resolution by $1/\sqrt{N}$ is expected[2]. However, this implies a setting accuracy of

$$\sigma' \simeq \frac{150\,\mu}{\sqrt{160/3}} = \pm\ 21\,\mu$$

for the 160 wires using 3 points for a p-measurement. The accuracy of $\sigma = 150\ \mu$ for individual wires of equivalent length has been achieved in existing chambers[1]. Since the maximal drift path is 9.8 cm the effects of diffusion have to be diminished by having the chamber at above atmospheric pressure.

The dimensions and parameters of the chamber are given in Table 2. At these huge sizes the deflection of the walls under pressure will be substantial. We therefore will attach the 96 chamber segments to an entirely different cylindrical carrier which is put stress-free into the pressure tank. This carrier will serve as the reference frame for the setting accuracy.

---

* Much of the design has been learned from the JADE chamber[1].

TABLE 2

CENTRAL CHAMBER PARAMETERS

Structure	15360 signal wires in 96 segments of field shaped drift chamber with 160 signal wires.	
Wires	supported in middle, active length	500 cm
	gold-coated Tungsten Rhenium wire	diameter = 49 μm
	Tension	500g
	Field wires silver-coated Copper Beryllium	diameter = 100 μm
	Tension	1000g
Pressure Vessel	cylindrical with 5 cm Al walls (for 4 atm)	
	overall length	294 cm
	inner diameter	120 cm
	outer diameter	323 cm
Gas	2.5 atm Argon: 1.5 atm C_2H_6	
	total volume	150 m^3
	recycled/purified	900 m^3/day

TABLE 3

ELECTRICAL PARAMETERS

Voltage on signal wires	max 3.8 kV
Voltage on field wires	0 kV
Voltage on field shaping foil	-29.0 kV
Drift field	3.0 - 4.0 kV/cm
Drift velocity	5.1 cm/μs
Drift angle in 15 kG	~19°

Electronics

15630 amplifiers/discriminators with slew $\leq$ 1 ns

15630 time digitizers with 1 ns setting accuracy

SEGMENT STRUCTURE

The electrical parameters of the central precision chamber are summarized in Table 3. Figures 3 and 4 show the detailed structure of one segment and the way it is attached to the reference carrier. The design is governed by two considerations:

a. The muon momenta of these very heavy resonances will be about 50 GeV. Transversing the 160 cm of the segment in a 15 kG field will cause a sagitta of 3 mm only. That means most rays (90%) are confined to one segment without crossing the foil or the signal wire plane.

b. The precise momentum determination relies on the relative time differences measured by the 160 wires only. The absolute positioning of one of these segments affects only the opening angle and is uncritical for the mass resolution.

Consequently the design concentrates on having 160 measurements under identical conditions.

Therefore the field of the solenoid was optimized such that throughout the fiducial volume of the chamber the field is constant to better than 1% and thereby the drift angle due to Lorentz force, too.

However, the maximal drift distance changes from 4.65 cm at the innermost to 9.88 cm at the outermost wire. Structures with more homogeneous distances are inadvisable because they necessarily lead to track measurements invoking drift paths coming from left and right, which are different in the magnetic field. Furthermore, the absolute timing of the trigger signal becomes crucial[3] to $\leq$ 1 ns.

Therefore we introduce a field shaping foil compensating for the wedge shape to a constant drift field of 4kV/cm. The 200 μm G10 foil has 0.64 mm conductor alternating with 0.64 mm gap to provide insulation against breakdown. Having only 1.88° inclination, this grating is fine enough so one can safely neglect

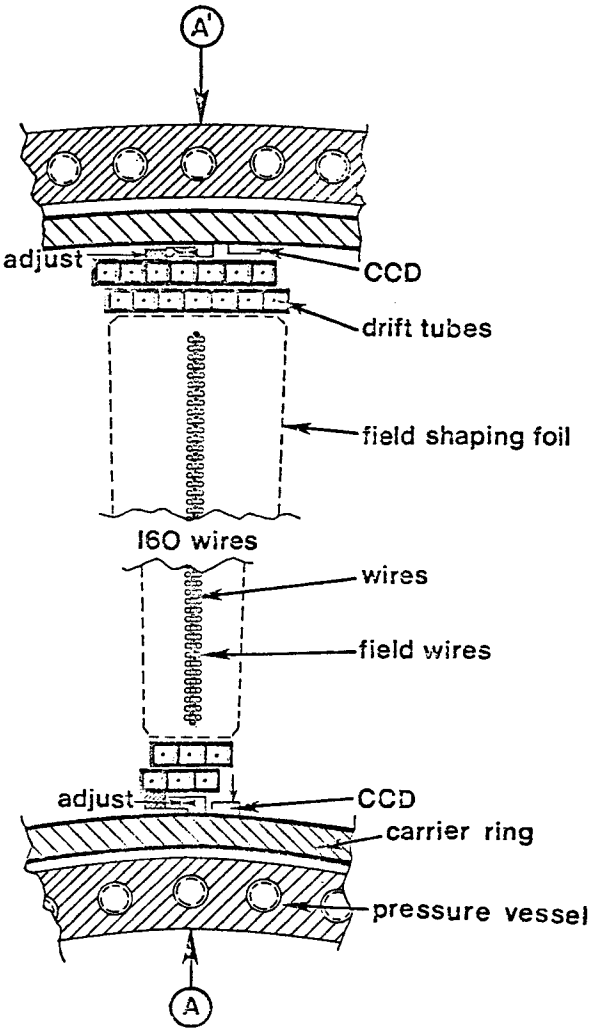
A'
adjust
CCD
drift tubes
field shaping foil
160 wires
wires
field wires
adjust
CCD
carrier ring
pressure vessel
A

Figure 3

perturbations on the drift times for all tracks not crossing the foil. The conductor stripes on both sides of the foil alternate in order to make it "opaque" for cross-talk to the neighboring segment. In case of a broken wire the foils confine the disabled region to 1 out of 96.

As discussed before, the accuracy depends on having the 160 signal wires of a segment aligned to a systematic accuracy of ~ 20-25 μ in one plane. Figure 4 shows an exploded view where we omitted all auxiliary frames for field wires which require less accuracy. The signal wires will be glued to the precision (~ 10 μ) ground surfaces of the bars (a) and (a') utilizing the same winding techniques employed in the chambers of the BNL J experiment[4]. This ensures correct wire spacing; the flatness of the surfaces guarantees alignment to 10 μ. The three bars are inserted into grooves of the support frame made from wedge-shaped aluminum and thick-walled drift tubes. Tightening the set screws (b) against surface (b') creates the tension of the wires. It will be adjusted to 500 ± 10 g by exciting the ground harmonic by capacitive coupling from high voltage sine wave excitation. Points 2, 4, 6 will define the plane while points 1, 3, 5 have to be adjusted with laser techniques. This procedure has to be repeated when the segment is mounted into the final carrier; however, in order to maintain the accuracy against thermal motion, etc., each of the six corners is equipped with a thin glass fiber on the wire frame illuminating a charged coupled device (CCD) glued onto the reference carrier. The centroid of the light intensity distribution is recorded and stored by computer. This will detect relative motions which in turn will be corrected by remote controlled adjustments (RCD) in active feedback. A schematic of one corner is shown in Figure 5.

The electrostatic configuration is given in Table 3. Figure 6 gives the corresponding electrical field strength, the equipotential lines and the electrical field lines which would be the paths of drifting electrons at B = 0. The electrical

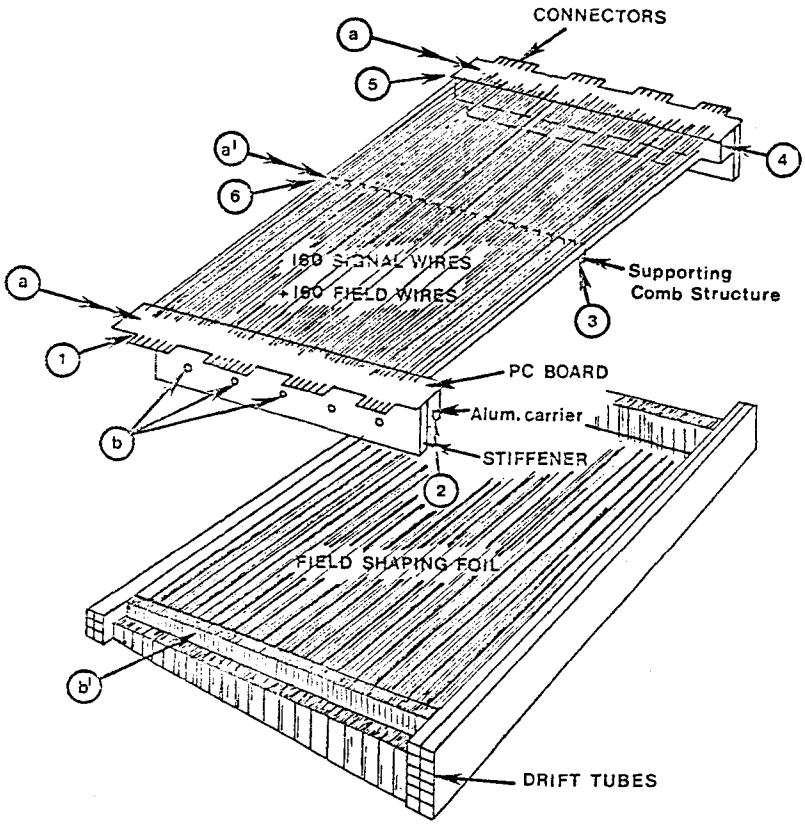
CONNECTORS
a
5
a'
6
4
180 SIGNAL WIRES
+180 FIELD WIRES
Supporting
Comb Structure
3
a
1
PC BOARD
Alum. carrier
b
STIFFENER
2
FIELD SHAPING FOIL
b'
DRIFT TUBES

Figure 4

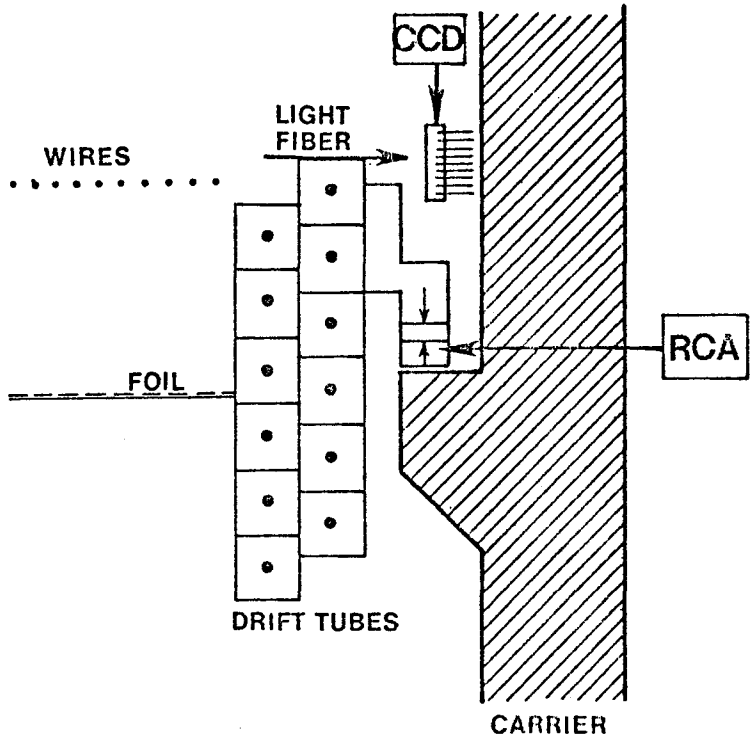

Fig. 5

field is rather homogeneous. The field wires serve two functions: they sustain part of the electrostatic attraction from the high drift field, and they influence the focusing and separation of field lines from neighboring cells. This is important because all correlations impairing the independence of the measurements must be avoided. This electrostatic structure has been calculated and was experimentally found to be stable, which is discussed in the next chapter.

ACCURACY

For 160 independent measurements over 160 cm radial distance L in 15 kG solenoidal field the projected transverse momentum resolution is given by[5]:

$$\frac{\Delta P_T}{P_T} = \frac{3.3 \times 10^3}{B(kG) \cdot L^2(cm^2)} \cdot P_T(GeV)\, \sigma \sqrt{\frac{720}{N+5}}$$

where N is the number of sample points, σ is the spatial resolution of one wire of 140 μ as was obtained in systems like JADE[1] and MARK II.

For an example we calculate the mass resolution for a 100 GeV particle, in back to back decay into muons; hence with $P_T = 50 \cdot \sin\theta$ GeV/c. In a 15 kG field we have

$$\frac{\Delta P_T}{P_T} = \frac{3.3 \times 10^3}{15 \cdot 160^2} \cdot 140 \times 10^{-4} \sqrt{\frac{720}{165}} \cdot 50 = 1.26\%$$

Figure shows the resulting mass resolution as function of angle θ. Δ m/m < 0.9% is obtained within $53^\circ < \theta < 127^\circ$, i.e. 60% of the solid angle. The two double layers of drift tubes (Figure 3) will resolve the left-right ambiguity.

Outside drift chambers[6] trace the continuation of the μ-track through 120/sin θ cm of iron. They measure the polar angle again to ~12 mr, thus

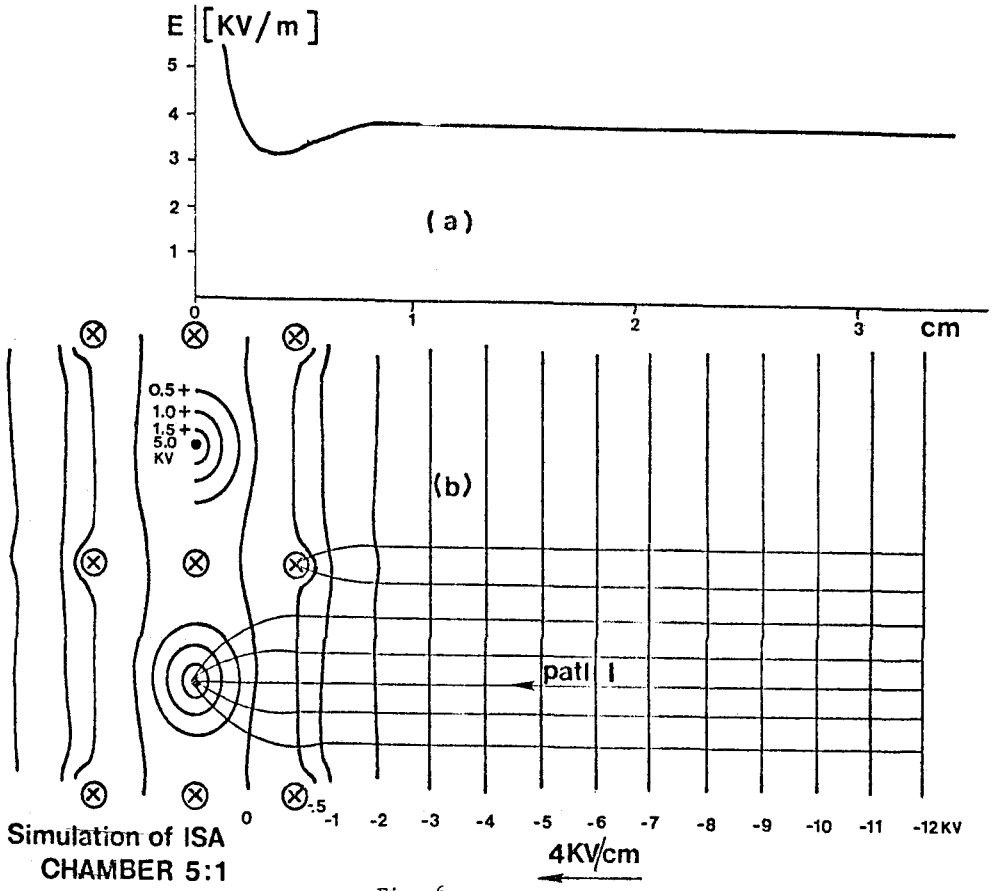
E [KV/m]
5
4
3
2
1
(a)
0
1
2
3
cm
0.5+
1.0+
1.5+
5.0
KV
(b)
patl
0
-.5
-1
-2
-3
-4
-5
-6
-7
-8
-9
-10
-11
-12KV
4KV/cm
Simulation of ISA
CHAMBER 5:1

Fig. 6

determining P_T. Then

$$\left(\frac{\Delta P}{P}\right)^2 = \left(\frac{\Delta P_T}{P_T}\right)^2 + \left(\frac{\Delta\theta}{tg\theta}\right)^2 \simeq \left(\frac{\Delta P_T}{P_T}\right)^2$$

$$\Delta m/m = \frac{1}{\sqrt{2}} \frac{\Delta P}{P} \qquad \text{For } \theta\mu\mu \simeq 180^\circ$$

The resulting mass resolution for the central chamber is shown in Fig. 7. The forward chambers (see Fig. 1) extend the region beyond the dotted line down to 25°. A systematic treatment of the precision determining factors is given in Appendix A.

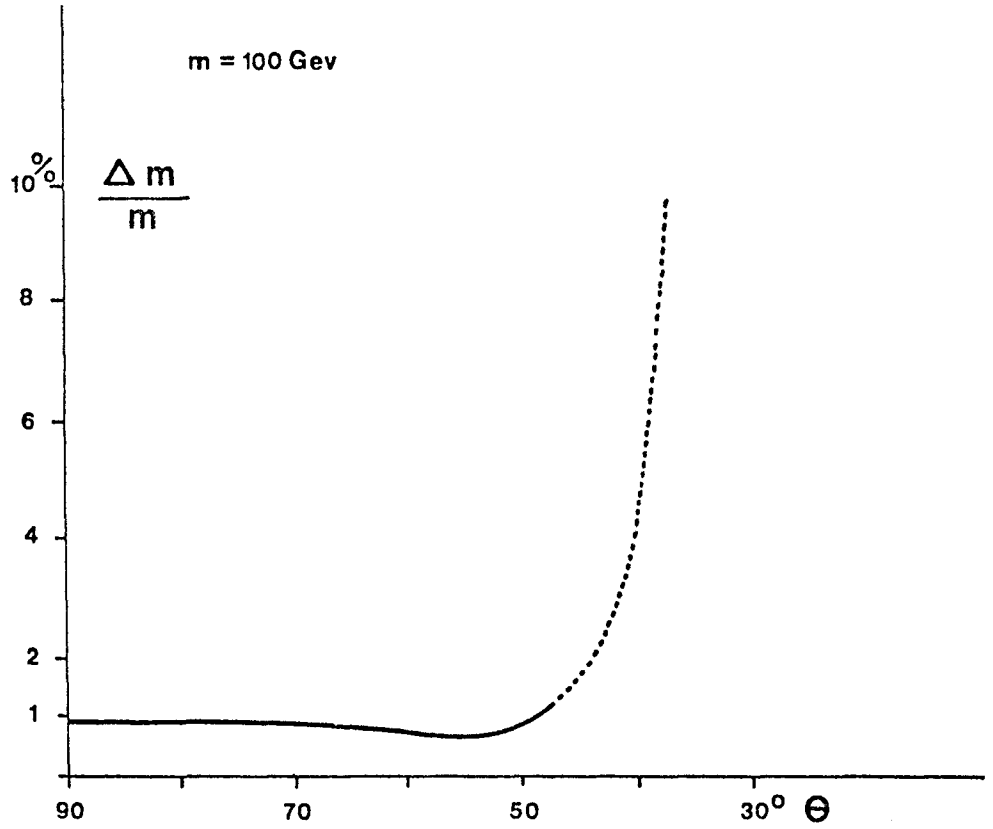

Fig. 7

REFERENCES

1. JADE chamber at PETRA and MARK II at SLAC.
2. U. Becker, J. Burger, M. Steuer, NIM 180 (1981), 61. With a 1 cm drift tube diameter we find 6% of the sampling measurements spoiled by δ-rays. The resolution was shown to be $156/\sqrt{N}$ μm.
3. JADE chamber observation, private communication by A. Wagner.
4. J. J. Aubert et al., Phys. Rev. Lett. 33, 1408 (1974).
5. R. L. Gluckstern, Nucl. Instrum. & Meth, 128, 593 (1963).
6. As used at MARK-J at PETRA, U. Becker et al., Nucl. Instr. & Meth. 24, 381 (1975).

II. TESTS AND CONSTRUCTION

DESIGN CONSIDERATIONS

As stated before, 3 mm sagitta requires 30 μm average planarity of the wire plane, which cannot be reached if the wires are supported in a place along the muon trajectory. By stretching 48 μm gold-plated tungsten wires with 500 g and supporting them in the middle (where no muon will pass), we achieve a stable electrostatic configuration with only 38 μm gravitational sag (compared to ~200 μm in conventional designs) which can be computer-corrected if necessary. Figure 8 shows the load characteristics of the wire which was used successfully.

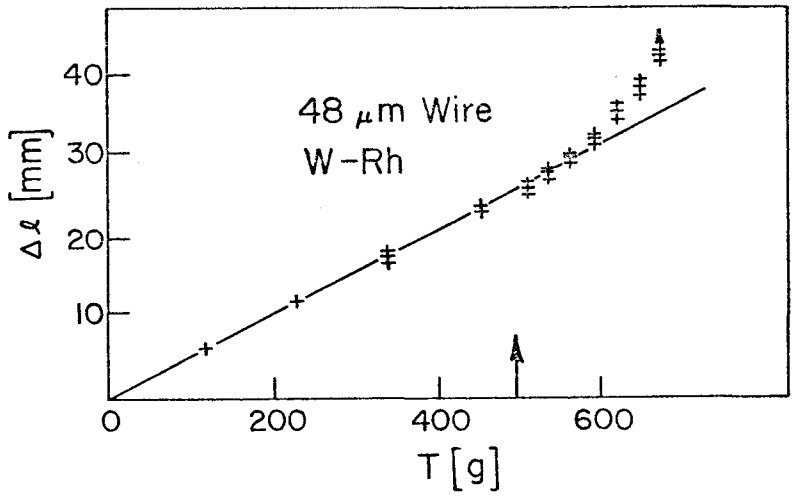

Fig. 8. Tension diagram of $\emptyset = 45$ μm Lumaplan Tungsten Rhenium wire.

To achieve 150 μm accuracy for each individual wire we have to reconsider the situation, because size, magnetic field, and other parameters are different from those in present designs. We consider:

a) Even good amplifiers will have time slew of 1 ns	~50 μm (5-50x threshold)
b) Time digitization to 2 ns least hit gives	σ = 50 μm
c) Allowing diffusion contributions of	100 μm
we obtain	125 μm.

This is acceptable. However, since the design has 9.8 cm maximal drift distance (in order to keep the total wire number at 15600), we must apply pressure as Fig. 9 shows clearly.

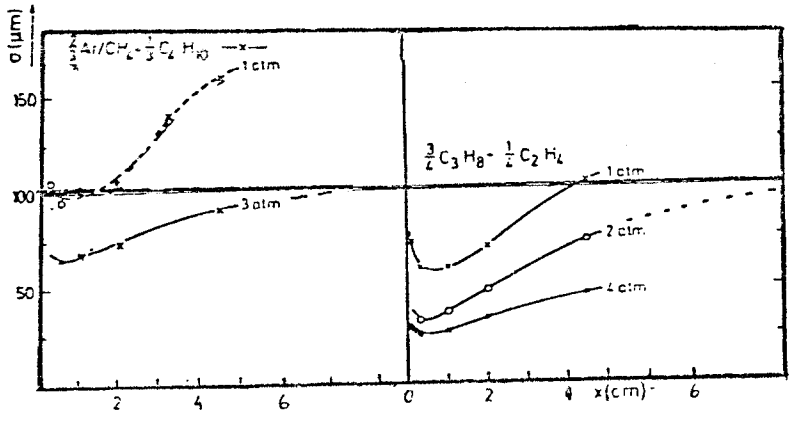

Fig. 9 Resolution as function of drift distance. From W. Farr, A.H. Walenta, NIM 156, 301 (1978).

Another crucial point will be the slanted path of the drifting electrons caused by the Lorentz force in the magnetic field, which is rather high in our case, of B = 15 kg with $tg \propto \frac{vB}{E}$. For comparison, JADE has 18^{o} with $E = \frac{.910kV}{m}$ in 5 kg. Restoring the geometry to this configuration requires 3 kV/cm in our case.

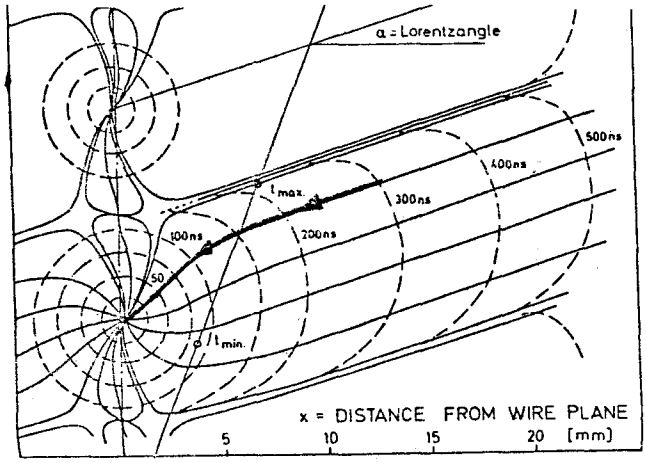

Fig. 10 Electrical field lines and isochronous lines for the JADE chamber.

In order to effectively handle all new problems arising from big size, high B, and accuracy, we split the problems (see Fig. 11) and studied each individually with a special setup.

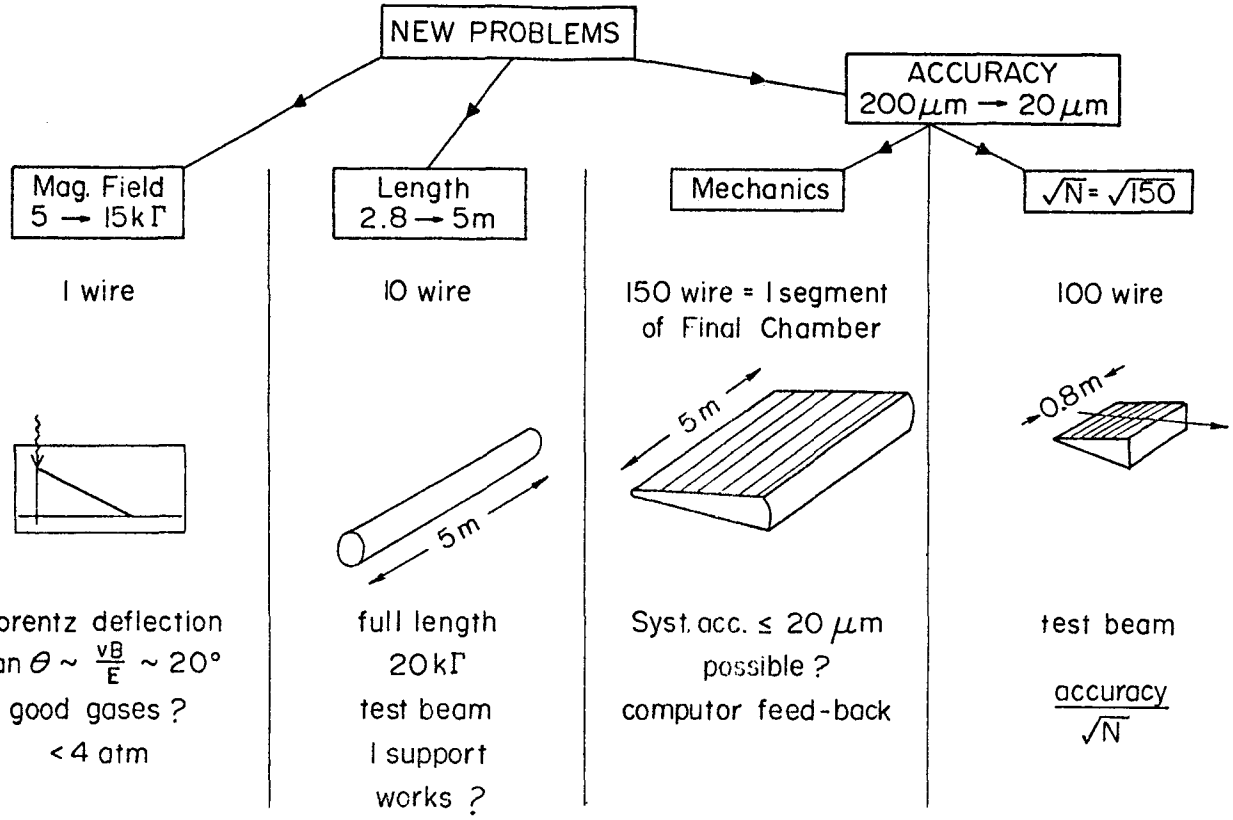
NEW PROBLEMS
ACCURACY
200μm → 20μm
Mag. Field
5 → 15kΓ
Length
2.8 → 5m
Mechanics
√N = √150
1 wire
10 wire
150 wire = 1 segment
of Final Chamber
100 wire
5m
5m
0.8m
Lorentz deflection
tan θ ~ vB/E ~ 20°
good gases ?
< 4 atm
full length
20kΓ
test beam
1 support
works ?
Syst. acc. ≤ 20 μm
possible ?
computor feed-back
test beam
accuracy
√N

Fig. 11

NEW PROBLEMS

Fig. 11 gives a diagram of the new problems arising over existing detectors and our efforts to understand them to a level to eliminate them in the general design.

(A) The one-wire chamber was specially designed by Dr. A. H. Walenta to investigate the properties of gases in magnetic field. Many gases were measured.

(B) Having wires of twice the length used before in accurate chambers can pose new electrostatic and signal problems. A 9-wire drift chamber working under "battle conditions" in a magnetic field up to 20 kg and in a test beam was built to prove and to demonstrate how individual wire accuracies of 150 μm/wire can be obtained for 5 cm long wires.

(C) The planarity requirement of $\leq$ 30 μm error on the sagitta of 3000 μm has two aspects: First, one must prove that the spatial resolution does increase proportional to $1/\sqrt{N}$. To find the working conditions, NIKHEF[1] has built a 100-wire chamber and used it in measurements in the BNL test beam.

(D) The mechanics of a 5 x 2 m frame which is one of 96 segments of the total chamber in all gravitational orientations cannot be achieved by inherent stiffness because of Young's modulus limitations and aging properties of materials. A computer feedback approach is evaluated to monitor and keep such a frame constant to 30 μm.

In the following, we describe these efforts one by one.

---

[1] High Energy Institute, The Netherlands, P. Duinker et al.

(A) One-wire Chamber in High Magnetic Field[1)]

It is designed to study deflections in fields up to 20 kg for various gas mixtures, to measure diffusion and drift velocity. These parameters define a "good" gas. It is shown in Fig. 12. A 10 ns X-ray burst induces ionization. The electrons start drifting toward the wire and the arrival time enables us to measure the drift velocity v_D. Turning on B the electrons follow the inclined path(b), taking a longer time. This determines the slant angle α. The delay line behind can be read out on both ends such that the effects of diffusion can be seen. This, however, is not the transverse diffusion D_T quoted in textbooks; it is $D_{\parallel}$, the longitudinal spread, which is relevant for the jitter in the arrival time and coordinate inaccuracy. Fig. 13 shows $D_{\parallel}$ to be substantially smaller than D_T. It is close to the theoretical limit of the electron temperature for an Ethylene : Methylal mixture, which is not practical.

Fig. 14 shows measurements of Argon : Methane which agree precisely to published ones and hence calibrate this apparatus. The Ar : C_2H_6 mixture at 4 atm assumed for the chamber is shown below, giving $\sim 22^{\circ}$ deflection at 15 kg and 3 kV/cm. This mixture can be used under experimental conditions because in Fig. 16b we see that $\pm$ 200 V variations on the drift field and 6% change in the gas mixture change α less than 0.5%, which corresponds to only 10 μm in the sagitta.

Fig. 17 addresses the question of inhomogeneities in the field shaping foil due to the relative sector alignment. The worst case of a 0.5 mm wall deformation for 50 mm drift distance will in fact cause a 1% change in electrical field E. At 3 atm of Ar : C_2H_6 and 3 kV/cm, however, the drift velocity is "saturated" and $d\,v_D/dE$ (3 KV) $\simeq$ 0, causing only $\sim$4 μm deviation by having the "wrong" drift velocity.

[1)] A. H. Walenta, C. M. Ma, BNL.

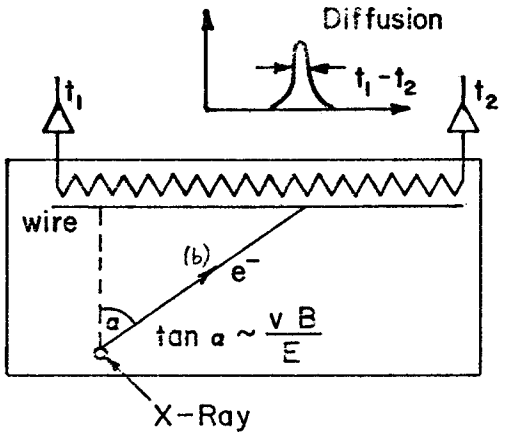

Figure 12

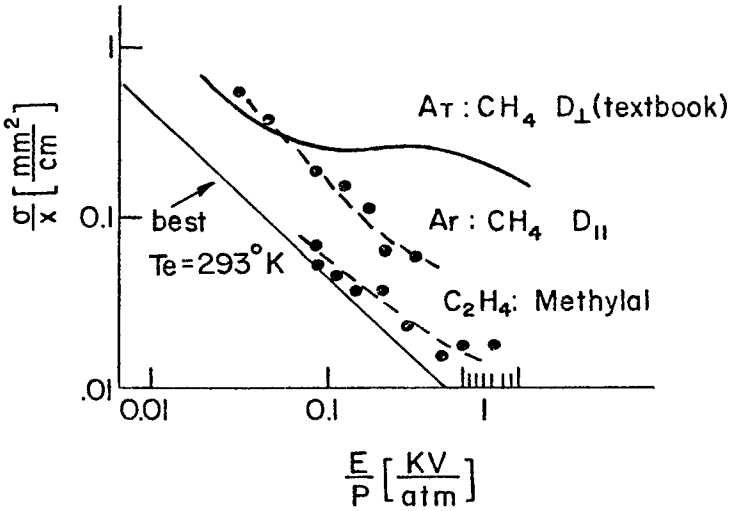

Figure 13

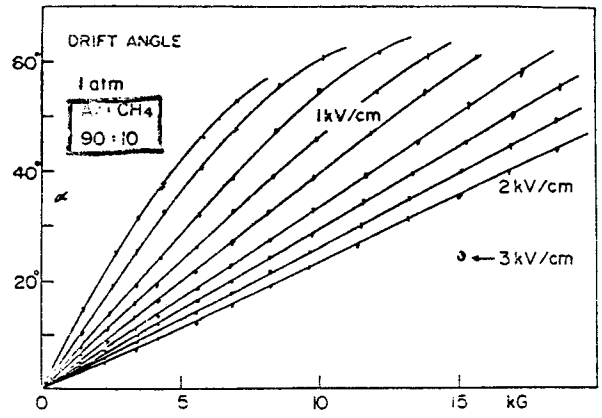

Figure 14

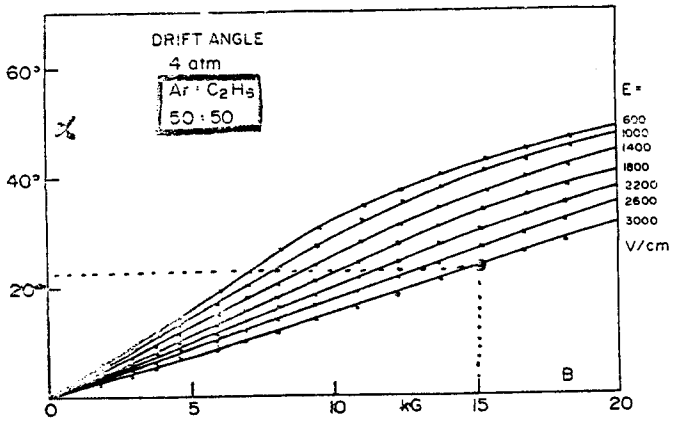

Figure 15

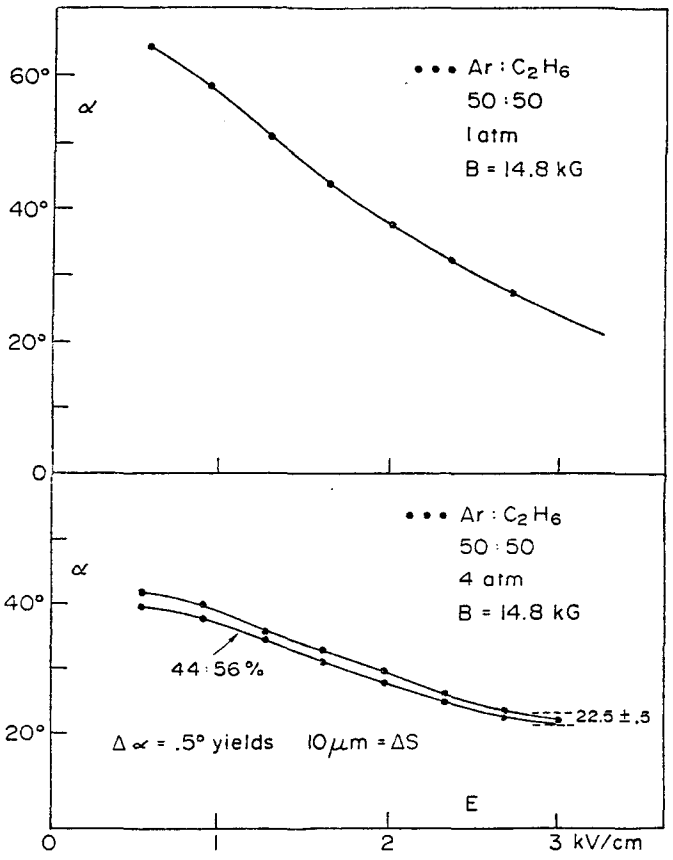

Figure 16a

Figure 16b

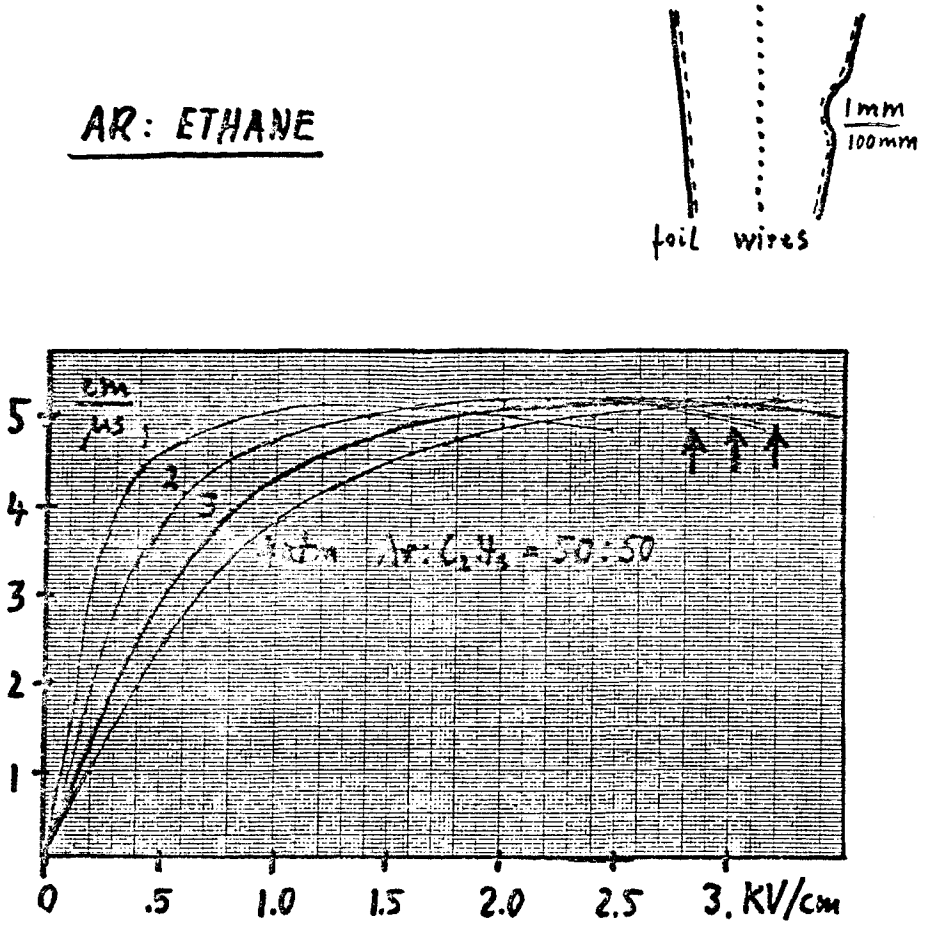
AR: ETHANE
1mm
100mm
foil
wires
cm/μs
5
4
3
2
1
1 Cm Ar: C2H6 = 50:50
0
.5
1.0
1.5
2.0
2.5
3. KV/cm

Figure 17

Fig. 18a

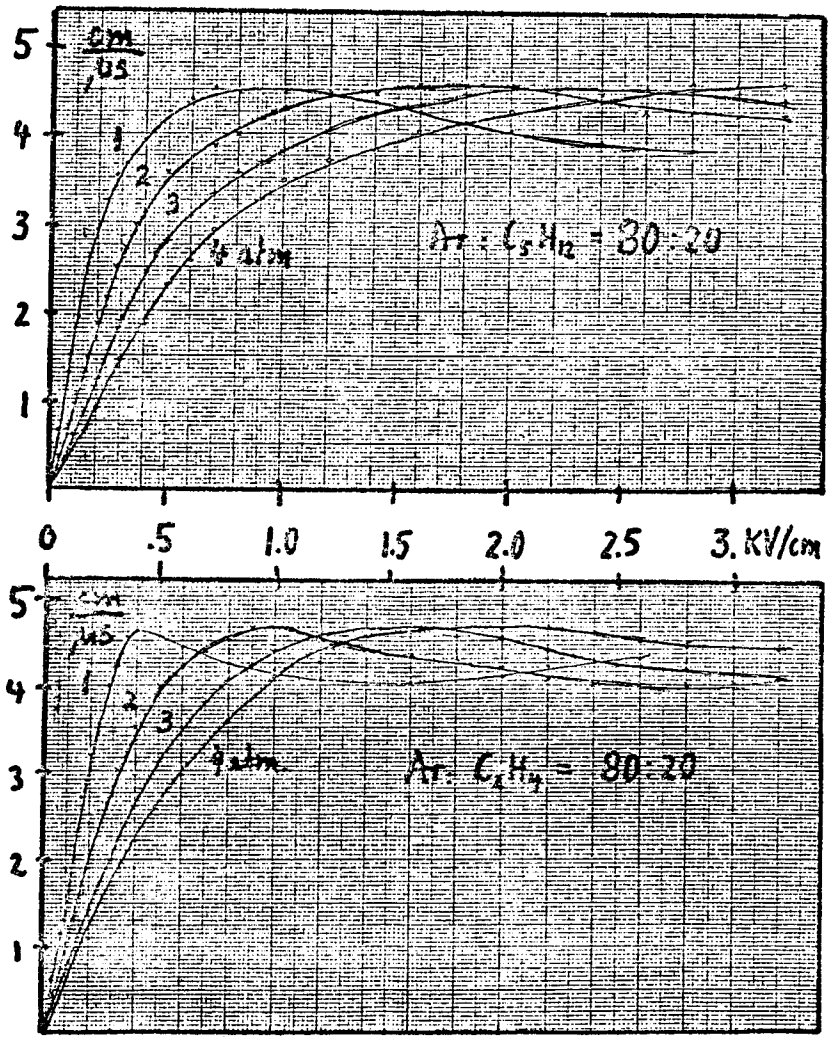

Fig. 18b

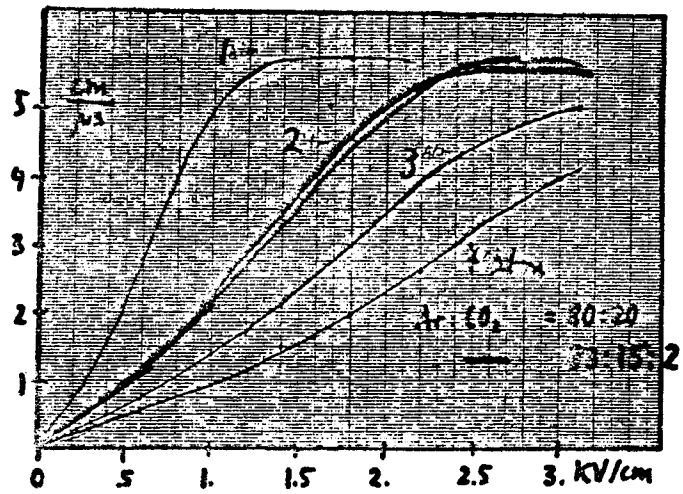

Fig. 19

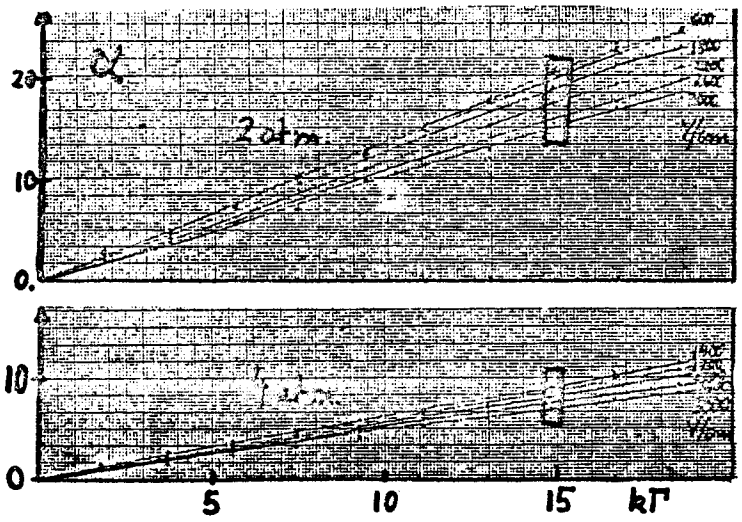

Fig. 20

Fig. 18a gives an alternative of inexpensive propane, displaying almost the same features as the expensive pure ethane. The ethylene in the mixture of Fig. 18b is not ~~well saturated~~ very saturated, however it has the best diffusion properties. Finally, Fig. 19 shows an inflammable mixture using CO_2. Whereas the deflection angle is comfortably low, we notice sparking and crosstalk at high electrical field. This in turn may be cured by a small (2%) admixture of propane. We have adjusted this ratio at 2 atm to give otherwise the same performance in drift velocity as the 80 : 20 Ar : CO_2 mixture. The feature of being nonexplosive is valuable for quick repairs and safety considerations including the cost of safety systems, but has to be compared to the difficulties of keeping a 3-component gas stable.

Diffusion measurements are in progress.

(B) The 9-wire Module in the Test Beam

It resembles the last 9 wires of one segment of the big chamber, and therefore the worst case. Except for the use of 9 instead of 160 wires, the support of the wires in three places, the adjustment, and the survey procedure were done in the same way as for the full segment.

It was built at MIT[1)] with 5.4 m length. The 9 wires are accompanied by 3 field shaping wires each and located in a G10 box having fine-grained field shaping at the walls. The box was mounted with fine adjustments in a 20' long aluminum tube that served as a pressure vessel. Fig 21 shows both prior to insertion.

The tube, in turn, was located in a specially built[2)] small solenoid magnet capable of producing up to 20 kg. Fig. 22 gives the principle. Both the magnet and

---

[1)] We acknowledge J. Walker of BNL-AGS for the design, and P. Berges and D. Osborne for construction.

[2)] A 20 kg Solenoid Magnet, BNL Techn. Rep. To Harold Knudsen and George Korbut we are indebted for skillful manufacturing.

(C) Resolution Improvement $\sim 1/\sqrt{N}$

Fig. 32 shows a chamber built at NIKHEF which took data in December, 1980, with Argon : Ethane. Evaluation is underway and will be reported separately[1]. A preliminary investigation along these lines was carried out at CERN[2]. A drift tube module of 32 wires was put in a 28 GeV proton beam. Multiple scattering is not important, since the walls are only 250 μm of aluminum. This measures 32 times the same position. Comparison to external reference or internal comparison of 16 vs. 16 tubes can determine the improvement of accuracy with the number N of measurements. Fig. 33 gives the setup and the results.

Again the raw data contain δ-rays, spoiling the resolution. Making a 5 σ cut eliminated 7% of the data but showed in fact the improvement of resolution to be $\sigma(N) = 156 \pm 5\ \mu m/\sqrt{N}$. This is encouraging but does not eliminate the need to measure with the 100-wire chamber, because the drift tubes are separate entities as opposed to a track in one continuous gas volume.

(D) Segment of the Large Chamber

We outline here briefly the principal problems and our attempts at solutions:

1) How to obtain the 30 μm planarity of a wire plane. -- Fig. 34a gives a sketch showing all wires pulled over a very straight ($\leq$ 10 μm) glass ceramic bar before being attached to the printed circuit board. Such bars can be made and checked by optical industry. The relative wire distance is not crucial.

2) How to manufacture a chamber of 5-10 times more wires than existing ones in a comparable (< 3 y) time interval. --The wires will be wound on a drum,

---

[1] P. Duinker, J. C. Guo, F. Hartjes, B. Hertzberger, NIKHEF.

[2] U. Becker, M. Steuer, NIM 180, 61 (1981).

160 at a time, and stretched on the modular segment as outlined above. This technique has been used for the chambers in the J experiment. The segment structure has been described above, together with the position monitoring system.

A full-size frame, as described above and shown in Figs. 3, 4, 5, has been built at MIT and is shown in Fig. 35. The frame is equipped with wires. The relative deformation due to the collective tension was measured to be small (250 mm) and is automatically compensated by the tension procedure. It is equipped with light fibers and CCD's. Their longtime stability and the reliability of the digital centroid have been demonstrated over a period of several weeks. The remote controls consist of sawed jaws opened by a turnbuckle screw. Since it works on a deformation (400 lb. prestress increase to 700 lb. for a max. 300 μm opening) it is backlash-free. The electrical engines were checked; they work with and without an overlaid 15 kg axial field. They are geared down to 1 revol/3 sec. which performs one ± 150 mm adjustment cycle. Since it is cyclical the motion is confined to this absolute range.

Having recorded the motion of the frame for a few weeks without correction, we have now employed the feedback to compensate any deviation > 10mm and to record the "smoothed" status for a longer period. Fig. 36.

In summary we have:

a) Found a stable electrostatic configuration of 5 m long wires;

b) Measured the properties of many suitable gases;

c) Studied the resolution under actual beam conditions and found it adequate;

d) Shown with tubes that the accuracy $\propto 1/\sqrt{N}$;

e) Built a full-size frame for mechanical longterm evaluation with computer feedback.

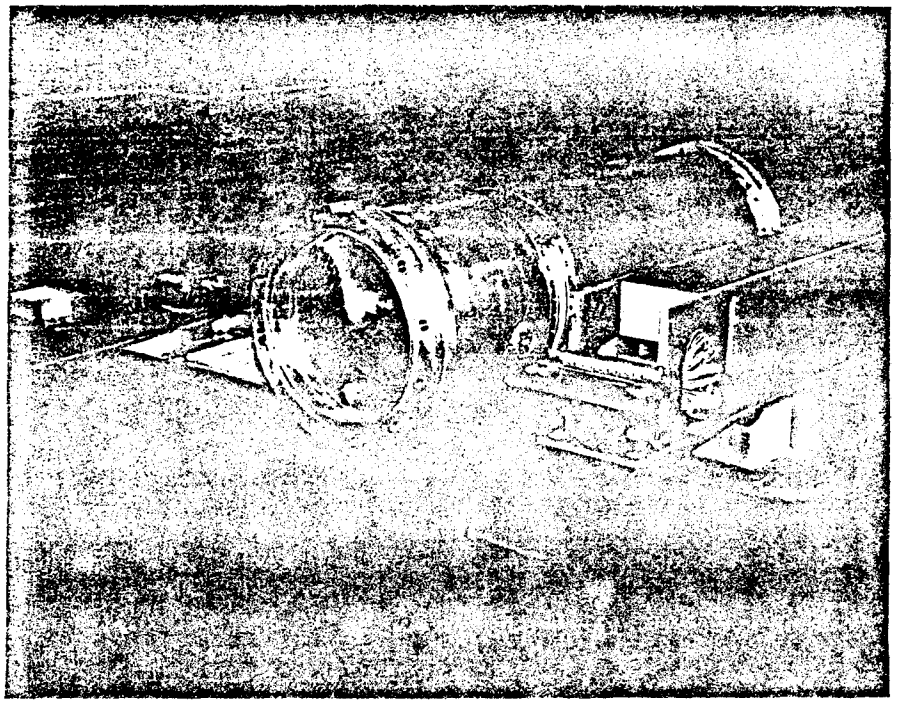

Figure 21

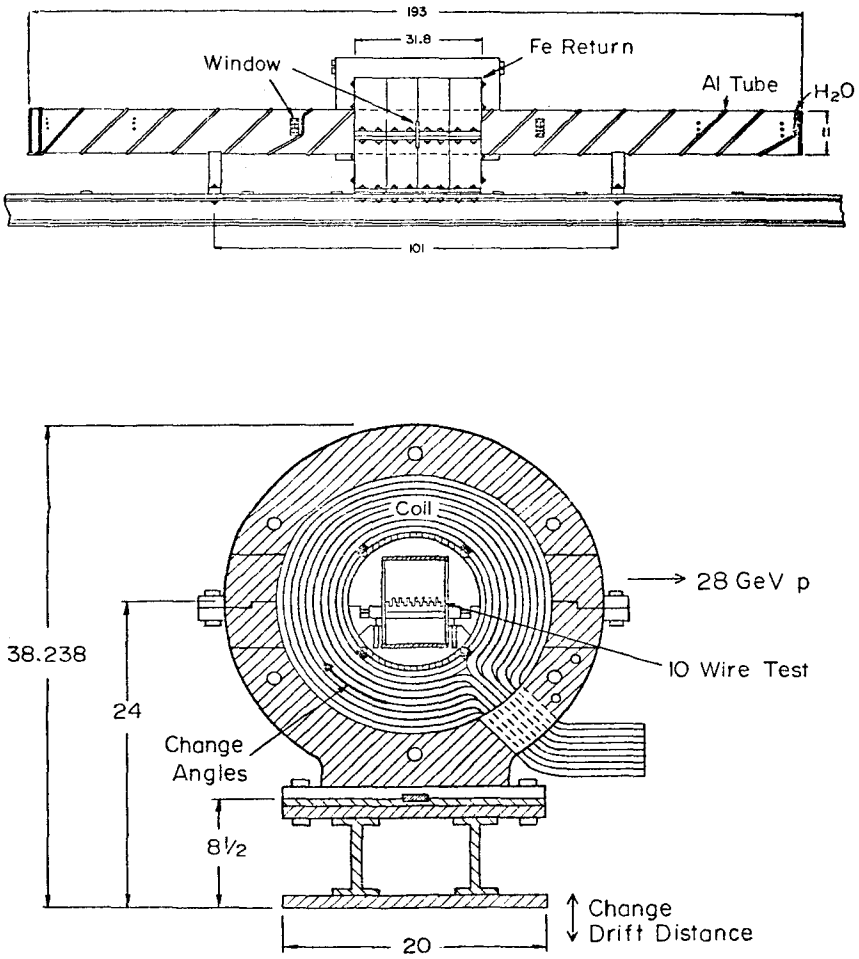
193
31.8
Window
Fe Return
Al Tube
H_2O
101
Coil
28 GeV p
10 Wire Test
38.238
24
Change
Angles
8½
Change
Drift Distance
20

Figure 22

the long tube were mounted on an extremely rigid "strong back" to maintain the straightness of the tube. The magnetic field along the central trajectory is given in Fig. 23. A magnified version is presented at the upper right corner together with the field corresponding to a displaced particle path with respect to the 9 wires indicated. All field deviations are < 1% and therefore can be neglected.

Fig. 24 gives the arrangement in the A2 test beam at BNL. Four scintillation counters and 5 pairs of beam drift chambers[1] define the beam. The NIKHEF 100-wire chamber is located upstream and will be described later. The 9-wire module, the drift tube, and the magnet have special windows to let the beam through for a minimum of multiple scattering. The strong back, together with magnet and tube, can be lifted and lowered by remote control. An optical grating counter registers the shift through the beam to 0.01 mm accuracy.

The first operation in December, 1980, used 1 atm of P101 90% Argon : 10% Methane. For calibration and comparison to existing measurements, operation was without magnetic field, 1 kV/cm drift field, and +2.3 kV on the 45 μm diameter signal wires stretched 450 g and the field wires at ground potential. From a displacement of 1.5" the corresponding change in arrival times was used to determine the drift velocity of 3.05 cm/μs, which is low, but in perfect agreement with the published measurements of Farr et al.[2] Lowering the electrical field yielded higher velocities, showing that the chamber was operationally understood (see Fig. 25).

Fig. 26 depicts the time spectrum. The spread of events is given by the 1/2" width of the trigger counters; the absolute time reflects the position as being 1½"

---

[1] I. Hung Chean and J. Smith developed these chambers.

[2] Farr et al., NIM 156, 362 (1978).

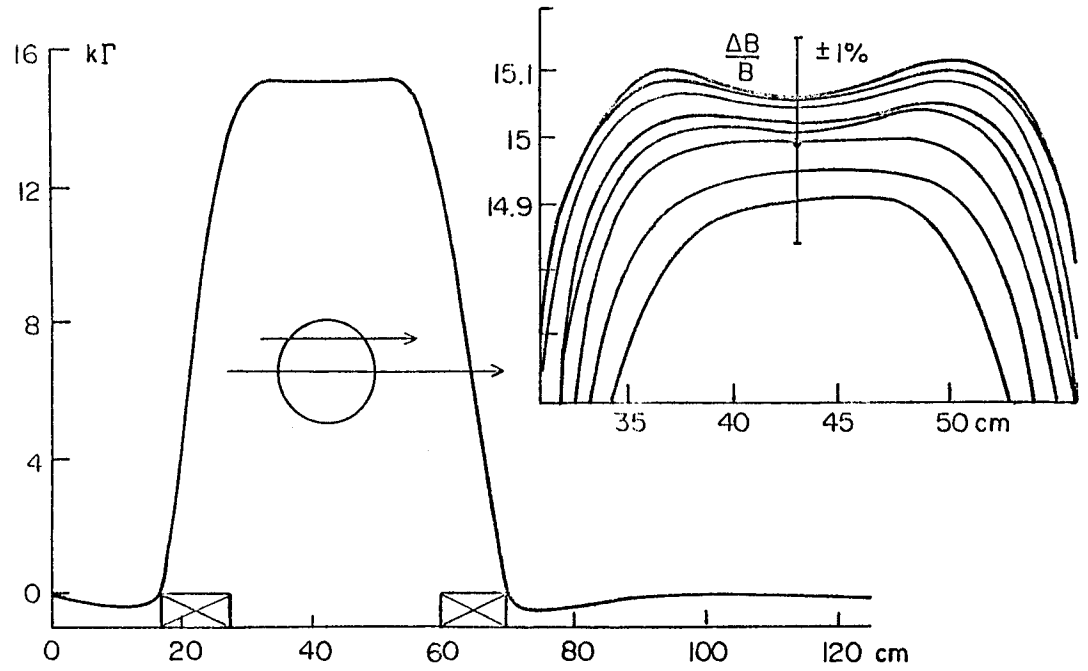

Figure 23

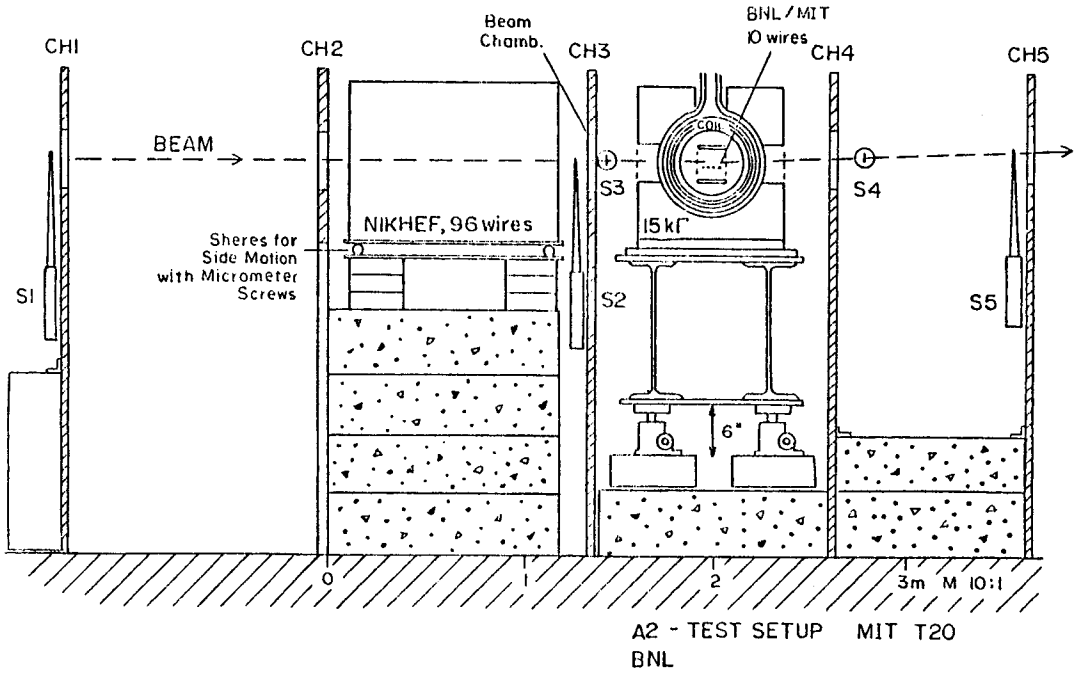
CH1
CH2
Beam
Chamb.
CH3
BNL/MIT
10 wires
CH4
CH5
BEAM
COIL
S3
S4
NIKHEF, 96 wires
15 kΓ
Sheres for
Side Motion
with Micrometer
Screws
S1
S2
S5
6"
0
1
2
3m M 10:1
A2 - TEST SETUP MIT T20
BNL

Figure 24

displace

beam
9 wires

$$V = \frac{1.5^{*}}{2600-1350\,ns} = 3.05\ \frac{cm}{\mu s}$$

change drift field

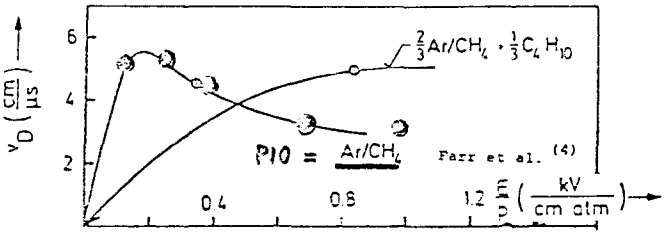

Figure 25

time spectrum

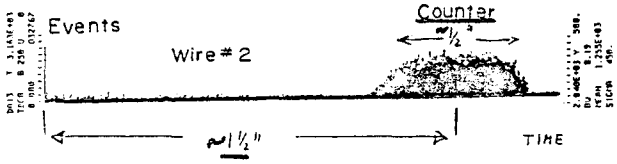

trigger on #2, look #4

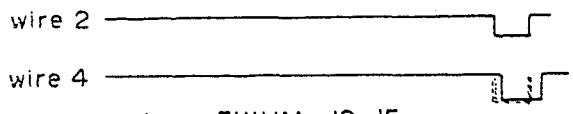

Jitter, FWHM 10-15 ns

$$\sigma_{wire} = \frac{1}{\sqrt{2}}\ \frac{15\,ns}{2.3}\ 30\ \frac{\mu m}{ns} \sim 140\,\mu m$$

Figure 26

from the beam. All 9 wires are horizontally aligned, and the beam is horizontal with little divergence. Therefore all 9 wires should have signals at the same time. The relative deviations are the measure of the achieved resolution (see Fig. 26). Observing 10-15 ns FWHM jitter on the scope converts with the drift velocity to a spatial accuracy of $\sigma \tilde{} 140$ μm.

In Fig. 27 the recorded times of wire 2 vs. wire 4 are displayed. Ideally both are the same, hence the plot should show only the diagonal line. A raw evaluation of the line width yields σ = 180 μm. We notice that the few background events are deviating substantially and therefore constitute an undue amount to this resolution. They are mostly δ-rays from the Landau fluctuations of energy loss. Admitting only those events with less than ± 18 ns deviation from each other eliminates only $\leq$ 10% of the data, yet improves the resolution immediately to 148 μm.

The results from Argon : Ethane = 5 : 3 in volume are given in Fig. 28. No difference for B = 0 or 5 kgauss was noticed in the plateau curve. When moving the chamber through the beam (Fig. 23b) the average delay (differences) yield the known drift velocity of 5.1 cm/μs. Deviations around x = 0, the wire position, are washed out by the finite beam size. Fig. 23 displays the time spectra of some of the wires together with the differences with respect to a common fitted straight line, including all systematic, positioning, and calibration errors of the 9 wires. Again, the raw evaluation yields 178 μm. Eliminating the knock on electrons, etc., by a ± 18 ns cut improves the resolution to σ 127 μm. This shows the Ar : Ethane mixture to be superior to P10 and demonstrates that the chamber functions as well as expected despite 5.4 m wire length and single-sided readout. Reducing the electrical field and comparing the v_D-values found with the 1-wire chamber measurement yielded good agreement, hence checking the operation.

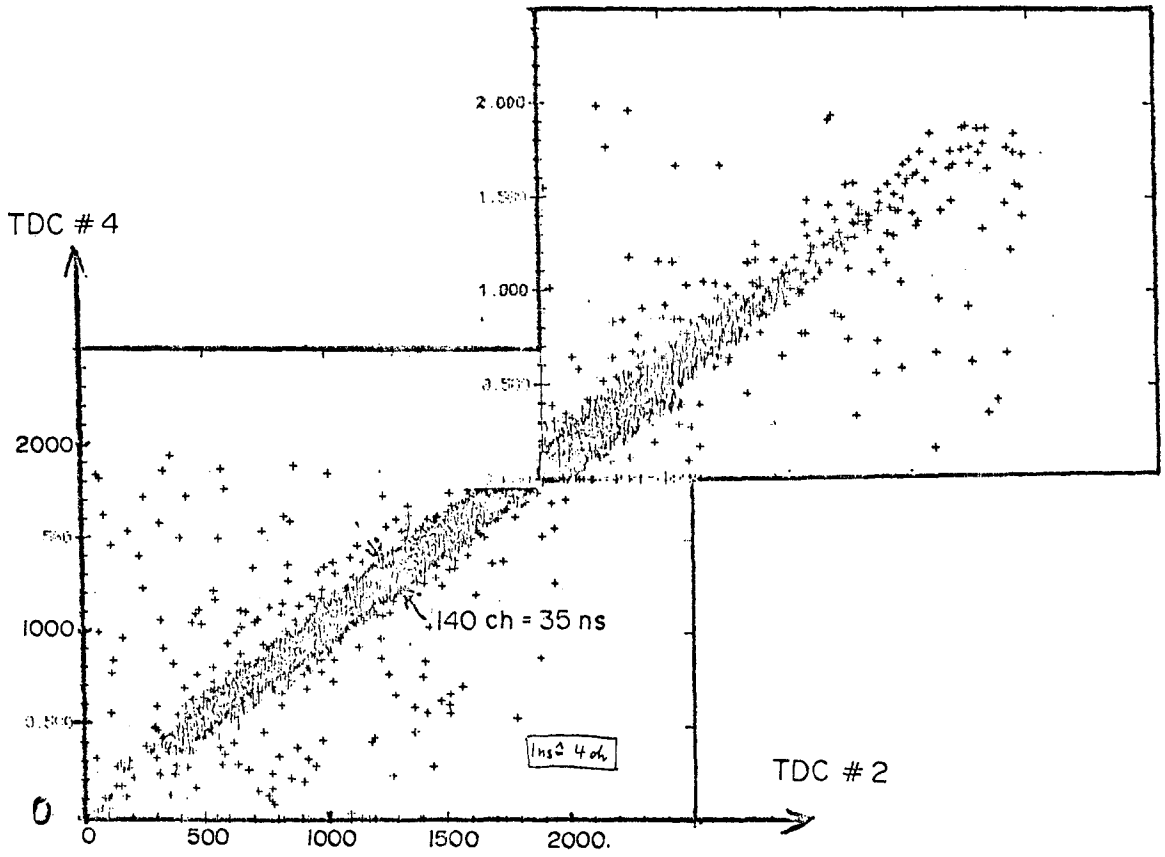
TDC # 4
2.000
1.000
2000
1000
0
0
500
1000
1500
2000.
140 ch = 35 ns
Ins2 4 ch
TDC # 2

Fig. 27

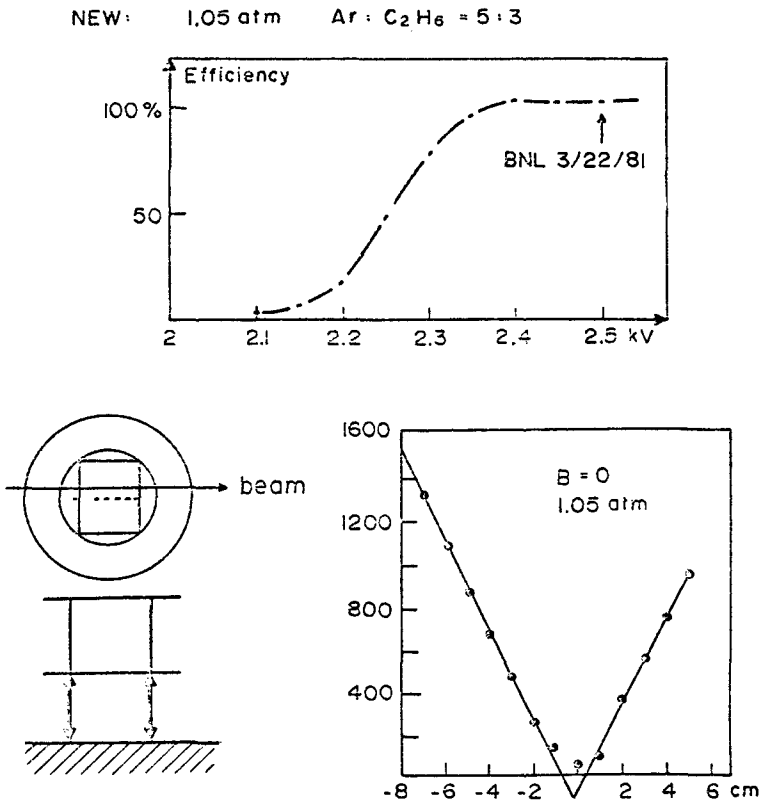
NEW: 1.05 atm Ar : C2 H6 = 5 : 3
Efficiency
100 %
50
BNL 3/22/81
2
2.1
2.2
2.3
2.4
2.5 kV
beam
1600
1200
800
400
B = 0
1.05 atm
-8 -6 -4 -2 2 4 6 cm

Figure 28

RESOLUTION 1.1 atm

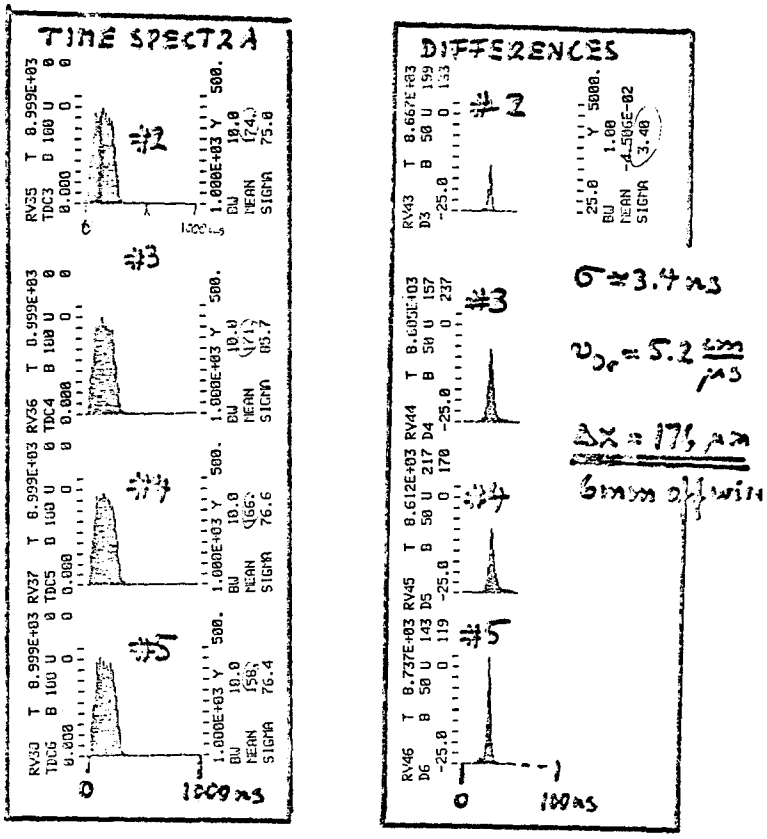

Figure 29

With 5 kgauss and -5 kV drift field, all times get longer due to the inclined drift path of the electrons. Comparing to the B = 0 measurement we find $\alpha = 29 \pm 2^{o}$.

Measurements at 2 atm were carried out at 10 kg and -10 kV drift field such that "E/p scaling" produces the same values of $v_D = 5.1$ cm/μs and $\alpha = 29^{o}$. We measure resolutions of 160 μm for distances up to 60 mm. Increasing the drift field to -15 kV yielded 150 μm resolution for drift distances of -80 to +50 cm with $\alpha = 20^{o}$ only. The high voltage on the wires was +3.1 kV. This performance meets the design goals for a 10 kg magnet well. Measurements were made close to the support, where the wires cannot move, and compared to those done in the middle, between supports. We find no difference and conclude that the system is stable against environmentally-induced oscillations.

Fig. 30a displays results obtained at 3 atm with the scaled drift field of -15 kV. The solid line gives the behavior at B = 0, leading to $v_D = 5.1$ cm/μs as expected. The measurements at B = 15 kg reflect the velocity derived from the 29^{o} slanted path (see Fig. 30b). Also, the slight displacement of the apparent center can be understood by the displacement of the 3.5 GeV particle trajectory due to the 15 kg. The voltage of the wires had to be raised to +3.6 kV, as shown in Fig. 31a. We obtain the resolution shown in Fig. 31b. Measurements with -20kV drift field reach the design accuracy with $\alpha = 22^{o}$. From these measurements we conclude that a chamber with 2-3 atm Ar : Ethane = 5 : 3 can meet our accuracy requirements.

To study the behavior of different field shaping foils and the behavior in the edges of the chamber as well as other gas mixtures, the measurements will be continued.

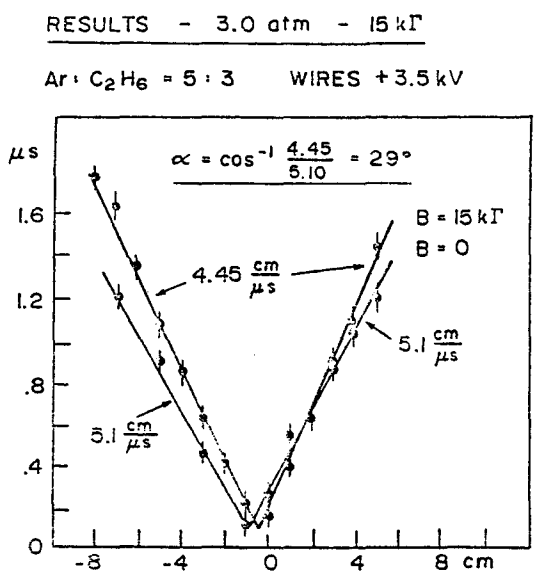

Figure 30a

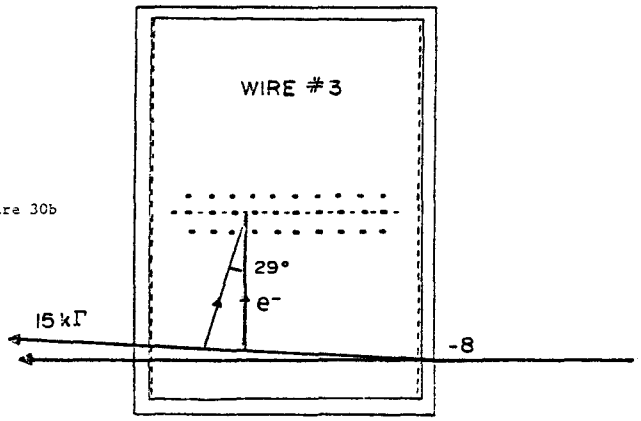

Figure 30b

15 kT 3 atm Ar: CH_4 - PRELIMINARY

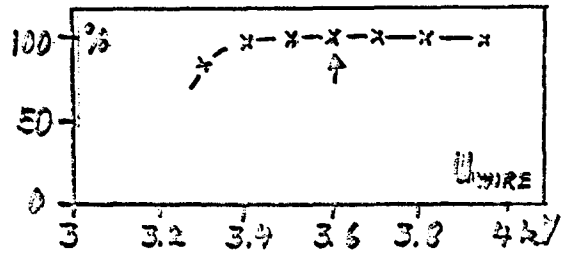

Figure 31a

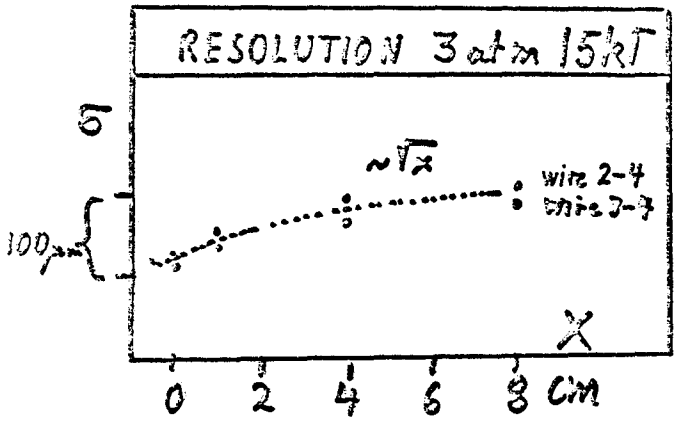

20 ns ≡ 1 mm cut

PEDESTAL not calibrated.

Figure 31b

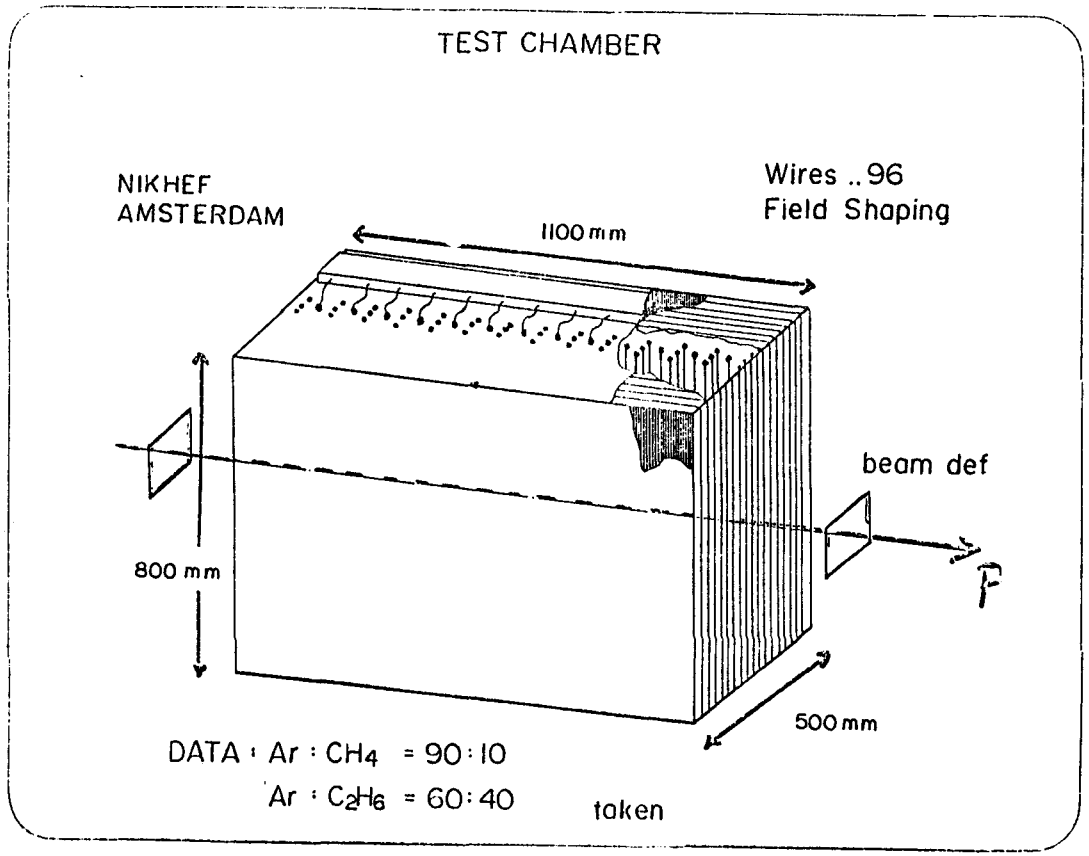
TEST CHAMBER
NIKHEF
AMSTERDAM
Wires ..96
Field Shaping
1100 mm
beam def
800 mm
500 mm
DATA : Ar : CH_4 = 90 : 10
Ar : C_2H_6 = 60 : 40
taken

Figure 32

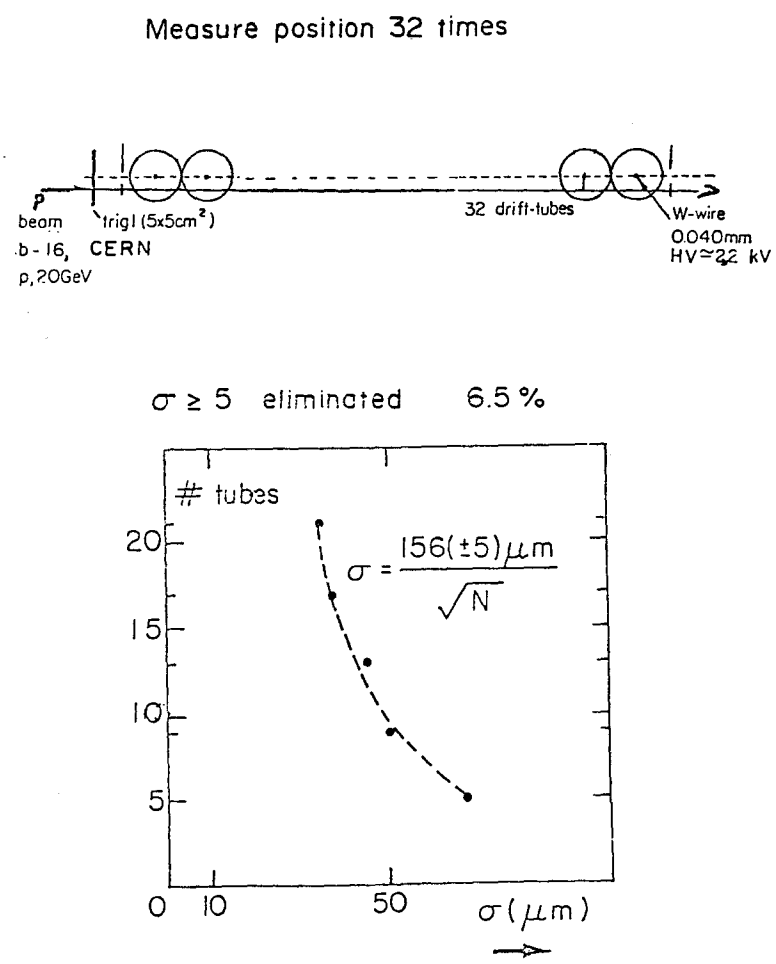
Measure position 32 times
p
beam
b-16, CERN
p, 20GeV
trig I (5x5cm²)
32 drift-tubes
W-wire
0.040mm
HV≃2.2 kV
σ ≥ 5 eliminated 6.5 %
tubes
20
15
10
5
0
10
50
σ(μm)
σ = 156(±5)μm / √N

Figure 33

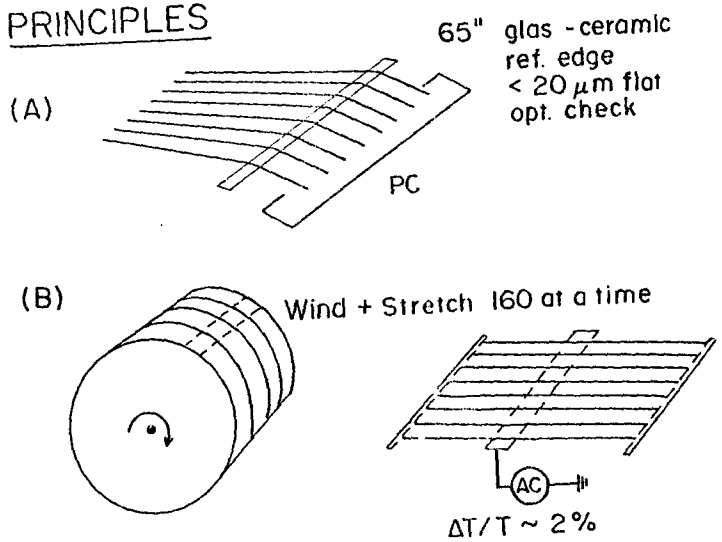
PRINCIPLES
65" glas - ceramic
ref. edge
< 20 μm flat
opt. check
(A)
PC
(B)
Wind + Stretch 160 at a time
AC
ΔT/T ~ 2%

Figure 34

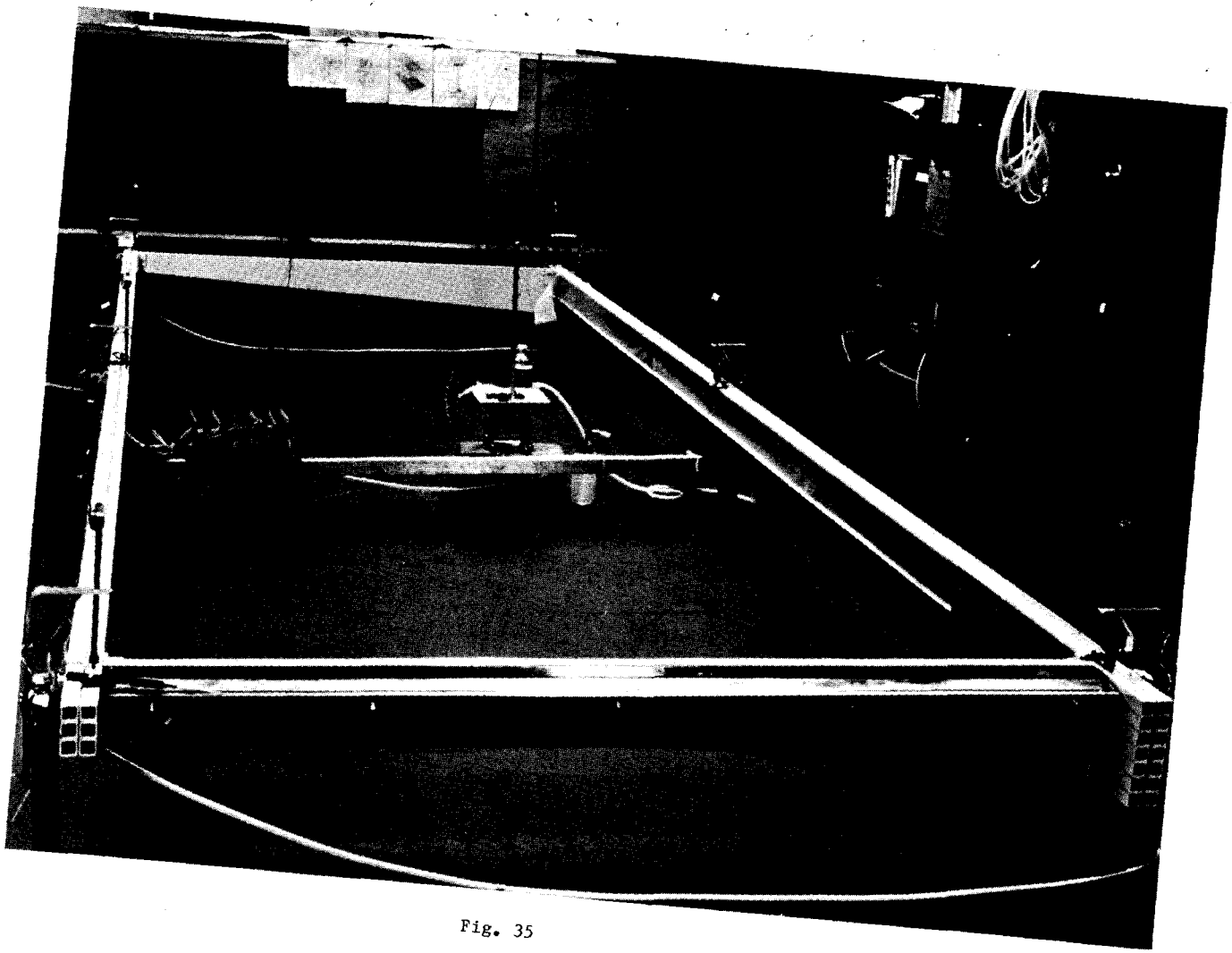

Fig. 35

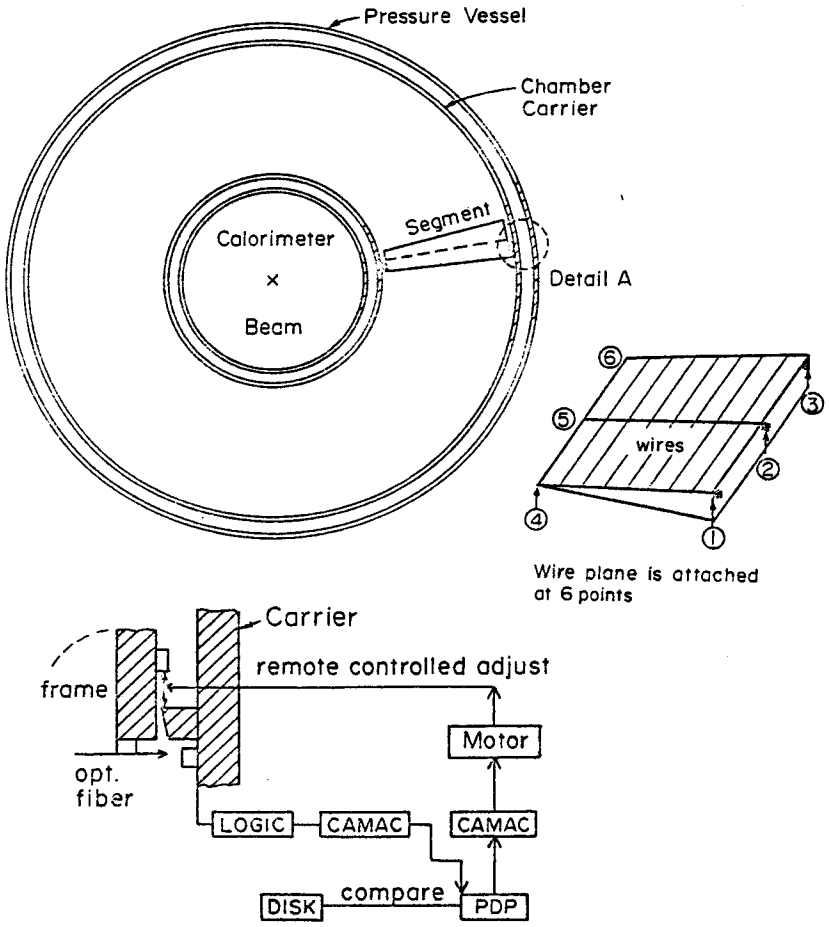
Pressure Vessel
Chamber
Carrier
Segment
Calorimeter
×
Beam
Detail A
⑥
⑤
③
wires
②
④
①
Wire plane is attached
at 6 points
Carrier
remote controlled adjust
frame
Motor
opt.
fiber
LOGIC
CAMAC
CAMAC
compare
DISK
PDP

Figure 36

The results obtained so far give confidence that 1% mass resolution in fact can be obtained for polar angles of $45 \leq \theta \leq 135^{o}$,

Finally, Fig. 37 gives a reduction of an engineering drawing on how this complicated detector can be assembled. The calorimeter is mounted with a tube on the left end plug. The pressure vessel is shown in place with the drift chamber mounted in the carrier to the right, ready to move in. Clearly the complexity and size of such a precision detector requires thorough preplanning and design engineering in advance.

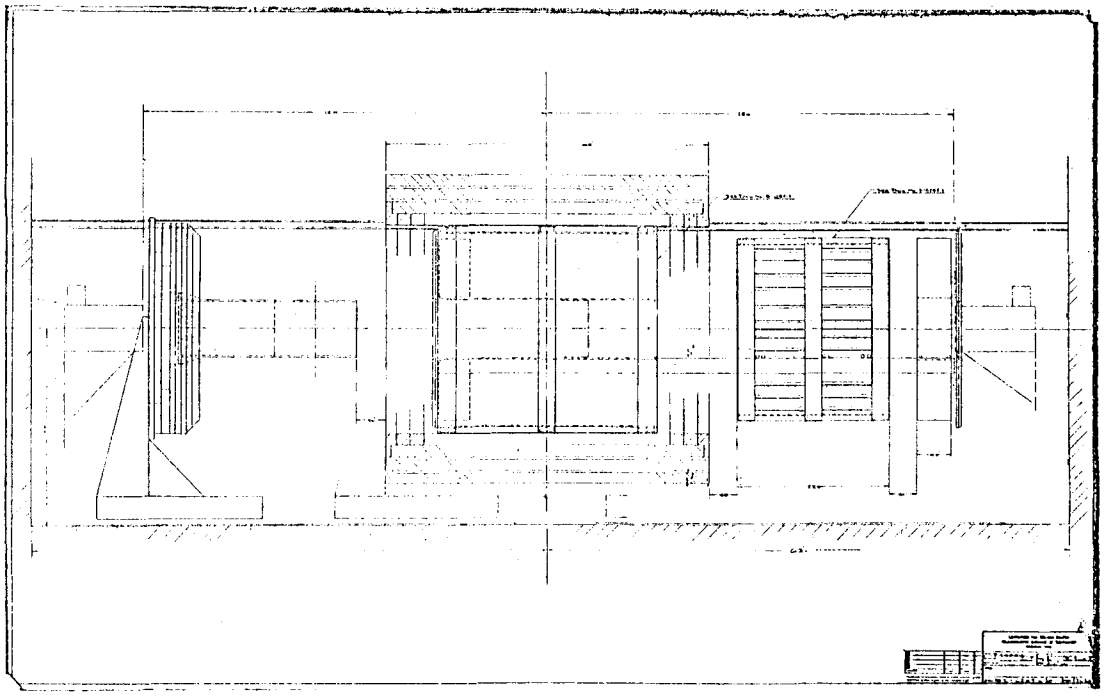

Figure 37

EXPERIENCE WITH THE AXIAL FIELD SPECTROMETER DRIFT CHAMBER AT THE ISR

Brookhaven-CERN-Copenhagen-Lund-Rutherford-Tel-Aviv Collaboration
Presented by H.J. Hilke

I. INTRODUCTION

The Axial Field Spectrometer (AFS) at the CERN ISR was designed to study events characterized by large transverse momenta. It required a low mass vertex detector providing good momentum resolution in a solenoidal magnetic field of 0.5 T, powerful pattern recognition for high event rates and particle densities and particle identification in the non-relativistic region (1). The detector has been operated at typical luminosities up to $L = 2 \times 10^{31}/cm^2sec$ over the past 1.5 years and recently, for periods of hours only, up to $L = 10^{32}/cm^2sec$.

II. CHAMBER DESIGN AND OPERATION

A cylindrical drift chamber with 4° azimuthal segmentation was constructed (2), combining drift time measurement for the azimuthal coordinate with charge division readout for the coordinate along the wires (Fig. 1). The chamber is 1.4 m long and extends from a radius of 0.2 m to 0.8 m. Each 4° sector contains 42 resistive sense wires (30 μm diameter, 8 mm spacing), arranged radially into three crowns. The sense wires are staggered by ± 0.4 mm to resolve the left-right ambiguity. Sector boundaries consist of grids of 100 μm wires. Particle identification in the nonrelativistic region is obtained from multiple ionization sampling (dE/dx). The drift chamber was built in two half-cylinders to permit rapid retraction from the magnet. The outer section of the chamber experiences magnetic field inhomogeneities of more than 30%, due to the open magnet structure.

The chamber is operated with an argon/ethane mixture (50/50 vol.%) at atmospheric pressure. A gas amplification of $(3\text{-}6) \times 10^4$ is chosen as compromise between acceptable chamber lifetime and dE/dx resolution on the one side and good space resolution on the other. Chamber lifetime studies in test chambers have indicated, that a 15% reduction in gas amplification occurs for

a total integrated charge of 3×10^{16} electrons/mm wire (3). This corresponds to about 2 years of ISR operation with average luminosity $L = 10^{31}/cm^2sec$ and a gas amplification of 5×10^4.

III. PERFORMANCE

III.1 Drift Time Measurements

The CERN DTR units are used for drift time digitization, contributing $\sigma = 60$ μm to the space resolution. For all tracks, visible radially over > 50 cm, we obtain a point resolution with FWHM/2.35 = 200 μm, averaged over the full azimuth and all points with valid z information. The residue distribution is well approximated by a Gaussian in the central part, contains, however, stronger tails. Near the sense wires and the sector boundaries the resolution is worse, in between these zones it is better. Corrections are applied for electrostatic wire deflections, magnetic field inhomogeneities, drift velocity variations and also for time slewing and crosstalk (-4 to -6%). A substantial improvement was gained by the introduction of the last two corrections: a general time slewing term, similar for all wires, and an additional crosstalk term only for the "far wires". These wires, because of staggering, receive their avalanche signal only some 16 ns after the crosstalk signal from the adjacent wires and, therefore, experience additional time slewing.

III.2 Charge Division

As expected, a strong correlation is observed between the resolution from charge division and pulseheight (PH): FWHM (cm) = A + B(noise/PH). For a gas amplification of 5×10^4, the average resolution for all reconstructed tracks is FWHM/2.35 = 1.4 cm, i.e. 1% of the wire length.

III.3 Particle Identification by dE/dx

Averaging over all tracks containing > 30 time digitizations and z-

measurements, we obtain for the truncated mean of the 60% lowest pulse heights: FWHM/mean = 24%, a value very close to that predicted by Monte-Carlo estimation. As Fig. 2 shows, protons may be identified up to 1.0 GeV/c, pions and kaons up to 0.6 GeV/c. For high particle densities, the superior granularity of this system offers a substantial advantage over a standard time-of-flight system. As an illustration of the performance in complex events, the preliminary spectrum of the total charged transverse energy E_T is shown in Fig. 3, for pp and αα collisions. It was obtained with minimum bias trigger and uses only particle identification in the drift chamber, assuming the pion mass, whenever no identification is obtained. A simple Monte-Carlo fit is added, based on measured multiplicity distributions and inclusive spectra, which will reproduce data from other experiments.

III.4 Diverse

The track reconstruction efficiency of the analysis program is greater than 95%, even at high multiplicities ($N_{ch} > 20$). An example of an event containing 45 reconstructed tracks from an αα collision is shown in Fig. 4. Data from cosmic rays are being actively studied for surveying purposes and for obtaining better knowledge of systematic errors, e.g. for momentum measurements.

In parallel, a laser beam was set up to produce ionization tracks in one sector of the drift chamber, with magnet on and off conditions (4). The preliminary results are very encouraging. Clean tracks were observed all through the sector (60 cm), although the beam had to cross field shaping wires. From trackfitting to 40 cm of the track (28 wires), $\sigma_{r\phi}$ = 100 μm (from drift time) and σ_z < 1 cm (from charge diversion) was obtained for single point resolution. The inner section of the track was not used in the fit, as the laser beam passed through the sense wire plane and produced disturbing pulses on the potential wires. The pulse height distribution showed a FWHM/mean < 25% for single wires, without corrections for fluctuations of the laser intensity.

The increased precision in (rφ) and z indicates that the chamber geometry and the electronics delay corrections permit a resolution $\sigma_{r\phi} < 100$ μm and that, therefore substantial improvement on the resolution for beam tracks should still be possible. Indeed, various calibration errors have been detected through the analysis of the first laser tracks. We are pursuing these tests and we are confident that they will lead to a better understanding of the numerous correction terms in the track fitting procedure.

REFERENCES

1. a. S. Almehed et al., A Study of a Large Transverse Momentum Phenomena, CERN/ISRC/76-36/P95 (1977). b. H. Gordon et al., The Axial Field Spectrometer at the CERN ISR, to be published in the Proceedings of the 1981 INS International Symposium on Nuclear Radiation Detectors, Tokyo.
2. a. D. Cockerill et al., Operation of a Drift Chamber Vertex Detector at the ISR, Nucl. Instrum. and Methods 176 (1980) 159. b. J.C. Berset et al. The Drift Time and Charge Division Electronics System for the AFS Vertex Detector, Nucl. Instrum. and Methods 176 (1980) 251. c. D. Cockerill et al., Performance of the AFS Vertex Detector at the CERN ISR, Physic Scripta (1981) 649.
3. See our contribution to these proceedings: Comments on Chamber Lifetime.
4. See also contribution to these proceedings: Status and Prospect of Laser Beam Calibration for Imaging Chambers.

FIGURE CAPTIONS

Fig. 1. Schematic view of the drift chamber geometry and one sector.

Fig. 2. dE/dx: truncated mean vs. momentum. Clear π/k/p separation is achieved in the non-relativistic region.

Fig. 3. Total charged transverse energy (E_T) spectrum, obtained from momentum measurement and particle identification by dE/dx in the drift chamber. Curve from Monte-Carlo fit, based on inclusive spectra and multiplicity distributions.

Fig. 4. High multiplicity event with 45 tracks reconstructed. Minimal calorimeter trigger on an αα interaction at $\sqrt{s}$ = 126 GeV.

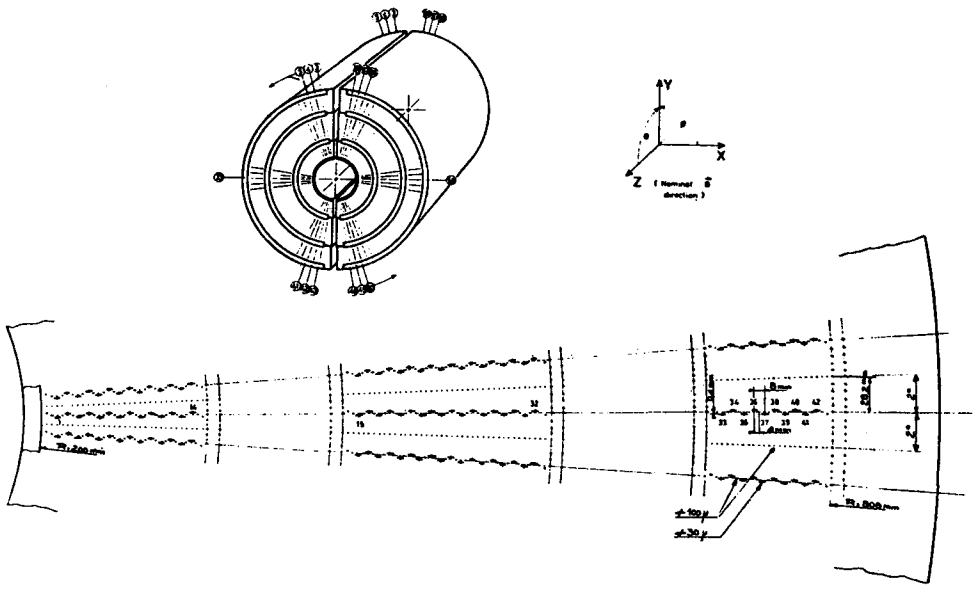

Fig. 1

Schematic view of the drift chamber geometry and one sector.

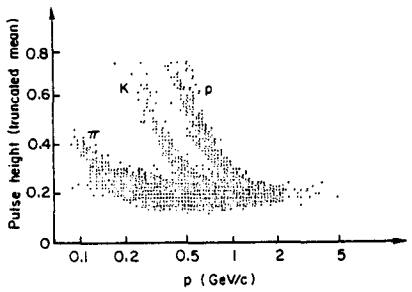

Fig. 2

dE/dx: truncated mean vs. momentum. Clear π/k/p separation is achieved in the non-relativistic region.

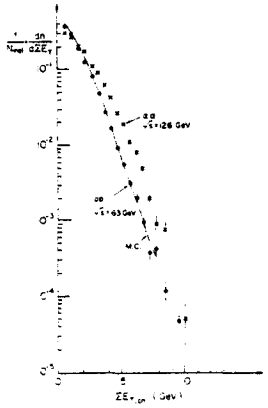

Fig. 3

Total charged transverse energy (E_T) spectrum, obtained from momentum measurement and particle identification by dE/dx in the drift chamber. Curve from Monte-Carlo fit, based on inclusive spectra and multiplicity distributions.

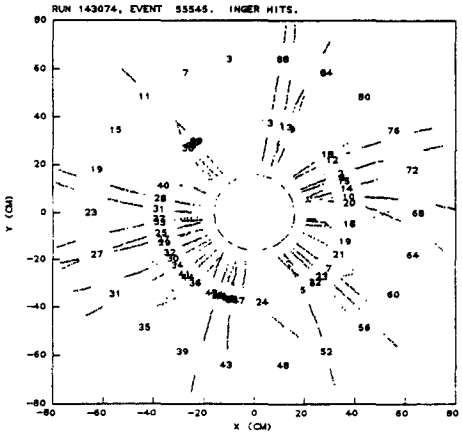

Fig. 4

High multiplicity event with 45 tracks reconstructed. Minimal calorimeter trigger on an αα interaction at $\sqrt{s}$ = 126 GeV.

MPS II DRIFT CHAMBER SYSTEM AND RELAVENCE TO ISABELLE EXPERIMENTS

E.D. Platner
Brookhaven National Laboratory

The MPS drift chamber[1] structure is shown in Figure 1 along with relevant performance numbers. Modules containing 5 or 7 anode readout planes are distributed throughout the 15 by 6 by 4 foot magnetic field volume of the MPS. Figure 2 is a typical high voltage curve for these drift chambers indicating a very broad region of stable operation. The drift time vs. position is shown in Figure 3 showing a very linear time vs. position relationship.

A complete module has 3 X-measuring planes and 2 Y-measuring planes (Figure 4). Three of these modules also have $\pm 30^{o}$ to Y cathode strip readout for 3 dimensional track reconstruction. All of the amplifier-shaper-comparator and digital delay-register electronics are on printed circuit boards mounted right on the chamber. The frames of the chamber planes are made of an extruded fiberglass-polyester pultrusion, the die for which shapes the O-ring grooves, reliefs, etc. to the precise dimension desired (Figure 5). This material is unusually stiff for a plastic (6×10^{6} psi) which makes tensioning the wires relatively easy.

In the course of planning MPS II extensive computer modeling of Monte Carlo generated events was undertaken to find the optimum module configuration and module placement. Figure 6 is a scale plot of the 7 drift chamber modules and the 4 triggering PWC's placement for the physics planned in Exp. 747.[2] To better appreciate the pattern recognition problems, Figure 7 is the same event with a greatly expanded vertical scale. The X's are anode wire hits and the vertical bars are the drift times. The pattern recognition fitted straight lines through the local triplets and then circles to the straight lines. To evaluate the effectiveness of this pattern recognition technique, 100 Monte Carlo events were generated and then messed up by randomly removing 4% of the hits, then adding 4% noise hits. A track was considered found when > 70% of its hits were found and the correct point slope identified for 90% of those found hits. With this criteria, the efficiency for finding low mass $\phi\phi$ events was 93%, which increases to 96% at a mass of

3 GeV. This efficiency is a great improvement over that obtained with the original MPS spark chambers.

Central to the development of MPS II was the successful design and production of 3 custom IC's, one of which is a truly state-of-the-art device. Figure 8 is a block diagram of the electronics mounted on the drift chamber. A more complete description of it is given in the section on wire chambers in this document. Detailed specifications of the 3 micro circuits is shown in Tables I, II and III.

Several features of this drift chamber system should be mentioned as to their relavence to Isabelle experiments. Because of the short drift distance, no time vs. distance correction need be made for angle or magnetic field effects. Also the short drift distance allows operation at high rates. Since the electronics is deadtimeless, the physics of the avalanche formation process sets the only rate limitation. The electronics converts the time information to digital at the earliest possible stage and there are no needs for offset time, time vs. distance slope or slope linearity corrections on a wire to wire basis. Thus large systems will be manageable. If finer time resolution is required, the shift register can sample as quickly as 3 ns intervals. The shift registers can be cascaded to achieve sample storage greater than 256 bits or they could be stagger-clocked to achieve time resolution as short as 1 ns.

The electronics for large drift chamber systems (100 K wires) could be built for $10 to $20 per channel using these microcircuits. Thus with the successful operation of MPS II we believe that we will have demonstrated a viable solution to the tracking detector requirements of Isabelle.

REFERENCES

1. A. Etkin, IEEE Transactions on Nuclear Science Vol. NS-26, No. 1, 54-58 (1979).
   A. Etkin and M.A. Kramer, IEEE Transactions on Nuclear Science, Vol. NS-27, No. 1, 139-144 (1980).
   S. Ozaki, MPS Note #51, 1979.
2. AGS Proposal #747, A High Statistics Study of ϕ and $\phi\phi$ Production from π p and K p Interactions at 22 GeV/c (1979).

FIGURE CAPTIONS

LIST OF TABLES

Table 1

BNL TRA401

AMPLIFIER CHARACTERISTICS

Characteristics	Minimum	Maximum	Units	Remarks
Input Type	True Differential			
Input Noise (RMS)		0.25	uA	8 nsec integration time constant.
Input Resistance		80	ohms	
Input Protection		1.13×10^{-4}	J	47 pF charged to 2.2 kV.
Transfer Impedance	20		Kohms	
Delta Transfer Impedance	-10%	+10%		Lot to lot mean within lot.
Gain Stability		0.25	%/°C	
Output Impedance		50	Ohms	
Rise Time		4.4	nsec	
Max. Linear Output	1.2		Volts	
Propagation Delay		10	nsec	
Delta Propagation Delay		1.5	nsec	Applies to amplifiers on common chip
Temperature Range	0	50	°C	
Supply Currents				
+5.5 V ± .1		65	mA	
-2.5 V		45	mA	

JUNE 1981

Table 2

BNL MVL400
DISCRIMINATOR CHARACTERISTICS

Characteristics	Minimum	Maximum	Units	Remarks
Input Resistance	3		Kohms	
Input Z Threshold Control	1.5		Kohms	
Threshold Control Range (1:1)	0	1.5	Volts	
Threshold Hysteresis	6	10	mV	
Threshold Match		±5	mV	Applies to disc. on common chip.
Crosstalk between Inputs of Channels		-40	dB	
"0" Logic Level		1.8	Volts	Driving 100 ohm pull-down resistor to +1.5V.
"1" Logic Level	+3.5		Volts	Driving 100 ohm pull-down resistor to +1.5V.
Output Response Time		4.4	nsec	Driving 100 ohm pull-down resistor to +1.5V.
Slewing		3	nsec	For 2 to 20X threshold.
Double Pulse Resolution		20	nsec	
Input Capacitance		6	pF	Each comparator input.
Propagation Delay	14.5	17.5	nsec	
Operating Temperature	0	50	°C	
Supply Currents				
+5 V		200	mA	Including current in 100 ohm pull-down resistors.
-5 V		22	mA	Including current in 100 ohm pull-down resistors.

JUNE 1981

Table 3

Clock speed	0 to > 330 HHz
Ch to Ch phase to phase delay NS clock	< 1 ns
Readout delay NS clock	40 - 60 ns
Max readout speed	40 MHz
Vcc	5 ± 5 V
Power at 250 MHz	160 mw

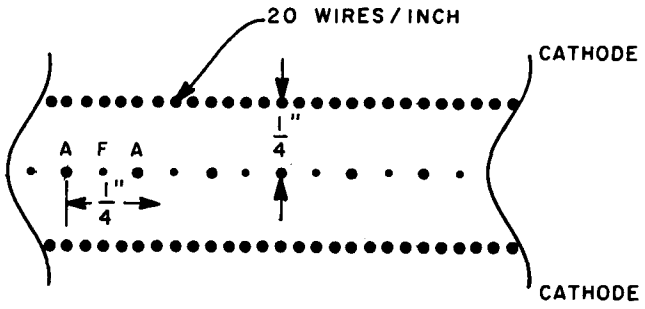

Anode wires 0.001" diam. goldplated tungsten
Field + cathode 0.003" diam. S.S. (Nitronic 50)
Drift field > 7KV/cm
Drift velocity 1 mm/20 ns - fully saturated
Maximum drift time - 60 ns

Figure 1

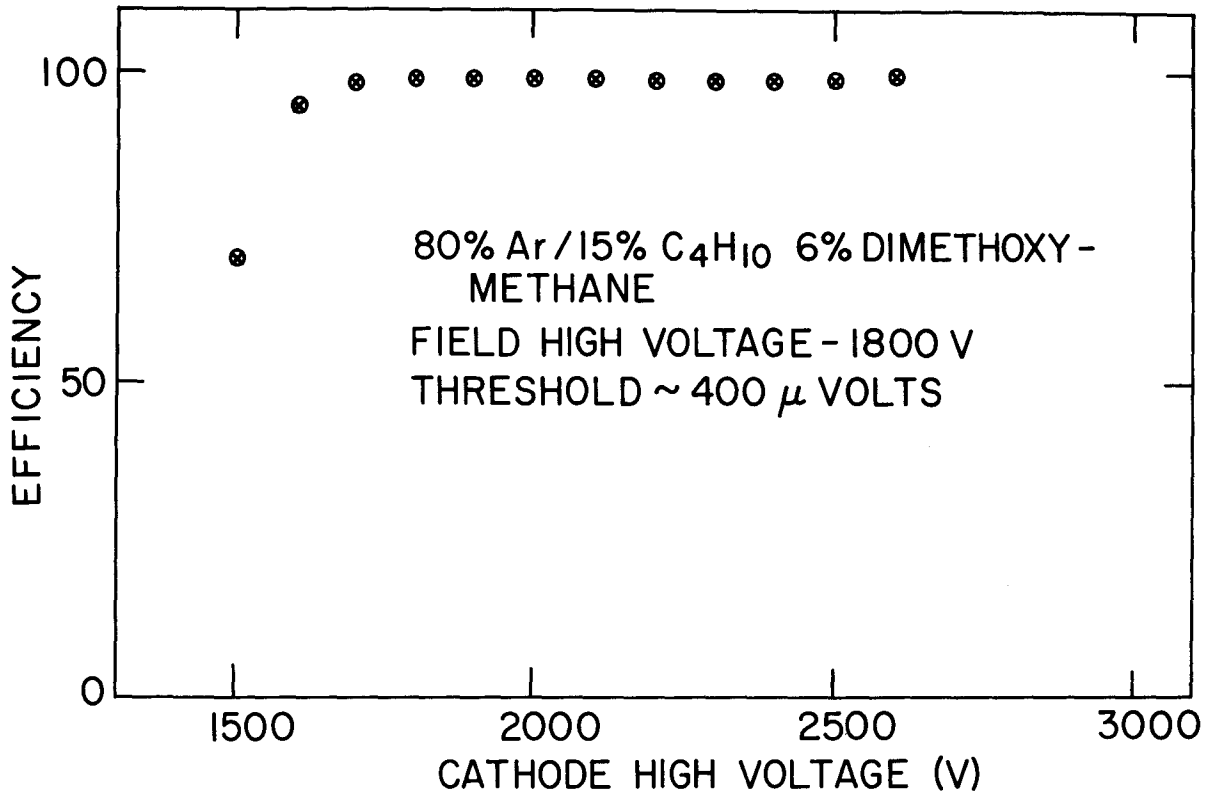
100
50
0
EFFICIENCY
80% Ar / 15% C_4H_{10} 6% DIMETHOXY-
METHANE
FIELD HIGH VOLTAGE - 1800 V
THRESHOLD ~ 400 μ VOLTS
1500
2000
2500
3000
CATHODE HIGH VOLTAGE (V)

Figure 2

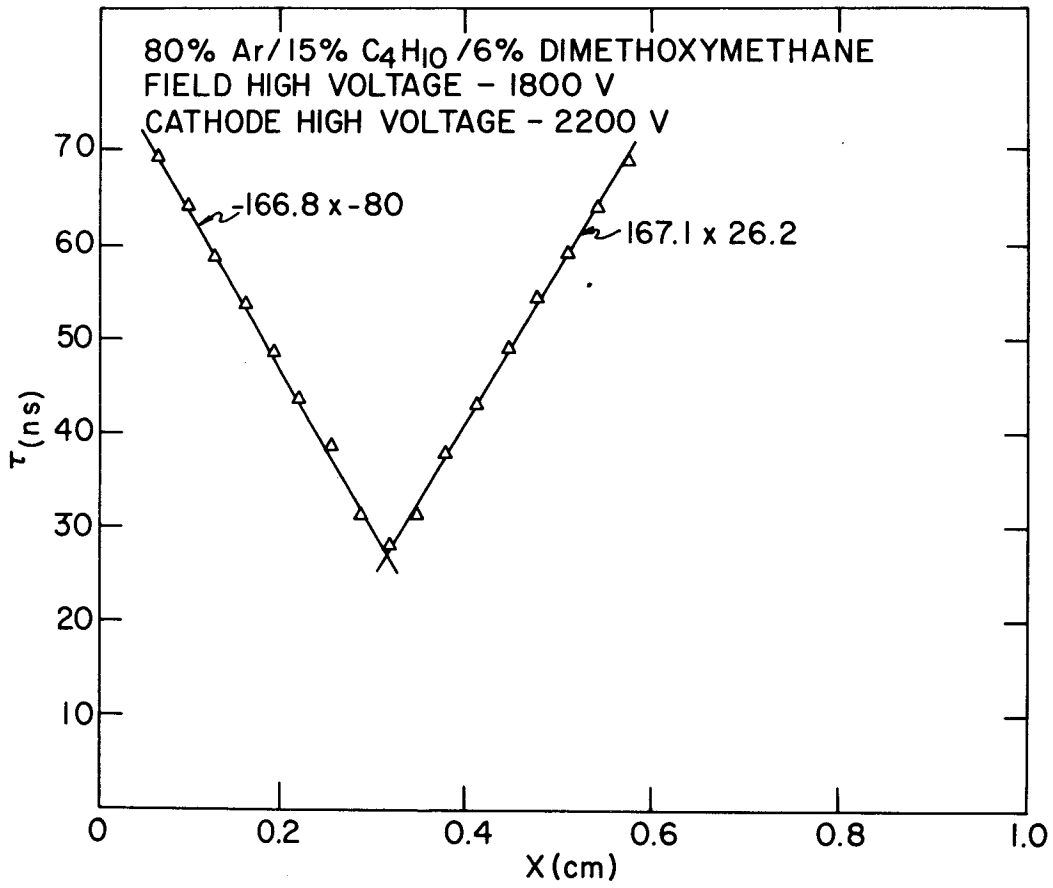
80% Ar/15% C_4H_{10}/6% DIMETHOXYMETHANE
FIELD HIGH VOLTAGE - 1800 V
CATHODE HIGH VOLTAGE - 2200 V
-166.8 x -80
167.1 x 26.2
70
60
50
40
30
20
10
τ (ns)
0
0.2
0.4
0.6
0.8
1.0
X (cm)

Figure 3

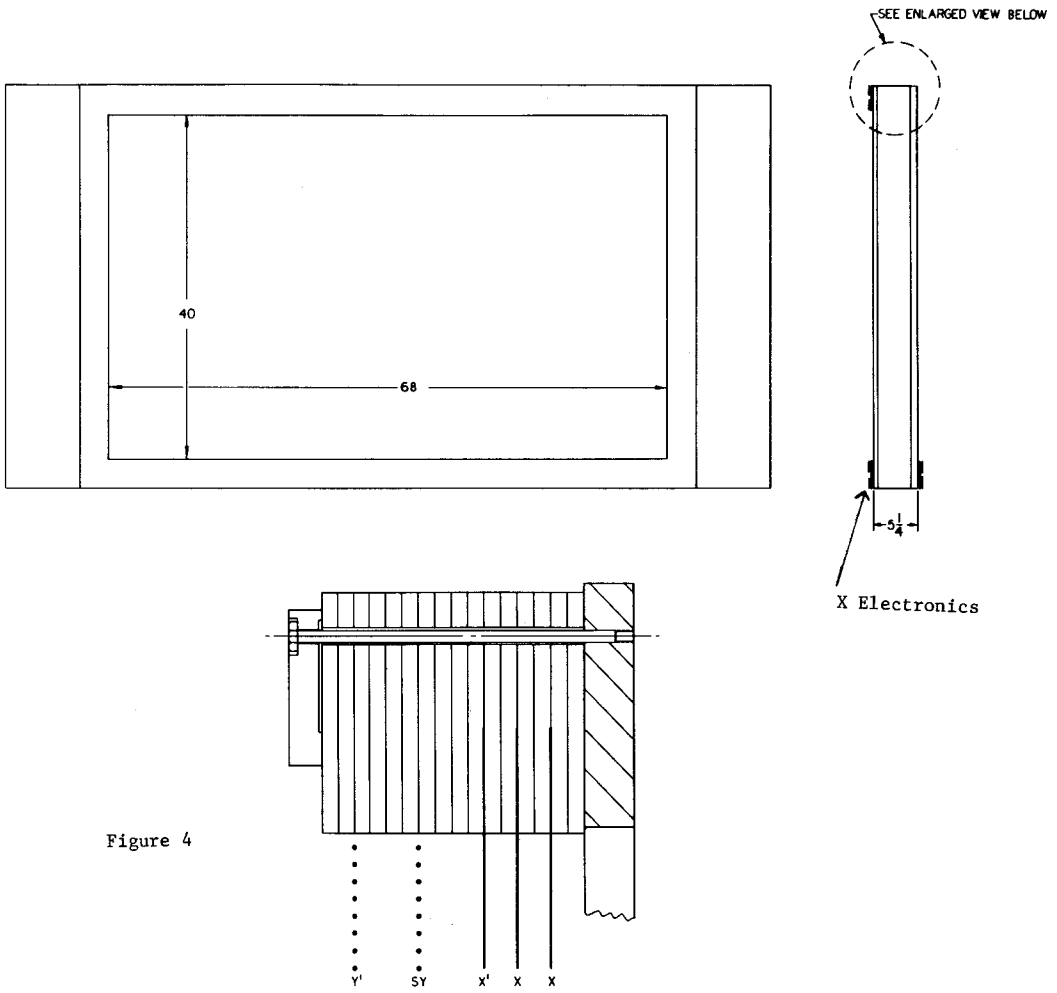

Figure 4

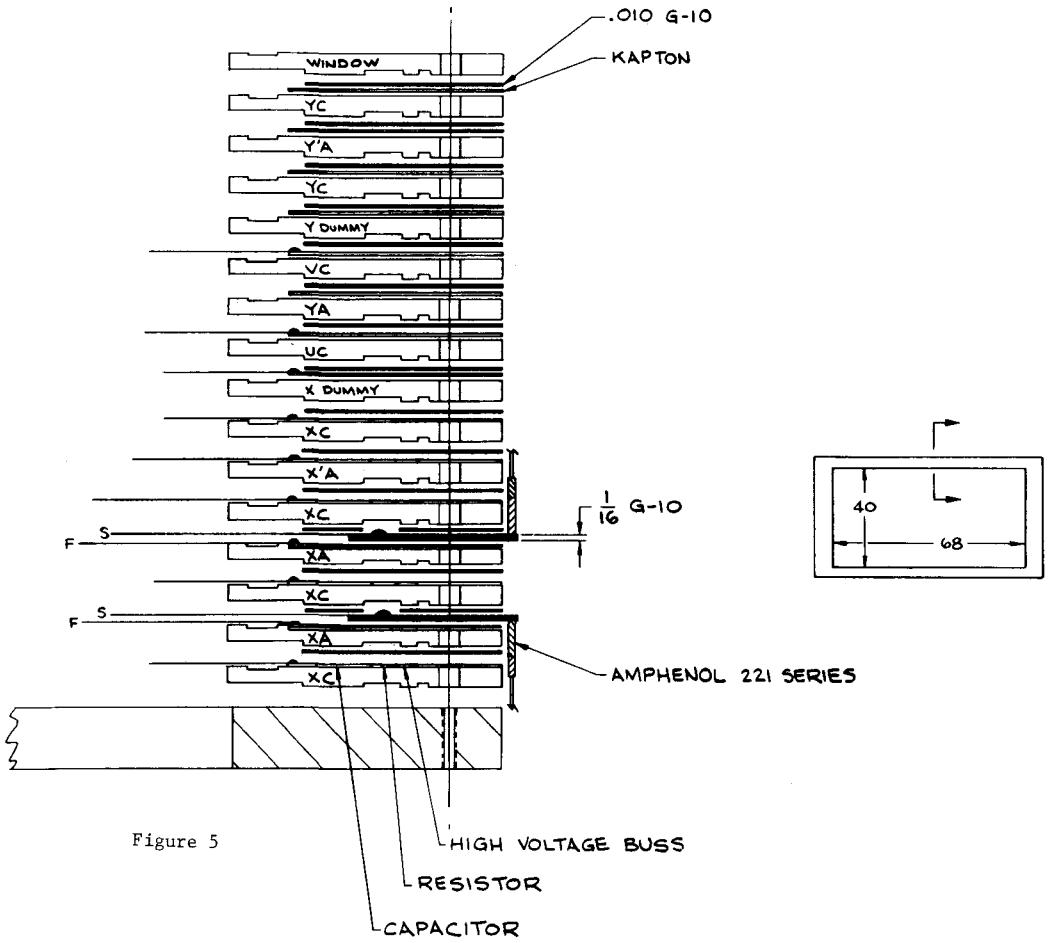
.010 G-10
KAPTON
WINDOW
YC
Y'A
YC
Y DUMMY
VC
YA
UC
X DUMMY
XC
X'A
XC
S
F
XA
XC
S
F
XA
XC
1/16 G-10
AMPHENOL 221 SERIES
40
68
HIGH VOLTAGE BUSS
RESISTOR
CAPACITOR

Figure 5

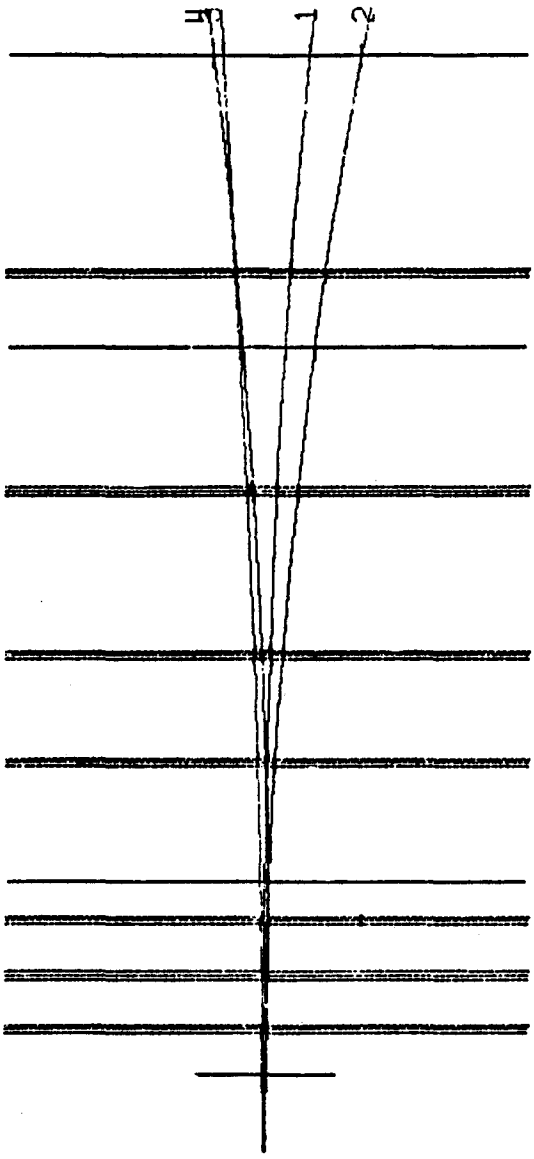

Figure 6

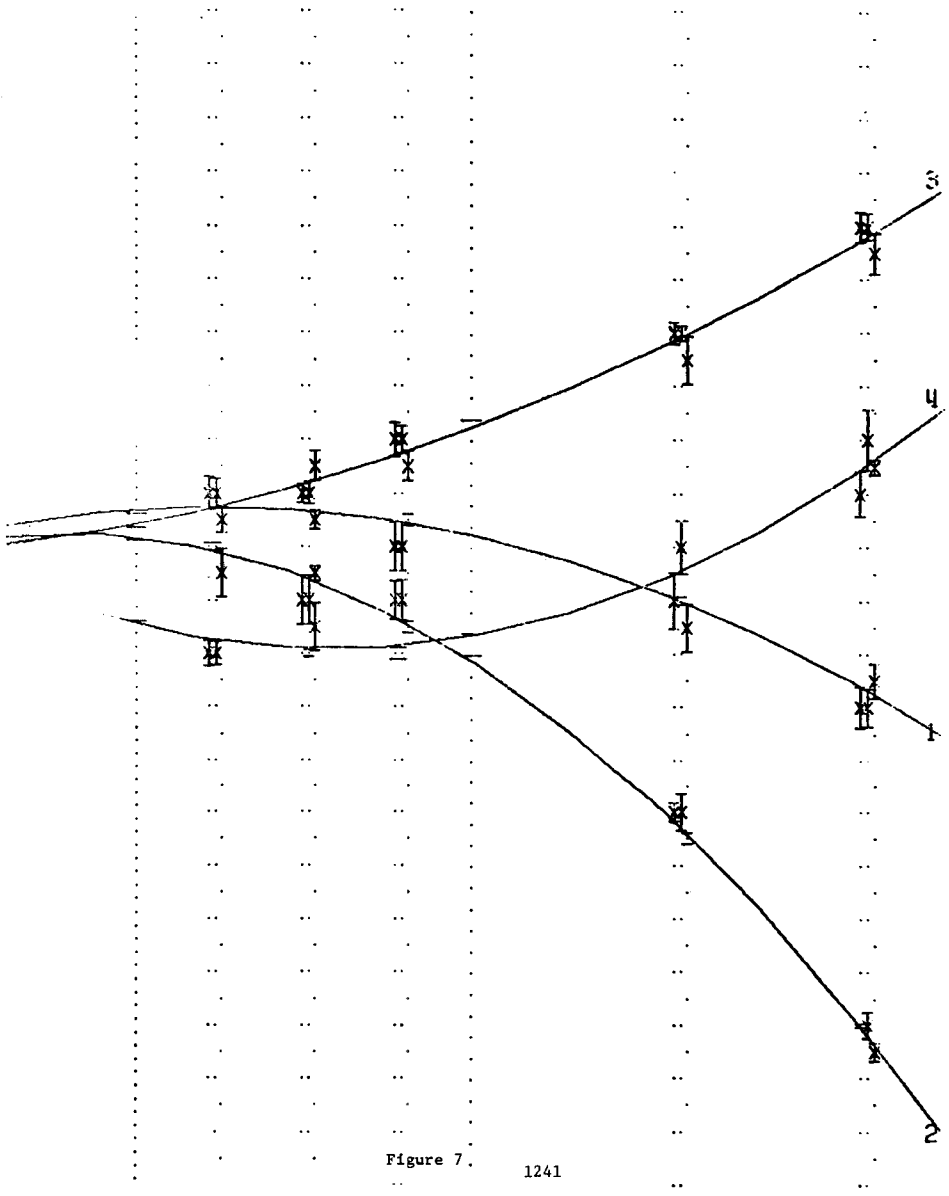

Figure 7.

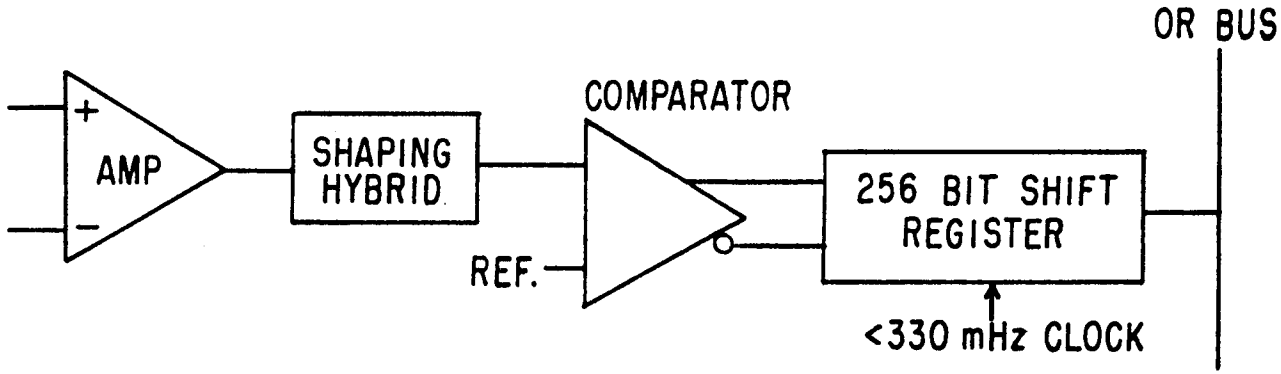
OR BUS
COMPARATOR
+
AMP
−
SHAPING
HYBRID
REF.
256 BIT SHIFT
REGISTER
<330 mHz CLOCK

Figure 8

SMALL CELL DRIFT CHAMBERS AND DRIFT CHAMBER ELECTRONICS AT ISA

E. Platner, BNL

ISA (phase 1) is designed for bunched beam operation with 10 ns bunch width every 220 ns. This matches a drift cell size of 10 mm or less, since interactions from previous crossings are swept away. Also, in the small drift path limit the complications due to a magnetic field can be ignored. Double track resolution is given by the arrival times of the particles' ionizations. If the arrival times merge separation is difficult. Separation requires > 100 ns between tracks, and this problem is also side stepped by the use of small cells.

Small cell size is also advantageous at the ISA because of the high charged multiplicity per event ($\langle n \rangle \simeq 50$). At 0.2 interactions per crossing ($L = 3.10^{31}$ $1/cm^2$) the absolute rate should not be a problem.

However, the major fiscal and experimental problem will consist of reading out huge numbers (> several x 10^4) of wires via reliable densely packed electronics. A packing density of 4 channels (signal to digital) per inch of circumference at a cost of less than $25 per channel has been reached by the design described below. Equipping both ends of a large cylindrical wire array with this system is feasible.

In the course of developing the new detector systems for MPS II,[1] several custom IC's have been produced which should be of interest to others involved in High Energy Physics detectors. The circuit requirements were determined by the desire to achieve performance limited only by the physical processes of the detectors. The detectors reside in 5-10 Kg magnetic fields and must efficiently detect multibody final state events in the presence of beam levels approaching several times 10^6 per second.

The tracking detectors are narrow drift space (3 mm) drift chambers and could be arranged in modules of X, X, X', U-Y-V, Y' planes. The U and V planes are ±30° to the Y plane. Because of the high rate and high multiplicities planned for MPS II experiments, the electronics must be essentially dead-timeless. In order for sophisticated event selection logic to perform its function, the real time data from each channel must be delayed

without loss for a period of $\lesssim 1$ μs. Because of the large number of channels (16,000) it was deemed crucial that each channel have a minimum number of parameters describing its properties, e.g. reference time (t_o), time to digital conversions slope, slope linearity, etc. Thus a technique was developed which requires none of these potential corrections. Also the large number requires a high degree of compactness. These considerations led us to develop a series of multi-channel custom integrated circuits, one of which is a true state-of-the-art device.

Figure 1 is a block diagram of one channel in the drift chamber electronics. The amplifier is a differential transresistance amplifier having a gain of 20K, .25 μa rms input noise (with 7ns shaping) and a 4 ns risetime. It comes 4 amplifiers to an 18-pin dip which has propagation delay variance < ± .75 ns. The shaping circuit has a 60 ns differentiating time constant and an overall 7 ns integrating time constant. It is packaged in a 4-channel 18-pin hybrid.

The comparator IC is also 4 channels when used in TDC applications. It has 8 mv of hysteresis, a propagation delay variance < ± 1.5 ns and an X10 overdrive slew time of < 3 ns. Its output is differential to minimize coupling to the amplifier IC which might cause oscillation. This 4-channel comparator also contains two additional comparators and some logic so that the IC can also function as a 2-bit, 2-channel ADC.

The final IC in this drift chamber electronic system is a truly state-of-the-art device. It is functionally a 4-channel, 256-bit shift registor IC that is fabricated with the CMOS silicon on Saphire (SOS) process. It is capable of acquiring data at > 330 MHz on each channel. Figure 2 is a detail of the internal logic of the device. To achieve this speed performance, the device is internally an 8-phase structure. Thus each phase runs at $\leq$ 330 MHz ÷ 8. To provide practical external clock risetime and levels, the clocking is done with a 4-phase clock driver. This clock then must operate at no more than 330 MHz ÷ 4 or 83 MHz, a much simpler task than operation at the primary frequency of $\leq$ 330 MHz. A consideration of great importance in a multi-phase shift register is the relative delay between the time data is actually acquired in each of the 8 phases. This has been measured at 250 MHz to be 4 ± 0.5 ns in absolute range on a large number of devices. The standard

deviation of this variance, a number of greater relevance to drift chamber applications, is .3 ns.

Propagation delay is ± .75 ns for the amplifier, ± 1.5 ns for the comparator and ± .5 ns for the shift register which in the worst case comes to ± 2.75 ns. This translates to ± 140 μ in space resolution. Probably a more realistic measure of this performance variance is the standard deviation. With a purely random selection of devices, this is 60 μ, which is also the rms quantization error. Thus at this level of measurement precision no correction for reference time variation (t_o) need be made. Since time is determined by a crystal oscillator operating at the same frequency for all channels, no corrections need be made for time to digital conversion slope or slope nonlinearity.

The data is acquired by running the shift register at 250 MHz. Then 1 μs after an event of interest has taken place, the clock is stopped. Channels with data will then have a string of "1"'s somewhere in the last 32 bits of the 256 bit register, the position of the furthest "1" being a precise measure of the drift time for that drift chamber cell. Data is extracted by use of the enable circuitry which allows selection of clocking for one channel only and gating of the end shift register element to a common "OR" bus. Once a channel has been selected for readout, the clock is turned on at < 50 MHz primary frequency for 32 ticks and the "OR" bus data is digitized by an encoder common to one whole plane of the drift chamber.

Figure 3 is a picture of an 64 channel printed circuit which contains everything required for this drift chamber readout system except the clock controllers and the digital encoders which are common to each plane of the detector. These circuit boards are mounted on the chamber support frames and do not extend into the chamber fiducial space. They are less than 1/2 inch thick so that chamber modules can be spaced as close together as 8" each.

Excluding the development costs for these 3 custom IC's the cost of each of the devices in the quantities required for MPS II are: amplifier, $2.50/ch., shaping hybrid, $2.50/ch., comparators, $4.00/ch. and shift register, $4.25/ch. All three of these devices should find broad applications in a variety of High Energy Physics systems. The amplifier and comparator are well-suited to use with current source detectors such as phototubes, PWC's,

and avalanche photodiodes. The shift register has already been employed in 100 MHz ADC's. Since it is more than twice as fast as any existing comparably sized memory device commercially available, one can see broad applications in addition to the obvious TDC use, for ADC memory, logic analyzer memory and ultrafast digital oscilloscope usage.

I wish to thank my MPS colleagues for making this rather extensive development project possible.

REFERENCES

1. A. Etkin, IEEE Transactions on Nuclear Science Vol. NS-26 No. 1, 54-58 (1979).

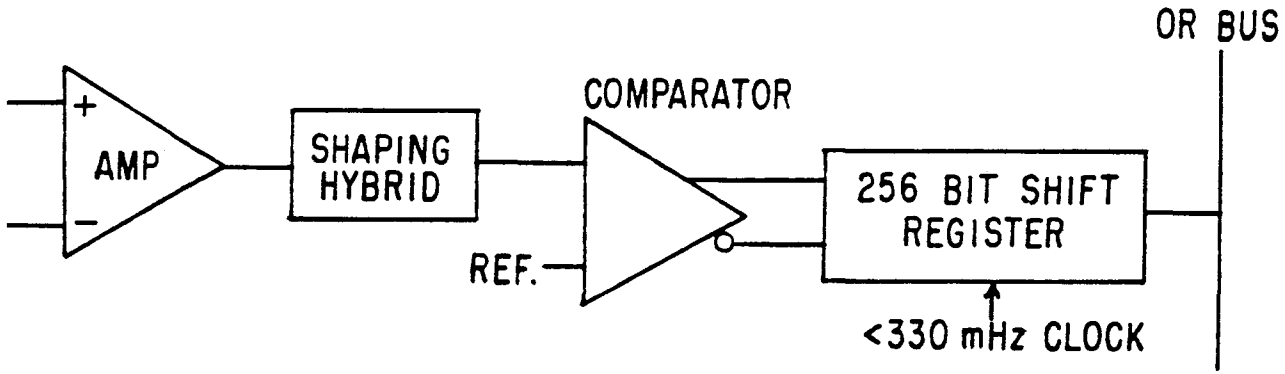
OR BUS
COMPARATOR
+
AMP
−
SHAPING
HYBRID
REF.
256 BIT SHIFT
REGISTER
<330 mHz CLOCK

Fig. 1

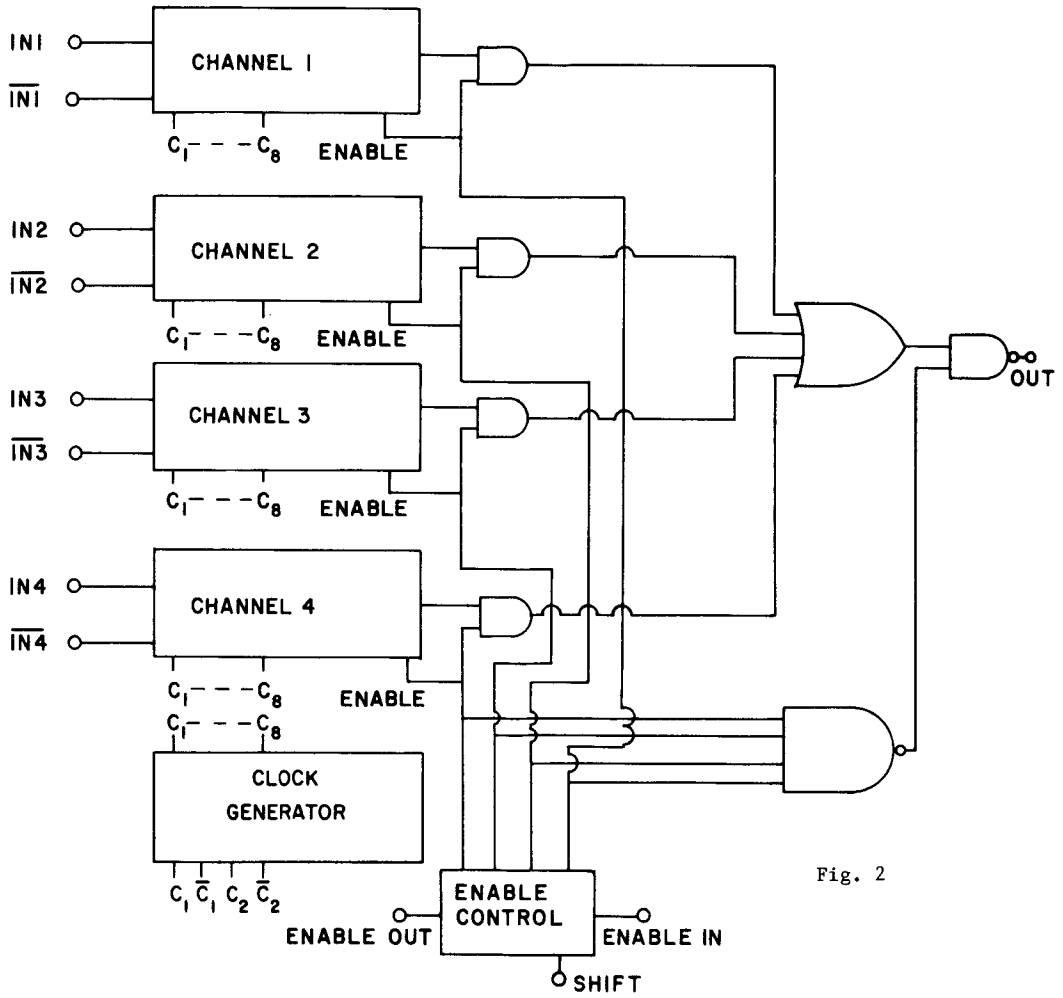
IN1
$\overline{IN1}$
CHANNEL 1
$C_1 - - - C_8$
ENABLE
IN2
$\overline{IN2}$
CHANNEL 2
$C_1 - - - C_8$
ENABLE
IN3
$\overline{IN3}$
CHANNEL 3
$C_1 - - - C_8$
ENABLE
IN4
$\overline{IN4}$
CHANNEL 4
$C_1 - - - C_8$
ENABLE
$C_1 - - - C_8$
CLOCK
GENERATOR
$C_1\ \overline{C}_1\ C_2\ \overline{C}_2$
OUT
ENABLE
CONTROL
ENABLE OUT
ENABLE IN
SHIFT

Fig. 2

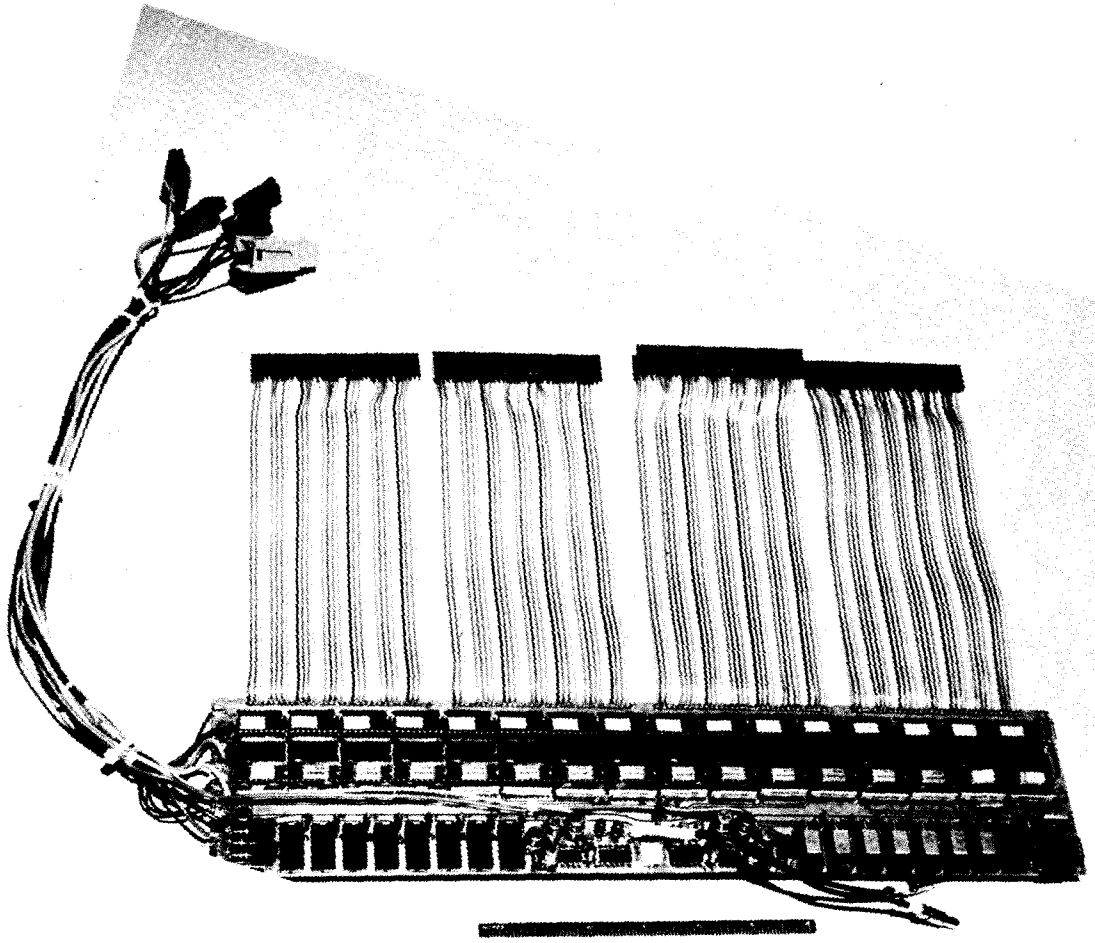

Fig. 3

VERTEX DETECTOR

P. Duinker, J.C. Guo, D. Harting, F. Hartjes, B. Hertzberger,
J. Konijn, G.G.G. Massaro -- NIKHEF, Amsterdam

A special chamber with 96 wires was used in the test beam at BNL from December 1980 to March 1981. The purpose of the measurement was to verify that the momentum resolution

$$\frac{\Delta p}{p} = \frac{p}{0.03} \frac{\sigma}{BL^2} \frac{1}{\sqrt{A_N, (N+5)}}$$

indeed improves with the number of track samples N = 96.

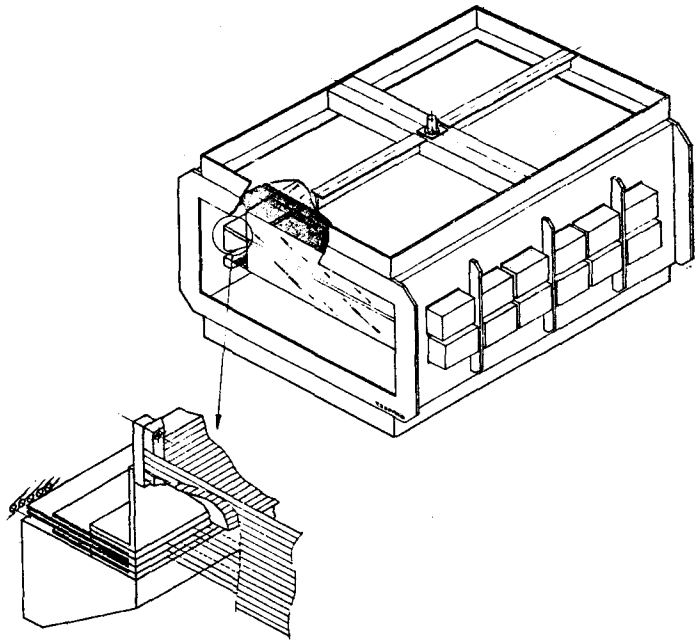

Figure 1. The chamber has a size of 1 x 0.8 x 0.4 m with ±10 cm of drift distance. Field shaping foils provide excellent drift field homogeneity.

The gas mixture used was Argon -Ethane 50:50. Figure 2 gives the efficiency curves as function of the potential wire voltage. The configuration is given in the insert. All 90 of 96 wires behave the same. Figure 3 shows the population in a short run as recorded by the computer.

The chamber was mounted in the BNL A2 test beam. Particles passed parallel to the vertical wires. A displacement mechanism allowed us to change the drift distance with the results shown in Figure 4. The chamber was then tilted in the beam which is an elegant way of measuring the resolution for various drift distances immediately. Figure 5a. gives the principle. Figure 5b. shows the residuals in ns versus commonly fitted straight line, yielding a resolution of 1.88 ns or $\sim$ 190 μm. Other values are plotted in Fig. 6, showing the typical behaviour. At close distance the spread of ionization decreases the accuracy and at big distances diffusion enforces a $\sqrt{x}$ behaviour. These resolutions are close to theoretical expectations.

Evaluation of correlations in time accuracy and pulse height are underway, as well as the the precise analysis to prove the $1/\sqrt{N}$ behaviour.

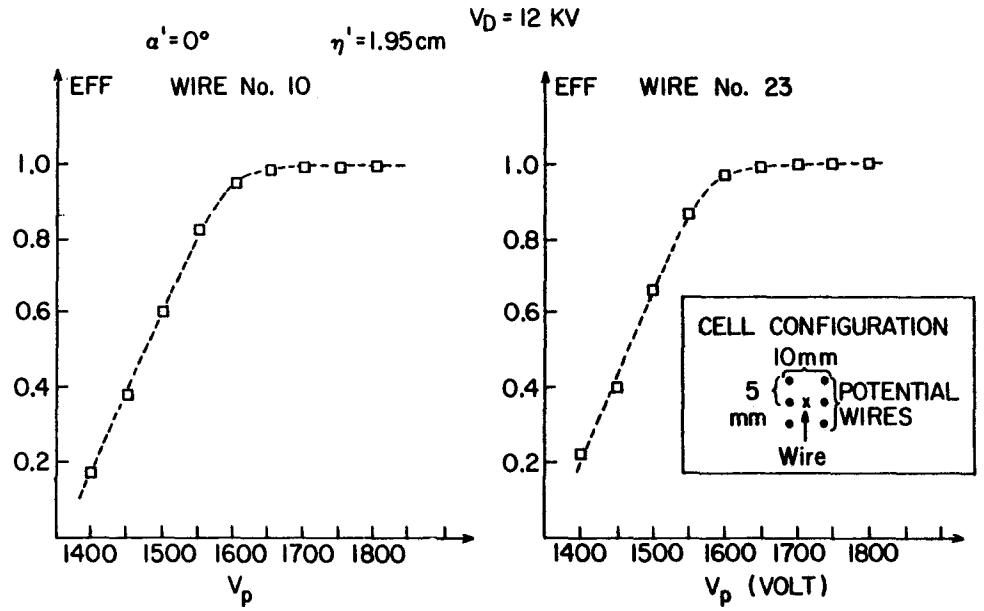
V_D = 12 KV
α' = 0°
η' = 1.95cm
EFF
WIRE No. 10
1.0
0.8
0.6
0.4
0.2
1400 1500 1600 1700 1800
V_p
EFF
WIRE No. 23
1.0
0.8
0.6
0.4
0.2
1400 1500 1600 1700 1800
V_p (VOLT)
CELL CONFIGURATION
10mm
5 mm
POTENTIAL WIRES
Wire

Fig. 2

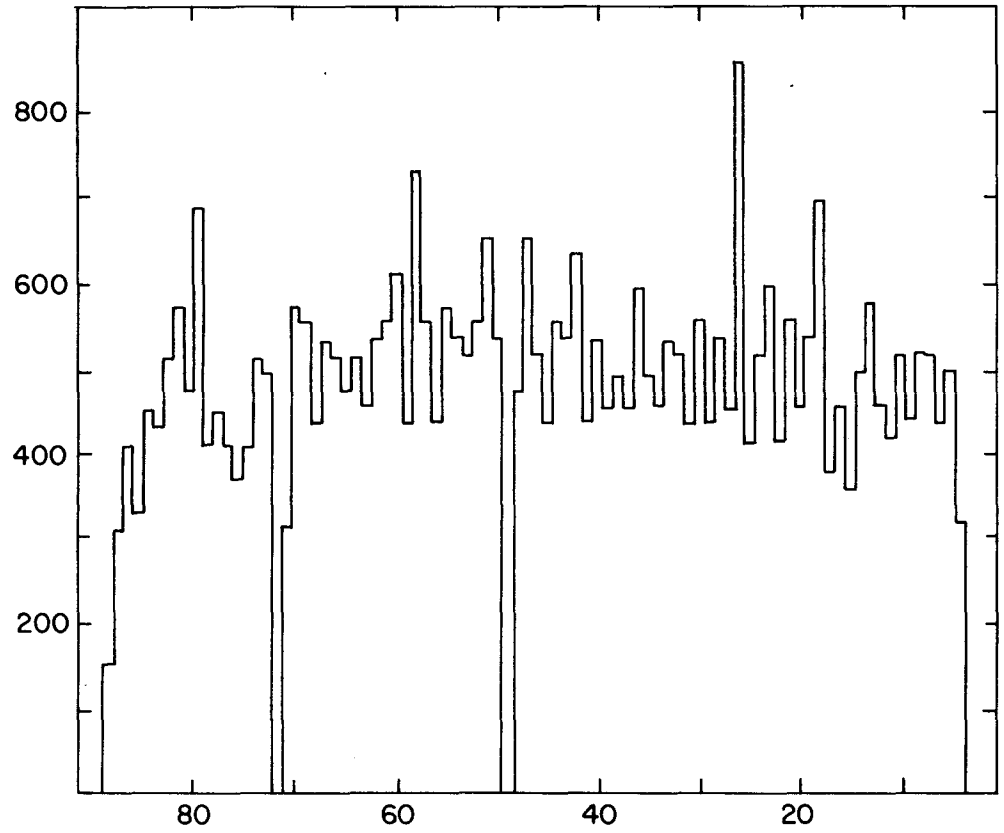

Fig. 3

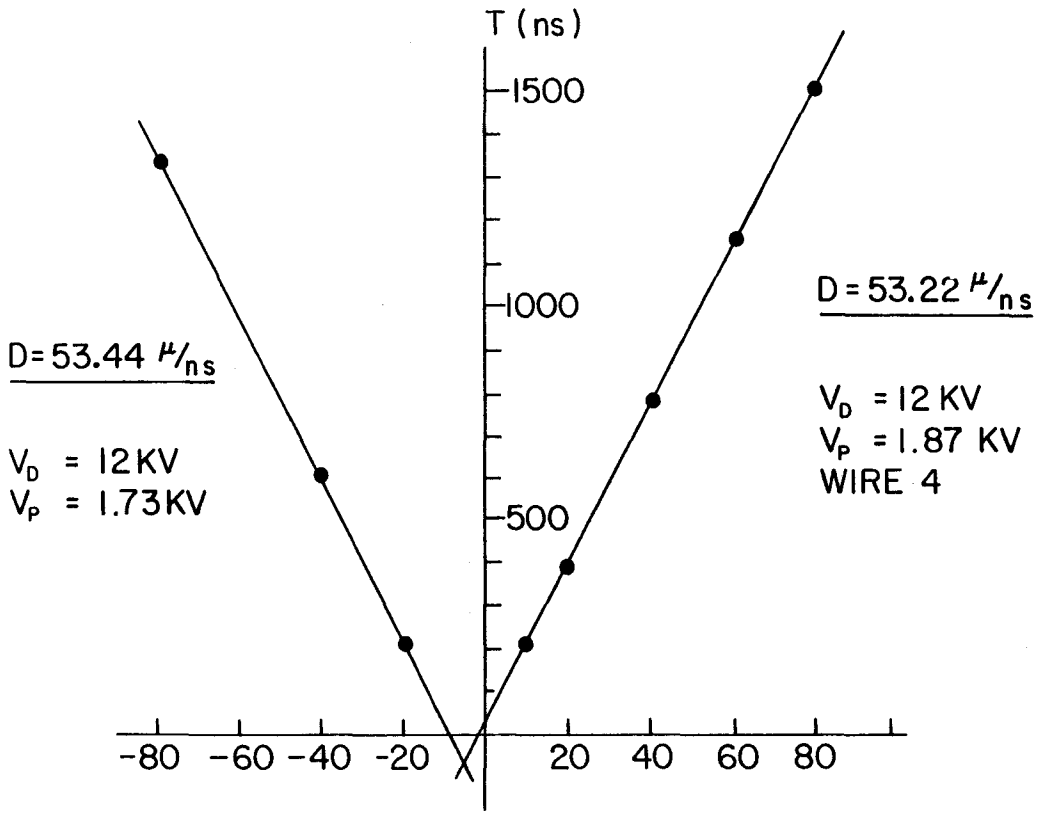
T (ns)
1500
1000
500
D = 53.44 μ/ns
V_D = 12 KV
V_P = 1.73 KV
D = 53.22 μ/ns
V_D = 12 KV
V_P = 1.87 KV
WIRE 4
-80 -60 -40 -20 20 40 60 80
S (mm)

Fig. 4

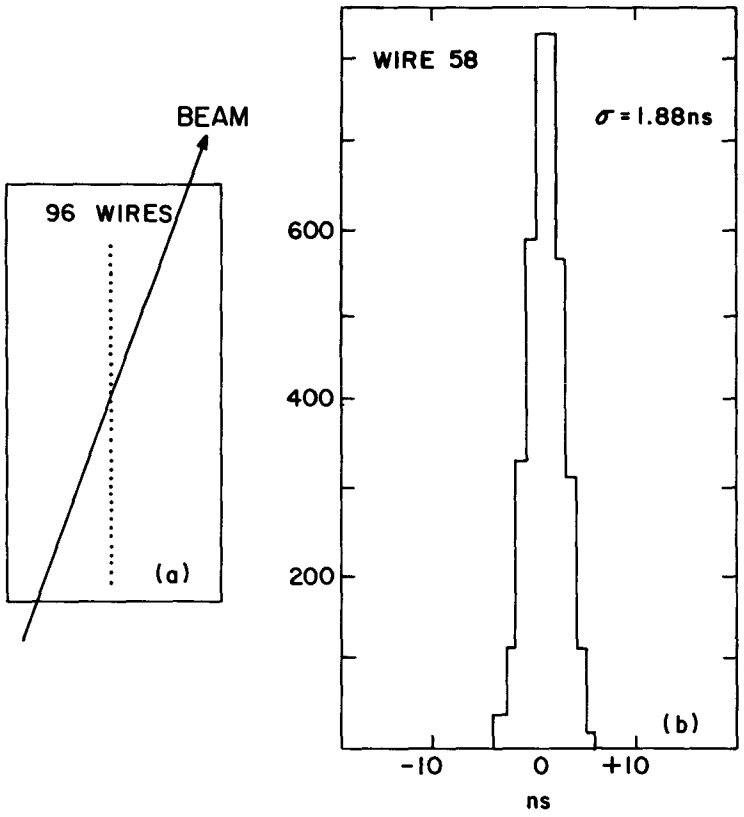

Fig. 5

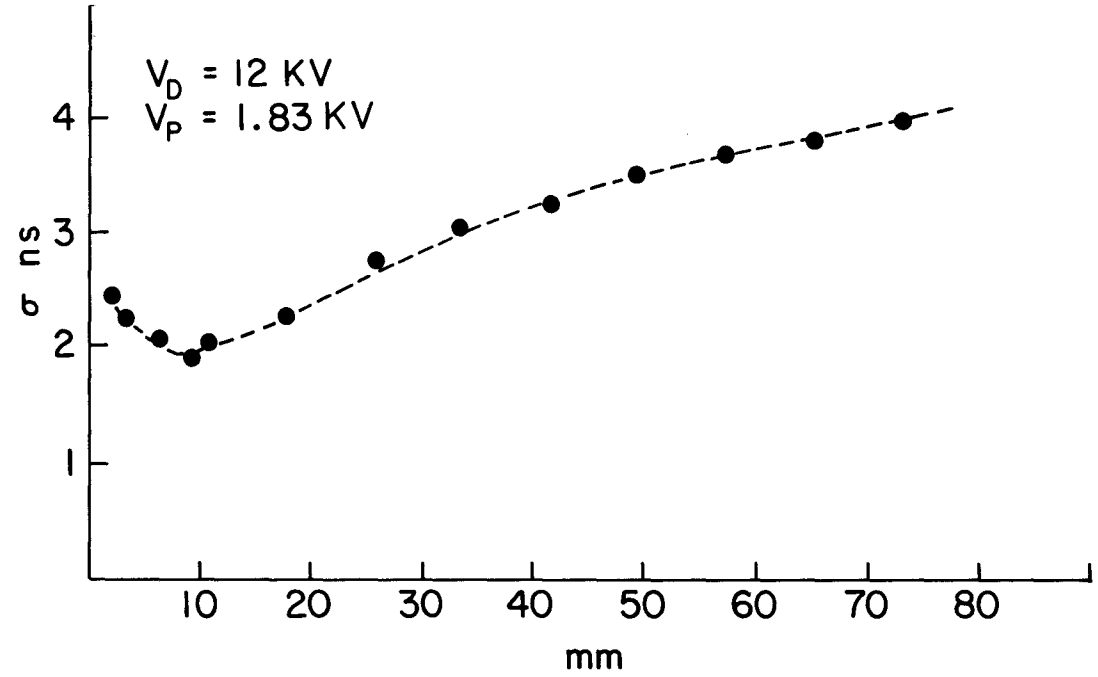

Fig. 6

PROPORTIONAL DRIFT TUBES FOR THE NEUTRINO EXPERIMENT AT BNL

Katsuya Amako
University of Pennsylvania

I. PHYSICS AND REQUIREMENTS TO THE DETECTOR

The initial physics interest centers upon precision measurements of neutral current phenomena at low E_ν. In particular elastic scattering of ν_μ (and $\bar{\nu}_\mu$) from protons and from electrons:

$$\left(\begin{matrix}\nu_\mu\\ \bar{\nu}_\mu\end{matrix}\right) + e^- \rightarrow \left(\begin{matrix}\nu_\mu\\ \bar{\nu}_\mu\end{matrix}\right) + e^- \text{ and } \left(\begin{matrix}\nu_\mu\\ \bar{\nu}_\mu\end{matrix}\right) + p \rightarrow \left(\begin{matrix}\nu_\mu\\ \bar{\nu}_\mu\end{matrix}\right) + p$$

Measurements on several other reactions must be made simultaneously as they contribute to background and/or normalization for the reactions of interest; among those are:

$$\begin{array}{ll} \nu_\mu + n \rightarrow \mu^- + p & \bar{\nu}_\mu + p \rightarrow \mu^+ + n \\ \nu_\mu + N \rightarrow \nu_\mu + N' + \pi & \bar{\nu}_\mu + N \rightarrow \nu_{\bar{\mu}} + N' + \pi \\ \nu_e + n \rightarrow e^- + p & \bar{\nu}_e + p \rightarrow e^+ + n \end{array}$$

Demands placed on the apparatus for suppression and understanding of background are somewhat different than at high energy; the design of the detector under construction has attempted to take these differences into account in order to achieve a goal of high background rejection and low systematic errors (<12%). These aims dictate that the detector possess:

1. good discrimination between single electrons and gamma ray conversions.
2. good angular resolution on individual tracks.
3. good discrimination between pions and protons.
4. ability to distinguish extra, low energy tracks at the vertex, neutrons and gamma rays in an event, and events with a decaying muon.

The salient features which result from considerations (1)-(4) are then:

1. a nearly completely active target
2. fine granularity
3. multiple measurements of dE/dx
4. multiple hit and timing capability
5. high electron density and moderately long radiation length in space.

II. DETECTOR

The physical parameters for the detector to achieve features described above are as follows:

1. Composition: 80% scintillator, 10% acrylic, 10% aluminum
2. Construction: Modular; each module consisting of a 4.25m x 4.25m vertical plane of calorimeters (for timing and dE/dx) backed by a vertical plane of X and Y proportional drift tubes (for position and dE/dx).
3. Completed detector to consist of 112 such modules for a total weight of >140 metric tons (75 metric tons fiducial) with dimensions of 4.25m x 4.25m.
4. Each calorimeter plane consists of 16 individual cells of dimensions 7.5 cm x 25 cm x 425 cm with two photomultipliers - one viewing each end. The total number of cells is $\sim$1800.
5. Each (X or Y) proportional drift tube (PDT) plane consists of 54 cells each 3.75 cm x 7.5 cm x 425 cm. The total number of cells is $\sim$15,000.
6. The effective radiation length is $\sim$60 cm in real space thus providing multiple position and dE/dx measurements in each event.
7. The main detector is backed up by a γ-catcher which detects escaping electro-magnetic showers. It is also backed up by the magnetic spectrometer which measures the momentum of μ's from charge current events to normalize the beam flux.

III. PROPORTIONAL DRIFT TUBES (PDT)

Requirements needed for the PDT are as follows:

1. position resolution < 3/4 mm
2. pulse height resolution $\sim$ 60% (FWHM)

As we need about 15 K cells, the PDT must have:

1. low mass
2. simple assembly for the construction
3. low cost

A. Construction

The cells are constructed from 0.5 mm aluminum sheets and I-beam dividers as shown in Fig. 1. The I-beam dividers are made by a roll forming technique out of 0.5 mm aluminum. Each cell has injection-molded end caps. At the center of the end cap, there is a brass pin which holds a stainless anode wire of 3 mil. The tension of the wire is set around 400g using a resonance-oscillation technique. After finishing the test, two planes are joined together to form the X and Y planes for rigidity. The average production rate is $\sim$1 plane/day. The production costs is $\sim$\$2.6 K/plane (= \$48/cell).

B. Electric Field

The potential of the anode wire is kept at +2.5 KV and the aluminum sheet and I-beam at ground. Additional voltage could be applied to the I-beam for a better space-time relation but it would cause a loss of some amount of primary electrons and make the PDT construction more complicated.

C. Test System

After the construction of each plane, the quality of cells have to be measured one by one. Since there are $\sim$15,000 tubes it is impossible to adopt the standard technique of measuring the pulse height by using a radioactive source and pulse height analyzer because:

1. it takes enormous amount of time and manpower
2. it can only check sampled points

In order to solve the above problem, a better technique has been developed.

When a radioactive source is put on the surface of the PDT as shown in Fig. 2, the average d.c. current (i) induced is

$$i \propto G \cdot I$$

where I is the intensity of the source and G is the gas gain of the tube. This means that the gas gain can be checked by measuring the induced d.c. current. Also the local gas gain in a cell can be checked by moving a collimated source along a wire. A typical value of i is $\sim$100 nA when a ^{109}Cd of 500 μC is used and the tube is operated at 2.4 KV using P10 gas. An automatic scanning machine has been constructed. The schematics of the entire test system is shown in Fig. 3. The induced d.c. current is recorded on a chart strip recorder while the source scans along a wire. Typical examples of the induced current along several wires are shown in Fig. 4. This technique is quite powerful for measuring quickly the average gas gain over the entire cell. Also it is easy to identify a defective wire, a corona discharge in a cell or an inefficient gas flow. The typical time needed to check one plane is $\sim$30 min.

IV. READOUT SYSTEM

A simplified view of the PDT signal processing electronics is shown in Fig. 5. Low level signals are handled by an "Analog" card and timing is measuring on the "Digital" card. Each of these cards processes signals for eight wires, and there are seven pairs of A/D cards on a 54 wire plane.

The signal current from a single PDT anode wire is amplified by a transresistance amplifier with a gain of $R_T = 20K\Omega$ ($V_{out} = I_{in} \times R_T$). A linear amplifier provides additional gain (x11) and a gated integrator stores the resulting signal as voltage on a capacitor (1 volt out $\simeq$ 3.6 pC in).

In the timing measurement, the CLOCK can be counted by two counters whenever the CLOCK GATE is on. A pulse over threshold at the discriminator enables the first counter (T1) and the second pulse over threshold enables the second counter (T2). The counters stop counting at the end of the CLOCK pulse train so that the time measurement has a common stop. The least count for the time measurement is 10 ns.

A simplified view of the entire data acquisition system is shown in Fig. 6. The data in the detector electronics is transferred by the readout scanners to the memories of LSI-11/03 microprocessors, from there to the D.E.C.-PDP 11/34 memory, and then to magnetic tape. The data is sent in sample mode to a D.E.C. PDP-10 for on-line analysis.

V. PERFORMANCE

A. Results from Test Beam

The property of the PDT was measured by radiating several sample cells in the A.G.S. test beam. The gas used was P10 (Ar 90% + CH_4 10%). The position-time relation in normal beam entrance is shown in Fig. 7. The pulse height distributions for π^+, e^+ and p at 0.8 GeV/c are shown in Fig. 8. The pulse height resolution for all particles is $\sim$50% (FWHM). The peak values of the pulse height of π^+, e^+ and p at various momenta are shown in Fig. 9.

B. Preliminary Results from the Main Detector

We are now running the experiment with 64 modules ($\sim$1/2 of full detector). We have been running more than one month without any damaged PDT cells. We have replaced $\sim$30 broken electronics boards. This number corresponding to $\sim$3% of entire PDT electronics. The raw pulse height distribution of minimum ionizing particles which go through all detectors is shown in Fig. 10. It shows a clean Landau distribution even though it is the summing up of pulse height information from different modules. The resolution is $\sim$80% even without a correction for incident angle of the particle or gas gain compensation from one module to another.

FIGURE CAPTIONS

Fig. 1 Cross-section of PDT plane.

Fig. 2 Principle of measuring the gas gain by monitoring the induced current.

Fig. 3 Schematics of the test system.

Fig. 4 Typical examples of the induced current along several wires.

Fig. 5 Signal processing electronics of PDT.

Fig. 6 Data acquisition system.

Fig. 7 Drift time vs. position relation.

Fig. 8 The pulse height distributions of π^+, e^+ and p at 0.8 GeV/c.

Fig. 9 Peak values of the pulse height of π^+, e^+ and p at various momenta.

Fig. 10 The raw pulse height distribution of minimum ionizing particle.

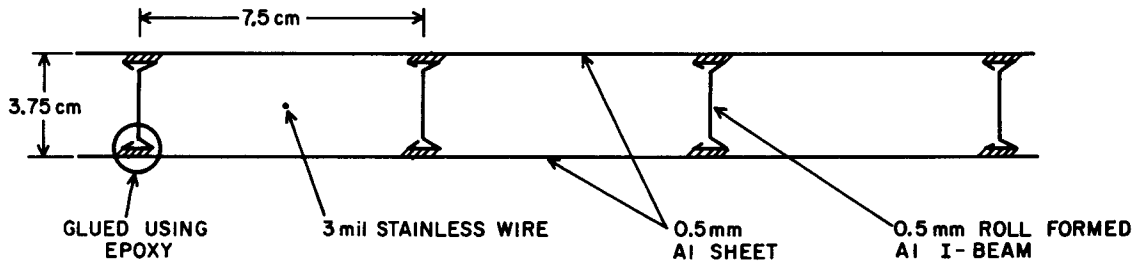
7.5 cm
3.75 cm
GLUED USING EPOXY
3 mil STAINLESS WIRE
0.5 mm Al SHEET
0.5 mm ROLL FORMED Al I-BEAM

Fig. 1

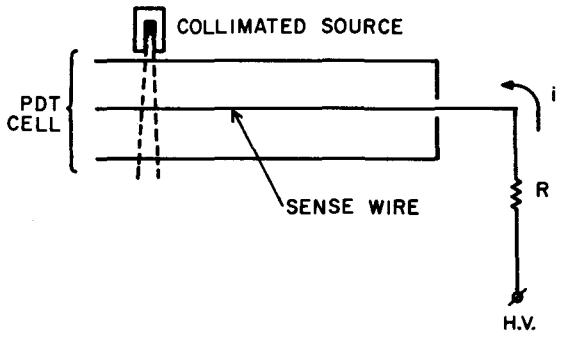

$i \propto G \cdot I$

G: GAS GAIN

I: INTENSITY OF THE SOURCE

Fig. 2

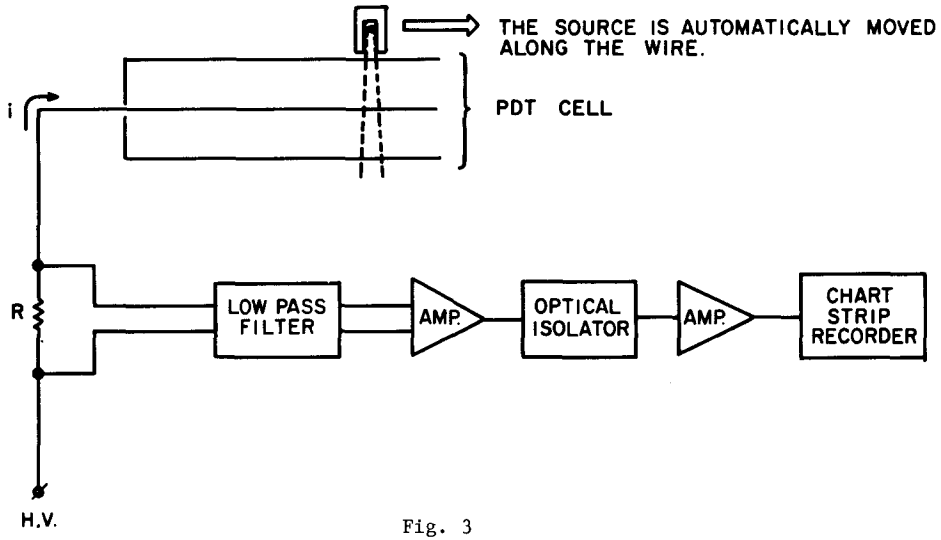
THE SOURCE IS AUTOMATICALLY MOVED ALONG THE WIRE.
PDT CELL
i
R
LOW PASS FILTER
AMP.
OPTICAL ISOLATOR
AMP.
CHART STRIP RECORDER
H.V.

Fig. 3

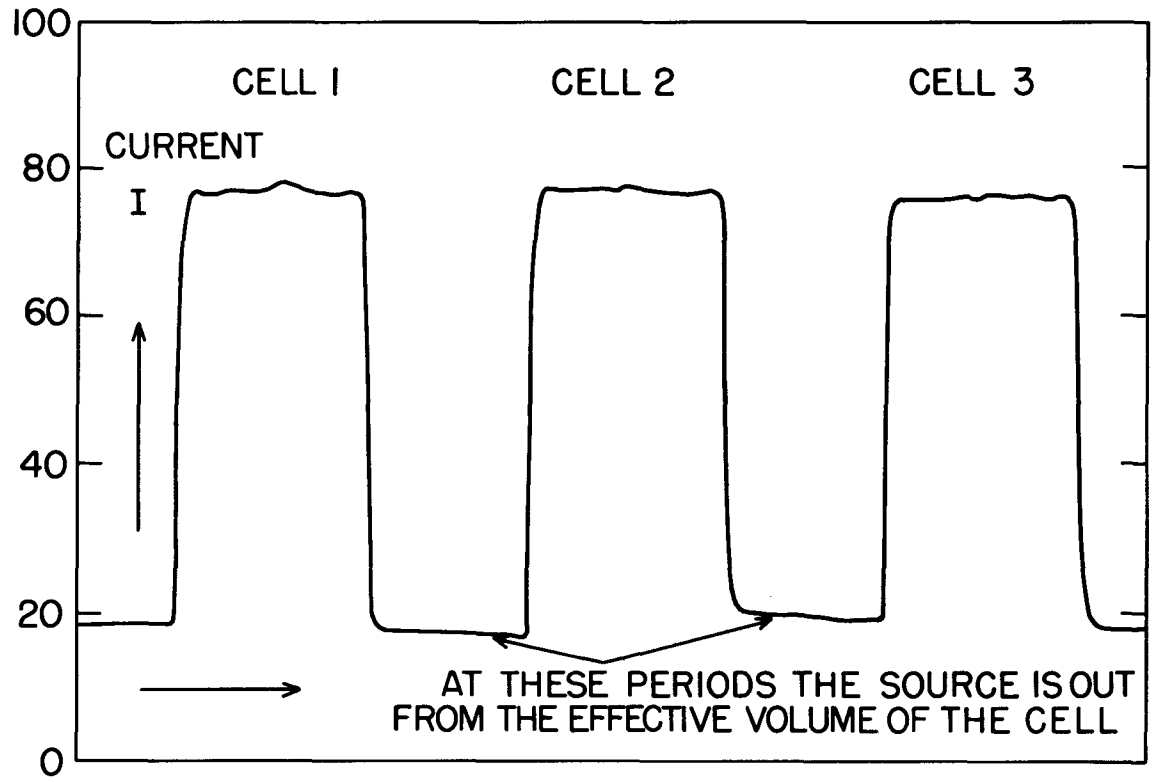
100
80
60
40
20
0
CELL I
CELL 2
CELL 3
CURRENT
I
AT THESE PERIODS THE SOURCE IS OUT
FROM THE EFFECTIVE VOLUME OF THE CELL

Fig. 4

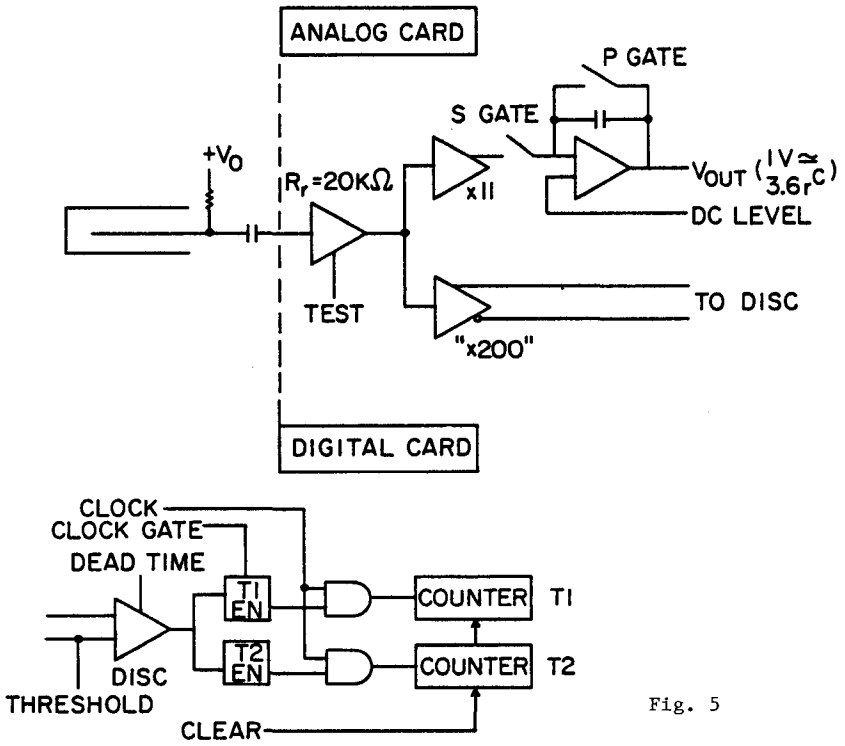
ANALOG CARD
P GATE
S GATE
+V0
Rf=20KΩ
x11
VOUT (IV≃3.6rC)
DC LEVEL
TEST
TO DISC
"x200"
DIGITAL CARD
CLOCK
CLOCK GATE
DEAD TIME
T1 EN
T2 EN
COUNTER
T1
COUNTER
T2
DISC
THRESHOLD
CLEAR

Fig. 5

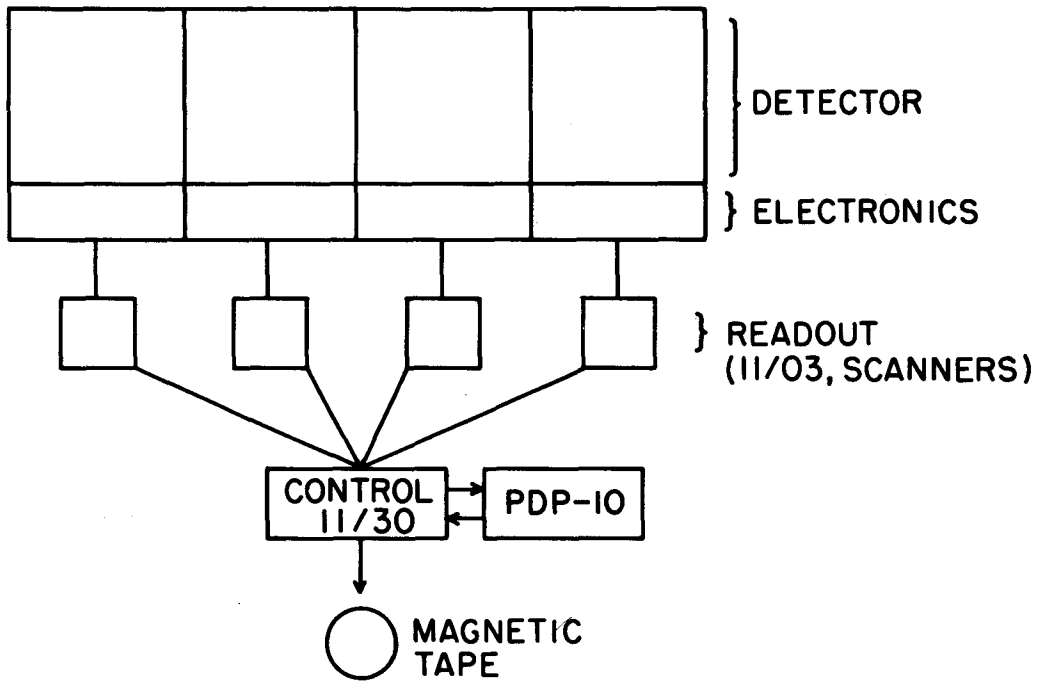
DETECTOR
ELECTRONICS
READOUT
(11/03, SCANNERS)
CONTROL
11/30
PDP-10
MAGNETIC
TAPE

Fig. 6

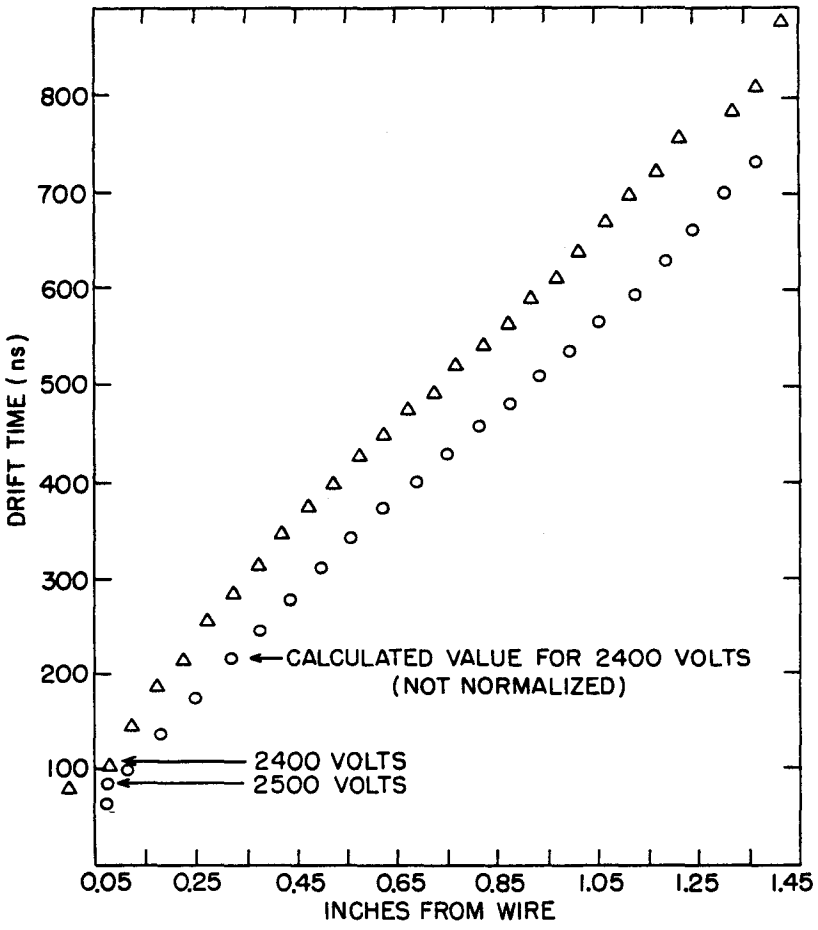
DRIFT TIME (ns)
800
700
600
500
400
300
200
100
0.05
0.25
0.45
0.65
0.85
1.05
1.25
1.45
INCHES FROM WIRE
CALCULATED VALUE FOR 2400 VOLTS
(NOT NORMALIZED)
2400 VOLTS
2500 VOLTS

Fig. 7

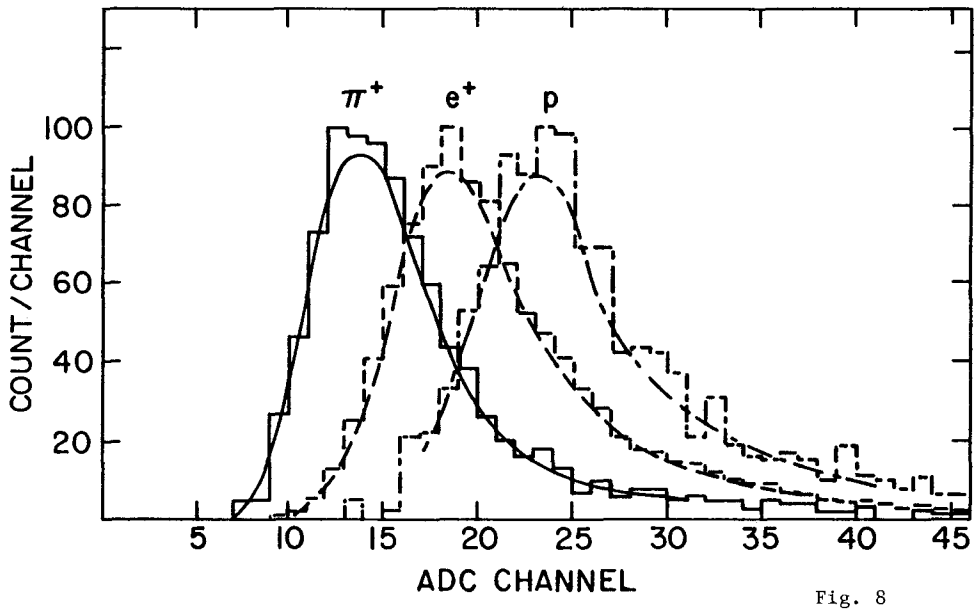
π+
e+
p
100
80
60
40
20
COUNT/CHANNEL
5
10
15
20
25
30
35
40
45
ADC CHANNEL

Fig. 8

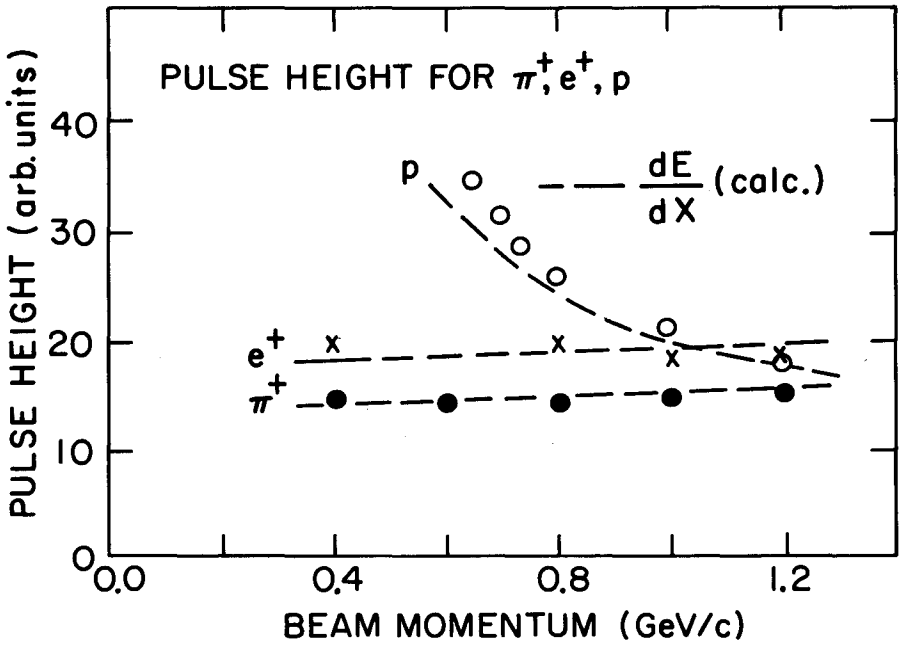
PULSE HEIGHT FOR π^+, e^+, p
PULSE HEIGHT (arb. units)
40
30
20
10
0
0.0
0.4
0.8
1.2
BEAM MOMENTUM (GeV/c)
p
$\frac{dE}{dX}$ (calc.)
e^+
π^+

Fig. 9

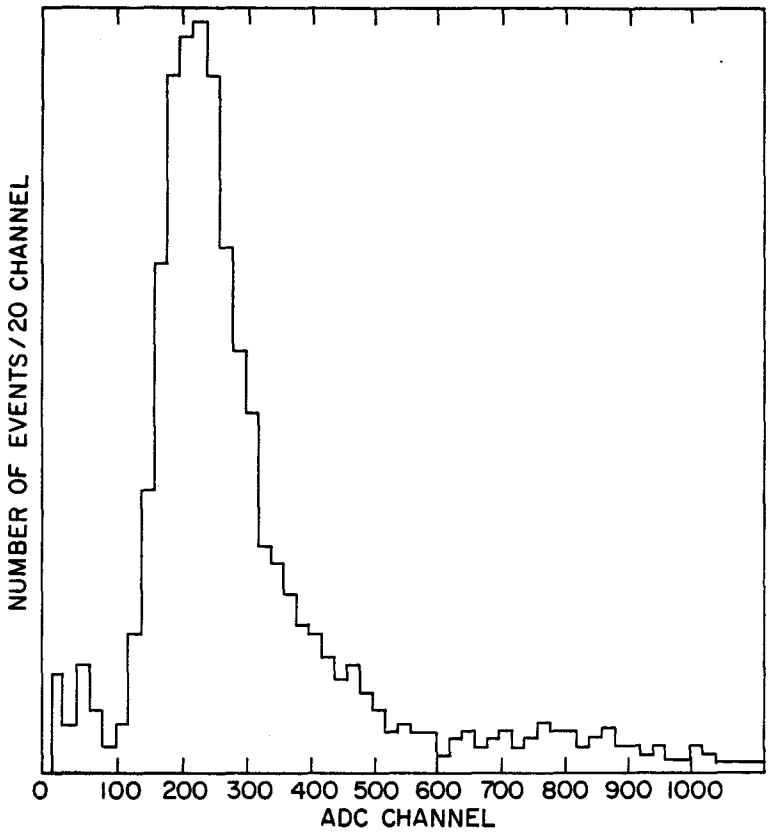
NUMBER OF EVENTS/20 CHANNEL
0
100
200
300
400
500
600
700
800
900
1000
ADC CHANNEL

Fig. 10

SOME USABLE WIRE DETECTOR CONFIGURATIONS FOR ISABELLE

U. Becker and M. Capell, Massachusetts Institute of Technology

The features of the principal central wire chambers in some existing (or close to) experiments were updated in a summary[1]. All were developed for either e^+e^- colliders or low luminosity $p\bar{p}$ machines. Considering ISA intensities, and the 10 ns bunched structure with 220 ns pause the following configurations were considered of merit:

A. A calorimeter around the beam pipe measures hadrons and thereby reduces the rate of penetrating particles (mostly muons) to conditions of low multiplicity. Very accurate momentum determination is possible in this case and has been described.[2]

B. In the forward region, 4-20° from the beam, rates are high and tracks close. A new development of densely packed and affordable electronics[3] offers the possibility of an effective detection device.

1. Choosing the drift distance less than 1 cm width is equivalent to 200 ns and will automatically clear all cells from events of the previous crossing.

2. Having such small cell size allows magnetic fields up to 15 kG without substantial distortion of accuracy.

3. Selecting triplets of planes oriented at 0°, 120°, and 240° is a powerful means of selecting valid unambiguous coordinates of tracks by demanding $N_1 + N_2 + N_3 = \text{const}$. This technique has been used under extremely high rate conditions successfully.

4. Having two such triplet plane chambers close to each other will provide a local slope of each track. Rotating them 30° removes degeneracies from adjacent tracks. This will allow rejection of small angle background.

5. Two such arrays can determine forward tracks. However, with magnetic field 3 or more are required.

C. The central region $20 < \theta < 160°$ usually requires a tracking device. In an "open" (that is not shielded by a calorimeter) configuration the background has to be considered. Estimates based on Etkins[4] formula lead only to 2-3 tracks deposit from the average background event, occuring with 20% probability in 200 ns for phase I. (Phase II poses a 10-20 times harder

problem which will demand other solutions.) The estimates are too low , the average charged multiplicity $\langle n \rangle \approx 20$ assumed in 1977 is already reached at Petra energies and $\langle n \rangle = 40$-50 may be an updated guess. Similarly F. Paige's event simulations show higher multiplicities.

1. Having 1 cm diameter proportional tubes orthogonal and immediately around the beam pipe is an extremely effective means to select events from background as shown with Mark-J at Petra. Drift tubes survive synchrotron radiation blasts worse than ISR beam spray. The detection of the event vertex within the FWHM = 25 cm interaction some will enable "sorting old tracks out".

2. Radially outward a small distance drift chamber with 3-6 layers parallel to the beam and 200 cells/layer will be able to sort tracks in azimuth reasonably well. Discontinuities to tracks into the central chamber will again identify events not occuring at the time of the trigger.

3. This principle has been used in the Cleo detector. If one would attempt to recover the entire pattern, including δ-rays, decays, etc. one would need more radial samples. In regular radial distance small cell drift regions should provide unambiguous points with local slope information. The computer then can start searching tracks from those and reduce the picture fast.

REFERENCES

1. M. Capell, these proceedings.
2. The MIT design for a muon detector at ISABELLE, described in these proceedings.
3. E. Platner, these proceedings.
4. E. Etkin, Proc. 1977 ISABELLE Summer Workshop

The Parameters of Some Central Detectors

CENTRAL DETECTORS

	Size			Coordinates		Wires			Resolution			
	R min - max	L	Magnetic Field	left-right Ambiguity?	Z-coord	Point/Track drift+prop.	Total # of wires	Max. drift path	$\sigma_{r\phi}$	σ (elec.)	σ_z	σ (double track)
Mark II	45-150 cm	240 cm	-	stereo		16 + 0	3100	2 cm	210 μm	0.9 ns	4 mm	-
TASSO	18-123	284	5 kG	stereo		15 + 4	2340	1.7	220	0.75	4	16 mm
CELLO	17-75	-	13	stereo	Charge division on PC's	7 + 5	-	1.0	210	0.92	4	-
JADE	19-80	234	4.5	off-line	Charge division	48	1536	7.5	180	2.17	16	7
AFS	19-80	128	5(axial)	staggering	Charge division	42	3400	2.8	200	1.15	15	4
UA1	20-95	-	varies, dipole	double wires	Charge division	80	6100	18	-	1.15	-	-
TPC	19-100	200	15	TPC	TPC	192	14000	100	-	-	-	24 x 21
MPS II*	(planer)	172	10	cells offset	30° stereo	25	16000	0.3	160	-	"160μ"	3

(Ref: Wagner, Central Detectors, DESY 80/83)

except * E. Platner, these proceedings

Notable omissions: CLEO, Mark III, HRS

Compiled July '81 by M. Capell, M.I.T. for use in thinking about ISA detectors.

COMMENTS ON CHAMBER LIFETIME

H. J. Hilke, CERN

We will summarize previous measurements on chamber deterioration - due to deposit formation on the electrodes - and comment on some new results.

To define a scale, we take typical irradiation levels found at the ISR for 30 x 30 GeV pp with $L = 10^{31}/cm^2$ sec. The values were measured in the inner section of the AFS drift chamber: R = 20 - 31 cm, $\Delta\phi = 4°$, sense wire separation = 8 mm.

With a gas amplification of 5×10^4, the irradiation was:

$$Q_{1y} = 1.5 \times 10^{16}\ e^-/\text{mm wire/year},$$

assuming 50% operation and twice the average irradiation for the hottest area. This value includes a high fraction from background irradiation.

Previous and new results are summarized in Table 1. We call Q_c (electrons/mm wire) the critical integrated charge for which an aging effect was observed. $Q_c > \ldots$ means, that no effect was seen for this irradiation. It is not yet clear, whether the total integrated charge is the only important parameter or whether the gas amplification or the rate of irradiation have an effect.

Comments:

In the earlier tests (Ref. 1), polymerization products seemed to settle first on cathodes. It, therefore, seemed reasonable that the rate of aging was strongly dependent on the cathode configuration (wire, mesh or flat electrodes).

In the recent tests (Ref. 5), electron microscope investigations showed strong deposits on the anodes but nothing on the cathodes. The main component is clearly Si, except possibly for elements with $Z < 11$, which were undetectable. One finds glass like layers all around the wire and sometimes in addition big lumps. The quantity is frightening, roughly 1 atom per 10^3 electrons hitting the wire.

Similar Si deposits have been observed by several other groups at CERN.

Ar/CO_2 mixture showed a similar aging behavior as Ar/C_2H_6 (Ref. 5).

Possible causes as gas contamination and G10 are being investigated, others like plastic pipes, filters and bubblers have been shown not to be responsible (at least as major cause, Ref. 5). Chambers not containing G10 have also shown aging effects (Ref. 6).

We conclude that there are other effects than the polymerization of the main gas components which may determine the chamber lifetime. In view of the disturbing results (e.g. gain dropping by 15% after 2 years at $L = 10^{31}/cm^2$ sec) it seems highly indicated to continue intensive studies on the chamber lifetime problem.

REFERENCES

1. NIM 99, (72), 279.
2. TPC group, Berkeley (unpublished).
3. CERN, EP int. 77-10, Friedrich, Sauli.
4. ISABELLE Summer Workshop 1978, p. 141 ff.
5. Tests by the AFS collaboration (D. Cockerill et al., CERN, ISR, details unpublished. Electron microscope studies carried out at Brookhaven and at CERN.
6. H. Walenta, private communication.

Table 1

Gas	Ref.	$Q_c(e^-/mm)$	Comments	
Ar/Isobutane/CF_3Br	(1)	2×10^{13}	wire cathode	(a)
(75/24.5/0.5%)	"	10^{15}	mesh "	(a)
"	"	2×10^{17}	flat "	(a)
Same +4% Methylal	"	$>10^{18}$	" "	(a)
Ar/CH_4 (80/20)	(2)	$>6 \times 10^{14}$	one flat, one wire cathode	
Ar/C_2H_6 (60/40)	(3)	10^{15}	flat cathode	
Ar/CH_4 (90/10)	(4)	5×10^{17}	flat cathode	(b)
Ar/Isobutane (70/30)	"	5×10^{17}	" "	(b)
Ar/ " + Methylal (4%)	"	3×10^{18}	" "	(b)
Ar/CO_2 (80/20)	"	$>10^{19}$		
Ar/C_2H_6 (50/50)	(5)	$<10^{16}$	wire cathodes; gain dropping	(c)
		$<5 \times 10^{16}$	" " ; discharging	

(a) Avalanche size assumed to be 7×10^8. During strong irradiation this value might have been smaller, which would reduce the limits Q_c correspondingly. To determine Q_c, shifts in the beginning and the end of the single rate plateau were measured.

(b) The onset of an increase in the width of the Fe^{55} spectrum was determined.

(c) $-\Delta gain/gain = 5\%/10^{16}\ e^-/mm$

STATUS AND PROSPECTS OF LASER BEAM CALIBRATION FOR IMAGING CHAMBERS

H. J. Hilke, CERN

1. INTRODUCTION

Large imaging chambers, designed for precise tracking and particle identification, require rapid and powerful calibration techniques. The most interesting features of laser induced ionization tracks for this application are:

- no deflection in a magnetic field,
- no δ electron emission,
- precise definition in space, time and amplitude (no Landau fluctuations),
- repeatability, simplicity and flexibility
- simple two track formation.

2. RESULTS

Results have been published by two groups using commercial lasers (Ref. 1,2) and one group using a special design to obtain at the same time high power, short pulses and small beam divergence and cross section (Ref. 3). At least 5 more groups are preparing tests at various laboratories.

Nitrogen, Nd-Yay and tuneable dye lasers were used, providing photon energies of 3.7; 4.7 and 2.76 - 2.90 eV, respectively.

Tracks were obtained in a great variety of gases: Ar/CH_4; Ar/C_2H_6; Ar/C_3H_8; Ar/CO_2; $Ar/C_4H_{10}/CF_3Br$/Methylal; $Ne/He/C_4H_{10}$ and $Ne/He/CH_4$. Some groups also used additives with low ionization potential: $Ni(C_5H_5)_2$ with E_{ion} = 6.5 eV (Ref. 1), 4-amino-azobenzene (Ref. 1) and Diethyl-aniline (Ref. 2; E = 7 eV).

We will concentrate on the results obtained by Ref. 3. The special design of a two stage nitrogen laser operating at $\geq$ 1 atm lead to higher precision on the ionization tracks.

The laser operated at 1-5 Hz, with pulses of $\leq$ 200 μf in 0.5 ns, beam cross section: 1 x 2mm, beam divergence: $\sqrt{}$0.8 mrad.

A recently developed, miniaturized version of this laser has given satisfactory results so far only in a 2m streamer chamber. This is due to its

reduced output power of 20 μf. On the other hand, the low beam divergence of ~0.15 mrad (close to the diffraction limit) allows the formation of narrow tracks several meters long. Efforts are taken to increase the power output whilst keeping the divergence low. The beam cross section was $\geq$ 0.5 x 2mm.

It should be noted that the diffraction limit in nitrogen leads to the relation (somewhat depending on the beam profile)

$$\text{divergence} \geq \frac{0.3 \text{ mrad}}{w} ,$$

where w is the beam width in mm.

2.1. Test chamber results

These were obtained in a small drift chamber with the beam parallel to the sense wire plane.

2.1.1. Ionization densities

Densities of > 100 e^-/cm were obtained over distances > 1 m (minimum ionizing particles deposit ~70 e^-/cm). With stronger focussing, up to 15 x minimum ionization was achieved over a few cm, the ionization density following linearly the beam intensity over a range of 1:10. The pulse height spectrum was very narrow in the upper part of the linear region. A FWHM/mean = 9% was obtained, i.e. about 1/10 the width of the Landau distribution. Normalization to the laser output might further reduce this width.

Additives with low ionization potential have been found to increase the ionization density by a factor of 10 (Ref. 1,2).

2.1.2. Space resolution

σ_x = 50 μ r.m.s. was obtained over a few cm from the drift time measurement in Ar/C_2H_6, using standard large system electronics. A fast photodiode -catching a small fraction of the beam - provided the start signal.

2.1.3. Double tracks

For the study of jets, a good knowledge of the effects of a close second track on the resolution in space and dE/dx is becoming increasingly important. These effects are very difficult to investigate with particle beams, but in

principle easy to study by either splitting or reflecting the laser beam. Preliminary results indicate that indeed precise measurements are possible, due to the stability of the beam in space and pulse height.

2.2. Results from large chambers

2.2.1. AFS jet chamber at the ISR (Ref. 4)

Ionization tracks 60 cm long were produced in different locations of one 4° sector of the cylindrical drift chamber. For one position, tracks have been analyzed with B = 0 and 5 kG.

σ_x = 100 μ was obtained by track fitting over 40 cm, the last fraction of the tracks being useless, as they crossed the sense wire plane. When hitting wires, the beam ejects many electrons and may cause signals much larger than those from gas ionization. These large signals may be used to determine the maximum drift time through a cell, by hitting the cell boundary.

The ionization was similar to that from minimum ionizing tracks over the whole track.

For single wires, the amplitude variation was determined as

$$\frac{\text{FWHM (PH)}}{\text{mean PH}} = 25\%$$

2.2.2. Streamer chamber of the EMC detector (Ref. 5)

Ionization tracks were obtained over the full length of the 2 m streamer chamber of the European Muon Collaboration (gas: Ne/He + < 1% Isobutane). As the streamer density required was low, $\gtrsim$ 2 streamers/cm, the small laser with 20 μf output was adequate. The beam was used unfocussed and produced a beam diameter similar to that of the streamers, i.e. $\leq$ 2 mm, as seen through an image intensifier. Small variations in the streamer chamber field were readily visible.

2.2.3. TPC at Triumf (Ref. 6)

First calibration tracks, about 30 cm long, were produced in the TPC at Triumf, using a commercial UV laser. In this case, tracks were reconstructed by obtaining the center of gravity of the tracks from the induced pulses on the segmented cathode pads. A point resolution of σ_x = 140 μ was achieved with ionization densities close to that of minimum ionizing particles.

3. THEORY

Very little is known on the processes underlying the laser track formation, except that most likely double photon excitation is responsible. With respect to the photon energy of 3.7 eV for the nitrogen laser, the ionization potentials of the main gas components lie very high: e.g. at 11.6; 13.7 and 15.7 eV for C_2H_6, CO_2 and Ar, respectively. Multiphoton excitation of these seems highly unlikely. It is, therefore, assumed that two photon excitation of impurities with low ionization potentials is responsible. These impurities have to be omnipresent, as reproducible results have been observed in many gases and chambers. The excitation of additives with ionization potential around 7 eV has clearly been demonstrated: resonance absorption was detected with a tuneable dye-laser (Ref. 1) and the ionization density was found to increase by a factor of ten (Ref. 1,2).

4. CONCLUSIONS

It has been demonstrated that

- narrow track formation is possible ($\emptyset$ = 2mm over $\leq$ 10m),
- spatial calibration to $\leq$ 100 μ r.m.s. may be obtained over 1m,
- narrow pulse height distributions are achieved, allowing precise relative gain calibration and accurate studies, e.g. of time slewing and saturation effects.

Further improvements and studies are required on:

- Maximum achievable resolution in space and pulse height over longer distances, say $\geq$ 3m. Measurement of center of gravity versus drift time measurement.
- Long term stability in space and pulse height.
- Miniaturization: for UA1 at CERN, laser heads measuring 30 x 100 x 300 mm are being developed.
- Clarification of the ionization process.
- Effects of additives on drift velocities, angles and chamber lifetime. If these effects turn out to be acceptable, additives could be very useful to increase the signal and the resolution and to provide controllable conditions. Then, in some cases, even absolute pulse height calibration might be possible.

In conclusion, the laser beam technique has already become now a powerful calibration tool and will most likely see a rapid development in the nearest future.

REFERENCES

1. H. Anderhub, M.J. Devereux, P.G. Seiler: NIM 166 (79), 581; NIM 176 (80), 323.
2. J. Bourotte, B. Sadoulet: NIM 173 (80), 463.
3. H.J. Hilke: NIM 174 (80), 145.
4. See report in these proceedings: "Performance of the AFS drift chamber."
5. V. Eckardt, H.J. Hilke, unpublished.
6. C.C. Hargrove, private communication during this workshop.

MECHANICAL ACCURACY OF LARGE FRAMES ACHIEVED BY COMPUTER FEEDBACK

J.A. Paradiso, M.I.T.

Submitted to the Wire Chamber Group of the ISA Workshop, July 1981

I. INTRODUCTION

Tracking high energy particles from the upcoming generation of colliders through magnetic fields of 10-20 kgauss will pose new problems because of the extremely small deflections involved. Accuracy of survey measurements is essential for providing high resolution in detectors using precision drift chambers. For example, in a detector[1] for operation at ISABELLE, 96 large drift-chamber packages (5 × 1.6 meters in area) will be mounted in equi-angular segments about the intersection region. This size, together with a 1% momentum resolution requirement at 40 GeV, is a considerable step up from present day central detectors[2]. To fully utilize the resolving power of drift chambers ($\sigma_D \sim 150$ μ m), the supporting structure must be reproducible to an amount $\Delta x << \sigma_D$. Stresses introduced via temperature variation, pressurization, gravitational and tensor forces, settling, etc., are expected to deform the chambers and affect the accuracy of the initial survey measurements over a long time period. To effectively confront this problem, we have developed a simple position-monitoring system employing optically sensitive charged-coupling device (CCD) arrays. Even though a digital position monitoring device is more elaborate than analog designs, we choose the digital approach for long term stability; i.e., the digital centroid will be insensitive to long-term fluctuations due to temperature and other factors.

Figure 1 shows a sample drift chamber mounted in the detector[2]. Linear CCD arrays 256 cells long (13 μm/cell) are mounted opposite each corner of the chamber on stable, stress-free carrier rings. Light-emitting diodes affixed to the chamber are focused onto the corresponding CCD arrays. After installation and initial surveying, the centroid of the focused LED illumination on all CCDs is recorded and stored via computer. The CCDs are periodically checked thereafter. A deflection of the chamber will change the position of the LED relative to the CCD and thus move the focused centroid. When a discrepancy is noticed, the computer brings the centroid back to its

original value by restoring the chamber position with small motor drives under feedback control (labeled "adjust" in Figure 1). In this way, the deformation of individual chambers is compensated, and survey measurements remain accurate.

II. ELECTRONICS AND READOUT

Figure 2 shows a block diagram of the CCD readout system. There are 3 major system components; the controller, the distributor, and the driver/digitizer. The controller generates the complex clocking signals required to read the CCDs. It addresses one out of sixteen CCDs in each distributor, and stores a 2 × 256-bit digital rendition of the optical pattern detected by the selected CCD into self-contained buffer memory which may later be sequentially read via CAMAC.

The distributors generate a necessary power supply voltages and fan out clocking signals to groups of 16 CCDs. When a distributor is "on-line", the data and fed-back clocking signals from the addressed CCD only are routed to the controller along the bus. "Off-line", no clocking signals are fed to the CCDs and no signals are output over the bus. The distributors may be switched on- or off-line by CAMAC commands, thus (putting only one distributor on-line at a time) the four addressing bits output from the controller specify a unique CCD.

The driver/digitizers are simple circuits required by each CCD which buffer the clocking signals and digitize the video output of the CCD into 2 bits. We are presently using analog comparators as digitizers, creating 3 possible digital states (i.e., 0, 1, 3). The driver/digitizers also buffer an output which activates a light-emitting diode during the read sequence, creating light focused onto the corresponding CCD.

The controller is "daisy-chained" to the distributors by a 14-line bus, hence the system is easily expandable; the quantity of CCDs is fixed only by the number of distributors, which may be added arbitrarily to the system. We are presently clocking our CCDs in the vicinity of 50 KHz; here the thermal "dark signal" is manageable, and we can drive CCDs successfully over several meters of inexpensive ribbon cable. Using a simple Fortran program, a CCD is

completely read into computer memory within 1/2 second; faster software can shorten this delay considerably.

III. TESTING

Figure 3 shows photographs of the test setup. Photograph a) is an edge view of a prototype chamber frame, 1.5 × 5 meters in area. CCD/LED assemblies (as depicted in photo b)) are placed at the 4 corners of the frame and midway along either side. A simple motor drive (see photo c)) which moves the frame vertically ≃ +/- 150 μm is placed at each CCD/LED site and is controlled via a PDP-11/03 microcomputer. The CCD controller, distributor, and a prototype driver/digitizer are shown in photo d).

Figure 4 shows the actual CCD output; the signal from the focused LED is evident, and generally spans 10 → 20 CCD cells with our present optics (better resolution is obtained by removing the glass window over the CCD).

We have developed a simple computer program to test the feasibility of automatic position restoration as described in Section I. First, the centroids of all LEDs at the rest position are stored in computer memory. Next the frame is deflected, either by applying mechanical stress on the frame itself or by randomly torquing a motor drive. This shifts the position of the LED w.r.t. the CCD typically 50 → 100 μm, as monitored by precision deflection gauges affixed to the test frame. By incrementally moving the motor associated with the deflected portion of the frame, the centroid of LED illumination can be restored to its previous value. This process has repeatedly brought the frame back to within 10 μm of the original, undeflected position (as measured by the gauges) compatible with the 13 μm CCD cell width.

Figure 5 shows the response of the compensation system to deflection caused by a 10 Kg load. The load was introduced at t = 3 seconds (as indicated), and deflected the frame ≈ 85 μm. The compensation program immediately began stepping the motor drive; however after two increments the computer realized it was moving the frame in the wrong direction (initial direction is chosen at random), and reversed the motion at t = 10 seconds. After each crossing of the reference position (indicated by the dotted horizontal lines), the motor step size was decreased and the direction was reversed, until a final convergence was reached at t = 50 secs., where the frame was restored

to within 5 μm of the reference. At t = 56 secs., the 10 Kg weight was removed (as indicated), now causing the frame to deflect ≈ 90 μm in the opposite direction. The compensation program was invoked, and at t = 90 secs. the frame was again restored to within 5 μm of the reference position. The compensation program was purposefully slowed in this test in order to enable manual reading of the deflection gauges; convergence to the reference position is normally achieved within 20 → 30 secs.

A top view of the test frame configuration is given in Figure 6, showing the location of the 6 CCD/LED sites and motor drives. In the test of Figure 7, all CCD/LED sites were continually scanned, and the resulting average positions at 1-minute intervals are plotted in units of CCD cells. Whenever a deviation of > 0.7 CCD cell from the reference (dotted lines) was detected, the compensation program was invoked, and the frame was restored. At t = 4 minutes a 10 Kg weight was applied at site #1; this is seen to have deflected both site #1 and the adjacent site #6 (site #6 was particularly elastic). At t = 5 minutes these deflections are already compensated, and both sites are back at the reference positions. The 10 Kg loads were successively applied to the remaining corners (sites #6, 3, and 4; see Fig. 6), as indicated; the resulting deflections were all compensated, and at t > 16 minutes the frame is seen to be stable at the reference positions, although 10 Kg loads are present at all 4 corners.

Figure 8a) shows the mean position of the focused centroids (read by the CCDs) for all 6 sites, plotted in units of CCD cells as a function of time over a 24-hour period. The CCDs were sampled very 15 seconds and the averaged positions (as plotted) were calculated every 15 minutes. Gradual shifts in the mean positions can be noticed, due to temperature variations, etc. Figure 8b) is analogous to Figure 8a); however, during this 24-hour period the computer program was instructed to restore each centroid to its original position (via the motor drives) whenever a deviation in the 15-minute averages of > 0.5 CCD cell was detected, thus compensating for the gradual motion of the frame and keeping it centered at the reference positions.

IV. CONCLUSIONS

We have developed a digital position monitoring system with long-term stability and active feedback, which is insensitive to environmental influences and can keep a drift chamber plane in place within ± 10 μm. This feature is necessary for precision momentum determination of highly energetic tracks. After an initial calibration (by laser[3], for example) long-term stability is required for computer corrections. However since huge mechanical structures, even if tempered, will always "work" internally, active compensation will be necessary. We point out that these considerations apply to all large precision chambers, and not only to the specific geometry mentioned.

V. APPENDIX: HARDWARE DETAILS

A) The Controller

A block diagram of the controller is shown in Figure 9. There are three somewhat independent sections of this circuit:

The CCD Distributor Addressing Latch

This is a 4-bit latch (7475-L4) which loads the 4-bit CAMAC "A" field when an F9, C, or Z is sent to the controller. The output of this latch is buffered via transistors and is sent over lines Bus #1 → Bus #4 (and displayed via LEDs).

The CCD Clocking Circuitry

Two oscillators are used as clocking sources; oscillator CLK1 is preset via an on-board trimmer potentiometer, while CLK2 can be adjusted via an external potentiometer on the front panel. The CLK Source selector switch (S3) enables one to select either clock. One may also set the switch in a "null" position, thus enabling an external clocking pulse to be input via the "ext clk" connector.

The clock source is introduced into the CCD clocking circuitry. This is a complex arrangement of gates, flip-flops, and counters which is described in the Fairchild CCD-110 application notes[4]. The 5 output signals are buffered via transistors and output onto lines Bus #5 → Bus #9.

The CCD Control and Readout Circuitry:

This comprises the major portion of the apparatus. Three CAMAC commands are accepted: an F0, an F2, and an F9. They are decoded by a 74154 demultiplexor.

Upon receipt of an F0, the read sequence starts. All processes are timed via the $V_{\phi XB}$ and $V_{\phi R}$ signals fed back from the CCD driver/digitizer to guarantee synchronism. The read sequence is itemized below and depicted in a timing diagram (Figure 10).

i) CAMAC N · F0 · S1 sent.

ii) Readout latch (L1, 74279) is set. This holds the output latch open (L3, 7475), and enables the fed-back $V_{\phi XB}$ pulses to clock counter C1 (7493). [The $V_{\phi XB}$ pulses are output at the beginning of each cycle through the CCD.] The V_{LED} bus line (Bus #10) goes high; this triggers the LEDs, illuminating the CCDs attached to any distributors that are currently on-line.

iii) Nothing else happens for the first 4 cycles through the CCD; only counter C1 is advanced. This is done to avoid any transient effects. At the start of the fifth cycle (≥ 4 $V_{\phi XB}$ pulses), the $V_{\phi R}$ pulses are allowed to clock counter C2 (the $V_{\phi R}$ pulses go high for each "cell" of video data output). These $V_{\phi R}$ pulses first trigger a monostable trigger delay (P1-555) which shifts the phase and broadens pulse-width such that the video data is sampled in the center of each "cell" (see below).

iv) Nothing happens for the first 3 $V_{\phi R}$ pulses; only counter C2 is advanced. This delay is introduced since the first 3 video cells are supposedly "dummies", i.e., they contain no video data, and are required to advance the data through the analog shift register inside the CCD. After the 3rd $V_{\phi R}$ pulse, the delayed $V_{\phi R}$ pulses are allowed to advance counter C3 and are input to a pulse generator (P2), creating the shift register gate. This is a narrow ($\simeq$ 500 nsec) pulse which clocks the shift register in the middle of each "cell" of video data (the 2 data bits--DATA 0, DATA 1 -- from Bus #3 and Bus #4 are input to the shift register).

v) The shift register and counter C3 are clocked for the next 256 $V_{\emptyset R}$ pulses. After the 256th pulse, the $V_{\emptyset R}$ pulses are inhibited from further advancing either counter C3 or the shift register.

vi) Nothing happens until the 5th $V_{\emptyset XB}$ pulse is received. At this time the "data present" latch (L2) is set and a "reset" pulse is created which clears all counters (C1 → C3) and resets the readout latch. This closes the output latch (L3) and inhibits all further clocking pulses (V_{LED} is also brought low). The readout sequence is now complete, and the module may be sequentially read into computer via CAMAC.

Data from the shift register is read cell by cell into CAMAC via the F2 function--"read and advance." The CAMAC F2 is gated by the readout latch (V_{LED}) output and the reset timer (P3). If either a readout is in progress or the module is resetting itself (these define a "busy" criterion), the CAMAC F2 will have no effect, and the module will return X = 0 and Q = 0.

If the controller is not busy, a CAMAC F2 will first open the output latch, allowing the current data to be written onto CAMAC read lines R1 (DATA 0) and R2 (DATA 1). Upon receipt of F2 · S2 (later in the CAMAC cycle), the shift register is cycled and counter C3 is advanced. If counter C3 is advanced to 256, all further shift-register advance pulses are inhibited. The data present latch governs the "Q" response of the F2 command. After an F0 readout sequence has been completed, this latch is set. Upon receipt of an F2 (provided the controller is not busy) it will respond with Q = 1 and X = 1. If 256 reads have been attempted, the next read (i.e., shift-register advance) will clear the data present latch, but will still answer Q = 1, X = 1, however all subsequent F2s will yield Q = 0, X = 1. Thus, one can read this module in a "halt on Q" mode, but in this case 257 words will be read, the last word being a "dummy" required to reset the data present latch.

The manual shift-register advance pushbutton emulates a CAMAC F2 and allows one to advance and examine the memory manually.

After the controller's memory has been read and emptied, a CAMAC clear is required before sending another F0 and starting the sequence anew This can be done by a CAMAC C, Z, or F9--all are or'ed together (there is no manual

"clear" on the controller). This resets all counters and latches (and loads the CAMAC "A" field into the distributor address latch; of course, for C and Z this field is zero) and returns the controller to a "ready" state.

B) The Distributor

The distributor performs essentially 3 tasks:

- buffers and fans out all CCD clocking voltages (including V_{LED}) to 16 ports
- effectively multiplexes the return signals from the 16 ports (i.e., each port is uniquely addressable)
- supplies the voltages required by the driver/digitizer modules.

The design of this circuit is extremely simple, but it is complicated by the 16-fold redundancy. Figure 11 shows the block diagram.

The on/off line state of the unit is defined via an RS latch. The latch is set (on-line) by the CAMAC F1 bit or the on-line position of switch S1. The latch is reset (off-line) by the CAMAC F2 bit, a CAMAC C or Z, or the off-line position of switch S1 (note that the F1 and F2 bits only are used to simplify command decoding--hence, an F3, an F7, etc., will have undefined effects).

The CCD clocking signals and V_{LED} (Bus #5 → Bus #10) are first Schmidt-trigger conditioned and gated by the output of the latch; thereupon they are routed through a driver to 16 separate buffers and appear at B5 → B10 of each port. Because these signals are gated by the latch, no signals appear at the 16 ports when the module is off-line. When the module is on-line, however, these signals will be present at all 16 ports.

There are 4 signals (B1 → B4; 2 data + 2 feedback) received from the addressed port which are written onto lines Bus #1 → Bus #4. These 4 signals are first Schmidt-trigger conditioned at all 16 ports and then brought to the inputs of four 16-to-1 data selectors (74150) which have common addressing lines derived from Bus #11 → Bus #14 (from the distributor address latch in the controller). The output of each of these selectors is brought to the bus via an open-collector driver. The data selectors are all gated by the latch output; when the unit is off-line, the data selectors will not pass data and

are effectively "disconnected" from the bus write lines. When the unit is on-line, the data selectors pass data from the addressed port and it is written onto the bus.

The CCD power supply is very straightforward. The -6 volts comes straight from CAMAC with no buffering or decoding. The +15 and +8 volt supplies are derived from the CAMAC +24 volts via integrated circuit regulators (the 7815 and 7808 are used respectively). These power supply voltages always appear at the 16 ports regardless of the on/off-line state of the distributor.

C) The Driver/Digitizer

This unit plugs into an output port of a distributor (via ribbon cable) and performs 3 general functions:

- buffers the 5 CCD clocking signals and shifts their swing to 0 → 7 volts before applying them to the CCD (also feeds back $V_{\phi XB}$ and $V_{\phi R}$).
- digitizes the video output of the CCD (via comparators) into 2 bits.
- buffers V_{LED} (B1) and provides a variable LED driver; an LED can be attached which flashes on when a readout is in progress, and can be focused onto the CCD.

This circuit is exceedingly simple--purposely so, since one is required with each CCD. There are only 6 chips present, counting the CCD.

The block diagram is portrayed in Figure 12. The 6 signals received from the cable (B5 → B10) are first conditioned and inverted by Schmidt-triggers and then routed through open-collector drivers where they are shifted to 0 → 7 volts and fed to the CCD (with the exception of B10, V_{LED}). The $V_{\phi XB}$ and $V_{\phi R}$ signals are fed back onto B1 and B2 respectively. V_{LED} is fed through a series of buffers and drives the "active" LED indicator and an emitter-follower with base-voltage varied by trimmer T1, An LED can be plugged into the "LED output" connector which is fed via this emitter-follower; thus T1 varies its brightness, and it is illuminated only when a readout sequence is in progress.

The video output of the CCD is first isolated via an emitter-follower and then applied to two analog comparators. These are fast LM318 operational amplifiers, and the threshold of each is set independently via trimpots T2 and T3. The outputs of these comparators are monitored by 2 LEDs and clamped

0 → 5 volts through zener diodes before being fed to TTL buffers which invert these signals and feed them onto B3 (DATA 1) and B4 (DATA 0). Since comparators are used for digital conditioning, only 3 states are possible:

Both comparators below threshold (0,0)

One comparator above threshold (0,1)

Both comparators above the threshold (1,1).

The state (1,0) does not exist independently.

This driver/digitizer circuit can easily be altered, and other approaches can be examined; i.e., simple A → D converters can replace the analog comparators (yielding a more precise digital rendition of the video waveform), the trimpots can be eliminated by a biasing network, the CCD video signal can be preamplified before being applied to the comparators (thus reducing threshold shift caused by drifting input offset current in the OP-AMPS), etc.

D) The Motor Controller/Driver

This circuit enables the computer to address 1-out-of-16 motor drives, and set it into "Forward" or "Reverse", motion. The block diagram is given in Figure 13. The Forward and Reverse commands (F7 and F8) gate the CAMAC A-field into latch L2 which drives a 4-to-16 line address decoder, thus enabling the 4-bit A-field to specify 1-out-of-16 outputs. The F7 and F8 commands also set latch L1 which gates the address decoder; when L1 is set, the address decoder is enabled and the output line specified by the CAMAC A-field is asserted. The F9, C, and Z commands re-set L1, and thus inhibit all address decoder output lines. Switch S1 overrides the output of L1, thus providing a manual motor control. Switches S3 → S5 are or'ed into the output of L2, and provide a manual motor address select. In addition, the F8 command is input to Latch L3. This latch is gated by all accepted CAMAC commands; however it is set only when an F8 is sent, and thus is used as a "Forward/Reverse" control line (Switch S2 provides a manual override). The address decoder outputs feed the "enable" inputs of "Analog Converters", and the output of L3 is fed to the "Forward/Reverse" inputs of these modules. The "Analog Converters" are simple circuits which enable digital control of a 3-state analog output, and have the transfer function:

Logic Inputs		Analog
Enable	F/R	Output Voltage
1	1	- 15
1	0	+ 15
0	(anything)	0

The outputs of the analog converters are buffered by driver transistors, and power the motors. Simple DC motors are used, and move the frame +/- 150 μm by means of an elementary lever-wedge assembly.

In summary an $F7 \cdot A_n$ sets motor #n into forward motion, an $F8 \cdot A_n$ sets motor #n into reverse motion, and an F9, C, or Z halts all motors. Only one motor may be controlled at a time with this circuit.

ACKNOWLEDGMENTS

Infinite thanks go to Ulrich Becker for fruitful discussions and assistance. I am happy to thank Ron Hoffmann, Peter Berges, Dave Osborne, Jim Donahue, and Paula Reddick for their technical help. I am grateful to Ed Paradiso and Adrienne DeLeonardo for their assistance in preparing the figures and graphics.

REFERENCES

1. U. Becker et al., MIT Large Detector Study, ISA Workshop, July 1981.
2. A. Wagner, Central Detectors, DESY preprint 80/83 (1980).
3. See H. Hilke, "Status and Prospects of Laser Beam Calibration", contribution to the Wire Chamber Group at the ISA Workshop, July 1981.
4. Application notes for Fairchild CCD110 and CCD111, Fairchild, Inc.

FIGURE CAPTIONS

Fig. 1 Cross-sectional view of a drift chamber mounted in the detector[1]. The LED/CCD configurations are shown, and the motor drives are labeled "adjust".

Fig. 2 Block diagram of the CCD readout configuration.

Fig. 3
a) Photograph of the test frame (1.5 × 5 meters in area).
b) A CCD/LED assembly; light from the LED (mounted on the frame) is focused onto the CCD (mounted on a bracket fixed to the floor) via a cylindrical lens.
c) A computer-controlled motor drive, capable of moving the frame vertically ≈ +/- 150 μm.
d) CCD readout electronics. The CCD controller and a distributor are mounted in the CAMAC crate, and a prototype driver/digitizer is seen in the foreground.

Fig. 4 CCD video signal (lower trace) and a digitized comparator output (upper trace) arising from focused LED illumination. Photo a) shows an entire cycle through the CCD (256 cells), while photo b) has an expanded time scale and shows outputs from individual CCD cells.

Fig. 5 Response of the compensation system to the "step" impulse created by a 10 Kg load. Fig. 5a) shows the frame position as read by the CCD and computer (in units of CCD cells) while Fig. 5b) shows the frame position as read by the mechanical deflection gauge (in μm) at the CCD/LED site. The times at which the load was introduced and removed are indicated; the compensation system is seen to restore the frame to within 5 μm of the reference position (horiz. dotted line) in both cases.

Fig. 6 Sketch of test frame configurations, showing CCD/LED/motor sites. The vertical lines represent drift wires (the actual drift wire density differs from that portrayed here). CCD/LED/motor sites are located at the 4 corners of the frame and midway along either side (where the drift wire supports are mounted), thus monitor the position of the drift wire plane.

Fig. 7 Response of all 6 CCD/LED sites to 10 Kg loads successively placed at each corner of the frame. The CCDs were scanned continuously, and mean positions were calculated and plotted each minute. The site #'s at which loads were placed are indicated at the bottom of the figure. The positions are plotted in units of CCD cells (as read by the computer). The response of site #4 to the 10 Kg load is opposite to that of the other sites; this is because the CCD at site #4 is inverted w.r.t. the scale convention.

Fig. 8 Average centroid positions (integrated over 15-minute intervals, sampling each CCD every 15 seconds) as a function of time over a 24-hour period. In Fig. 5a), the internal motion of the frame was uncompensated; in Fig. 5b), the motor drives were used to restore the centroids to the reference position whenever deviations of > 0.5 CCD cell were detected. The vertical axes are in units of CCD cell-width (at 13 μm/CCD cell).

Fig. 9 Block diagram of the CCD controller electronics.

Fig. 10 Timing diagram for the CCD readout sequence, initiated by a CAMAC F0.

Fig. 11 Block diagram of the CCD distributor electronics.

Fig. 12 Block diagram of the CCD driver/digitizer electronics.

Fig. 13 Block diagram of the Motor Controller/Driver electronics.

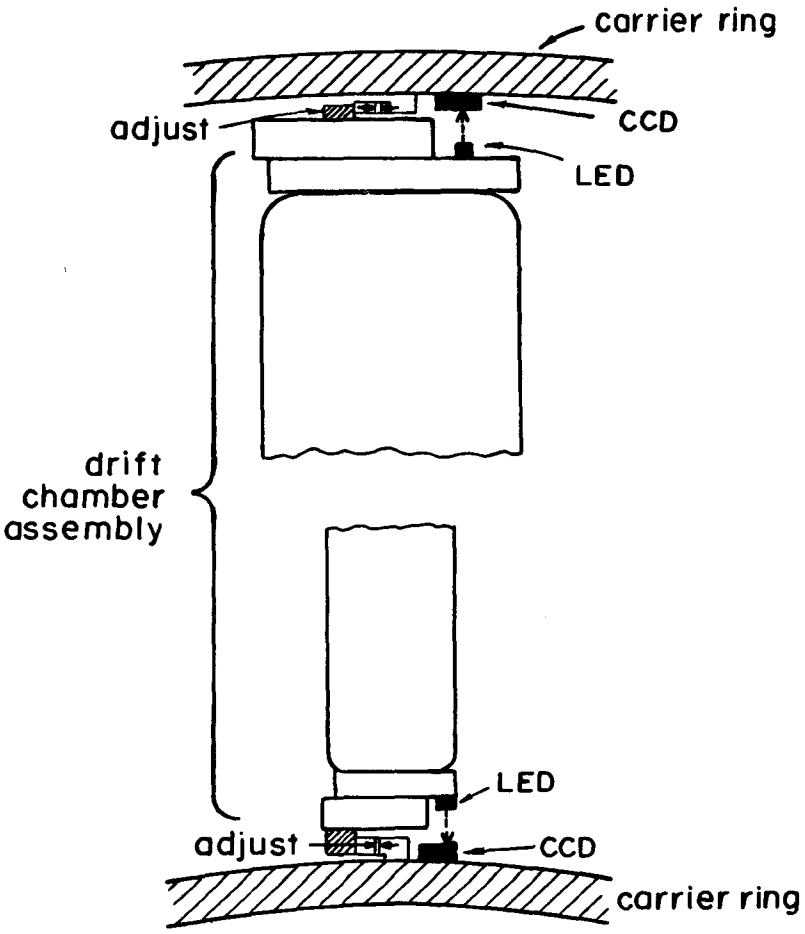
carrier ring
adjust
CCD
LED
drift
chamber
assembly
LED
adjust
CCD
carrier ring

Fig. 1

CCD SYSTEM - GENERAL CONFIGURATION

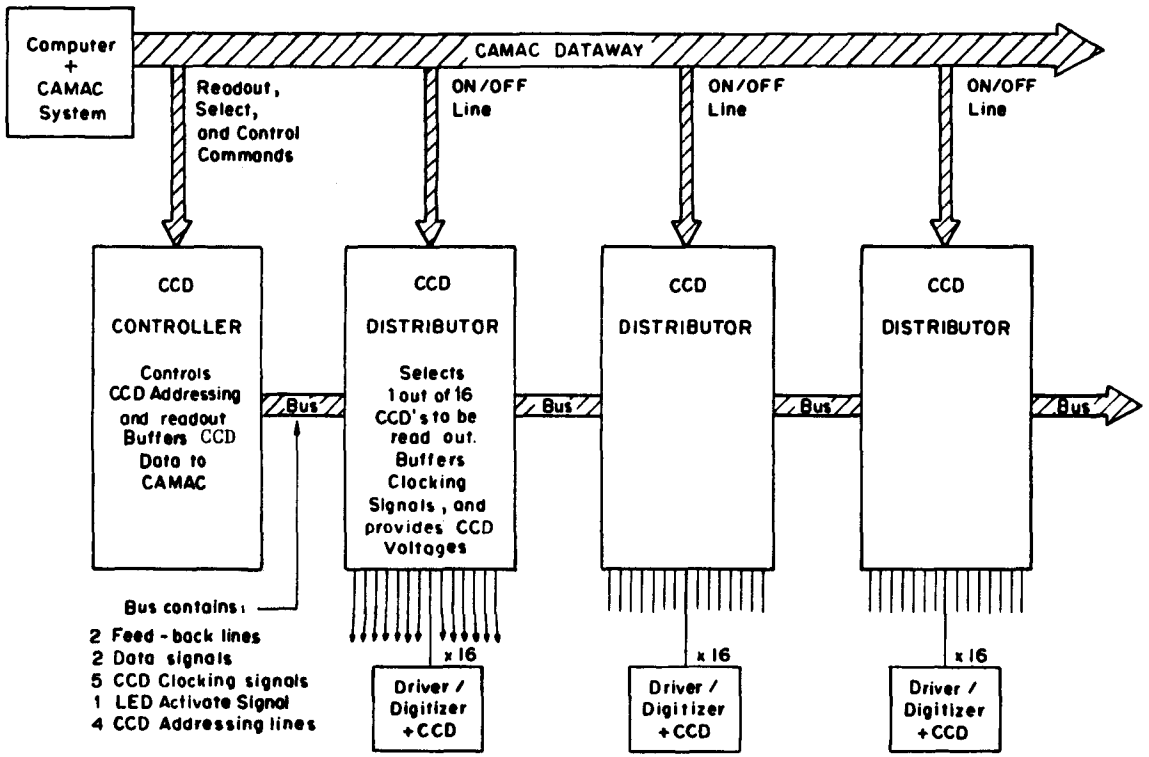

Fig. 2

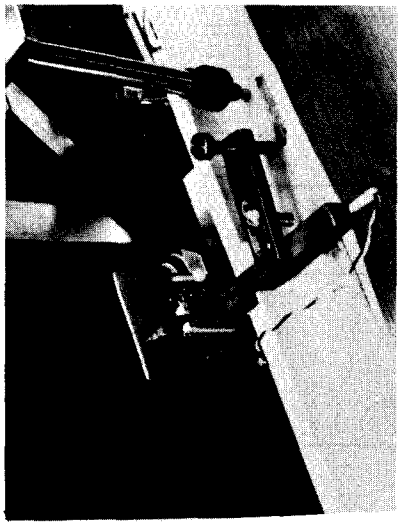

(b)

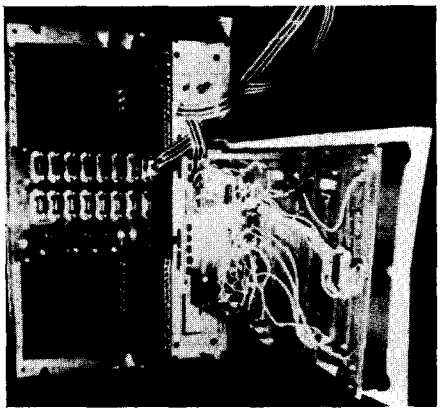

(d)

Fig. 3

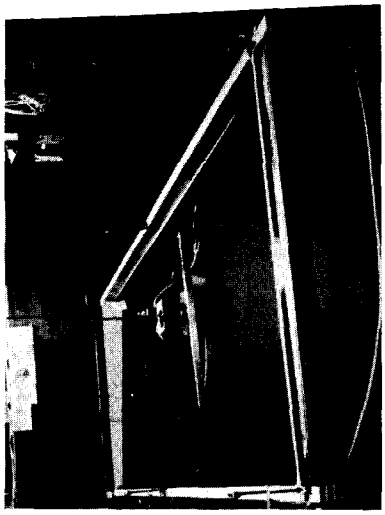

(a)

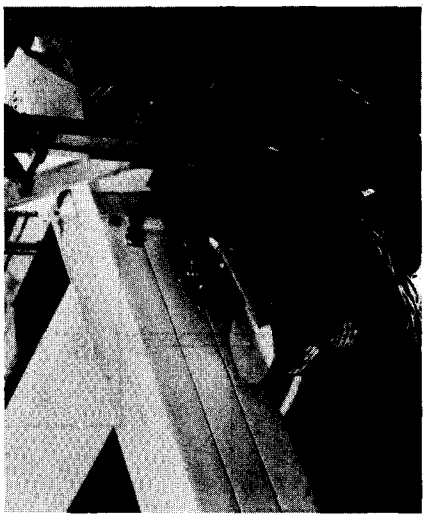

(c)

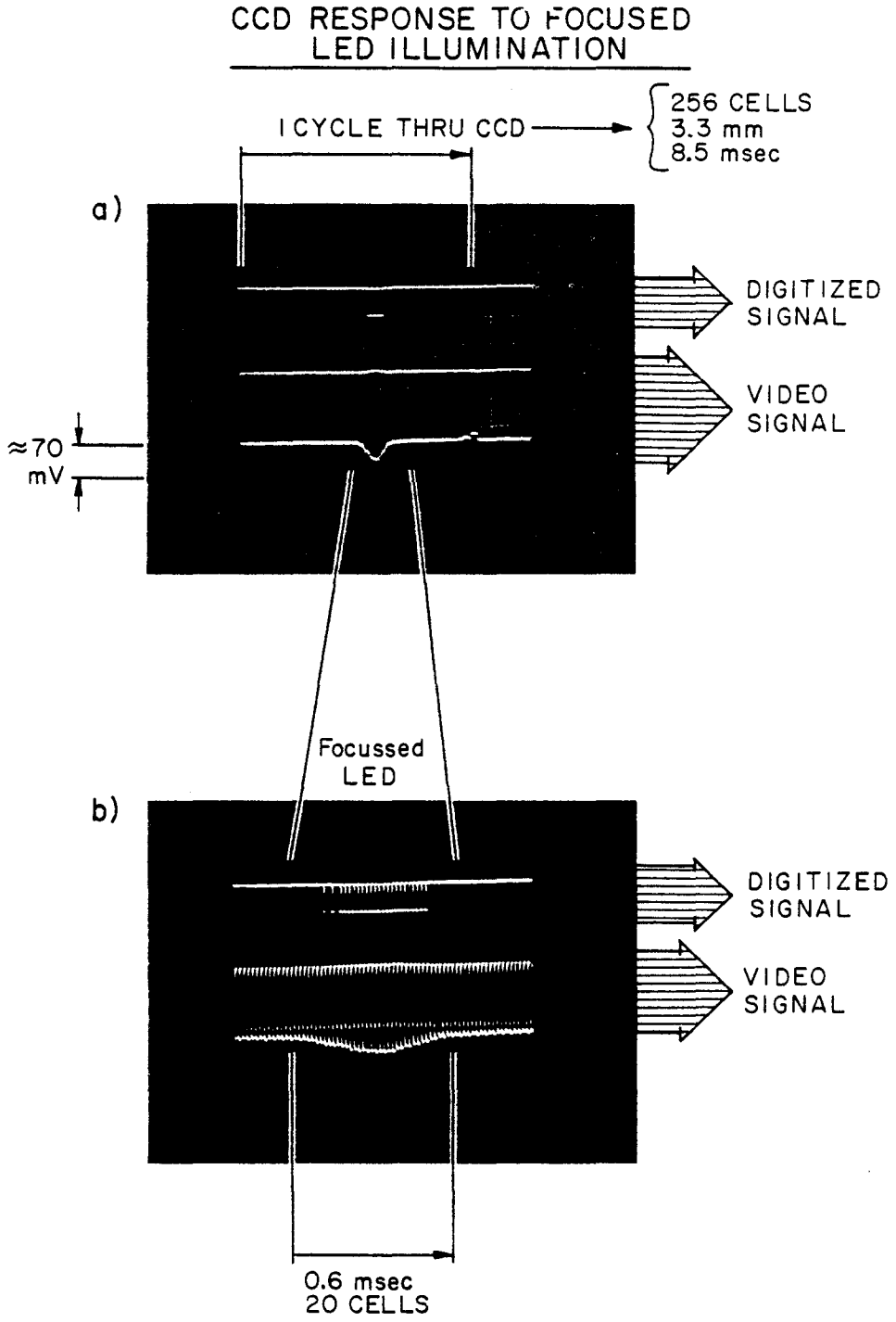
CCD RESPONSE TO FOCUSED LED ILLUMINATION
1 CYCLE THRU CCD
256 CELLS
3.3 mm
8.5 msec
a)
DIGITIZED SIGNAL
VIDEO SIGNAL
≈70 mV
Focussed LED
b)
DIGITIZED SIGNAL
VIDEO SIGNAL
0.6 msec
20 CELLS

Fig. 4

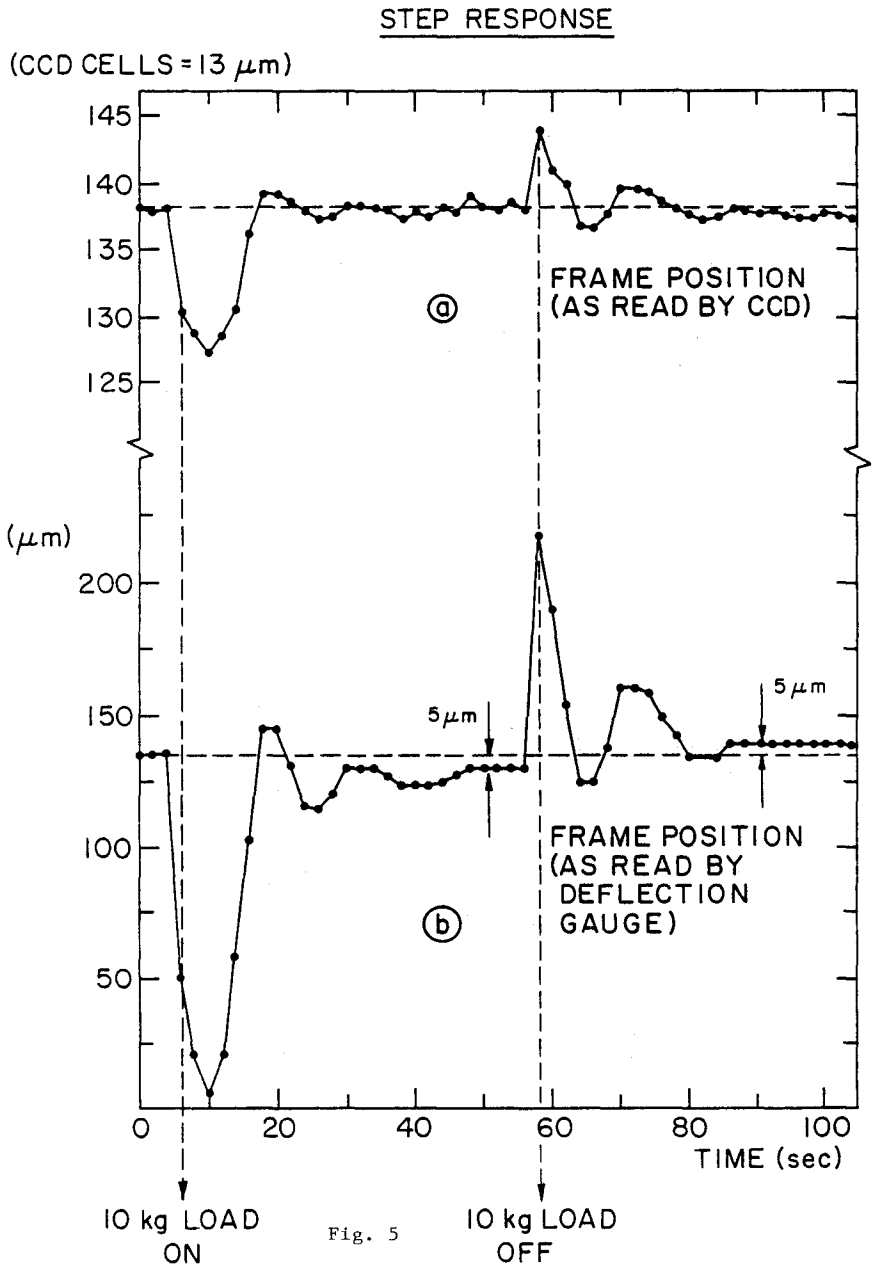
STEP RESPONSE
(CCD CELLS = 13 μm)
145
140
135
130
125
(μm)
200
150
100
50
FRAME POSITION
(AS READ BY CCD)
ⓐ
5μm
5μm
FRAME POSITION
(AS READ BY
DEFLECTION
GAUGE)
ⓑ
0
20
40
60
80
100
TIME (sec)
10 kg LOAD
ON
10 kg LOAD
OFF

Fig. 5

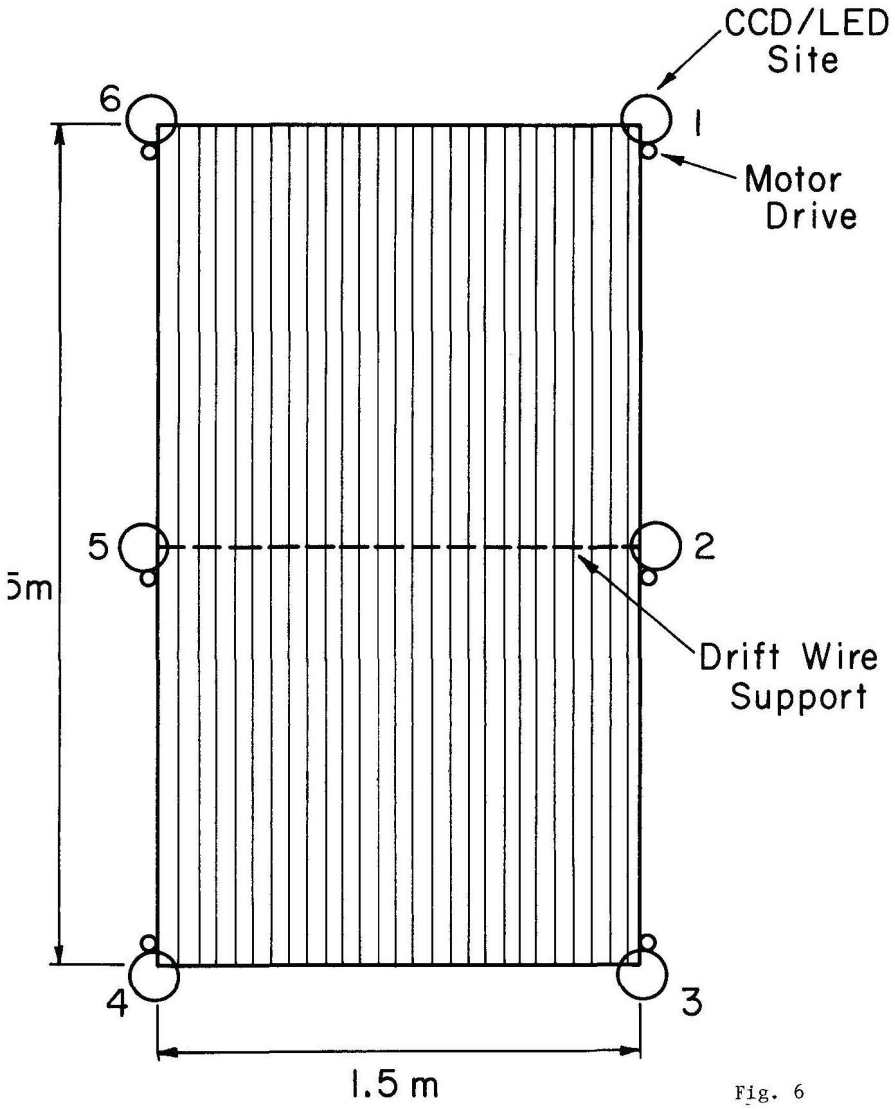

Fig. 6

TEST FRAME (TOP VIEW)

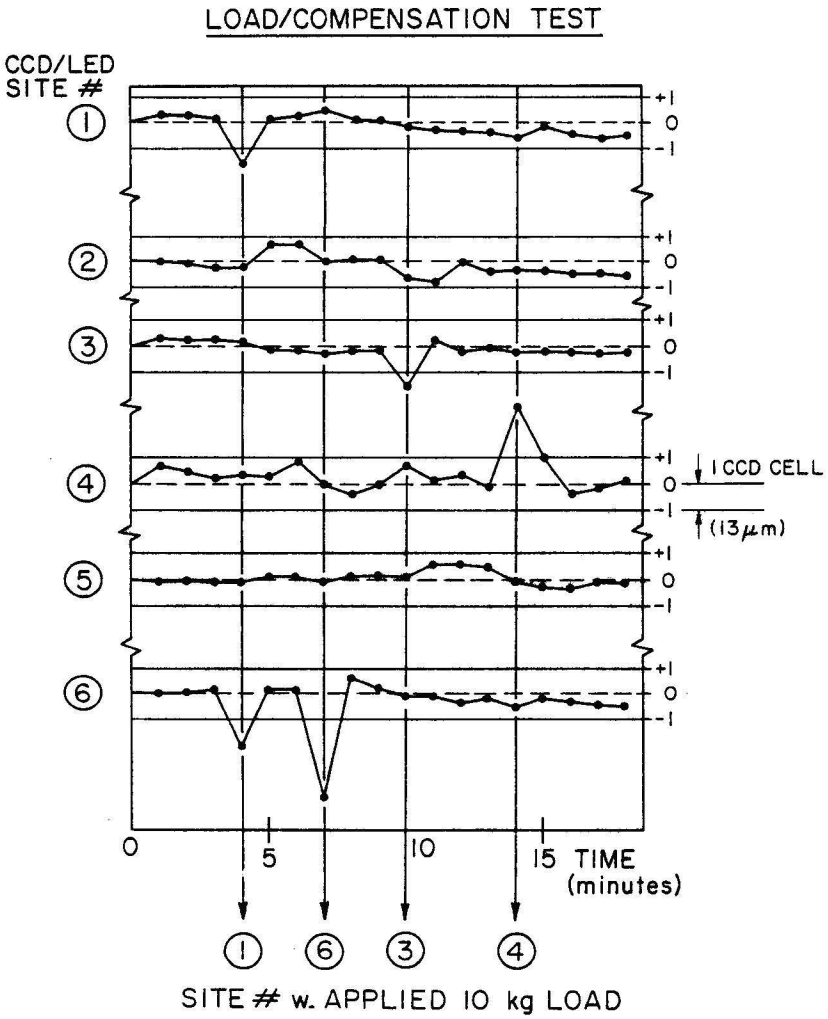
LOAD/COMPENSATION TEST
CCD/LED SITE #
1
2
3
4
5
6
+1
0
-1
1 CCD CELL
(13μm)
0
5
10
15 TIME (minutes)
1
6
3
4
SITE # w. APPLIED 10 kg LOAD

Fig. 7

LONG-TERM STABILITY

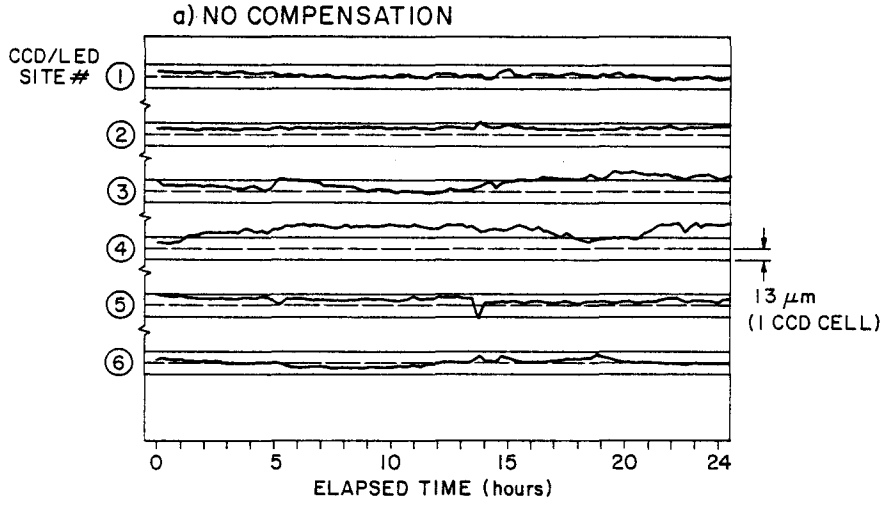

Fig. 8

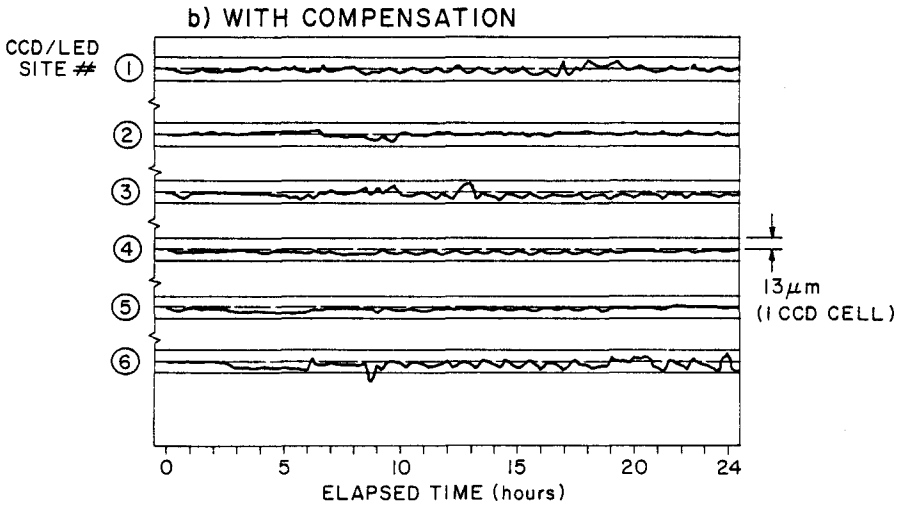

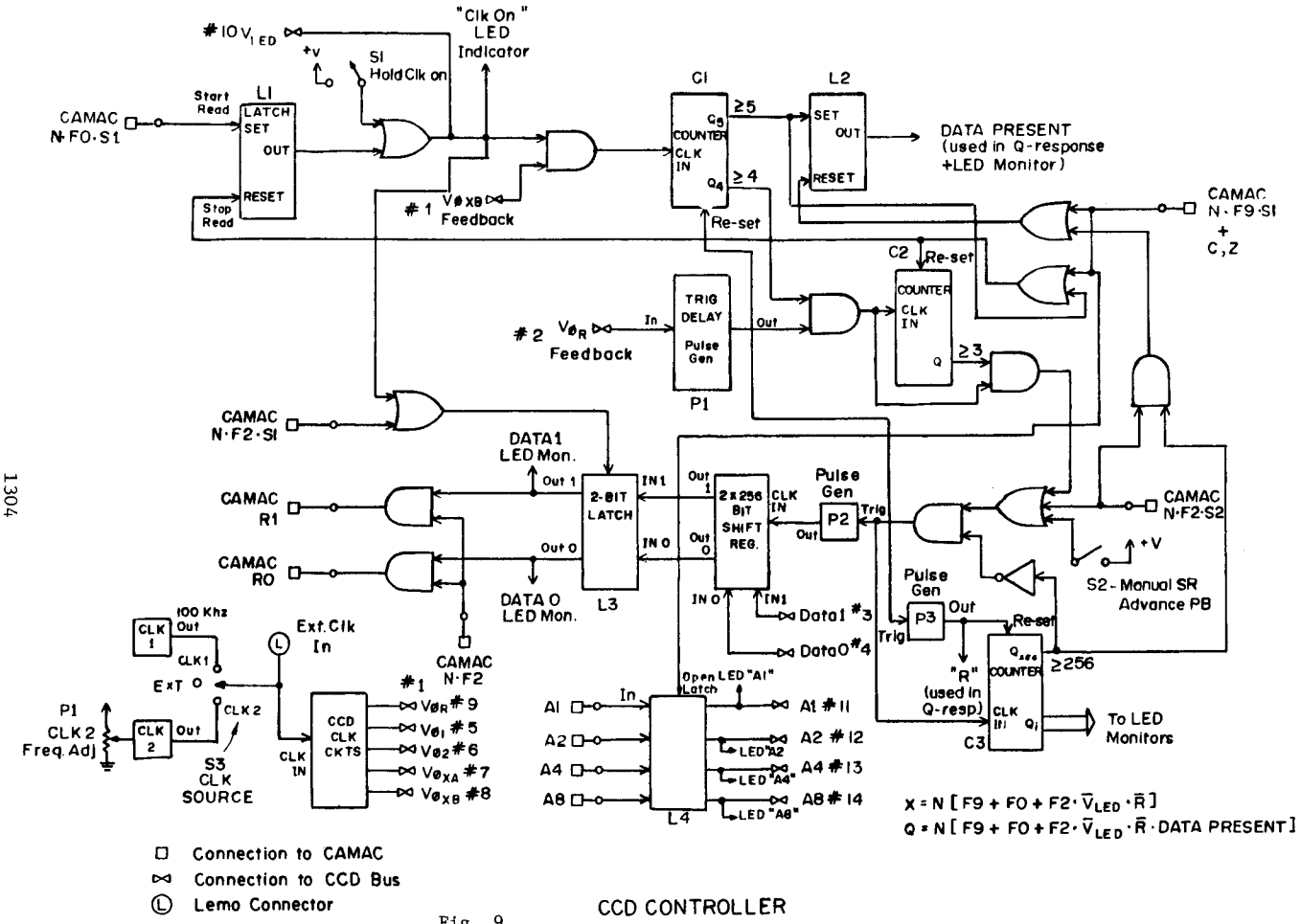

Fig. 9 CCD CONTROLLER BLOCK DIAGRAM

READOUT SEQUENCE – TIMING DIAGRAM

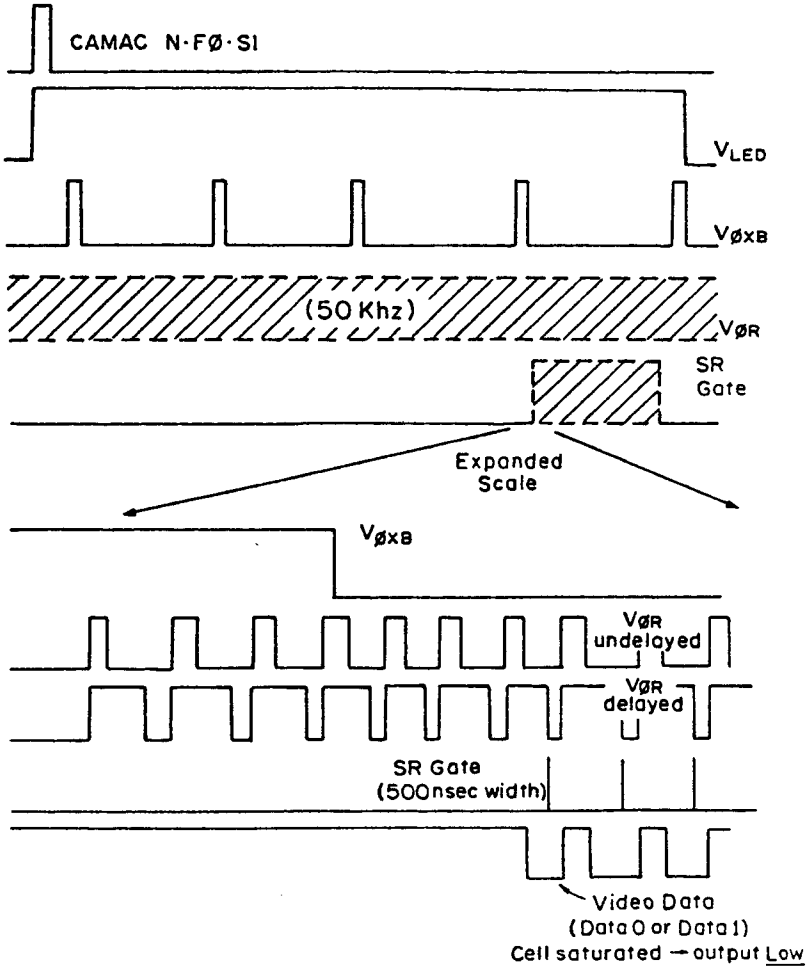

Fig. 10

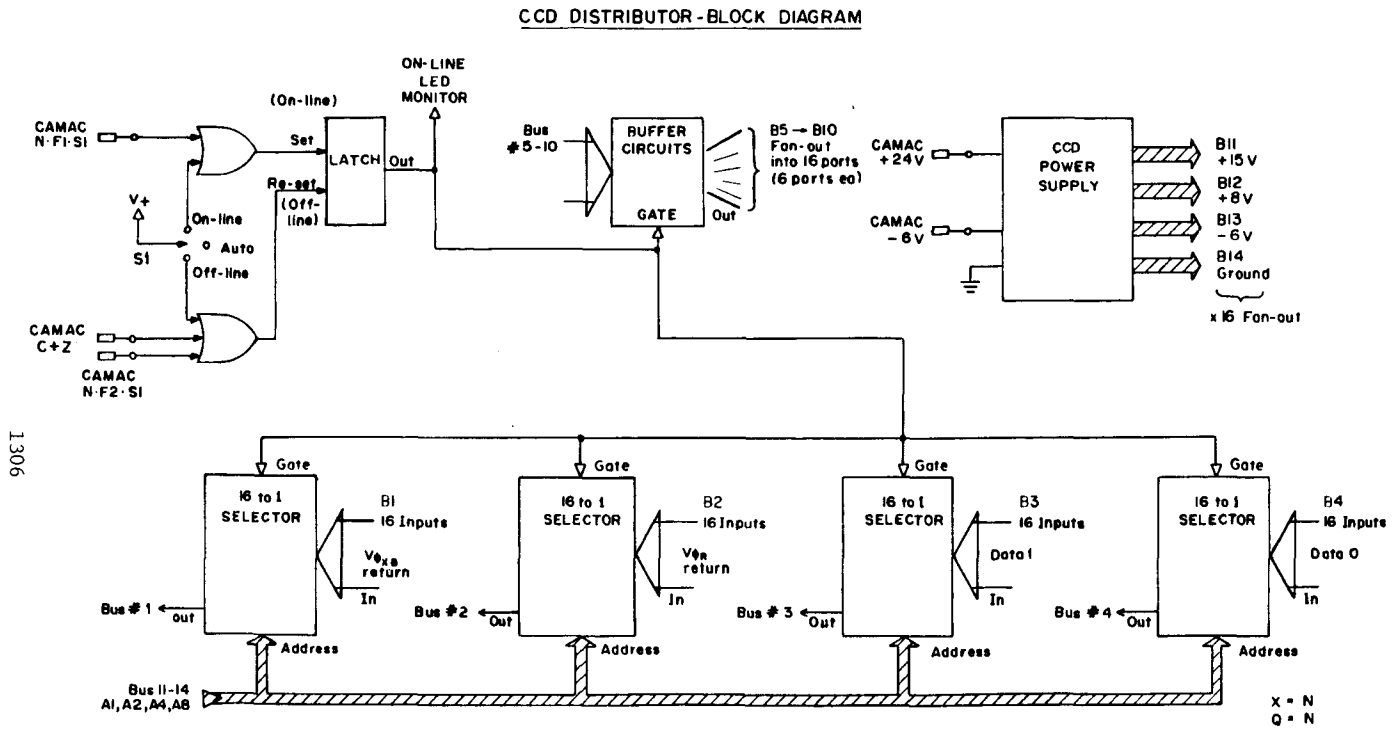
CCD DISTRIBUTOR - BLOCK DIAGRAM
ON-LINE LED MONITOR
(On-line)
CAMAC N·F1·S1
Set
LATCH
Out
Re-set
(Off-line)
V+
On-line
Auto
Off-line
S1
CAMAC C+Z
CAMAC N·F2·S1
Bus #5-10
BUFFER CIRCUITS
GATE
Out
B5 → B10 Fan-out into 16 ports (6 ports ea)
CAMAC +24V
CAMAC -6V
CCD POWER SUPPLY
B11 +15V
B12 +8V
B13 -6V
B14 Ground
x16 Fan-out
Gate
16 to 1 SELECTOR
B1
16 Inputs
Vφx return
In
B2
16 Inputs
Vφy return
B3
16 Inputs
Data 1
B4
16 Inputs
Data 0
Bus # 1
out
Bus # 2
Out
Bus # 3
Out
Bus # 4
Out
Address
Bus 11-14 A1, A2, A4, A8
X = N
Q = N

Fig. 11

CCD DRIVER/DIGITIZER

BLOCK DIAGRAM

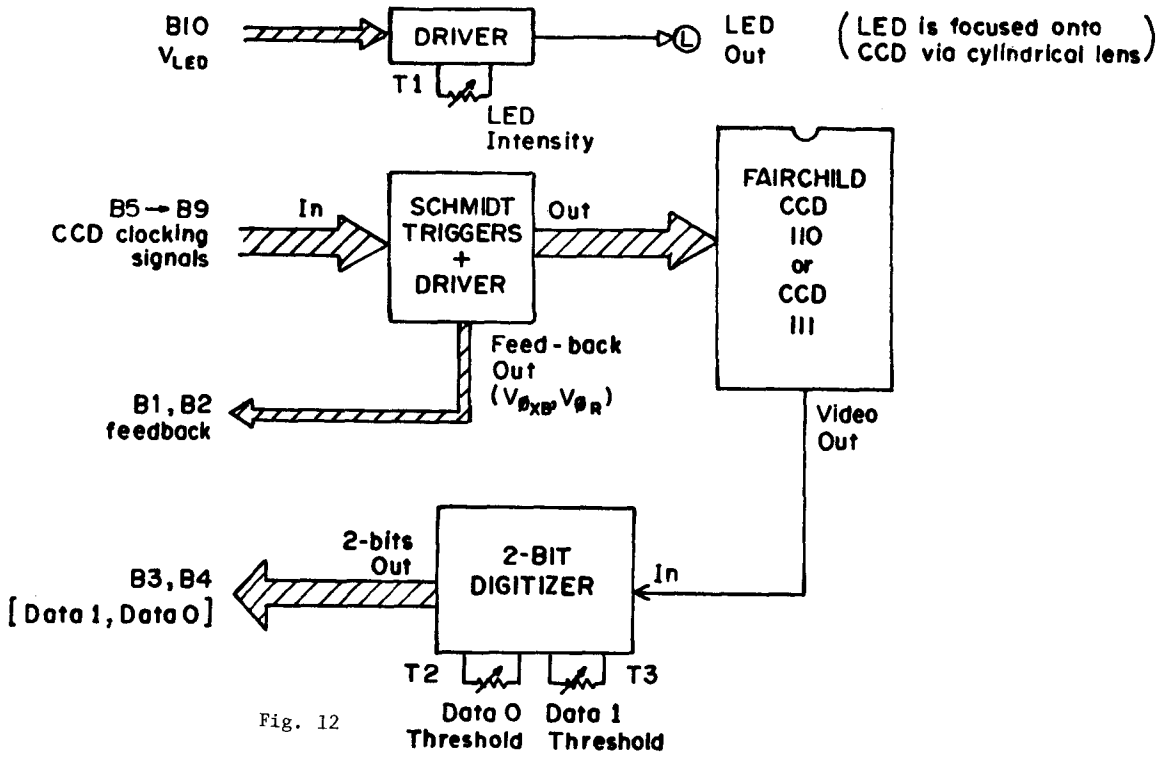

Fig. 12

MOTOR CONTROLLER/DRIVER

BLOCK DIAGRAM

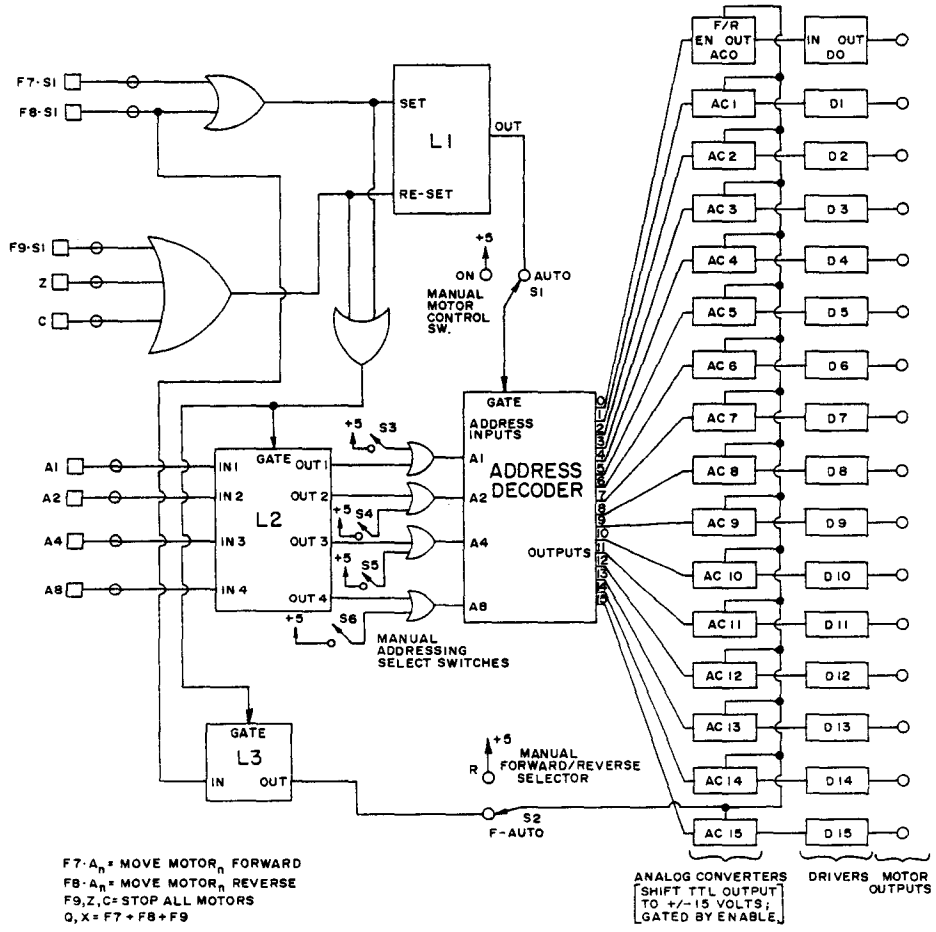

Fig. 13

WORKING GROUP ON PARTICLE IDENTIFICATION: SOME GENERAL COMMENTS

A.H. Walenta, BNL

The basic aim of particle physics can be described as investigation of the behaviour, transformation and interaction of different particles which obviously depends on proper identification of the latter. On this general sense any experiment does particle identification. A particular purpose of particle identification at Isabelle is the use of well identified particles emerging from the interaction zone as messengers for the physics phenomena produced in the collisions. Muons can be used for this purpose and their identification is straightforward but not necessarily easy.

From the experimental side of view it is challenging to exploit the possibilities of particle identification in a hadronic jet and the requirements for Isabelle can be summarized as detecting protons, charged kaons and pions and possibly electrons in a jet of charged and neutral particles at high event rates.

For the moment there is no strong reason to trigger on a given particle (k or e) because they are abundant in any event. In a more detailed study (J. Thomson, see below) it was found, however, that the knowledge of the particle mass of a measured track increases the probability seven-fold of finding in a mass reconstruction a charmed meson originated from a heavy quark (b and t). In connection with a high precision vertex detector this may serve as an example how particle identification at Isabelle may become useful even in jets which, at the first glance, seem to be inaccessible to specific interpretation. Therefore the main emphasis of our study is the compatibility of an excellent magnetic multi-track detector and the particle identification which ultimately assigns the mass to each track found in the track detector.

Members of the working group are listed below. The results appear in the papers which follow.

Particle Identification

K. Amako	University of Pennsylvania, Philadelphia
J. Beingessner	Carleton University, Canada
S. Hagopian	Florida State University
C. Hargrove	Carleton University, Canada
Y. Inagaki	BNL, on leave from Kyoto University, Japan
D. Jensen	University of Massachusetts
J. Kirz	SUNY at Stony Brook
T. Miyachi	INS, Japan
J. Thomson	University of Pittsburgh
*A.H. Walenta	BNL
S. White	Rockefeller University, N.Y.
R.J. Wu	MIT, on leave from Institute of High Energy Physics, Peking

*Chairman

CONVENTIONAL dE/dx

A.H. Walenta

Particle identification by measurement of the relativistic rise of energy loss has the advantage of being automatically available from the pulse height of the tracking drift chamber system avoiding pattern recognition and correlation problems because whenever a track has been found, in principle the pulse height in connection with the curvature gives the momentum and mass of the particle. A few devices have been built (revised in Ref. 1) and results are expected soon. In preliminary measurements, however, one notices that the design resolution is not reached which is attributed to the lack of calibration possibilities for the large number of individual channels and variations in gas gain as function of a number of parameters. Since the advantage of combined tracking and particle identification is so obvious a detector for ISABELLE is proposed providing adequate e/π/K/-separation and an effort is spent to include a calibration system avoiding the shortcomings of existing systems.

The detector (Fig. 1) is of the JADE (bicycle wheel) type with a useful track length of 200 cm, subdivided in 200 samples (wires). The gas could be Ar/C_2H_6 (50:50) and added to this mixture a trace of 0.2% Xe at a pressure of 4 atm. From the graphs of Ref. 1 one obtains a resolution for the truncated mean σ=2.5% and for the relative difference of energy loss of π's and K's between 2 and 30 GeV/C $\Delta E_\pi - \Delta E_K / \Delta E_K$ = 16% which in turn gives a π-K-separation on 6.5 σ if the systematic errors of the energy loss measurement can be corrected.

The calibration system is shown in Fig. 2. A few x-ray tubes (here shown only one from each side) are arranged such that their uncollimated beam covers the whole sensitive region of the chamber. The x-ray energy is E_x=40 keV (Sm-anode) and the tubes are pulsed at a rate up to 2 MHz with pulses of 10 ns width. The x-rays have an absorption length of λ=1.9 m in the counter gas and therefore the intensity in the center decreases only to 0.48 of the value at the ends. The probability for absorption by the Ar is P(Ar)=75% giving a photoelectron of 37 keV and the rest energy of the deexitation of the Ar with

a vacancy in the K shell leading to a localized ionization of 40 keV or 37 keV (escape peak) and an extra photon of 3 keV with a range of λ_3 = 2 cm which is frequently recorded separately. The probability for absorption by Xe is P(Xe)=18% leading in 80% of the cases to an fluorescent x-ray of 30 keV with a range λ_{30}=0.95 m which then will be geometrical remote from the photoelectron of 5 keV. With the ionization caused by the subsequent L,M-transitions an ionization corresponding to 10 keV is obtained. In case the ionized Xe emits an Auger-electron the full energy will be observed in one spot. Therefore the amount of ionization measured in the chamber shows in 15% of all recorded signals the equivalent of 10 keV which is within the linear range of the measurement for dE/dx and in about 8% one observes 3 keV from the Ar-fluorescence. Since the x-ray tube is pulsed, the drift time measurement can be obtained and therefore the location of the ionization can be determined. The calibration can be done during data taking giving a calibration including all rate and space charge effects.

REFERENCE

1. A.H. Walenta, Physica Scripta 28, (81) 354.

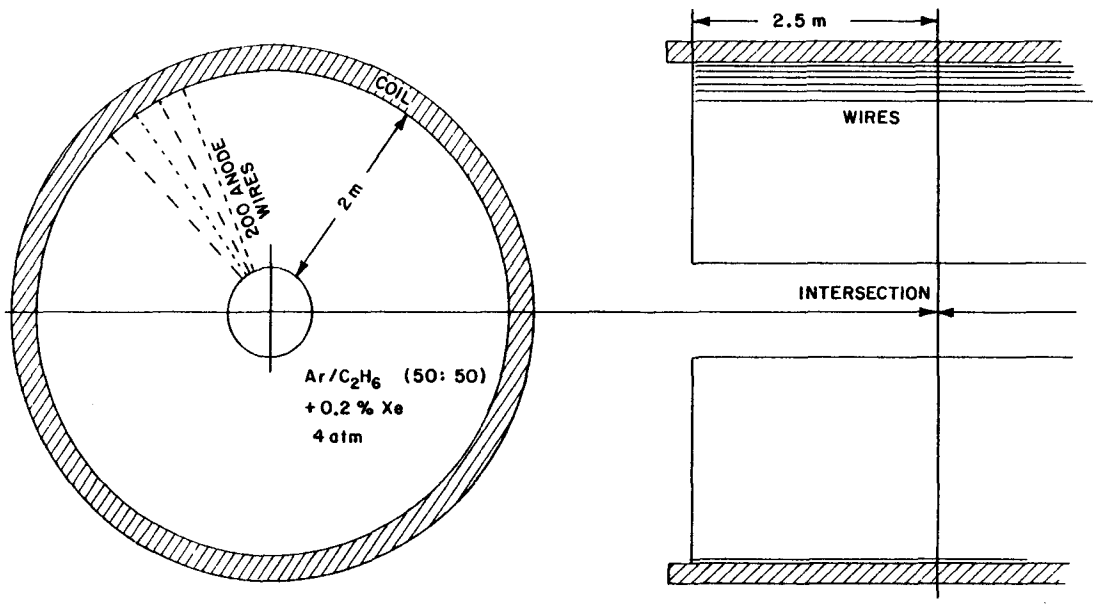
2.5 m
COIL
200 ANODE WIRES
2 m
WIRES
INTERSECTION
Ar/C2H6 (50: 50)
+0.2 % Xe
4 atm

Fig. 1

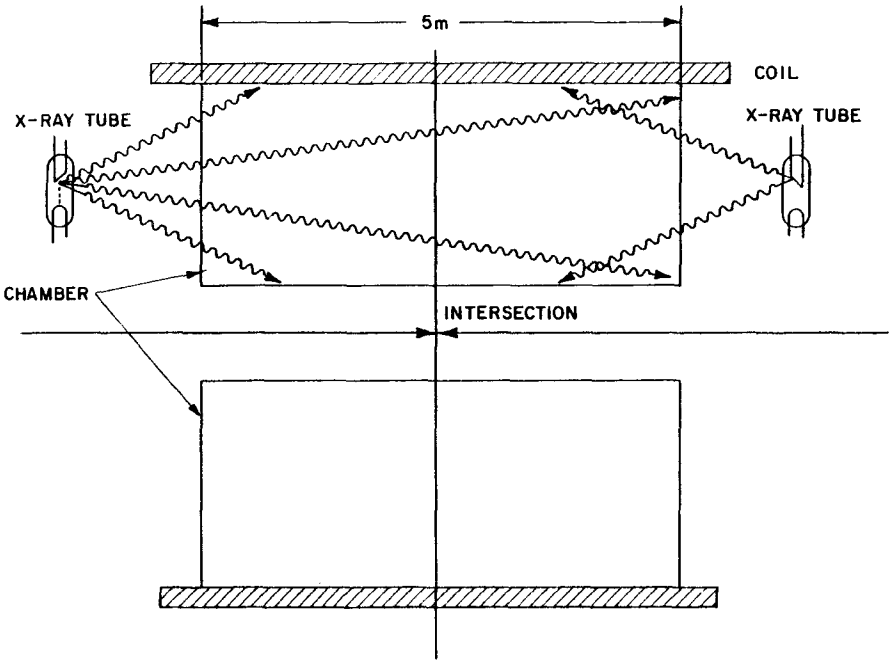

Fig. 2

PERFORMANCE OF A HIGH PRESSURE HYDROGEN TIME PROJECTION CHAMBER*

T.J. Chapin, R.L. Cool, K. Goulianos,
J.P. Silverman, G.R. Snow, H. Sticker and S.N. White
The Rockefeller University, New York, NY 10021 USA

and

Y. H. Chou
Institute of High Energy Physics
Beijing, The People's Republic of China

Presented by: S.N. White

INTRODUCTION

We have been using a high pressure hydrogen filled timed projection chamber (TPC) in a Fermilab experiment (E-612) which is investigating the diffraction dissociation of photons on hydrogen, $\gamma p \rightarrow Xp$. In this paper we present details on construction and performance of the chamber and describe briefly the experiment for which it was designed.

The chamber acts both as target and as track detector of recoil protons. It is used to measure the polar angle, θ, and dE/dx of protons with $10 < T < 50$ MeV and $45^0 < \theta < 90^0$. The energy of protons is determined by stopping them in plastic scintillation counters located inside the high pressure vessel.

The experiment is operating in Fermilab's tagged photon beam ($20 \lesssim p_\gamma \lesssim 170$ GeV/c) which provides a flux of $1\text{-}2 \times 10^6$ tagged photons per pulse with a momentum resolution of $\pm 2\%$. The variables t and M_x^2 are determined from the measured quantities p_γ, T and θ as follows:

$$t = -2M_p T$$

$$M_x^2 = 2p_\gamma \sqrt{|t|}(\cos\theta - \sqrt{|t|}/2M_p)$$

Figure 1 shows the mass spectrum expected from 50 GeV photons. A pressurized target and good detector coverage are needed to obtain a useful event rate. Good mass resolution is essential to the study of the resonances. A $\Delta M_x^2/M_x^2 = \pm 0.03$ may be obtained in the region $0.05 < M_x^2/s < 0.1$ with $\Delta t = 0.002$ (GeV/c)^2 and $\Delta\theta = 5$ mr. The latter is limited by multiple coulomb scattering in the target-detector combination. For this reason, a liquid target would be inadequate and a low Z drift chamber gas is desirable. The TPC that we have built is a target-detector combination that satisfies these requirements.

TREAD (The Recoil Energy and Angle Detector)

The recoil detector consists of two identical endcap assemblies mounted on a 26" I.D. × 84" long stainless steel tube. A schematic drawing is shown in Figure 2. The vessel may be pressurized up to 20 atm with hydrogen. The beam enters through a 2" dia. × 0.030" thick hemispherical beryllium window. Recoil protons from interactions of the beam with the hydrogen are stopped in 1 1/8" thick scintillation counters placed 9" away from the axis inside the high pressure vessel. The energy of the protons is determined from the counter pulse heights. Particles penetrating these counters register on anti-counters. The photon dissociation products exit through an 8" dia. × 0.080" thick aluminum window (not shown in the figure).

The ionization electrons generated along the path of the recoil proton drift along axial electric field lines towards a ground plate where they are detected by a set of concentric octagonal sense wires. Typically, at 15 atm of hydrogen with E = 2kV/cm drift field the drift velocity is 0.5 cm/μsec. The sense wires and associated electronics record the time and measure the amount of the ionization as it arrives. Time differences between sense wires are then translated into polar angles and pulse heights into dE/dx. From dE/dx and T (recoil energy measured by pulse-height counters) the mass of the recoil may be calculated.

Because the drift velocity of electrons in hydrogen is a function of the ratio of E to the gas density, angle measurements of the required accuracy demand tolerances on the electric field, temperature and pressure on the order of 0.1%. The temperature is maintained constant by an automatically controlled heating jacket surrounding the vessel. A pressure transducer controlled with

preset limits activates input and exhaust solenoid valves to keep the pressure within tolerances. In practice, allowing the gas to leak at a constant rate maintains the pressure within 0.01 psi of the low set limit. Finally, the electric field is kept uniform by two "cages" of field-shaping concentric metal rings. The outer cage consists of 48 rings made of 1/8" copper wire and connected by a bleeder chain of 48 × 100 MΩ metal film resistors. These rings are insulated from the wall of the vessel by a 1/2" thick polyethylene tube. The thickness of the wire was chosen to prevent corona discharge. Since the inner cage is located in an already uniform electric field, thin (0.002" diameter) wires were used for its construction.

The sense wires which are stainless steel or nichrome (35μ diameter) operate at 6.4 to 8 kV. They are located in the centers of 1/4" square grooves machined on the face of a 1/2" thick aluminum plate. With this arrangement, a track segment approximately equal to the width of the groove is focused onto each sense wire.

The drift time and gain stability of the TPC are monitored by ^{244}Cm α-sources positioned so as to leave ionization tracks directly over one wire of each sense wire plate. ZnS scintillation counters detect the α particles and provide a zero-time reference for drift velocity monitoring. Drift velocity measurements obtained in this manner are shown in Figure 3. We find that drift velocities scale as E/p to ± 2% over this pressure range.

SENSE WIRE GAIN

The sense wire gain in hydrogen was measured, prior to building TREAD, in a simple proportional counter consisting of an anode wire stretched along the axis of an 0.5" I.D. aluminum cylinder. Measurements were carried out

with 20μ and 50μ diameter sense wires at pressures from 5 to 15 atm. We have calculated the sense wire gain by integrating the first Townsend coefficient, α ,

$$\ell nG = \int_{r_1}^{r_2} \alpha(r)\, dr$$

from the anode (r_1) to the cathode (r_2) using a simple approximation for α suggested by low pressure measurements[1]:

$$\alpha/p = 5.1 \exp(-139\ p/E(r))\ cm^{-1}\cdot torr^{-1}$$

where p/E is expressed in $torr\cdot V^{-1}\cdot cm$. Our measurements agree well with the pressure and voltage dependence of the gain predicted in this manner. This is illustrated in Figure 4 which shows a comparison with our measurements at a gain of 10^4.

The maximum gain in the test counter and in TREAD was found to be in the range $2\text{-}5 \times 10^4$, essentially independent of sense wire diameter and gas pressure.

ELECTRON ATTACHMENT

Our gas purification system (Fig. 5) was designed primarily to remove oxygen impurities, since O_2 is expected to be the main electro-negative contaminant in the chamber. The chamber gas is recirculated at a rate of 3 volumes/hr. It passes through a "Deoxo" palladium catalyst which combines H_2 and O_2 to form water molecules which are subsequently adsorbed in a $4A^o$ molecular sieve. Under steady state conditions, we find that the pulse height attenuation with drift time is characterized by a decay constant of 1.8 msec. Using available data on three-body attachment[2] to O_2 impurities in H_2, this decay constant implies an oxygen level of < 1 part in 10^8.

SPATIAL RESOLUTION

Figure 6 shows the r.m.s. deviation of the drift time measured on a typical wire from fits to cosmic ray tracks passing through the axis of the chamber. Also shown is a fit of the form

$$\sigma^2 = \sigma_0^2 + \sigma_1^2 \cdot \left(\frac{Z}{1cm}\right)$$

where $\sigma_0 = 218$ μm and $\sigma_1 = 30$ μm.

The value of σ_0 depends on the sense wire discriminator threshold. The second term is due to electron diffusion. The diffusion width along the drift direction, calculated from known transport coefficients[3] in H_2, is $\sigma_D^2 = (68\mu m)^2 \cdot Z/1cm$. Due to statistics, for the sense wire threshold used in the cosmic ray data, we would expect an "ideal" $\sigma_1 = 0.3 \times 68 = 21\mu m$.

PERFORMANCE IN THE BEAM

During the previous run of the experiment, the chamber was operated at a sense wire gain of 1.5×10^2. At this gain, the total sense wire current was 2×10^{-8} Amps "on spill", caused primarily by low energy electrons produced in the beam halo. Under these conditions, we did not observe any deterioration of the chamber gain or spatial resolution due to space charge.

A scatter plot of sense wire pulse height vs. recoil kinetic energy obtained on-line is shown in Figure 7. The recoil proton band is clearly visible.

REFERENCES

* This research is supported in part by the United States Department of Energy.

1. D.J. Rose, Phys. Rev. 104, 273 (1956).

2. H. Shimamori and Y. Hatano, Chem. Phys. Lett. 38, 242 (1976).

3. L.G. Huxley and R.W. Crompton, *The Diffusion and Drift of Electrons in Gases* (Wiley, New York, 1974).

FIGURE CAPTIONS

Fig. 1 : Missing mass spectrum expected from 50 GeV photons.

Fig. 2a : TREAD.

Fig. 2b : TPC sense wire arrangement.

Fig. 3 : Drift velocity vs. E/p.

Fig. 4 : Voltage vs. Pressure at a fixed gain of 10^4.

Fig. 5 : The hydrogen purification system.

Fig. 6 : Resolution vs. drift distance.

Fig. 7 : dE/dx vs. recoil kinetic energy for raw events.

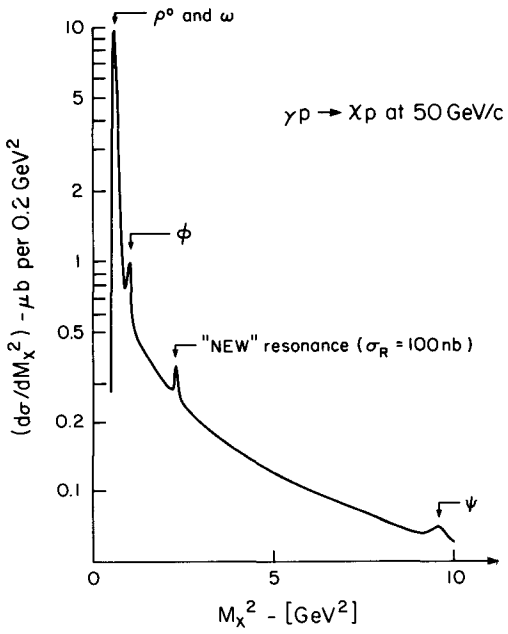
ρ° and ω
γp → Xp at 50 GeV/c
φ
"NEW" resonance (σR = 100 nb)
ψ
10
5
2
1
0.5
0.2
0.1
0
5
10
(dσ/dMX²) - μb per 0.2 GeV²
MX² - [GeV²]

FIGURE 1

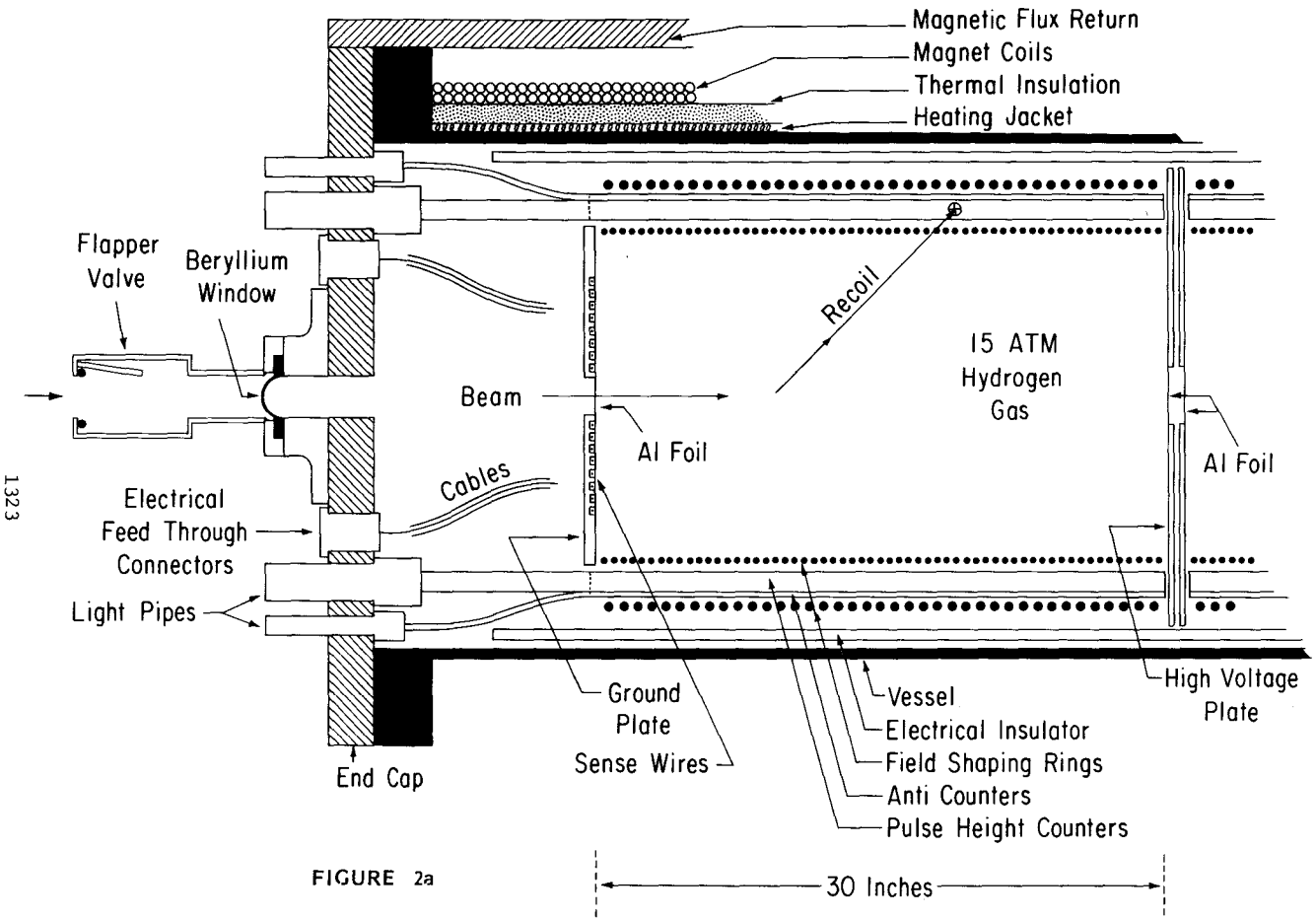
Magnetic Flux Return
Magnet Coils
Thermal Insulation
Heating Jacket
Flapper Valve
Beryllium Window
Recoil
15 ATM Hydrogen Gas
Beam
Al Foil
Al Foil
Cables
Electrical Feed Through Connectors
Light Pipes
Ground Plate
Sense Wires
End Cap
Vessel
Electrical Insulator
Field Shaping Rings
Anti Counters
Pulse Height Counters
High Voltage Plate
30 Inches

FIGURE 2a

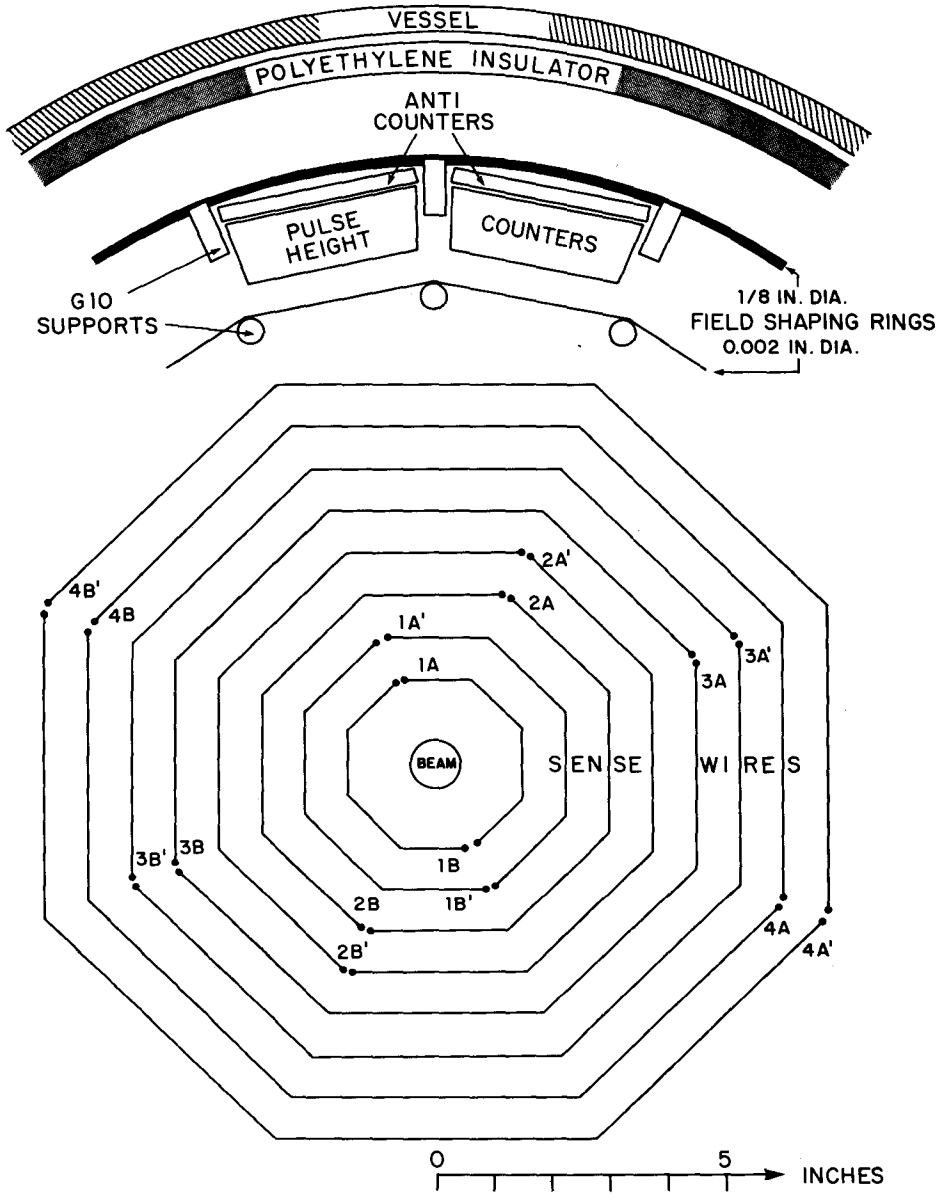
VESSEL
POLYETHYLENE INSULATOR
ANTI
COUNTERS
PULSE
HEIGHT
COUNTERS
G10
SUPPORTS
1/8 IN. DIA.
FIELD SHAPING RINGS
0.002 IN. DIA.
4B'
4B
2A'
2A
1A'
1A
3A'
3A
BEAM
SENSE WIRES
3B'
3B
1B
2B
1B'
2B'
4A
4A'
0
5
INCHES

FIGURE 2b

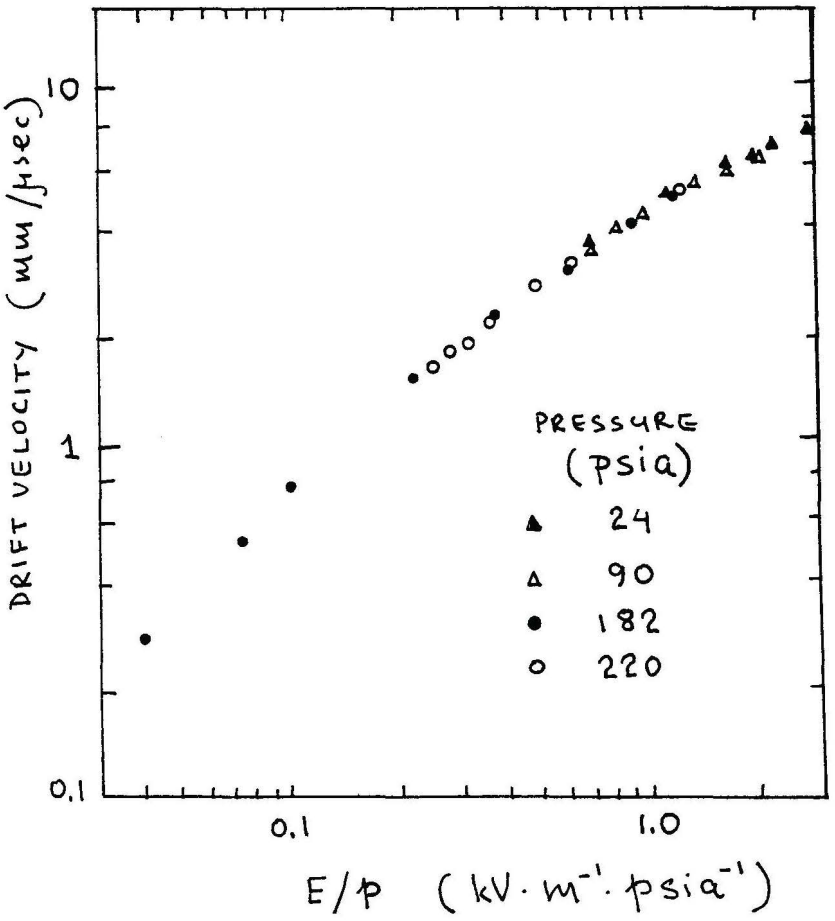
DRIFT VELOCITY (mm/μsec)
10
1
0.1
0.1
1.0
E/p (kV·m⁻¹·psia⁻¹)
PRESSURE (psia)
24
90
182
220

FIGURE 3

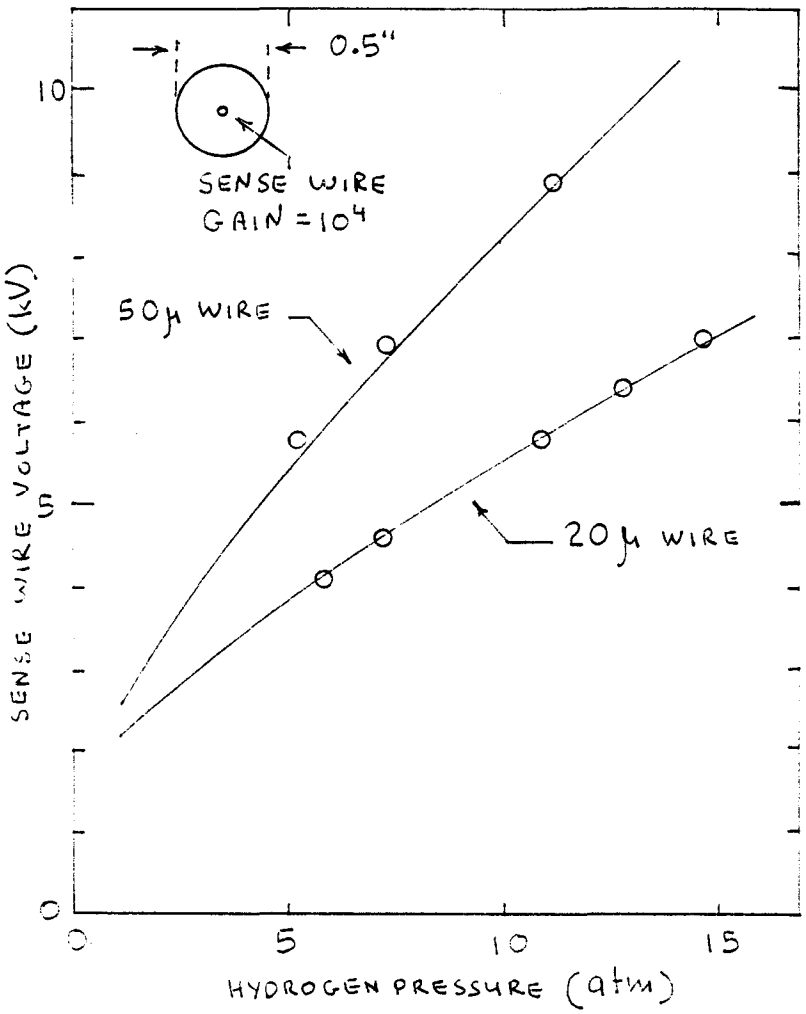
0.5"
SENSE WIRE
GAIN = 10^4
50μ WIRE
20μ WIRE
SENSE WIRE VOLTAGE (kV)
HYDROGEN PRESSURE (atm)
0
5
10
15
10

FIGURE 4

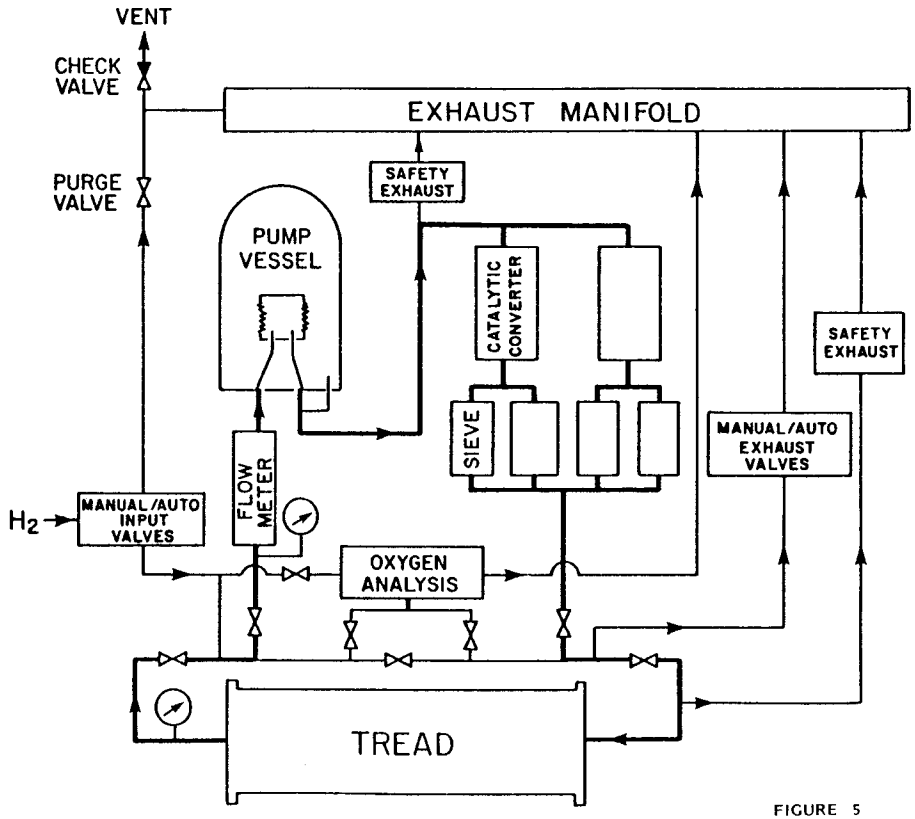
VENT
CHECK VALVE
PURGE VALVE
EXHAUST MANIFOLD
SAFETY EXHAUST
PUMP VESSEL
CATALYTIC CONVERTER
SAFETY EXHAUST
SIEVE
MANUAL/AUTO EXHAUST VALVES
FLOW METER
H_2
MANUAL/AUTO INPUT VALVES
OXYGEN ANALYSIS
TREAD

FIGURE 5

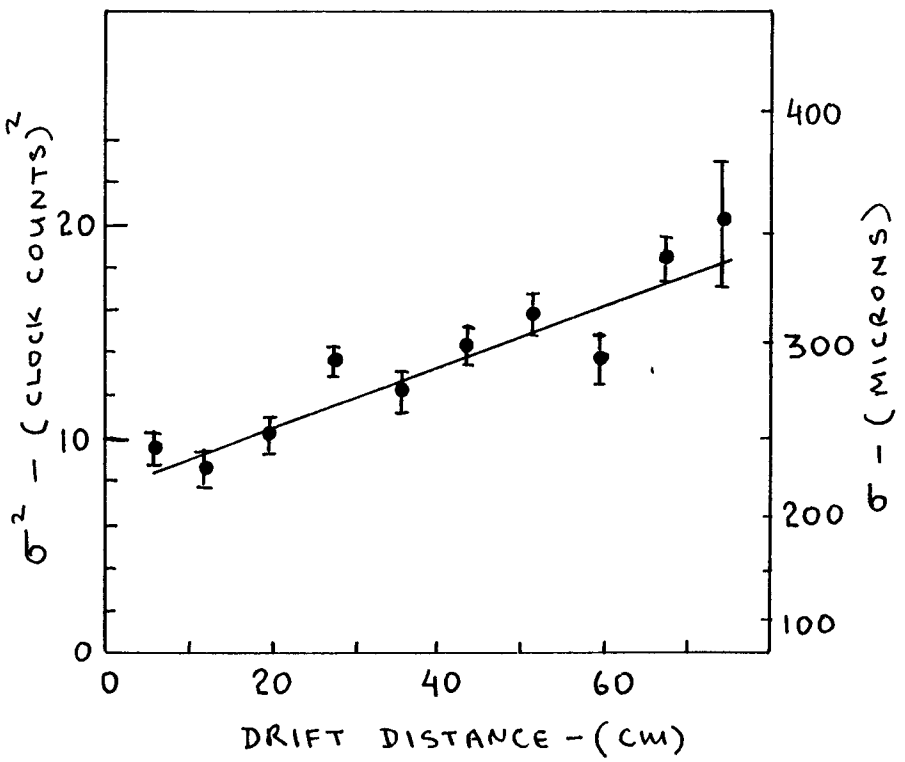
σ^2 - (CLOCK COUNTS)^2
0
10
20
0
20
40
60
DRIFT DISTANCE - (CM)
100
200
300
400
σ - (MICRONS)

FIGURE 6

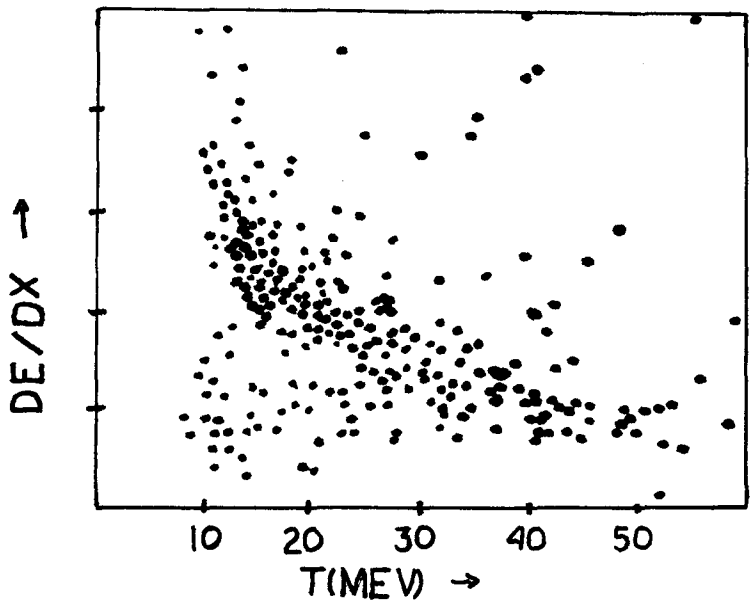

FIGURE 7

RELATIVISTIC RISE MEASUREMENTS WITH VERY FINE SAMPLING INTERVALS: PROSPECTS FOR ISABELLE

T. Ludlam and E.D. Platner, Brookhaven National Laboratory

One of the most difficult problems of instrumentation for colliding beam experiments is that of identifying high momentum charged tracks over large solid angles. A natural approach is to exploit dE/dx measurements in wire chambers whose primary purpose is for tracking particle trajectories. This method works well for certain intervals of momentum below ~ 1 GeV/c, but is difficult at best for higher momentum particles where in principle the relativistic rise of dE/dx should permit particle identification up to ~ 50 GeV/c. To achieve this, ionization loss measurements with few-percent precision are required. For gases at atmospheric pressure this calls for ionization sampling over several meters of track length.[1] In some detectors (e.g. Jade, TPC) the sensitive gas is pressurized in order to reduce the necessary track length. This in turn reduces the useful momentum range for particle identification owing to the density effect. The difficulty is exacerbated by the fact that the tracking volume is generally at small radii, and imbedded in a magnetic field, so that one must deal with a multiplicity of highly curved (and crossing) tracks as well as the $\vec{E} \times \vec{B}$ effects on electron drift and charge collection.

What we need, if particle identification is a serious aim of the experiment, is a dedicated device, optimized for particle identification, preferably in a field-free region of the detector, and (for ISABELLE) capable of sustaining high rates.

In a recent (and ongoing) series of tests it has been shown that the sensitivity for charged particle identification via the relativistic rise in ionization loss can be significantly enhanced by using longitudinal drift and fast electronics to effect very small sampling intervals.[2] With the chamber geometry illustrated in Fig. 1b, electrons from individual ionizing collisions drift sequentially onto the anode wire with a time structure determined by the drift velocity in the gas. After fast pulse shaping (the signal is shaped by

a tail-cancelling pole-zero filter with 40 nanosecond shaping time), the resultant waveform is digitized with a fast-sampling ADC at a frequency of 100 MHz.

Figure 2 shows an oscilloscope trace of the output waveform for a track passing through such a chamber, and the output of the fast digitizer. The ADC samples the waveform every 10 ns. In the example shown here, each sampling interval corresponds to 0.5 mm of track length. This relationship can be adjusted by varying either the drift velocity on the clock frequency of the ADC.

For the tests described in Ref. 2 the smallest sampling interval was 1/4 mm, and the sensitivity of mass (velocity) discrimination was studied for 1 meter of track length with sampling intervals ranging from 1/4 mm/sample to 16 mm/sample the upper end of this range being typical of conventional ioniation sampling devices.

The results are summarized in Fig. 3, which shows the sensitivity for discriminating electrons from protons as a function of the number of samples per meter of track. The result achieved with 1 meter of conventional sampling (ISIS-I) is shown for comparison. For large sample sizes the results are comparable to those of traditional techniques, and a significant improvement is obtained when the sampling frequency is increased by roughly an order of magnitude. These results were gotten with a small test chamber in which meter-long tracks were simulated by piecing together many traversals of a single drift gap. It remains to be seen whether this improvement in sensitivity can be duplicated with a chamber of practical dimensions and many readout channels. Nonetheless, if we extrapolate from the ISIS-I point on Fig. 3, the indication is that the fast-sampling longitudinal drift technique can give the required discrimination power for $\pi/k/p$ separation in the relativistic rise regime with chamber depths much shorter than those required for the conventional method - perhaps as short as 1 meter for the overall length of the detector.

Tests are presently underway with a larger chamber in which each anode collects charge from a drift gap on either side of the sense plane. This chamber will test the practicality of the technique in a multiplane chamber with many readout chanels, and incorporates a wire configuration which is

more economical of electronics than the asymmetric "time expansion" geometry of Fig. 1b.

This device offers the possibility of a compact high resolution relativistic rise detector operating at atmospheric pressure (full momentum range) which has good tracking characteristics and is capable of sustaining high rates (by virtue of relatively high density of wires).

Because it is compact (let us say 1 meter in depth) it is conceivable to imbed such a device in a detector system of reasonable size and still decouple it from the major burden of tracking in a magnetic field. An example is shown in Fig. 4, where we assume a high resolution track chamber in a solenoidal magnetic field of relatively small volume, with a thin coil at 50 cm radius. The iron flux return and support structure is instrumented as active calorimeter elements. The instrumentation of the compact pole tips in this layout could be realized with a fine grain array of proportional wires, as described in Ref. 3. This geometry leaves a field-free region between 1 and 2 meters radius for a fine-sampling dE/dx chamber. The chamber can perform its primary function of particle identification on straight-line tracks at a distance from the vertex where the spatial proximity of tracks in the complex events of interest should be manageable. The tracking capability of the dE/dx chamber can now play a secondary role in pattern recognition and momentum determination, with the major burden for these chores falling to the high resolution inner chamber. Momentum resolution sufficient for relativistic rise particle identification up to 50 GeV/c (i.e. $\frac{\Delta p}{p2} \simeq 2 \times 10^{-3}$ GeV/c^{-1}) can be achieved with a spatial resolution in the bend plane of 50-100 μm for the inner tracking chamber and ~ 200 μm in the dE/dx chamber, assuming a solenoidal field of ~ 2 Tesla.

Other geometries are possible, of course. For example the LAPDOG design, described elsewhere in these proceedings, lends itself well to these considerations.

Using the sketch in Fig. 4 we can estimate the scale of cost and complexity of such a dE/dx device. We take the active "planes" to be cylinders of wires separated by 3.2 cm in radius as in Fig. 5 (30 cylinders in all) with 12 mm spacing between anodes on each cylinder. This gives ~ 24000 anode wires, each with its own readout. On the basis of present test

data we believe that a 3 bit flash encoder is required for each channel. Using the new high speed shift register chips described in Ref. 4, the cost per channel of such an encoder is estimated to be ~ \$16. The cost of preamplifier and pulse-shaping network should be comparable. Hence, the cost of the electronics up to and including the ADC is ~ $\$10^6$.

For events of interest we may assume that ~ 1000 wires have data, with the data on each wire being 100 digitized track samples of 3 bits per sample. The total information readout from such an event is then ~ 4×10^4 bytes (about 10 inches of high density tape).

REFERENCES

1. See, e.g., W.W.M. Allison and J.H. Cobb, Oxford Univ. Preprint 13/80 (to be published in Ann. Rev. Nucl. Sci.)
2. T. Ludlam et al., IEEE Trans. Nucl. Sci., NS-28 439 (1981).
3. T. Ludlam et al., Proc. IEEE, IEEE Trans. Nucl. Sci., NS-28, 517 (1981).
4. E. Platner, these proceedings.

(a) CONVENTIONAL SAMPLING

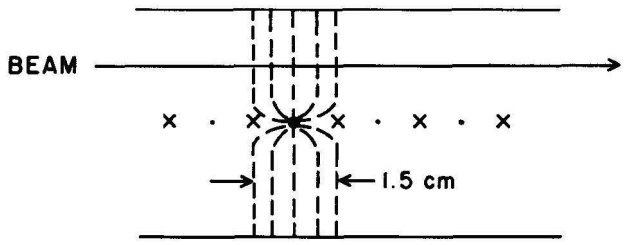

Fig. 1

(b) LONGITUDINAL DRIFT SAMPLING

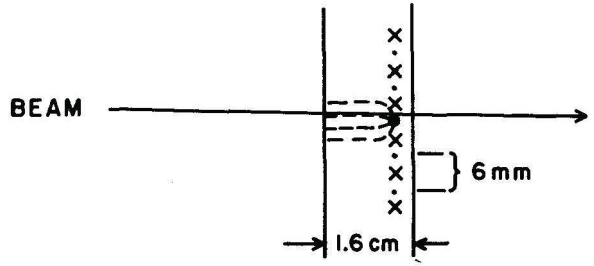

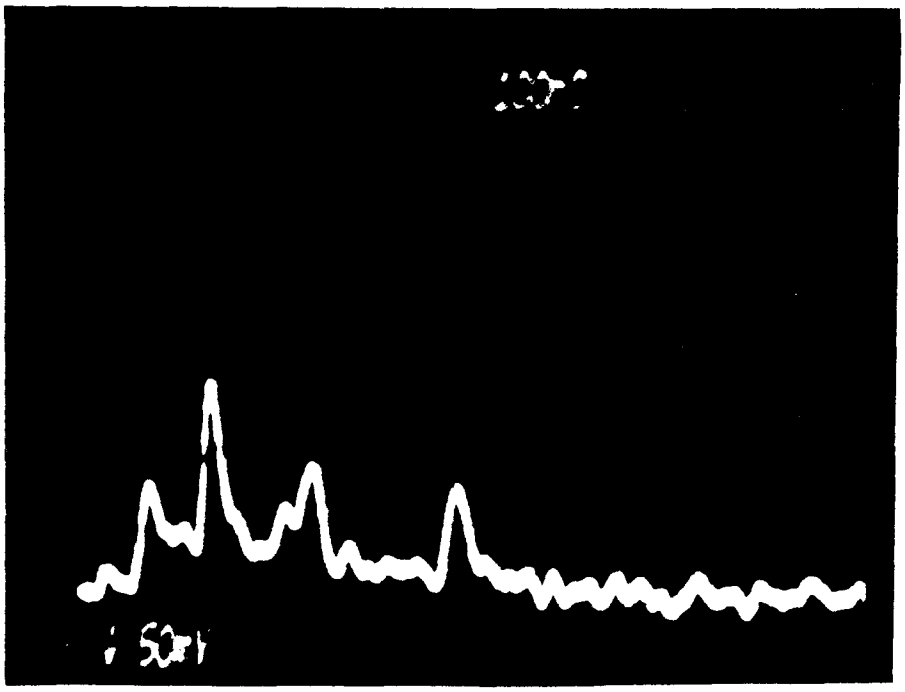

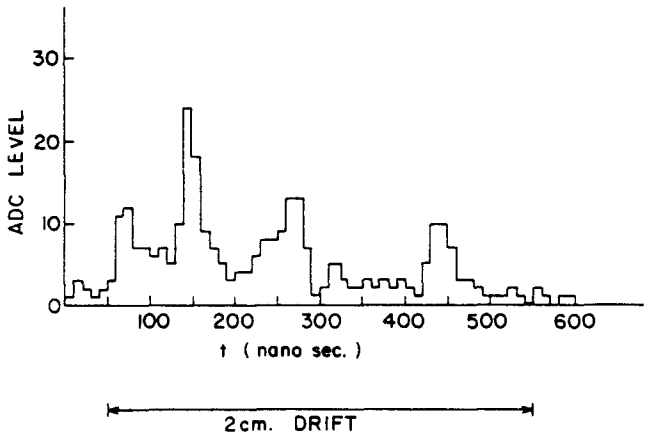

Fig. 2

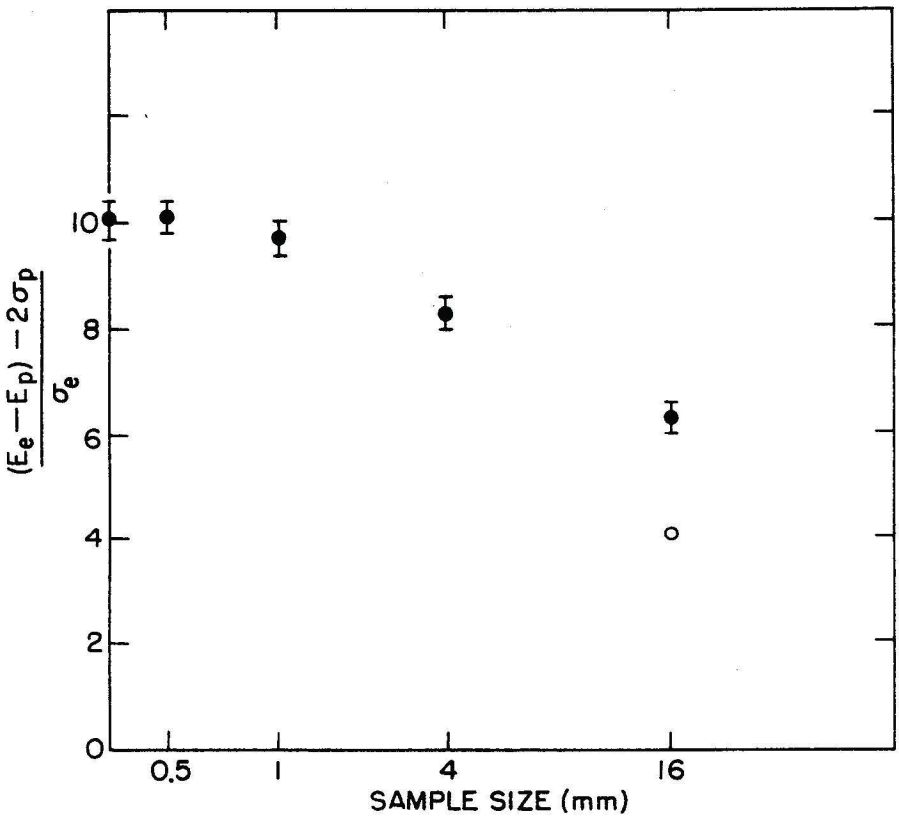

Fig. 3

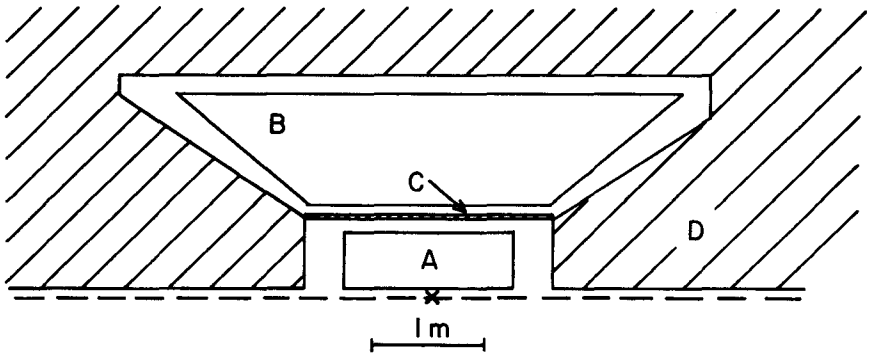

A HIGH RESOLUTION TRACK CHAMBER

B dE/dx CHAMBER

C THIN COIL

D IRON CALORIMETER / FLUX RETURN

Fig. 4

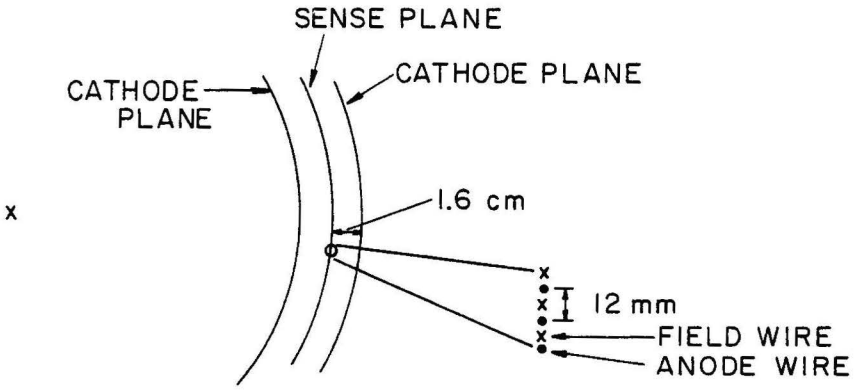
SENSE PLANE
CATHODE PLANE
CATHODE PLANE
1.6 cm
12 mm
FIELD WIRE
ANODE WIRE

Fig. 5

THRESHOLD CERENKOV COUNTERS WITH PHOTOIONIZATION DETECTORS

M. Capell, MIT
A.H. Walenta, BNL

Threshold Cerenkov counters represent a reliable tool in particle physics for particle identification. In experiments at intersecting storage rings they are only used occasionally and never to cover the full solid angle. The use of phototubes for light detection is prohibitive to design them with the desired qualities: operation in a magnetic field and fine segmentation.

A new development (Ref. 1), however, makes it attractive to study such a setup for a possible ISABELLE experiment. A photosensitive proportional counter serves as light detector and the useful spectral range is determined by the lowest photon energy able to ionize an organic vapor added to the counting gas (e.g. benzene, $h\nu_{ion}$ = 9.2 eV) and the transparency limit of the window (e.g. LiF, $h\nu_{ma}$ = 11.8 eV) sealing the counting gas from the Cerenkov medium. More practical combinations of TMAE ($h\nu_{ion}$ = 5.4 eV)and quartz gas ($h\nu_{max}$ = 7.5 eV) have been reported by Ypsilantis (see these proceedings). A typical detector is shown in Fig. 1. The Cerenkov light is focussed via an appropriately curved mirror onto the proportional chamber. Obviously the Cerenkov medium must be transparent to the spectral range of uv-light considered. Ar + N_2 (90:10) proved to be a useful mixture. Mirror, detector and gas are enclosed in a pressure vesel in a form of a tube. These individual cells can be arranged as proposed for the HRS at PEP shown in Fig. 2. For a particle identifier a number of layers can be considered. In the following we investigate a three layer system for π/K separation in a momentum range from p_{min} = 1.35 GeV/c to about p_{max} = 20 GeV/c. The lower limit gives a reasonable overlap with the time of flight method (see Proceedings of the 1978 ISABELLE Summer Workshop, p.96) and the upper limit has practical reasons as outlined below

Since the pion has to be detected positively we require a mean number of detected photons $\bar{N}$ = 3 assuming a detection efficienty of 95%. The number of

detected photons is given by:

$$\bar{N} = N_o \ell \sin^2\theta$$

where N_o characterizes the sensitivity determined by the accepted spectral range and detection efficiency, ℓ the length of the track in the Cerenkov medium and θ the Cerenkov angle. With

$$\cos\theta = \frac{1}{n\beta}$$

one finds for the threshold momentum for pions

$$p_T(\pi) = \frac{m_\pi}{\sqrt{n^2[1 - (\bar{N}/N_o e)] - 1}}$$

a relation for n if $N_o = 60\ cm^{-1}$, $\bar{N} = 3$ and ℓ are given. The useful momentum range for K-identification is limited by the K-threshold

$$p_T(K) = \frac{m_K}{\sqrt{n^2 - 1}}$$

A pressure variation ($\Delta p/p$) in the vessel will result in a variation of the refractive index

$$\frac{\Delta(n-1)}{n-1} \simeq \frac{\Delta p}{p}$$

It is taken here into consideration by lowering the necessary (n - 1) by 1% for the necessary pion threshold. Table I shows the calculated values for $n^A - 1$ and the corresponding K-threshold for a given length ℓ^A for $p_T^A(\pi) =$ 1.35 GeV/c where "A" designates the first counter layer

The detector length does not influence noticeably the momentum range of detection. Therefore, the shortest design will be adequate. If, however, the detector sensitivity decreases resulting in smaller N_o, then ℓ has to be increased correspondingly.

In order to increase the momentum range the second and third layer are calculated such that the K-threshold becomes the pion-threshold in the next layer correcting for 1% pressure fluctuation in the same way as above (Table II). As a general rule, one observes that each additional counter increases the range of momentum if the length is greater or at least the same as the previous one. A double layer of $\ell^A = \ell^B = 20$ cm would provide a compact detector with π-K discrimination up to 8.2 GeV/c.

Up to about 19 GeV/c discrimination is possible with a third counter when the second is increased to $\ell^B = 40$ cm and the third to $\ell^C = 100$ cm. The

total arrangement has a length of ca 2.0 m including walls and dead areas (Fig. 2). The total number of readout channels which equals the number of segments can be 10^3 giving a total coverage of 3π and an individual segmentation of $\Delta\Omega = 10^{-2}$ sterad.

It has been pointed out in the Proceedings of the 1978 ISABELLE Summer Workshop (p.104) that ideally 800 counters/sterad are required and the modularity proposed here can be considered as a step forward in this direction.

REFERENCES

1. D. Meyer et al., University of Michigan HEP 80-35

Table I

ℓ^A(cm)	$(n^A - 1) \times 10^3$	p_T^A(K)(GeV/c)
20	6.57	4.28
40	5.94	4.50
60	5.73	4.58
80	5.62	4.63

Table II

ℓ^B(cm)	$(n^B-1)\times10^3$	p_T^B(k)(GeV/c)	ℓ^C(cm)	$(n^C-1)\times10^3$	p_T^C(K)(GeV/c)
20	1.785	8.18	20	1.398	9.24
			40	0.7713	12.44
			60	0.6563	14.56
			80	0.458	16.14
40	1.16	10.16	20	1.347	9.41
			40	0.720	12.7
			60	0.512	15.23
			100	0.345	18.88
60	0.949	11.22	20	1.33	9.47
			40	0.70	13.0
			60	0.494	15.5
			100	0.328	19.3

FIGURE CAPTIONS

Fig. 1. Principle of a photoionization threshold Cerenkov counter.
Fig. 2. Possible detector arrangement for ISABELLE (schematically).

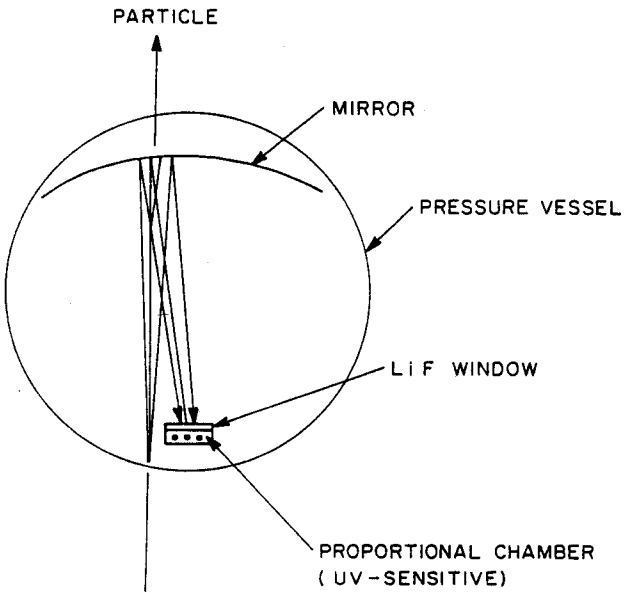
PARTICLE
MIRROR
PRESSURE VESSEL
LiF WINDOW
PROPORTIONAL CHAMBER
(UV-SENSITIVE)

Fig. 1

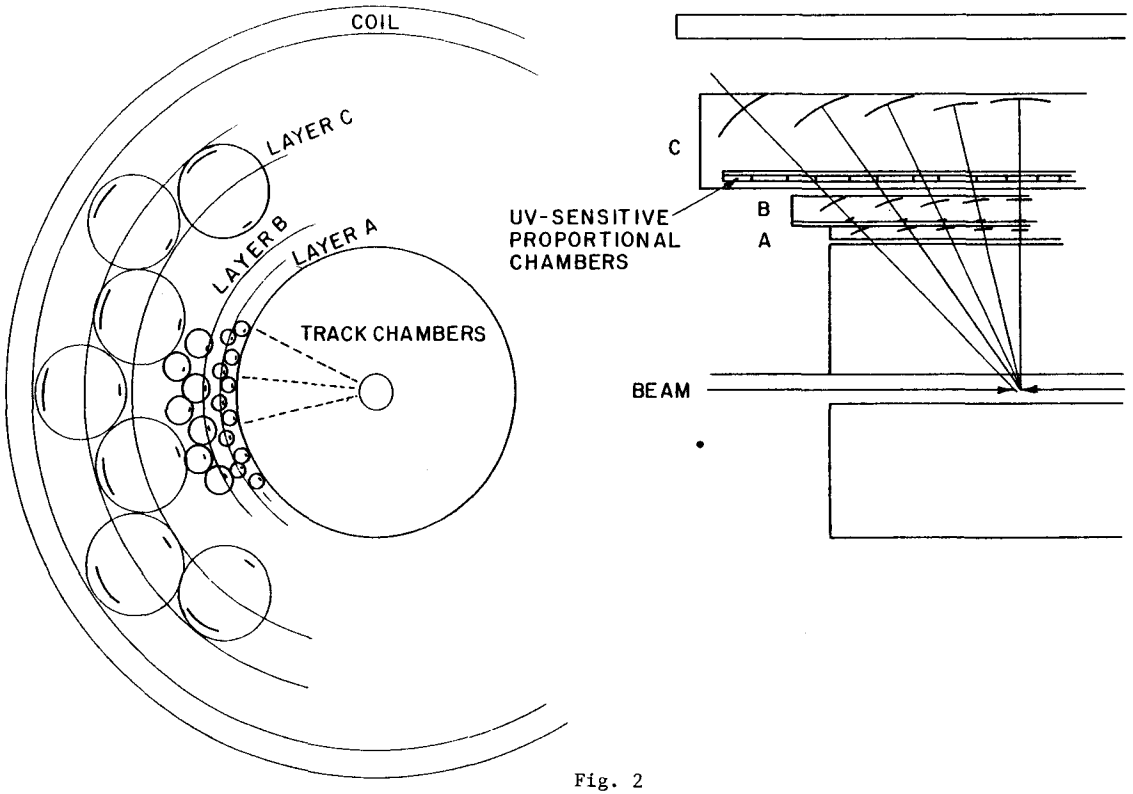
COIL
LAYER C
LAYER B
LAYER A
TRACK CHAMBERS
UV-SENSITIVE
PROPORTIONAL
CHAMBERS
C
B
A
BEAM

Fig. 2

RING-IMAGING CERENKOV COUNTERS

J. Beingessnen, J. Kirz, SUNY
A.H. Walenta, BNL

In order to achieve the highest possible segmentation and sensitivity for particle identification a ring-imaging Cerenkov counter has been proposed (Ref. 1) where the uv-part of the Cerenkov spectrum is used and the photons are detected in position sensitive proportional counters sensitized in the photon energy range in question. A detailed design of such counters surrounding an intersection point is described in these proceedings where by a careful match of the tracking detector including the magnetic field with the two Cerenkov-ring-image units has been achieved to allow the reconstruction of multiparticle events or jets. In the following the question of a more general use and the compatibility with other magnetic track detectors as well as the high rate capabilities will be investigated.

I. THE BASIC FORMULAE

$$\frac{dN}{dE} = \frac{\alpha}{hC} L \sin^2\theta_c \tag{1}$$

where dN/dE is the number of photons emitted per unit energy interval, L is the length of the radiator, and

$$\cos\theta_c = \frac{1}{\beta n} . \tag{2}$$

$$R = f \tan\theta_c , \tag{3}$$

where R is the ring radius, f the focal length of the mirror.

From (1), the number of detected photons (4)

$$N^1 = N_o L \sin^2\theta$$

where

$$N_o \approx \frac{370}{cm} \int \eta(E) dE$$

$370 \approx \alpha/hc$; $\eta(E)$ is the overall efficiency, including

- transmission of photons through radiator, window(s), detector entrance.
- reflectivity of mirror.
- efficiency of photoionizing material, and single e detection.

II. USEFUL APPROXIMATIONS

For $\beta > 0.9$, and $n-1 < 0.1$ [all gases, also liquid (neon, helium)]

$$\sin\theta_c \approx \tan\theta_c \approx \theta_c$$

$$1-\beta \to \frac{1}{2\gamma^2}$$

Then threshold for Cerenkov emission becomes

$$\gamma_{th} \to \frac{1}{\sqrt{2(n-1)}} \quad (5)$$

Cerenkov angle for $\beta = 1$ particle becomes

$$\theta_\infty \to \sqrt{2(n-1)} \quad (6)$$

For $\beta = 1$ particle, the number of detected photons per centimeter of radiator

$$N'_\infty \to N_o L \theta^2_\infty = 2N_o L(n-1) \quad (7)$$

and for slower particles

$$N' \to N'_\infty \left(1 - \frac{\gamma^2_{th}}{\gamma^2}\right) \text{ (see Fig. 1).} \quad (8)$$

III. PARTICLE IDENTIFICATION

The ring radius being

$$R \approx f\theta_c$$

difference between ring-radii

$$\Delta R \to f\Delta\theta_c \tag{9}$$

where $\Delta\theta_c$ is the velocity-dependent difference between Cerenkov angles. By adjusting f, R can be chosen to fit the detector resolution.

$$\Delta R \to \frac{f}{2\theta_c}\left(\frac{1}{\gamma_1^2} - \frac{1}{\gamma_2^2}\right) \simeq \frac{f}{2\theta_c p^2}\,(m_2^2 - m_1^2) \tag{10}$$

Evidently small θ_c and large f gives a larger ΔR.

In most practical systems it appears sensible to keep $\Delta R/R = \Delta\theta_c/\theta_c$ finite (e.g. > 1/100),

$$\frac{\Delta R}{R} \to \frac{1}{4(n-1)p^2}\,(m_2^2 - m_1^2) \tag{11}$$

In most cases $m_2^2 >> m_1^2$ (as in k/π, π/e, P/k) so

$$\frac{\Delta R}{R} \to \frac{1}{4(n-1)\gamma^2}\,, \tag{12}$$

where γ refers to the heavier particle.

Using (6) we have

$$\frac{\Delta R}{R} \to \frac{\gamma_{th}^2}{2\gamma^2} \tag{13}$$

IV. OPERATION IN A MAGNETIC FIELD

To keep the rings separated, the magnetic bend, θ_B, must be smaller than the difference of Cerenkov angles, $\Delta\theta_c$, over the length of the radiator.

$$\theta_B = \frac{3 \times 10^{-4}}{P}\,BL\,\frac{kG.cm}{GeV/c} \tag{14}$$

So we desire

$$\Delta\theta_c > \theta_B, \text{ or}$$

$$\frac{1}{2\theta_c P^2}(m_2^2 - m_1^2) > \frac{3 \times 10^{-4} BL}{P}, \text{ and } B < \frac{1.67 \times 10^3 (m_2^2 - m_1^2)}{\theta_c LP} . \quad (15)$$

Evidently the shorter the radiator (L), the larger field one can tolerate.

V. EXAMPLE: π/k/p SEPARATION AT ISABELLE

Assumptions:

1) Demand an average of > 20 detected photons for π, > 10 detected phototons for K.
2) The counter/detector system operates with N_o = 80/cm.
3) $\Delta\theta_c/\theta_c > 1/100$

- For π-s, from (7), $N' \approx N'_\infty \rightarrow 2 \times 80 \times L(n-1) > 20$, we therefore set

$$L \approx 1/8(n-1). \quad (16)$$

- To get N > 10 for K-s, we have from (8),

$$\gamma_K/\gamma_{th} > \sqrt{2} \quad (17)$$

- To get $\Delta\theta_c/\theta_c > 1/100$, we have from (13)

$$\frac{\gamma_{th}^2}{2\gamma_K^2} > \frac{1}{100} . \quad (18)$$

- Combining (17) and (18), we have

$$\sqrt{2} < \frac{\gamma_K}{\gamma_{th}} < \sqrt{50}. \quad (19)$$

This operating range is shown shaded in Fig. 2.

- For π/k separation, $m_2 - m_1$, = 0.23 GeV.^{2} From (15) and (16) we have then

$$B < \frac{1.67 \times 10^3 . 0.23}{\theta_c P . \frac{1}{8(n-1)}} = \frac{3.1 \times 10^3 (n-1)}{\theta_c P} \approx \frac{3.1 \times 10^3 (n-1)}{\theta_\infty P}$$

Using (6)

$$B < \frac{3.1 \times 10^3 (n-1)}{P\sqrt{2(n-1)}} \approx \frac{2.2 \times 10^3}{P} \sqrt{n-1} \qquad (20)$$

- lines of maximum permissible B are shown dashed in Fig. 2.

We conclude that (Fig. 2a) for $n-1 \gtrsim 2.5 \times 10^{-2}$ all of our requirements are met for 3 GeV/c < p < 16 GeV/c. For this momentum interval magnetic fields of 20 kG are compatible with $\pi/k/p$ separation. The thickness of the radiator $L \gtrsim 5$ cm [from (16)].

Note that:

1) protons with 3 < p < 4 GeV are below threshold in this counter, and are therefore identified by the absence of detected photons.
2) k/p separation extends up to ∿ 25 GeV/c.
3) For $n-1 = 2.5 \times 10^{-2}$ $\theta_\infty = 0.22$
4) to get a radius separation, $\Delta R = 2$mm at 16 GeV π/k or 25 GeV k/p, the focal length of the mirror $f = \Delta R/\theta = 2\text{mm}/2.2\text{mr} \gtrsim 0.91$ m.

All this seems attractive, although $n-1 = 2.5 \times 10^{-2}$ (liquid helium) may present some minor technical problems...

For electron identification (Fig. 2b) a similar picture emerges showing that a strong magnetic field (B ≳10 kG) is only compatible with a radiator of $n-1 \gtrsim 3.10^{-1}...10^{-1}$ which brings it in the range of liquid neon.

VI. RATE CAPABILITIES

The rate handling capability of these ring-imaging Cerenkov counters are limited by the photoionization detectors which are in principle sensitized gas filled detectors with provisions for position read out. The important difference compared to track detectors for charged particles is that an unambiguous reconstruction of a multihit event has to be obtained from one detector plane which limits and complicates the position readout by requiring a truly 2 dimensional detector (see Table 1). The simplest arrangement proposed and tested is a matrix array of Geiger-needle counters (Ref. 2). Up to now they have shown technical difficulties concerning stability and

efficiency. Their big advantage however, is the possibility of using high double hit resolution which is here labeled as "spacial resolution" to be distinguished from "position resolution" which is a measure of the accuracy of localization for a single hit. Although the dead time of these devices is rather long (3..5μs) there is such a large number ($2.5.10^5/m^2$) that even at a particle rate of 5.10^7 s^{-1} and a photon rate of 10^9 s^{-1} (assuming N = 20 photons/track) an efficiency loss of $1-\varepsilon \approx 1\%$ would be observed. The time resolution is much better (≈100ns) and therefore only a few random tracks/event are recorded. The number of random hits is obtained by multiplying with the number of detected photons/track (10...20). In the multistep chamber (Ref. 3) the photoelectron is amplified in a preamplification region (Ref. 4) and the charge then transferred into a drift region. It passes several grids, each giving one coordinate using induced signals. The special resolution is somewhat limited due to the width of the cloud of drifting charge and the range of induced signals. A gated grid can reduce the memory time to 100 ns thus limiting the number of random tracks.

Recently a drift chamber has been operated successfully as photoionization detector (Ypsilantis, these proceedings) exhibiting excellent efficiency, spacial resolution and position resolution. The long memory time of ≈1μs still could be handled at the ISA stage I intensity because a shift register read-out can easily accomodate the extra random hits ($200/m^2$/event). For ISA stage II however, one would expect $10^3...10^4$ extra hits and a more careful study has to be undertaken to determine if an efficient ring recognition can be obtained. Also a 10% loss due to the limited pixel size would be observed. There are possibilities that the limited streamer mode (see for example M. Atac, these proceedings) can possibly be used to give a large signal from single photoelectrons to achieve good position resolution with cathode strip readout on both cathodes at $\pm$ 45° to the anode. Drift time measurement can provide the third coordinate for multiple hit reconstruction.

It can be concluded that ring-imaging Cerenkov counters have a high potential as particle identification tools, however, it is not obvious how they can be combined with a large track detector in a strong magnetic field which is needed for unambiguous pattern recognition of the charged particles.

TABLE 1.

	Needle Chamber	Multistep Ch.	Drift Ch.	Limited Streamer
Efficiency (measured)	20%	50%	80%	?
Pos. resolution (σ)	600µ	600µ	300µ	500µ
Spacial resol.	2 x 2 mm^2	5 x 5 mm^2	5 x 2 mm^2	5 x 5 mm^2
No. of pixel/m^2	2.5.10	4.10	10	4.10
Memory time (time resol.)	100 ns	100 ns	1µs	100 ns
Dead time/pixel	3µs	determined by readout		$\approx$ 100 ns
Random/ISA I	1	1	6	1
Tracks/ Event/ISA II	30	30	300	30
Comments	Development Necessary	limited double hit resolution	Sensitive to Magn.field	Development Necessary

REFERENCES

1. J. Seguinot and T. Ypsilantis NIM 142(77)377.
2. G. Comby, Ph. Mangeot, J.L. Augueres, S. Claudet, J.F. Chalot, J. Tichit, H. Ligmires and A. Zadra, Saclay Report 79/06/08/227(79).
3. A. Breskin, G. Charpak, S. Majewski, G. Melchant, G. Petersen and F. Sauli, NIM 161(79)19.
4. J. Fischer and S. Shibata, Proc. Intern. Symp. "Nuclear Electronics", Versailles, France, Sept. 1968, Vol. 3 (Documentation Franganie, Paris, 1969) p. 2-1.

FIGURE CAPTIONS

Fig. 1. Number of detected photons as function of γ over threshold.

Fig. 2. Momentum useful for Cerenkov ring measurement (shaded) as function of n-1. Included necessary length for 20 photons and maximum permissible magnetic field.
a) for p,k,π, b) for electrons.

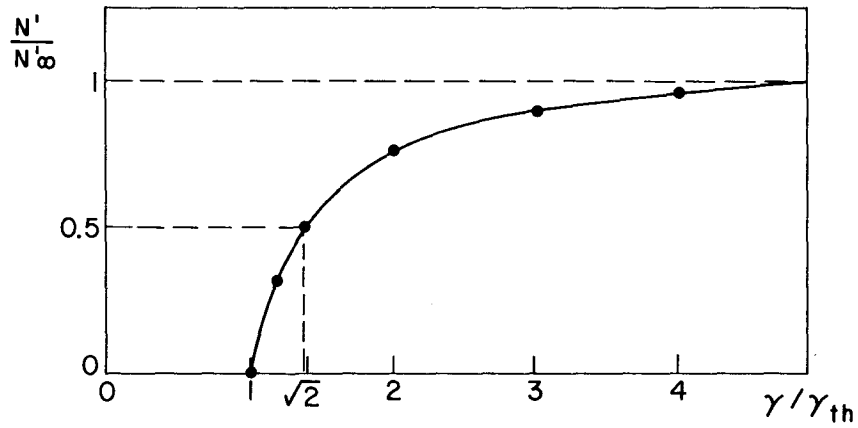

Fig. 1

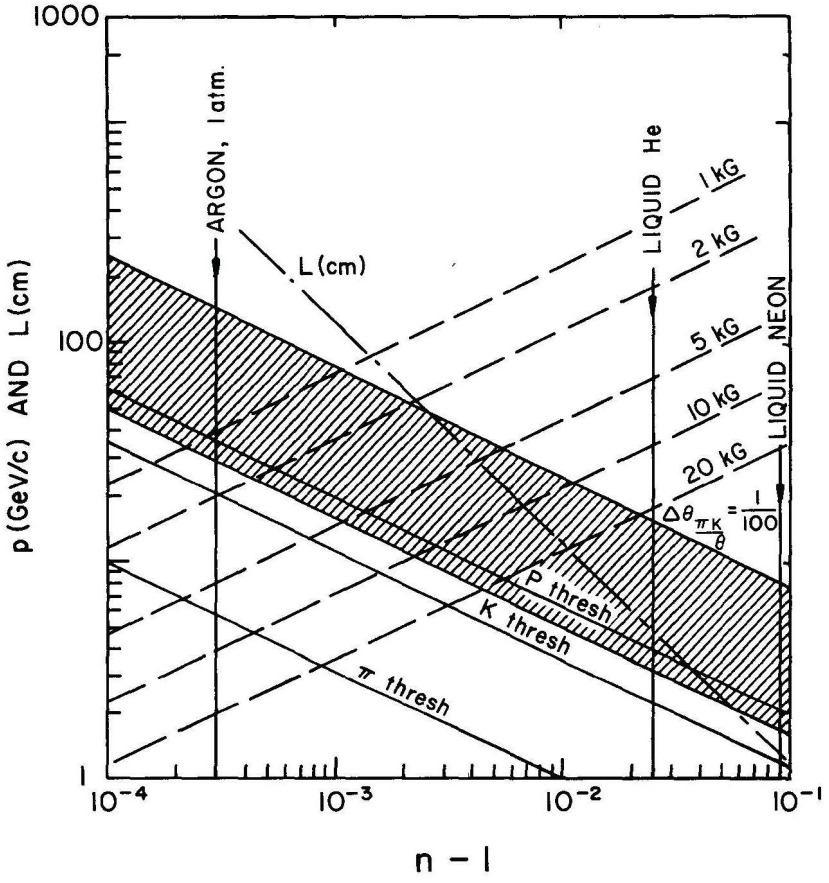
1000
100
1
p (GeV/c) AND L(cm)
ARGON, 1 atm.
L(cm)
LIQUID He
LIQUID NEON
1 kG
2 kG
5 kG
10 kG
20 kG
$\Delta\theta_{\pi K}/\theta = 1/100$
p thresh
K thresh
π thresh
10^{-4}
10^{-3}
10^{-2}
10^{-1}
n − 1

Fig. 2a

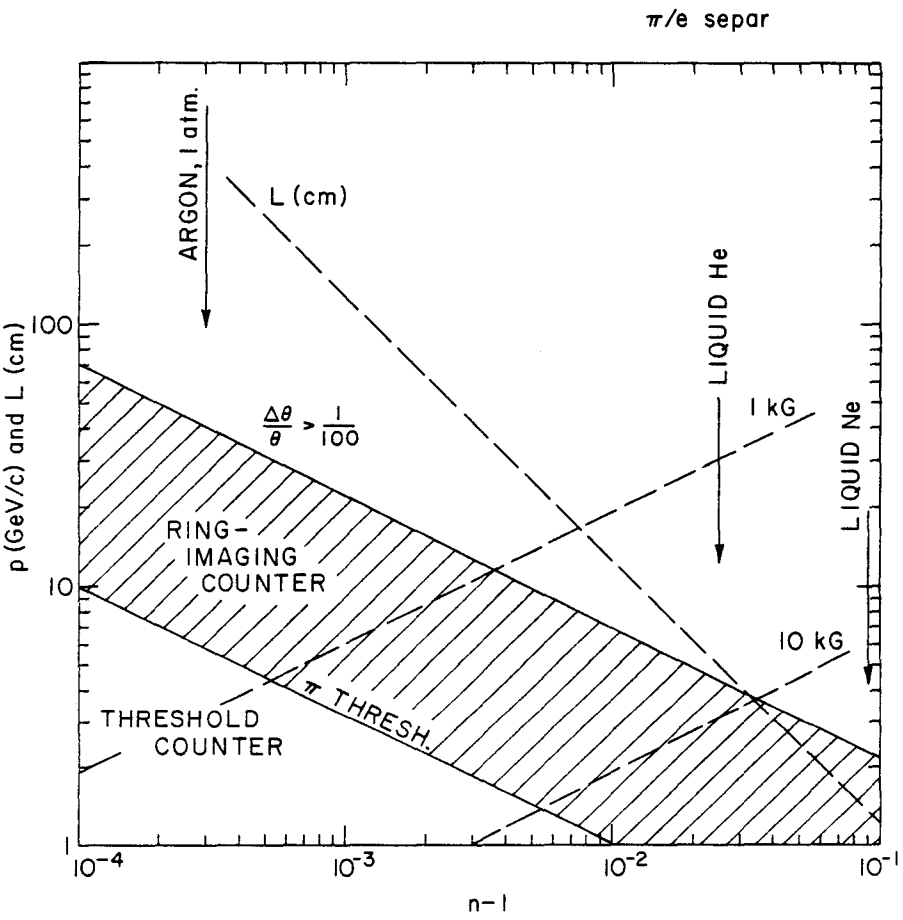
π/e separ
ARGON, 1 atm.
L (cm)
LIQUID He
1 kG
LIQUID Ne
10 kG
Δθ/θ > 1/100
RING-
IMAGING
COUNTER
π THRESH.
THRESHOLD
COUNTER
p (GeV/c) and L (cm)
100
10
1
10^-4
10^-3
10^-2
10^-1
n-1

Fig. 2b

IDENTIFICATION OF 200 GeV/c HADRONS OVER A WIDE APERTURE

Robert L. McCarthy, SUNY Stony Brook

Abstract

A CERN, Saclay, Stony Brook collaboration is constructing a wide-aperture ring-imaging Čerenkov counter for a high P_T experiment at Fermilab (E605). Prototype tests[1] indicate that our device will identify hadrons at least up to 200 GeV/c in momentum. Hence our technique is directly applicable to the forward-backward regions at ISABELLE if used in conjunction with magnetic analysis (which should ensure a low particle density in the detector).

I. THE IDENTIFICATION PROBLEM FOR E605

A CERN, Saclay, Stony Brook collaboration is constructing a wide-aperture ring-imaging Čerenkov counter in order to identify hadrons in Fermilab E605. A diagram of the experiment is shown in Figure 1. The production target is followed by a large magnet which focuses particles with P_T near 9 GeV/c (pairs with mass near 18 GeV/c) forward onto the detectors. A second magnet (kick~1 GeV/c) allows two momentum measurements (to minimize background). Since we hope to run with high intensity (3×10^{12} incident protons/second), the Čerenkov counter is placed behind the second magnet in order to obtain tolerable rates in the counter. Our counter is required to have a very wide angular acceptance ($\pm$ 60 milliradians vertically, $\pm$30 milliradians horizontally) because the counter follows a strong magnet and the experiment accepts a wide aperture (one steradian in the center of momentum). In Figure 2 we show the momenta accepted by the experiment. For single hadrons, possible momenta range from 60 GeV/c out to the kinematic limit near 300 GeV/c with measureable rates expected at least up to 250 GeV/c. The magnets eliminate low momentum particles and focus our attention only on leading hadrons. Thus, in particular, we are not attempting to identify all hadrons in a jet.

II. ČERENKOV RING IMAGING USING PHOTOIONIZATION OF TRI-ETHYL-AMINE

Development of ring-imaging Čerenkov counters has been pursued by several groups.[2] While the basic idea is old and simple, technical problems prevented the use of such detectors in previous experiments.

As is well known, Čerenkov radiation emitted at a fixed angle θ is focused into a ring in the focal plane of a spherical mirror, where the ring radius $R = f \tan \theta$ depends on the Čerenkov angle, and is thereby a measure of the particle velocity. To measure the radius with sufficient accuracy to separate hadrons at high momenta (say 200 GeV/c), a high resolution position - sensitive photon detector is needed with high quantum efficiency, and with a capability to handle high event rates. Development of multistep chambers by Charpak's group at CERN,[3] together with advances in the use of photoionizing vapors in such chambers[4,1] suggested that realization of the necessary photon-detector may be possible. Available photo-ionizing vapors require ultraviolet photons in the 1500A range (or lower), however, and this poses new challenges on the rest of the apparatus:

1. The mirror must reflect, and the window separating the radiator from the detector must transmit, these photons.

2. The radiator must be pure since most gases absorb strongly near 1500A: 0.2 ppm of O_2 is sufficient to poison the radiator.

3. Variation in the index of refraction over the accepted wavelength-range causes a spread of Čerenkov angles for a given particle and can wash out the desired separation between $\pi/K/p$. Few gases exist which have small enough dispersion near 1500A.

Our design utilizes a pure helium radiator with a multi-step photon detector. The detector utilizes tri-ethyl-amine vapor and is separated from the radiator by a calcium fluoride window. In order to gain experience with such a Čerenkov counter, we have constructed and tested a prototype.

III. PROTOTYPE TESTS - DESCRIPTION

The first tests of our prototype ring-imaging Čerenkov counter took place using an electron beam at CERN in December, 1980 and January 1981. Successful results at CERN led to a definitive and successful test at 200 GeV/c in the M1 beam at Fermilab in April and May of 1981.

Figure 3 shows our setup at Fermilab. An 8m long stinless steel vessel, 35 cm in diameter contained pure helium at 1 atmosphere. A spherical mirror (f = 8m) coated for high reflectivity in the vacuum ultraviolet formed the ring-image at the upstream end of the counter where the UV photons were detected. The detector (Figure 4) was a multistep chamber containing a calcium fluoride CaF_2) window followed by a conversion gap utilizing tri-ethyl-amine (TEA), a preamplification gap, a drift space, and a multiwire proportional chamber (MWPC).[5] In order to obtain three projections for each photon hit location, both cathode planes of the MWPC were read out (relative angle 90° - ADC each 2 mm) in addition to the anode plane (at 45° from the cathode wires). The active area of the detector was approximately 20 cm x 20 cm. The total gain of the multistep chamber was about 5×10^7. We believe that the single photo-electron efficiency was near 100%.

Detection of the ring images depended on photoionization of TEA, a process which requires photons in the range 7.5 - 8.7 eV (1400-1600A). Longer wavelength photons are below threshold for photoionization. Shorter wavelength photons are unsuitable due to increased dispersion in the radiator, as well as the lack of suitable windows to separate the radiator from the detector gas. In order to exclude dispersive photons we often added methane (CH_4) to our chamber gas (He/TEA(3%) CH_4(10%)).

To assure purity of the radiator gas, the vessel was constructed entirely of high-vacuum compatible materials, was thoroughly cleaned, evacuated to 10^{-5} Torr, and baked to 100°C before being filled with helium gas from the boil-off from a dewar of liquid helium.

To monitor the transparency of this radiator, a UV source/detector combination was also attached to the vessel, (Figure 3) with a spectrum designed to match closely that of the useful Čerenkov radiation. The source[6] consists of an alpha particle emitter in krypton. The emitter is also the cathode of an ionization chamber, whose anode is a mesh. The signal

from the anode can serve as a trigger to indicate the timing of the UV pulse, which is due to molecular processes in the krypton gas, excited by the α particle. The intensity of the light-flash can be increased by raising the voltage across the ion chamber. The krypton cell is separated from the radiator gas by another CaF_2 window. The detector is a solar-blind 15 stage photomultiplier with a CsI photocathode and CaF_2 window.

IV. PROTOTYPE TEST RESULTS

The results[1] of our prototype tests have been submitted to the IEEE 1981 Nuclear Science Symposium. In Figure 5 we show the on-line ring display resulting from summing up the hit patterns of 200 tracks. The width of this ring is largely due to the angular spread of the incident beam and can be reduced in off-line analysis through the use of our drift chambers (Figure 3). We reconstuct an average 2.5 photon hits per incident track.

Our π/K separation is shown in Figure 6. Using our drift chambers, we can reconstruct the incident particle's direction so that we measure the Čerenkov ring radius even for events with only one reconstructed photon hit. The pion rejection factor is approximately 100 to 1 for <u>each</u> photon detected. Consequently two detected photons provide unambiguous identification. Figure 6 includes all events with one or more photon hits (hence 93% of the incident tracks) and shows the number of events plotted versus the average ring radius per event.

The main problem on which we are still working is the reconstruction of the photon hit pattern from three projections. The full width at the base of a cathode photon hit is ~ typically 12 mm, roughly one-tenth of a Čerenkov ring diameter. The photon MWPC (Figure 4) was constructed with small cathode-anode gaps (3.2 mm) to minimize this width. Complex software is necessary to fully disentangle events with many photons. The software now in use shows appreciable loss of photons for events with 5 or more photon hits. Nonetheless, a track can be unambiguously identified if only two such hits are well-reconstructed; this can be accomplished with simpler software.

The roughly uniform background seen in Figure 5 is presumed due to reconstruction errors (in the simple on-line software) and random particle tracks through the photon chamber. One such background hit will perturb the average radius for a given event and generates a background of ~10 events/bin

in the wings of the distribution shown in Figure 6 (beyond the edges shown). This background is sufficient to obscure the very small $\bar{p}$ signal in our beam if we accept events with one photon hit. However, in Figure 7 we show a clean $\bar{p}$ signal from events with at least 3 photons. To obtain this plot the ring radius for each photon is calculated, then hits with a radius disagreeing with the consensus are thrown out. With similar populations of $\pi/K/p$ (expected at high p_T) K/p separation at 200 GeV/c will be easy in our detector since the K-p radius difference will be 8 mm. In the prototype test, 72% of the tracks were identified as π,K or proton without ambiguity.

V. THE E605 ČERENKOV COUNTER

After the successful test of our prototype, we are proceeding to construct the full scale counter for E605 shown in Figure 8. The radiator will be 15 m of pure helium gas at atmospheric pressure. This length is increased from the prototype so that we expect more photons/track and may use the counter as a threshold device in order to identify protons below 110 GeV/c momentum (proton threshold in helium). The mirror will cover 2.6 x 2.5 m^2, probably in 16 rectangular segments as shown in Figure 9. Each segment will consist of 3/4 inch thick pyrex ground to form a concave spherical surface with a focal length of 8 m. The segments will be coated with aluminum and magnesium fluoride in high vacuum in a manner assuring good reflectance ($\geq$ 80%) at 1500A. Our requirement on figure accuracy is that the blur circle at the focal plane be less than 0.7 mm diameter from any 14 cm diameter area of the mirror (Cerenkov footprint of one particle).

The mirrors will focus Čerenkov photons onto two detectors outside the particle aperture. Each detector is a multistep PWC (as in the prototype) with an active area of 40 cm x 80 cm. The calcium fluoride windows will be built using a mosaic of 10 cm x 10 cm crystals.

VI. GAS PURITY

A schematic diagram of our gas purification system is shown in Figure 10. We will not be able to evacuate our large counter (unlike the prototype) and hence must purge it to attain the required purity. Since our essential goal is to eliminate oxygen, we purge first with nitrogen (about 8 volume changes) before purging with pure helium (from the liquid). Once the required purity

is obtained we hope to maintain it using a circulation-purification system based on the catalytic conversion of oxygen, and a small amount of hydrogen added to the gas stream, to water. Water vapor and other contaminants are then removed with a molecular sieve. Two parallel moecular-sieve stages are to be built, so one may be regenerated while the other one is in service. The purifier will have a capacity of ~50 m^3/hour.

A particular problem which is still under study is the permeation of tri-ethyl-amine (TEA) through our calcium fluoride window. It is often convenient to hold the CaF_2 crystals in a frame using a soft glue. Many such glues are permeated by TEA even though they are helium tight. We have overcome this problem in the past using mylar tape. A satisfatory long-term solution is still being sought.

Walls of the vessel will be (high-vacuum) welded together from thin aluminum sheet. Thin aluminum windows (0.03 inch) will cover the upstream end of the counter where scattering is particularly detrimental to our mass resolution.

The vessel walls will be tack-welded to a strong external aluminum frame. The mirror mount structure will be bolted to the inner wall but in close proximity to pieces of the external frame.

We anticipate thermally insulating the entire counter in order to avoid spatial variations in the index of refraction due to temperature gradients. Temperature and pressure will be monitored at several locations in the detector volume.

VII. SPHERICAL ABERRATIONS

At first sight the problems caused by spherical aberrations appear devastating. In order to study the problem (and determine the sizes of the detectors) we tracked Monte Carlo events through the apparatus. The events were generated using Drell-Yan dimuon production kinematics. (This is probably a good guess for the production kinematics of dihadrons in our region of interest where each hadron possesses most of the momentum of its parent quark. We do not expect variations in the production kinematics to be important. Ring radii were constructed using the particle trajectory in order to determine the ring center. Using the measured photon hit location to

determine the photon's azimuthal emission angle, photon hit locations were caclcuated using the three mass-hypotheses $\pi/K/p$. These hypothesized photons were emitted from the center of the particle's trajectory in the Čerenkov tank and at the median photon energy expected from the parent particle. This same analysis procedure can be used with actual data. In particular we never require that the detected photons actually form a circle in the detector plane and measure only the difference between actual and hypothesized radii. Large, but predictable distortions from this circle occur and they are similar for $\pi/K/p$. Using this analysis procedure we eliminate correctable spherical aberrations and find that the remaining spherical aberrations are tolerable with f = 8 m.

In Figures 11 and 12 we show how the focal length of our counter was determined. In Figure 11 we plot the pion ring radius and the RMS ring radius resolution from dispersion and uncorrectable spherical aberrations as a function of mirror focal length, assuming a 15 m counter length (available space) and using detectors placed outside the aperture. In Figure 12 we show the πK separation at 300 GeV/c (units of σ from dispersion and uncorrectable aberrations only) and required detector size also as a function of focal length. At f = 8 m we obtain near optimum separation (ensuring that our resolution is not dominated by aberrations) with a tolerable detector size.

VIII. COSTS

The anticipated costs of our counter are summarized below:

Item	Cost (thousands of dollars)
Amplifiers	60
ADC	100
Multistep PWC	100
CaF_2 windows	60
Mirrors	70
Vessel (including mirror and purification system)	60
	450

We are attempting to complete this counter by March 1982.

References

1. G. Contrakon, M. Cribier, J.R. Hubbard, Ph. Mangeot, J. Mullie, J. Tichit, CEN Saclay; R. Bouclier, A. Breskin, G. Charpak, J. Million, A. Peisert, J.C. Santiard, F. Sauli, CERN; C.N. Brown Fermilab; D. Finley, H. Glass, J. Kirz, R.L. McCarthy, SUNY Stony Brook, Identification of 200 GeV/c Particles Using a Ring Imaging Cerenkov Detector, submitted to the IEEE 1981 Nuclear Science Symposium, San Francisco, Oct. 21-23, 1981.

2. See for example:
J. Chapman et. al., N.I.M. 158, 387 (1979)
R.S. Gilmore et. al., N.I.M. 157, 507 (1978)
G. Charpak et. al., N.I.M. 164, 419 (1979)
T. Ekelof et. al., CERN - EP/80-115.

3. A. Breskin et. al., N.I.M. 161, 19 (1979).

4. J. Seguinot et. al., N.I.M. 173, 283 (1980).

5. J.R. Hubbard et. al., N.I.M. 176, 233 (1980).

6. This design is due to F. Sauli.

FIGURE CAPTIONS

Figure 1. Fermilab experiment 605.

Figure 2. The region accepted by E605 in the p_T, p_L plane is shown cross-latched.

Figure 3. Prototype test setup in the 200 GeV/c negative M1 beam at Fermilab.

Figure 4. The prototype photon detector, a multistep MWPC.

Figure 5. The Čerenkov ring image accumulated in the on-line display from 200 tracks.

Figure 6. The π/K separation observed with our prototype counter. We plot the number of events observed with one or more photons at a given average ring radius.

Figure 7. The number of events observed with three or more phototons is plotted versus average ring radius. In this plot hits disagreeing with the consensus ring radius are excluded.

Figure 8. Diagram of the E605 Cerenkov counter.

Figure 9. A possible mirror configuration showing 16 rectangular segments.

Figure 10. Simplified diagram of the circulation-purification system.

Figure 11. The average pion ring radius (in cm) expected in E605 and RMS ring radius resolution (due to dispersion and aberrations only) are plotted versus Cerenkov mirror focal length. Radius resolution due to aberrations only (obtained by emitting photons at the average energy) is also plotted but becomes unreliable at low values of δr because of the finite bin size used in the Monte Carlo.

Figure 12. ΔX and ΔY, required photon chamber horizontal and vertical half-size, are plotted (in units of 10 cm) versus Cerenkov mirror focal length. These sizes are sufficient for 99% acceptance of photons from mass = 20 GeV dimuons. We also plot $(\Delta r/\delta r)$ the π/K separation at 300 GeV/c in units of RMS resolution due to dispersion and aberrations alone. The choice of f = 8m provides tolerable chamber size, but ensures that spherical aberrations will not dominate our radius resolution.

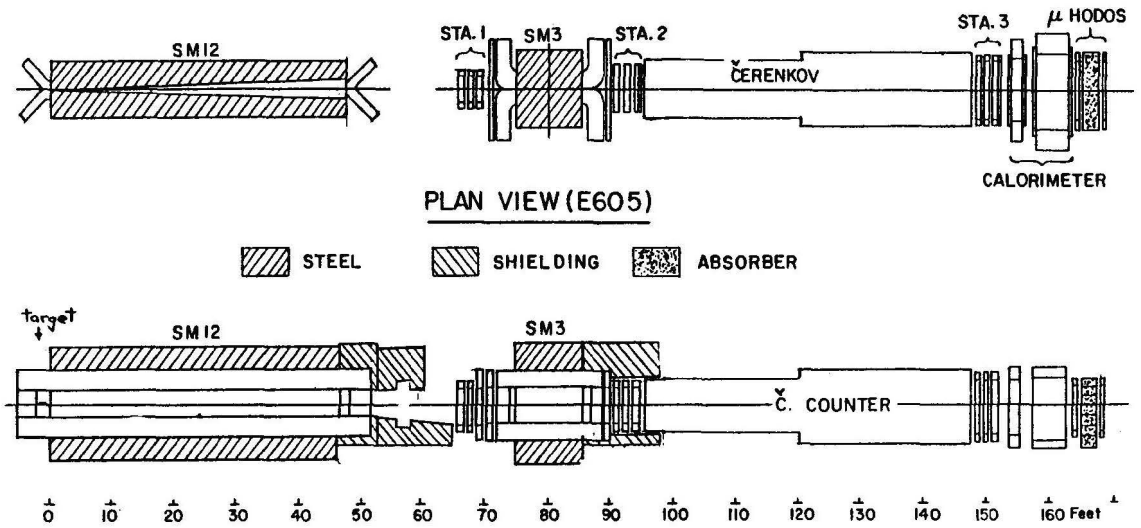
SM12
STA. 1
SM3
STA. 2
ČERENKOV
STA. 3
μ HODOS
CALORIMETER
PLAN VIEW (E605)
STEEL
SHIELDING
ABSORBER
target
SM12
SM3
C. COUNTER
0
10
20
30
40
50
60
70
80
90
100
110
120
130
140
150
160 Feet
ELEVATION (SECTION) E605

Fig. 1

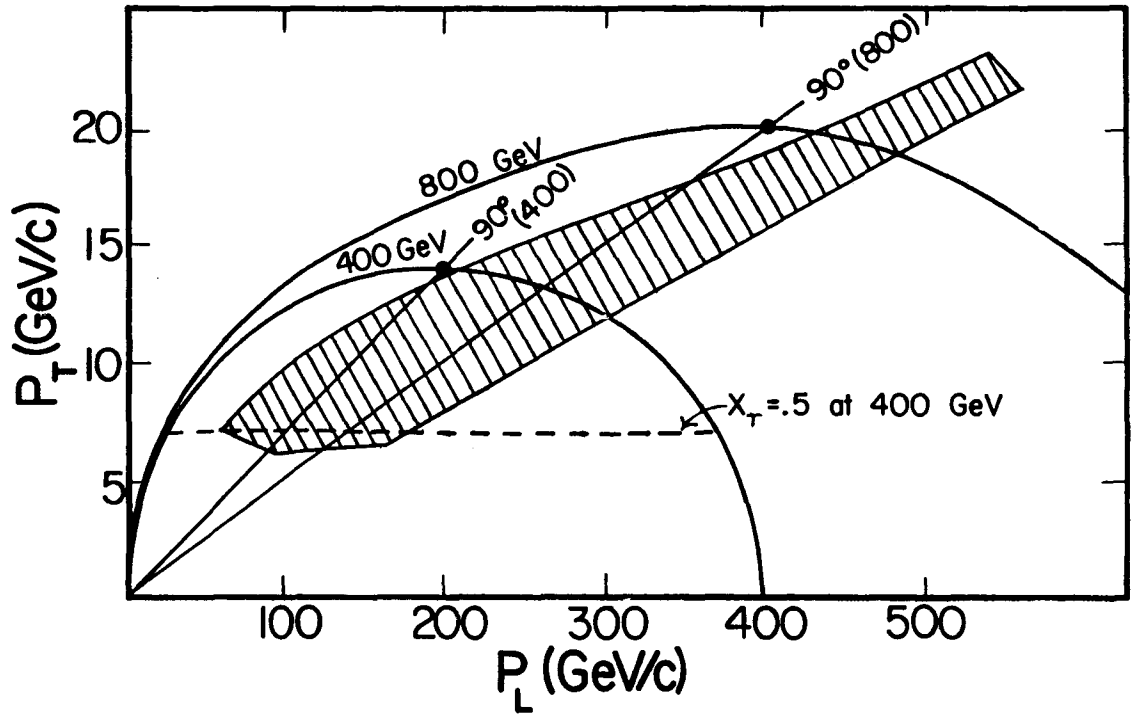
90° (800)
800 GeV
400 GeV
90° (400)
X_T=.5 at 400 GeV
P_T (GeV/c)
P_L (GeV/c)
20
15
10
5
100
200
300
400
500

Fig. 2

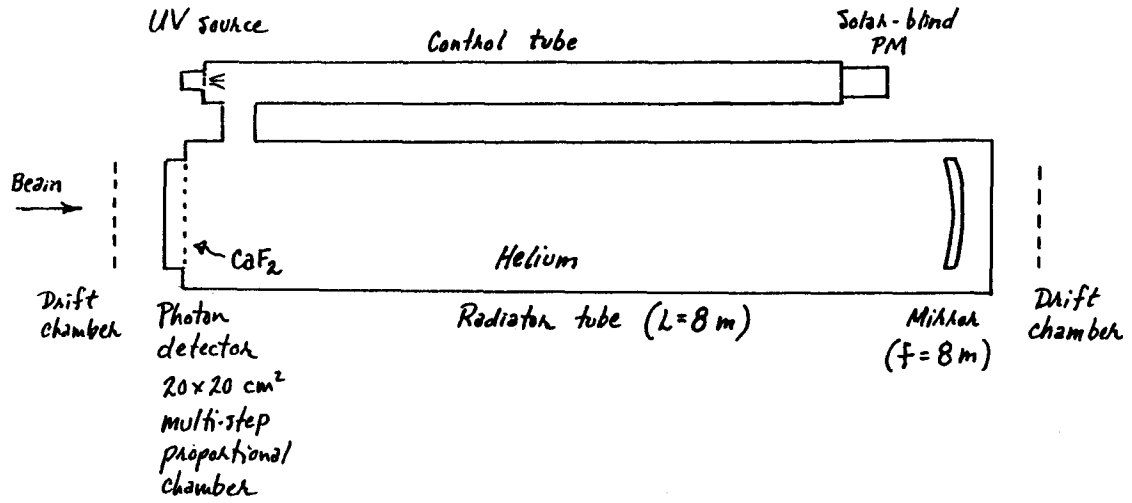
UV source
Control tube
Solar-blind PM
Beam
CaF_2
Helium
Drift chamber
Photon detector
20×20 cm² multi-step proportional chamber
Radiator tube (L=8 m)
Mirror (f=8 m)
Drift chamber

Fig. 3

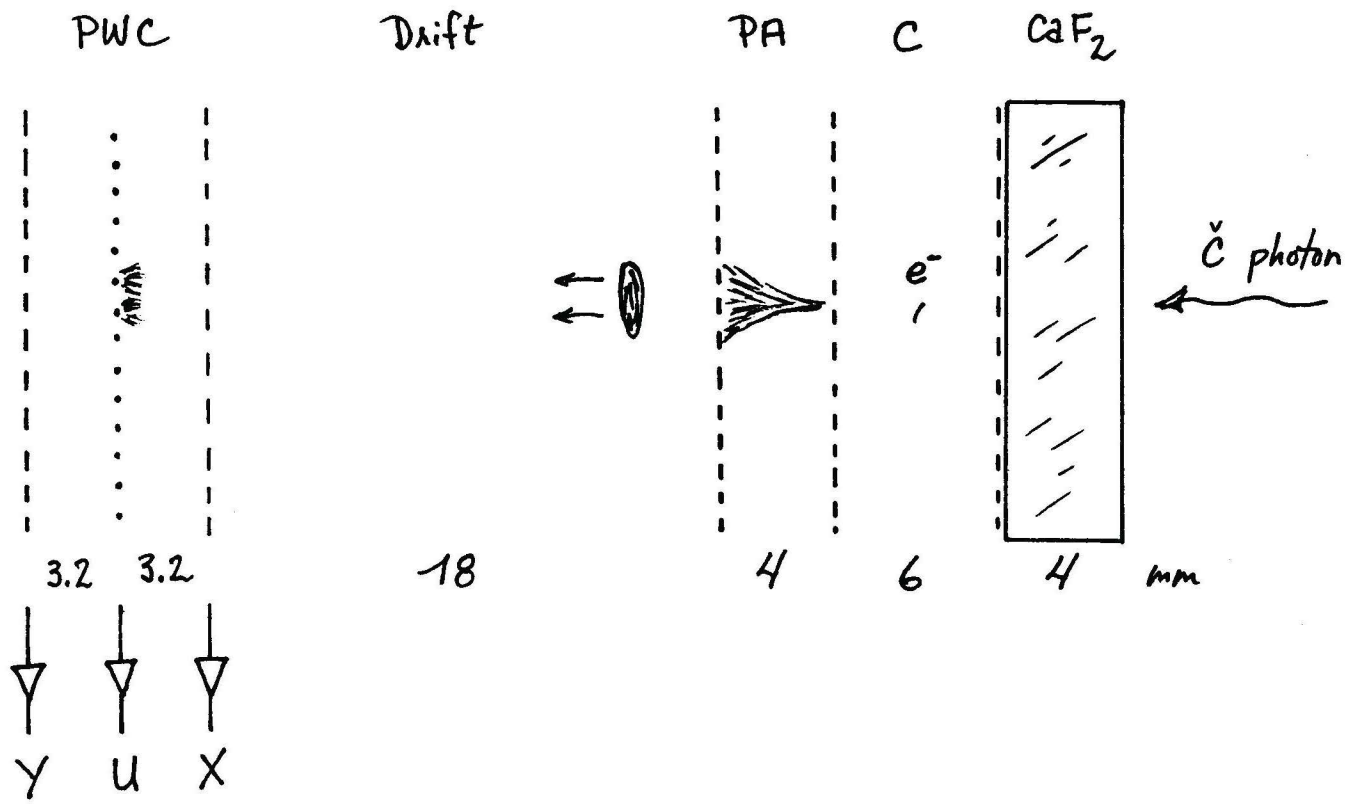

Fig. 4

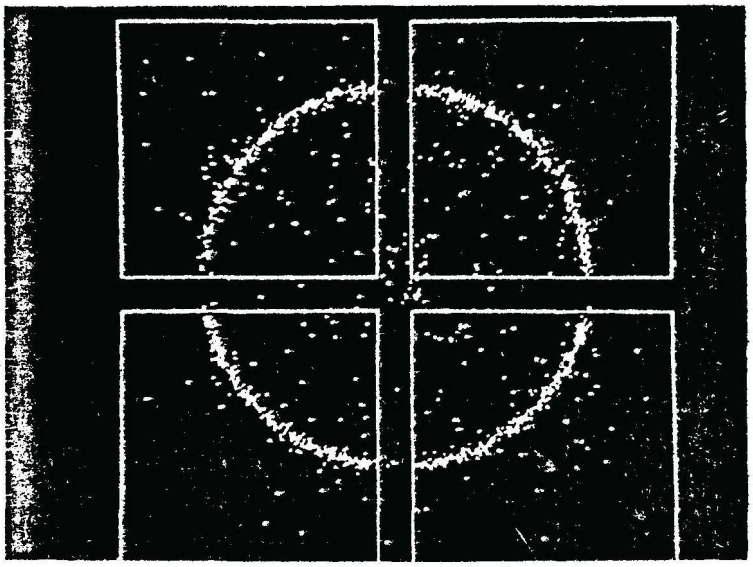

Fig. 5

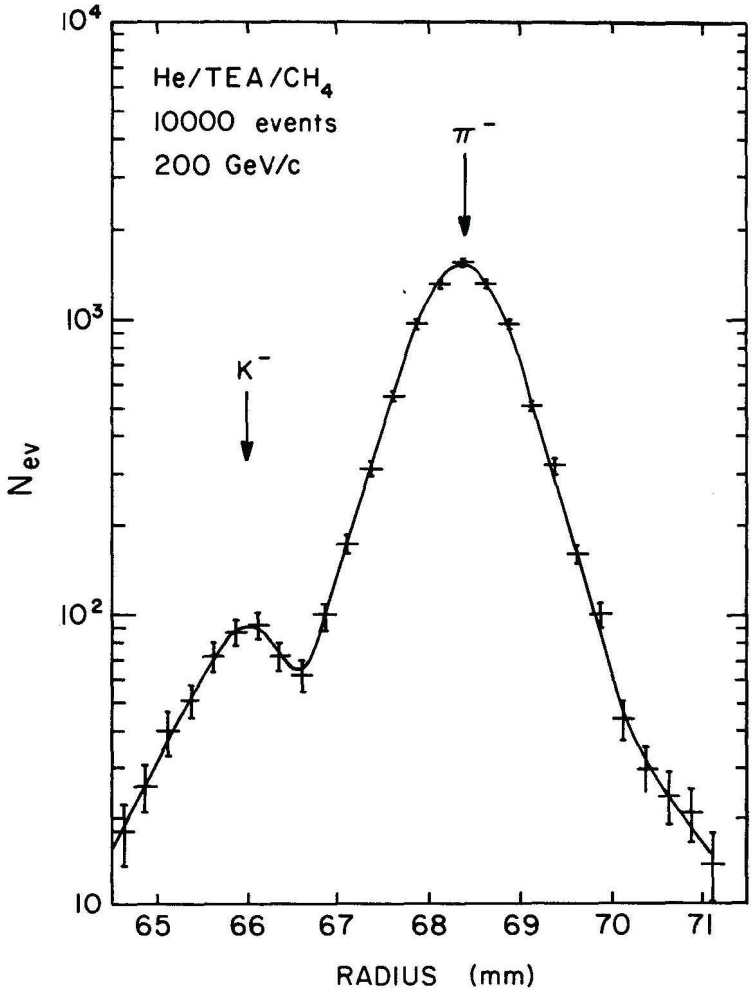
He/TEA/CH4
10000 events
200 GeV/c
π⁻
K⁻
Nev
10⁴
10³
10²
10
65
66
67
68
69
70
71
RADIUS (mm)

Fig. 6

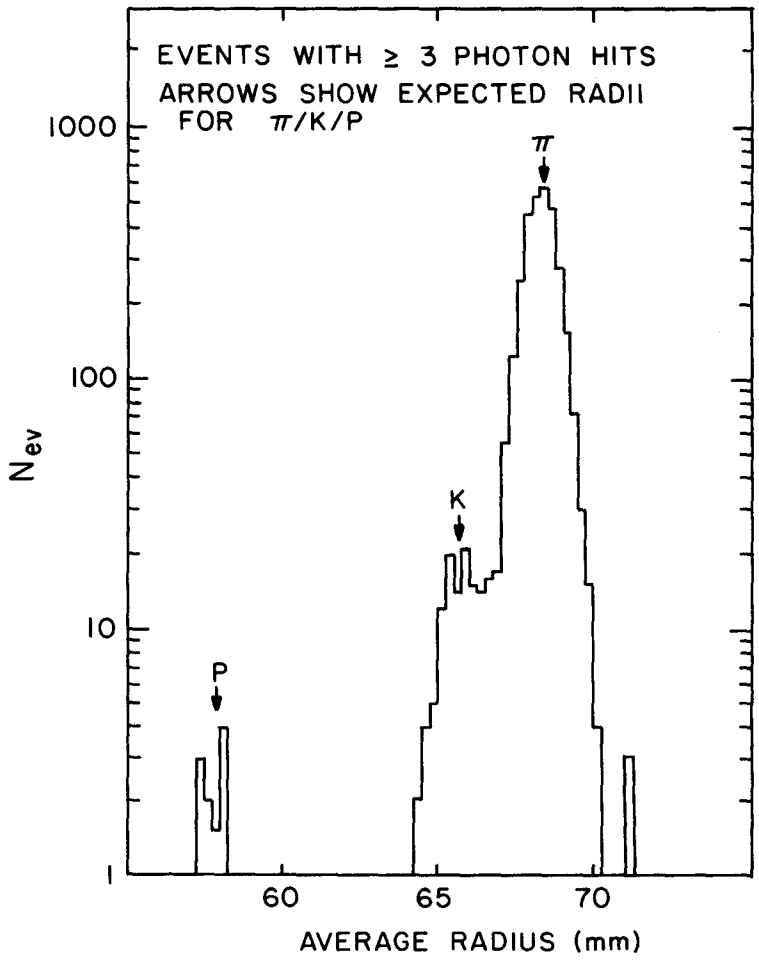
EVENTS WITH ≥ 3 PHOTON HITS
ARROWS SHOW EXPECTED RADII
FOR π/K/P
1000
100
10
1
N_ev
π
K
P
60
65
70
AVERAGE RADIUS (mm)

Fig. 7

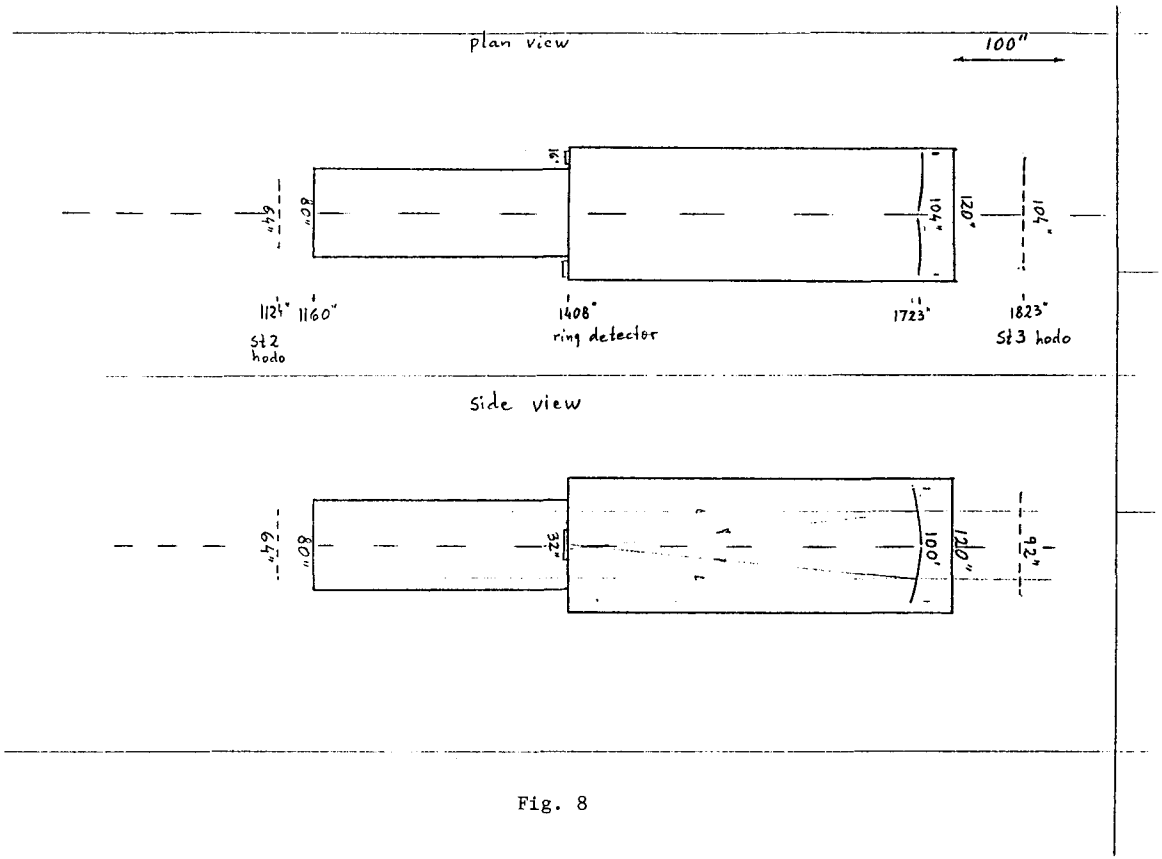
plan view
100"
80"
64"
104"
120"
104"
1121"
1160"
1408"
1723"
1823"
St2 hodo
ring detector
St3 hodo
Side view
80"
64"
32"
100"
120"
92"

Fig. 8

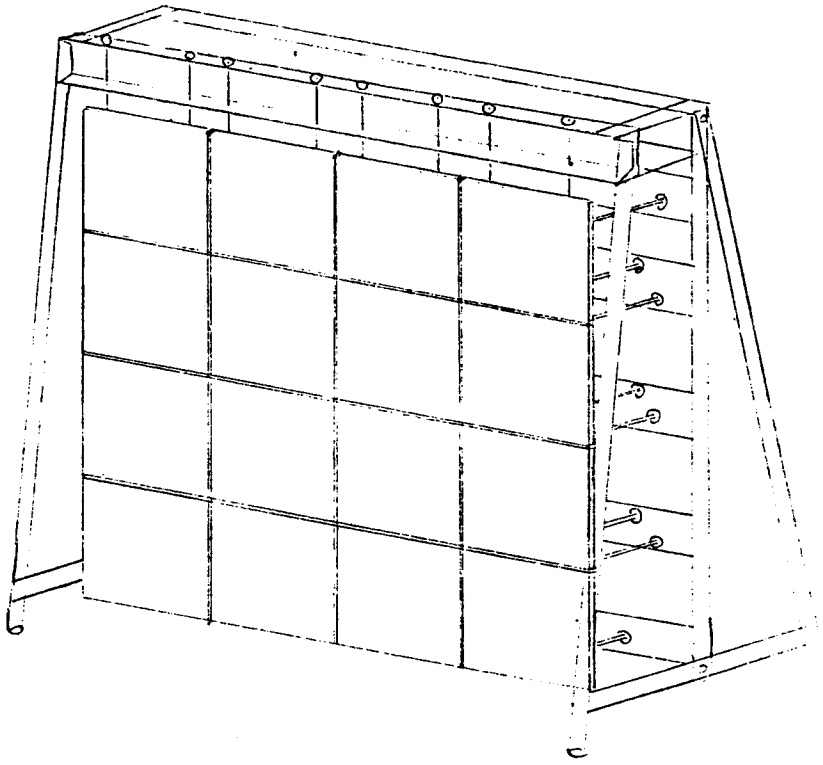

Fig. 9

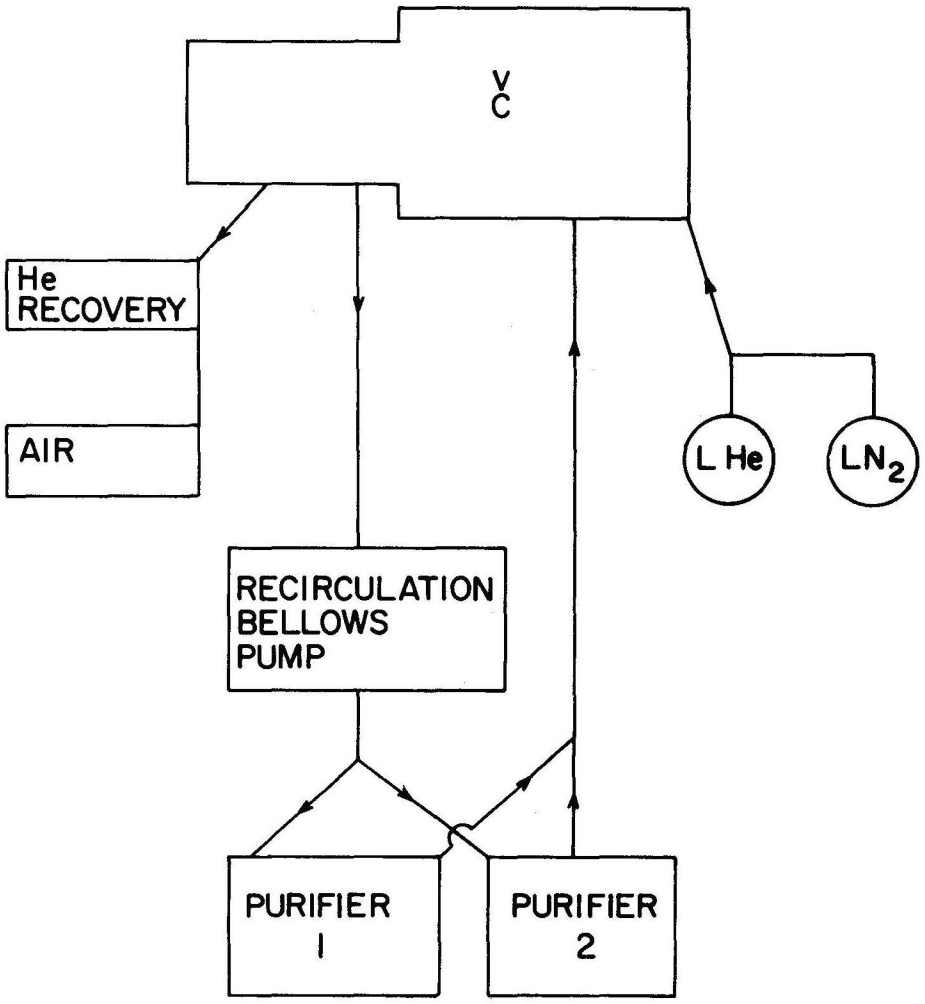
VC
He
RECOVERY
AIR
L He
LN2
RECIRCULATION
BELLOWS
PUMP
PURIFIER
1
PURIFIER
2

Fig. 10

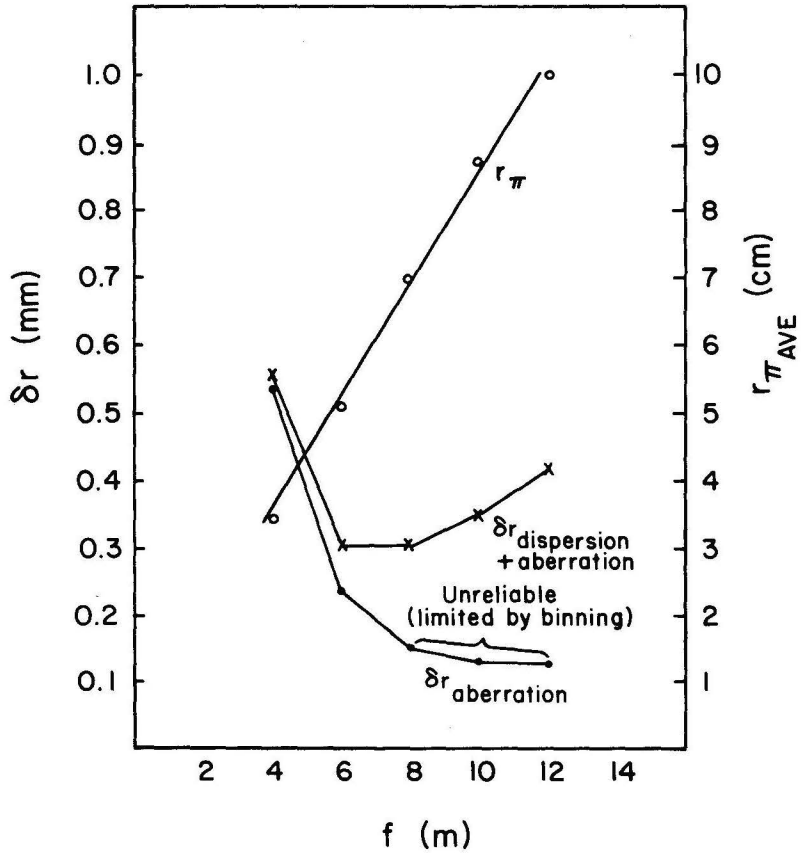
1.0
0.9
0.8
0.7
0.6
0.5
0.4
0.3
0.2
0.1
δr (mm)
10
9
8
7
6
5
4
3
2
1
$r_{\pi_{AVE}}$ (cm)
r_π
$\delta r_{dispersion + aberration}$
Unreliable
(limited by binning)
$\delta r_{aberration}$
2
4
6
8
10
12
14
f (m)

Fig. 11

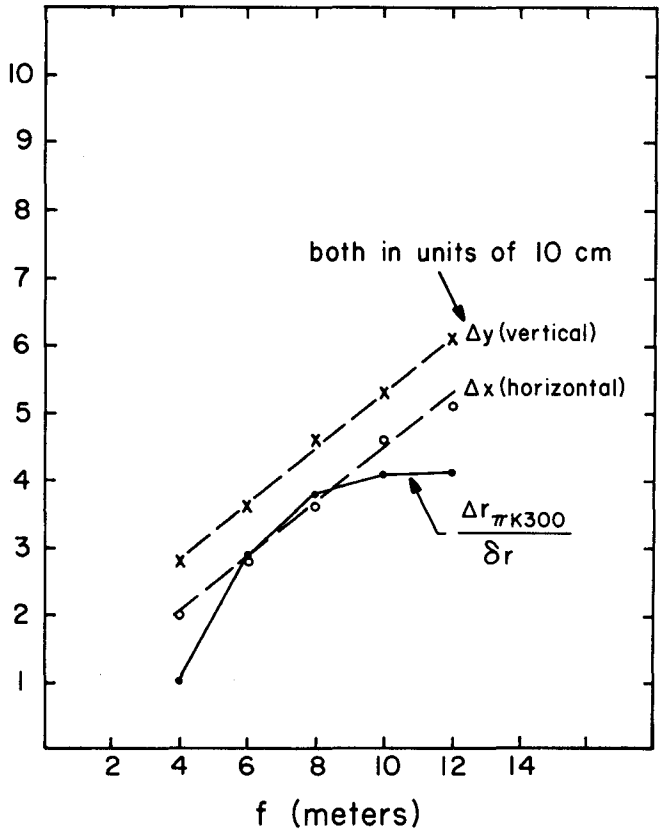
10
9
8
7
6
5
4
3
2
1
2
4
6
8
10
12
14
f (meters)
both in units of 10 cm
Δy (vertical)
Δx (horizontal)
Δr πK300 / δr

Fig. 12

TESTS OF THE RING IMAGING CHERENKOV DRIFT DETECTOR

E. Barrelet, J. Seguinot, M. Urban, T. Ypsilantis - Ecole Polytechnique, Paris, France
T. Ekelof - Cern
B. Lund-Jensen - University of Uppsala, Uppsala, Sweden
J. Tocqueville - College de Frande, Paris, France

A ring imaging drift detector, shown in Figure 1, has been tested recently on a 6-20 GeV/c π^- beam at the CERN PS. It is constructed as shown in Figure 1 with a CaF_2 entrance window between the Argon radiator gas and the drift volume. The drift volume was 15 mm thick in the case the filling gas was CH_4 + TEA (5 Torr) and was 45 mm thick when the filling gas was CH_4 + TMAE (1 Torr). In both cases a second window was added with field shaping wires on both sides of the second window in order to make a more uniform drift field in the photon conversion gap. With the photoionizing gas TEA the second window as a 5 mm thick 127 mm diameter CaF_2 single crystal whereas with TMAE the second window was a 5 mm thick 127 mm diameter fused quartz (Corning 7940). The drift field could be varied up to 1.5 KV/cm over the drift length of 15 cm. Single photoelectrons, produced by Cherenkov photons imaged onto the detector surface, drift to a picket fence of short 6 cm PC wires placed at the end of the drift gap. Full-unique determination of the conversion point was obtained by measuring the drift time of the electron to the wire (x) and the wire coordinate (y). The wire spacing in the TEA measurements was 2.54 mm giving a σ_y = 733 μ and the time binning in the x direction was 4 ns, which with a drift velocity of 10cm/ns gave σ_x = 115 μ. Longitudinal diffusion of electrons increase the σ_x to a value of σ_x = 685 μ for an average drift distance of 7.5 cm hence the resolution in the two different directions is about the same. For the TMAE measurements the wire spacing was 1.27 mm leading to a σ_y = 360 μ which probably is dominated by transverse diffusion (i.e., σ_y = 685 μ for 7.5 cm drift). The detector is also sensitive to the track of the charged particle as it passes through the detector on its way into the radiator volume. This gives rise to a large pulse (∿ 100 electrons) which all drift onto one or two wires. Upper level discrimination can distinguish between single photoelectrons and the swarm of dE/dx electrons. In these tests the impact point of the particle was outside of the drift volume as

shown in Figure 2 where an impact parameter of 16 cm is shown. This impact parameter $x = 16cm/R_m = .08$, where $R_m = 200$ cm is the mirror radius, causes the ring image to have an eccentricity of about 2.5%[1] which limits the resolution if a fit of the ring image is made to a simple circle.

As shown in Figure 2 the radiator length was L = 187 cm of Argon at 1.13 bar which corresponds to a γ threshold of 35 for Cherenkov radiation. The photon images obtained with TEA are shown in Figures 3 and 4 for single pions at 14.4 GeV/c. The average number of photoelectrons N observed was 7.5 which with the observed Cherenkov angle of 28.3 mr, radiator length L = 187 cm and second crystal transmission $T_z = .67$ (at 8.5 ev photon energy) gives the result

$$N_o = \frac{N}{L\sin^2\theta} \times \frac{1}{T_2} = 75 \text{ cm}^{-1}$$

This value is surprisingly high if one considers the loss of photons above 8.7 ev due to methane absorption (see Figure 5). The corresponding quantum efficiency of TMAE and absorption in fused quartz (shown in Figure 6) indicate that an $N_o = 125$ cm^{-1} can be expected for TMAE. The experiment gave N = 5.5 photoelectrons for a 10 GeV/c π beam with Cherenkov angle observed of 22 mr. Taking $T_2 = .75$ for quartz we find $N_o = 81$ cm^{-1} for TMAE which is less than the expected value of 125 cm^{-1}, which are based on laboratory measurements with a monochromator. We expect that technical improvements of the uniformity of the drift gap as well as improved quenching of the PC using CO_2 or Isobutane added to the gas (10-30%) will improve the value of N_o in this case. The addition of these gases is possible because they are as transparent as quartz as shown in Figure 7. CO_2 and Isobutane also may help because they "cool" the drifting electrons which may result in reduced transverse and longitudinal diffusion[2] as shown in Figure 8. The diffusion coefficient for Isobutane is thought to be 120 $\mu/\text{cm}^{1/2}$ whereas CH_4 is 280 $\mu/\text{cm}^{1/2}$ and CO_2 is 80 $\mu/\text{cm}^{1/2}$ at drift fields of about 1 kv/cm which is our range of operation (.2 kv/cm up to 1.5 kv/cm).

The detector was initially checked by orienting the drift gap parallel to the field shaping wires so that a minimum ionizing particle produced about 5.5 primary electrons per 2.54 mm PC cell in Argon + 20 Torr TEA. These ionization electrons drift to the PC cell and are detected and timed. A

straight line track was reconstructed as shown in Figure 9 which gave a fit with σ_T = 4 ns when the MTD bins were 4 ns wide. From the inefficiency for counting on each wire for 1000 events we were able to establish an average number of electrons collected by each wire as 5.5 indicating full collection and detection of the primary dE/dx electrons. By varying the detector position the collection versus drift distance was established to be flat over 15 cm of drift and in addition no significant loss in the fit of the straight line was observed for drift times up to 2 μs. These measurements are shown in Figure 10. The drift velocity in CH_4 + 5 Torr TEA is shown in Figure 11. The measurements with CH_4 + 1 Torr TMAE indicate a saturated drift velocity of 9.6 cm/μs at E > .6 kv/cm.

The images obtained (such as Figs. 3 and 4) were fit to circles and the histogram of fitted radii is shown in Figure 12. The fitted radius has $\Delta R/R$ = 3% and the fitted x and y centers are consistent with the scintillator trigger S_1S_2 (5 mm diameter separated by 3 meters, $\Delta\theta_{beam}$ = 1.2 mr). The position of the μ's in the beam is indicated and are not quite resolved because of the above-mentioned loss of a factor of 2 in resolution due to large impact parameter. An energy scan was undertaken with the results shown in Figure 13 and is in complete accord with theory. Finally a run at 6.2 GeV/c showed a definite π peak and an electron peak. This is shown in Figure 14 which exhibits πe separation for which the equivalent Kπ Cherenkov angles corresponds to p = 22 GeV/c.

REFERENCES

1. T. Ypsilantis, Physica Scripta 23, 371 (1981).
2. V. Palladino & B. Sadoulet, NIM 128, 323 (1975).

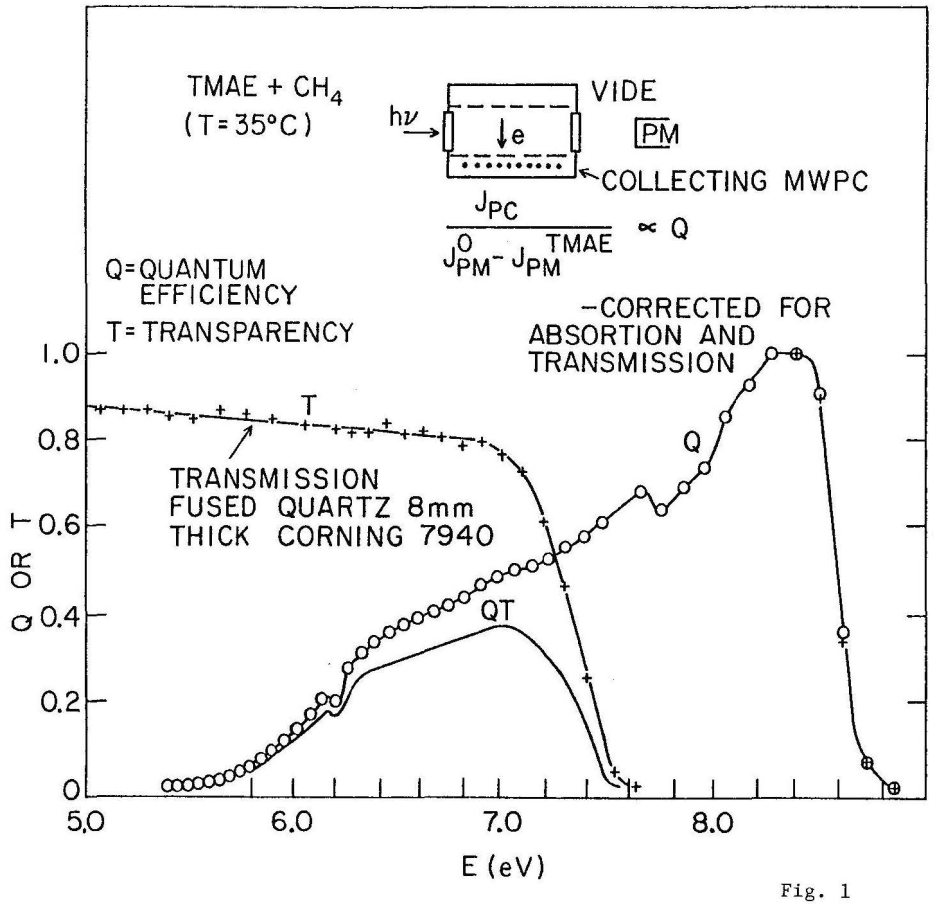
TMAE + CH_4
(T = 35°C)
hν
e
VIDE
PM
COLLECTING MWPC
$\frac{J_{PC}}{J^{0}_{PM} - J^{TMAE}_{PM}} \propto Q$
Q=QUANTUM EFFICIENCY
T= TRANSPARENCY
-CORRECTED FOR ABSORTION AND TRANSMISSION
T
Q
QT
TRANSMISSION FUSED QUARTZ 8mm THICK CORNING 7940
Q OR T
1.0
0.8
0.6
0.4
0.2
0
5.0
6.0
7.0
8.0
E (eV)

Fig. 1

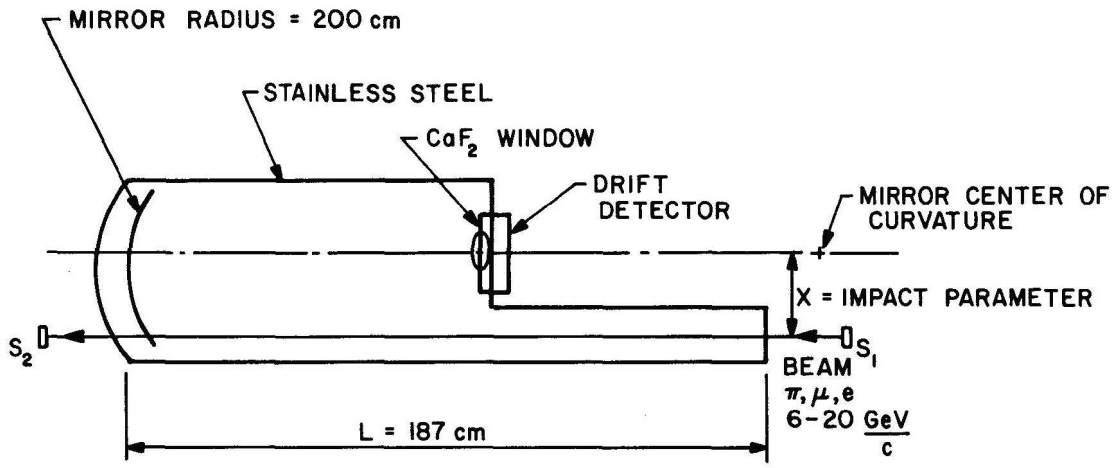
MIRROR RADIUS = 200 cm
STAINLESS STEEL
CaF_2 WINDOW
DRIFT DETECTOR
MIRROR CENTER OF CURVATURE
X = IMPACT PARAMETER
S_2
S_1
BEAM
π, μ, e
6-20 $\frac{GeV}{c}$
L = 187 cm

Fig. 2

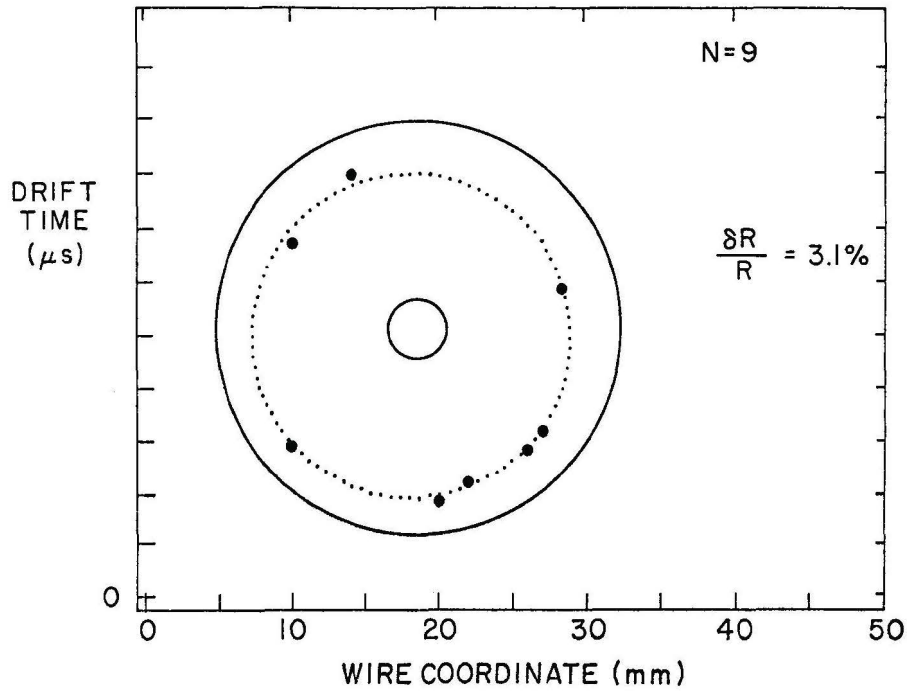

Fig. 3

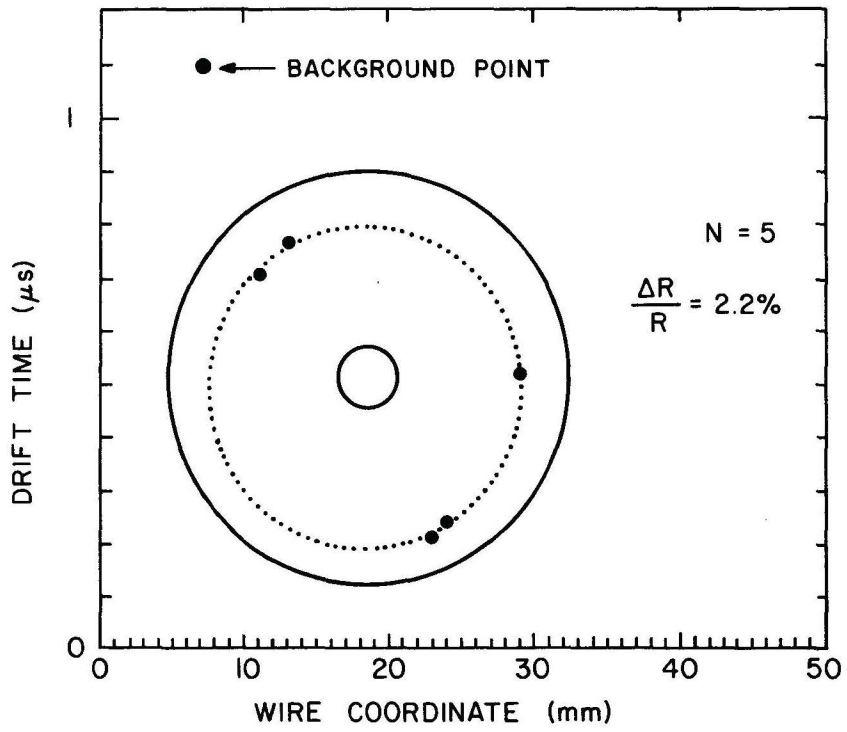
BACKGROUND POINT
N = 5
ΔR/R = 2.2%
DRIFT TIME (μs)
1
0
0
10
20
30
40
50
WIRE COORDINATE (mm)

Fig. 4

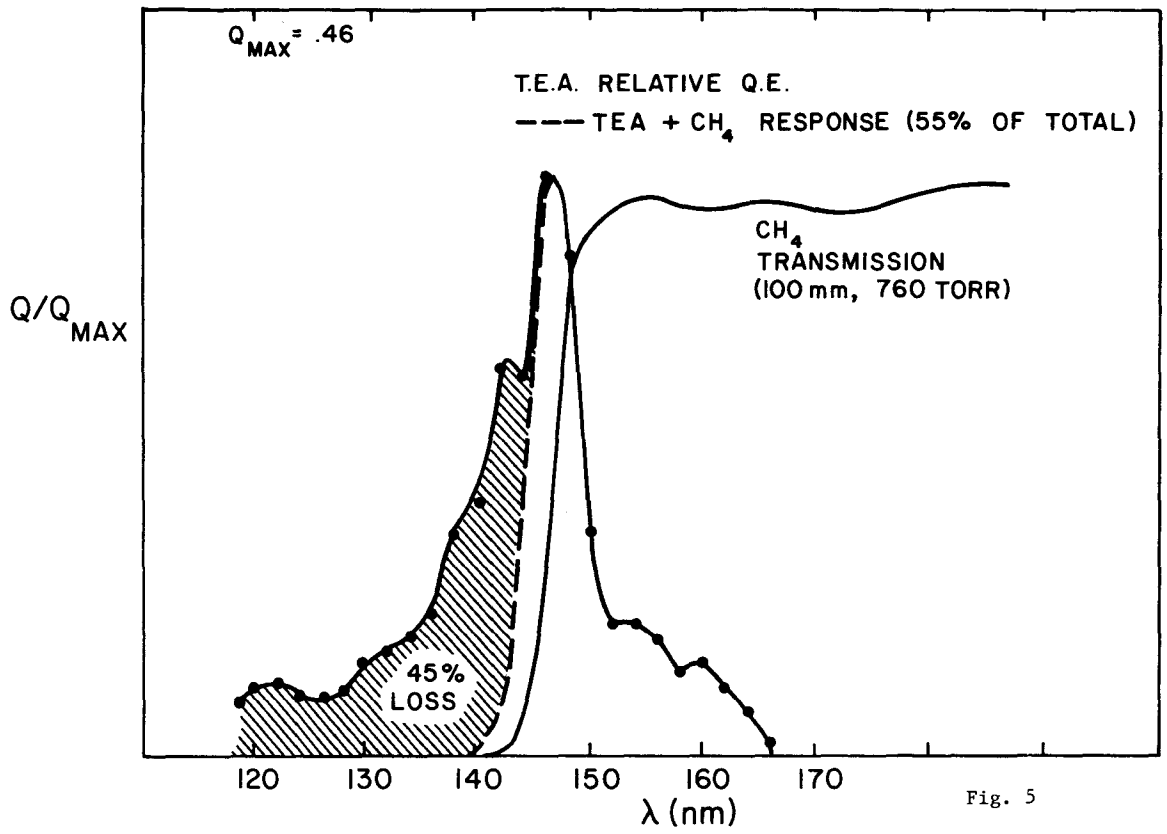
Q_{MAX} = .46
T.E.A. RELATIVE Q.E.
--- TEA + CH_4 RESPONSE (55% OF TOTAL)
CH_4
TRANSMISSION
(100 mm, 760 TORR)
Q/Q_{MAX}
45%
LOSS
120
130
140
150
160
170
λ (nm)

Fig. 5

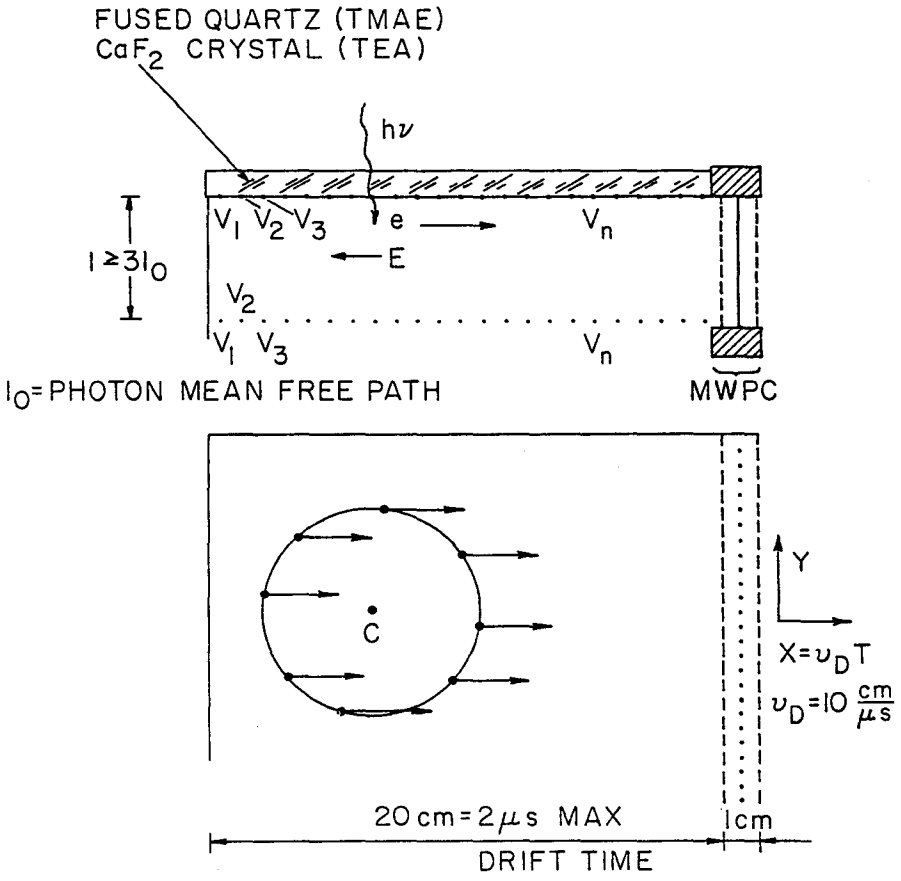
FUSED QUARTZ (TMAE)
CaF2 CRYSTAL (TEA)
hν
V1 V2 V3
e
Vn
E
l ≥ 3l0
V2
V1 V3
Vn
l0 = PHOTON MEAN FREE PATH
MWPC
C
Y
X = υD T
υD = 10 cm/μs
20 cm = 2 μs MAX
DRIFT TIME
1 cm

Fig. 6

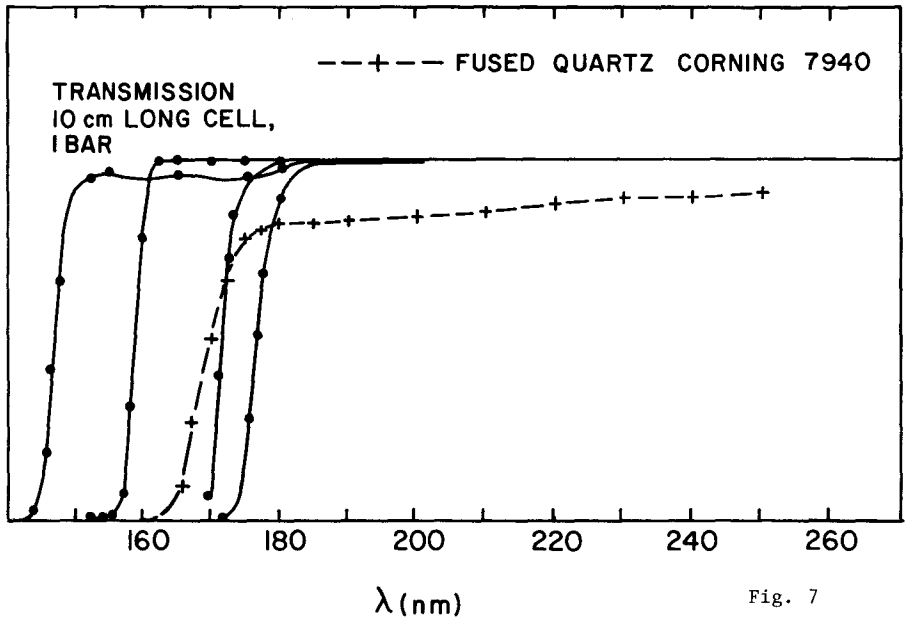
FUSED QUARTZ CORNING 7940
TRANSMISSION
10 cm LONG CELL,
1 BAR
160
180
200
220
240
260
λ(nm)

Fig. 7

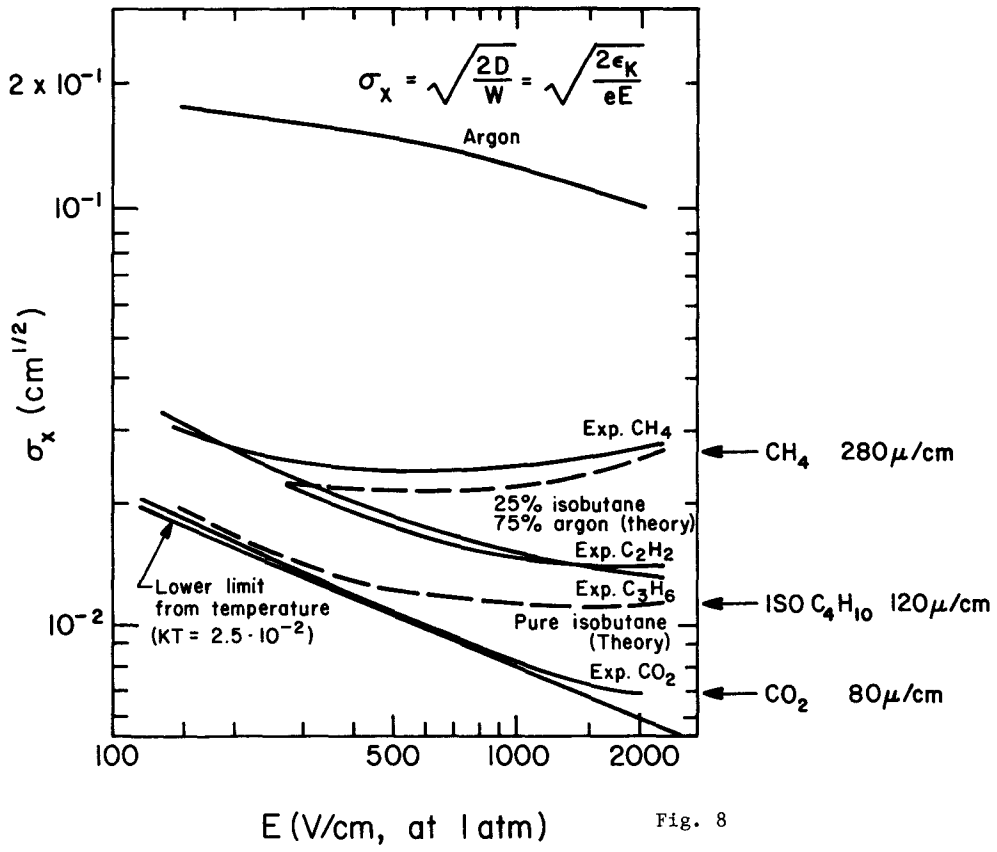
$\sigma_x = \sqrt{\frac{2D}{W}} = \sqrt{\frac{2\epsilon_K}{eE}}$
Argon
Exp. CH_4
25% isobutane
75% argon (theory)
Exp. C_2H_2
Exp. C_3H_6
Pure isobutane
(Theory)
Exp. CO_2
Lower limit
from temperature
(KT = $2.5 \cdot 10^{-2}$)
CH_4 280μ/cm
ISO C_4H_{10} 120μ/cm
CO_2 80μ/cm
σ_x ($cm^{1/2}$)
2×10^{-1}
10^{-1}
10^{-2}
100
500
1000
2000
E (V/cm, at 1 atm)

Fig. 8

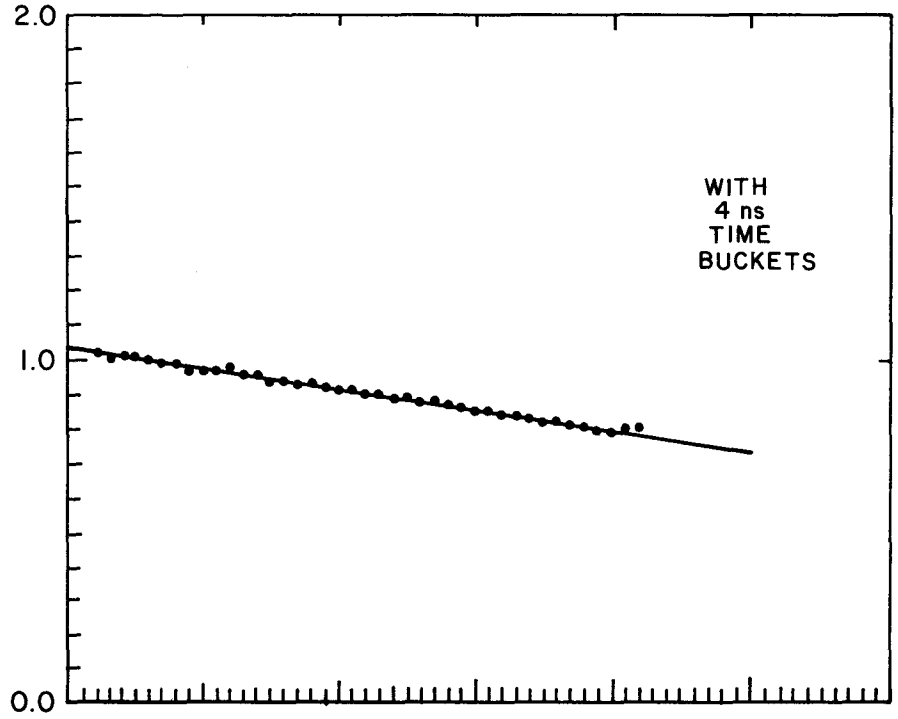

Fig. 9

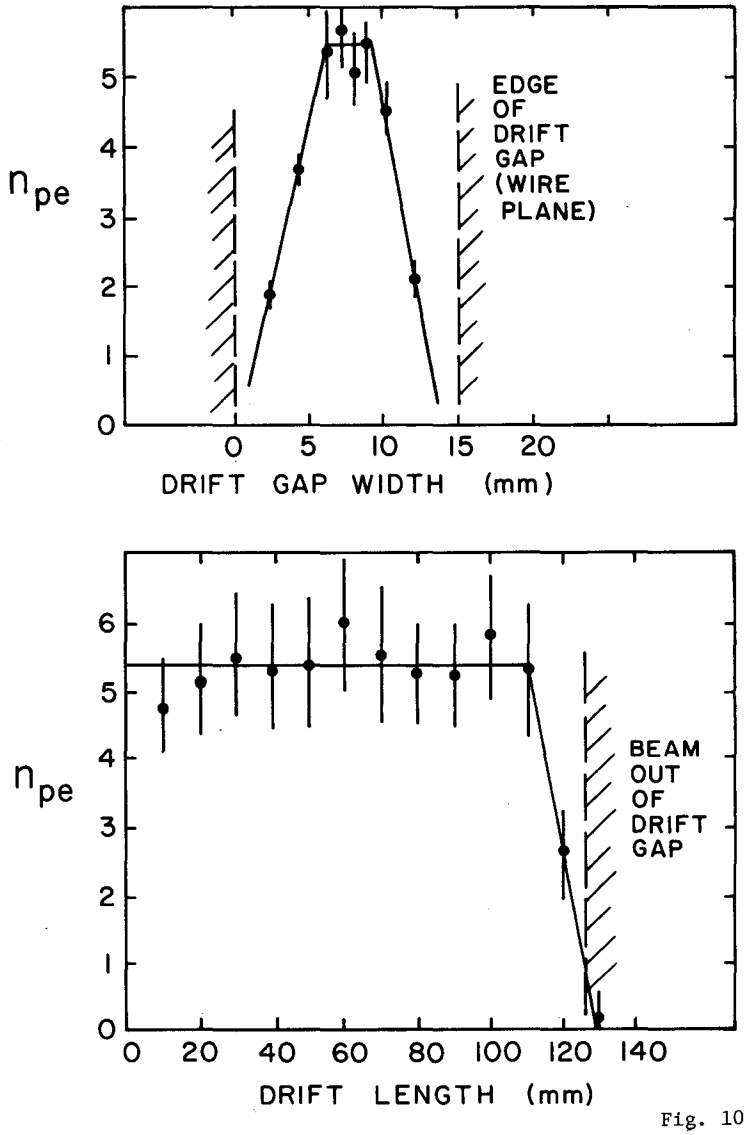
n_{pe}
EDGE
OF
DRIFT
GAP
(WIRE
PLANE)
0 5 10 15 20
DRIFT GAP WIDTH (mm)
n_{pe}
BEAM
OUT
OF
DRIFT
GAP
0 20 40 60 80 100 120 140
DRIFT LENGTH (mm)

Fig. 10

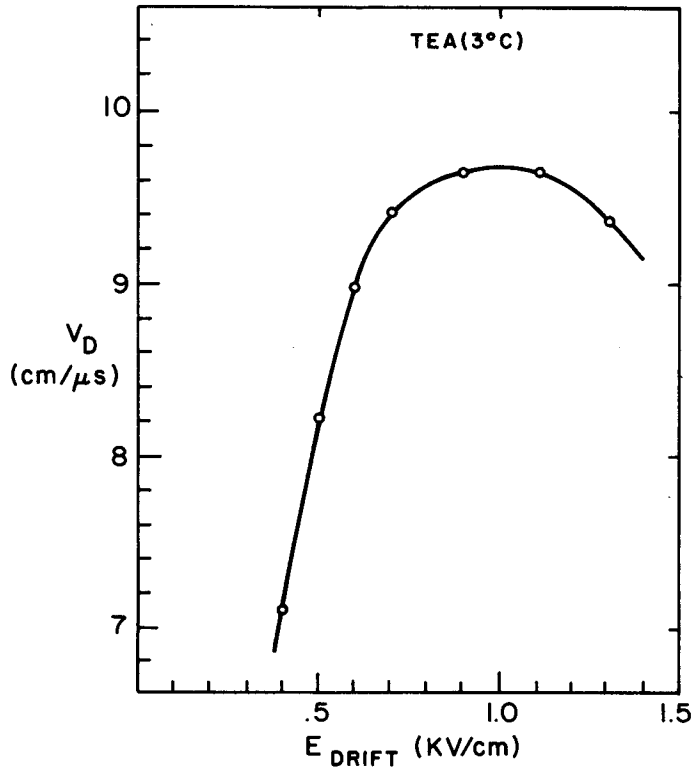

Fig. 11

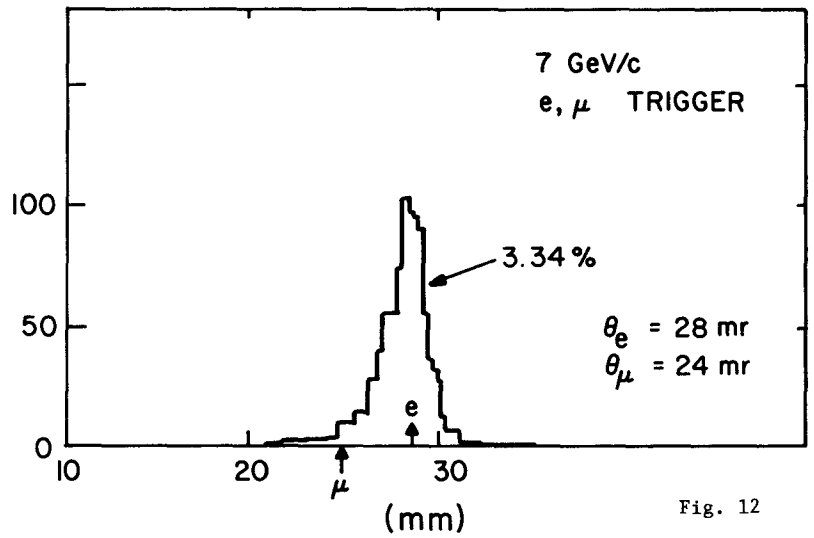

Fig. 12

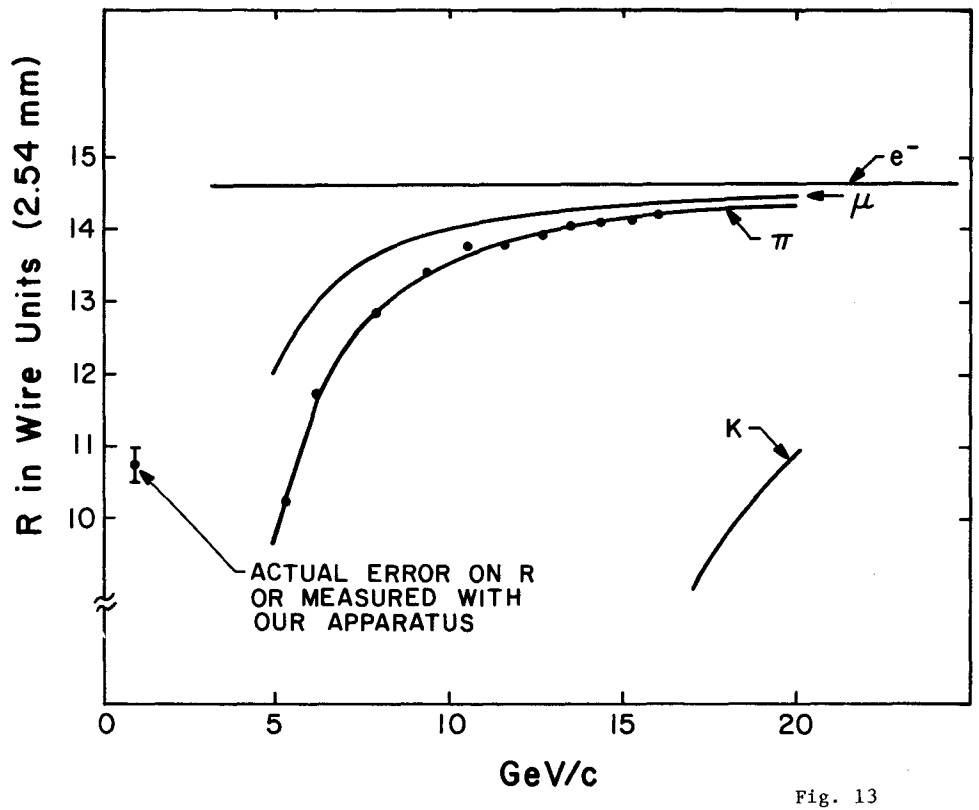
R in Wire Units (2.54 mm)
15
14
13
12
11
10
0
5
10
15
20
GeV/c
e⁻
μ
π
K
ACTUAL ERROR ON R
OR MEASURED WITH
OUR APPARATUS

Fig. 13

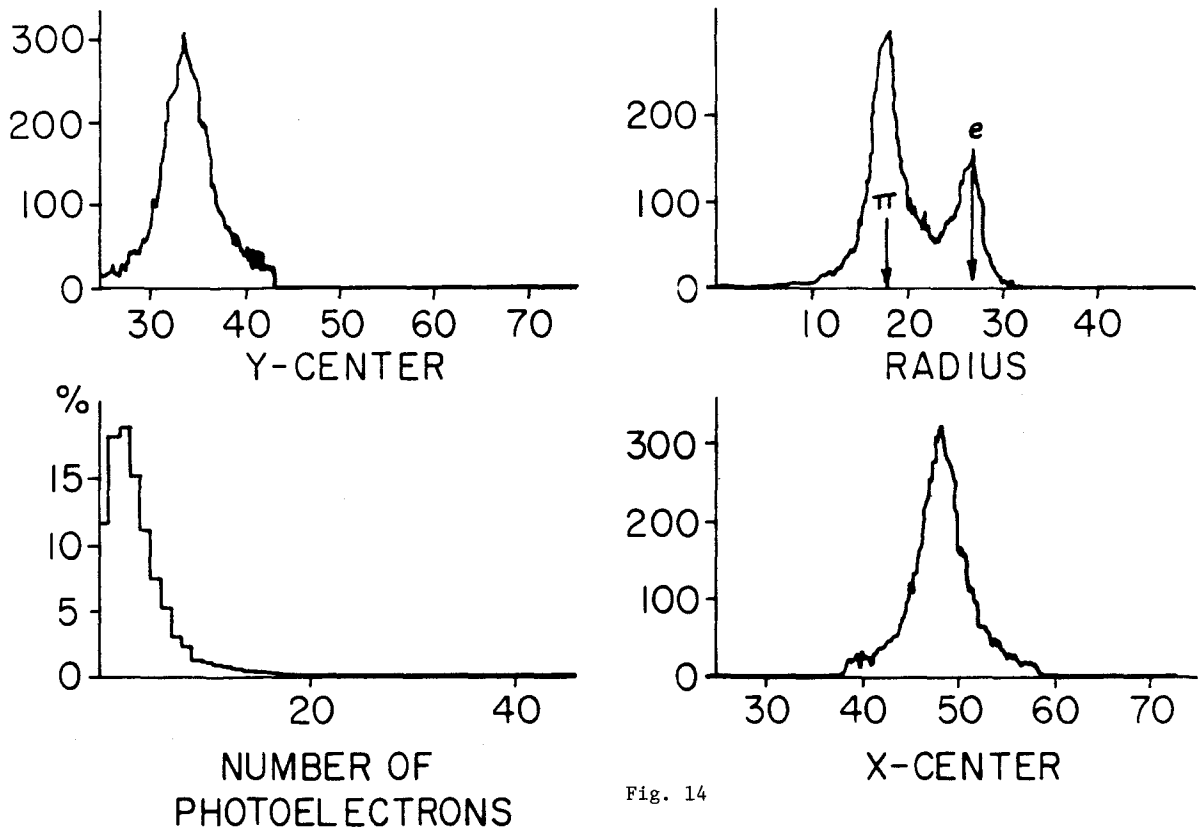
300
200
100
0
30 40 50 60 70
Y-CENTER
200
100
0
π
e
10 20 30 40
RADIUS
%
15
10
5
0
20 40
NUMBER OF
PHOTOELECTRONS
300
200
100
0
30 40 50 60 70
X-CENTER

Fig. 14

POSSIBILITIES OF USING THE PITT OPTICAL TRIGGERING DEVICE FOR RING RECOGNITION IN DISK CERENKOV COUNTERS

J. Thompson, University of Pittsburgh

At the University of Pittsburgh an incoherent optical processor is under development for use as an element in high energy physics triggers. The idea depends upon the distribution of light from an LED laser, into a preselected pattern onto an output plane. The LED or laser is triggered by a high energy detector element. In the output plane, light from each (optically independent) triggered light source adds incoherently. The pattern in which the light is focussed at the optical output light sources (or, equivalently, in the high energy physics detector elements) a large amount of light will be concentrated at the position of a light detector element in the output plane. This is shown schematically in Fig. 1.

At present, the optical black box for distributing the light is expected to be special type of computer generated hologram (called a kinoform). The status of the project is that we are presently working on technical, mechanical details of the kinoform production (few μ accuracy is required) and developing a test prototype for use in AGS Experiment 702 in the spring of 1982. Details of light source and light distribution uniformity, as well as light noise from an imperfect kinoform must still be investigated and could cause a worsening of the results presented in this note.

A general prescription for the recognition of a given pattern of interest has been developed.[1] Briefly, the light from a given LED (or laser) is distributed at the light output plane as the mirror image of the pattern of interest, displaced from the origin according to the input LED displacement. For the case of the disk Cerenkov counter (see Fig. 2), this is a very simple pattern, a circle centered at the position of the input photon measurement.

We have explored in detail (via computer Monte Carlo of the output plane) both the efficiency and the extra signals generated by an ideal kinoform element for a five-photon event for the method based on the picture in Fig. 2.

In this method, the input and output cell granularity are matched to the precision desired in the radius measurement. The radius against which one wishes to test the measurements is coded into the kinoform. If more than one radius is of interest, one must multiplex the kinoforms, at a cost of an increase in the number of output plane detectors. The chief problem with this method is cost. [Present estimates are $\sim$ \$2.-50./input channel solid state laser, or LED with good ($\lambda\Delta/\lambda$) and timing characteristics and $\sim$\$100.00/output channel (PIN diode with amplifier or APD)]. Results are shown in Table 1 and Figs. 3 and 4.

In Table 1 and Figs. 3 and 4, "clustering" involves grouping together cells adjacent to each other or one removed. This technique is extremely helpful in removing extra signals which might otherwise arise as light is shared by two output cells, over the threshold.

Table 1

Ring Recognition Results

Single Track Efficiency ($R = R_{desired}$)	No. Events With > 1 Circle Found (No Clustering)	No. Events With > 1 Circle Found (Output Clustering)	Precision of Circle Center Finding Output
99%	63%	1%	Cell size/2

CONCLUSIONS AND CAVEATS

1. Poisson statistics and non-ideal kinoform elements will degrade these results. Poisson statistics could be included but have not been; we do not yet know the degradation to be expected from use of a nonideal kinoform element.

2. The measurement precision is determined by the input precision, and light source and light detector spacings, rather than by the ring radius.

3. The technique is very sensitive to departures from the desired pattern. It would be excellent if the radius desired were a definite value [$\Delta r <$ (cell size/4)]. The sharpness of response would be a problem if one

wished to include all circles, but bin them according to size (many multiplexed kinoforms and corresponding proliferation of output plane elements and cost escalation). Since radius binning is likely to be the desired mode, a transformation of the coordinates (e.g., to r, θ coordinates, or a logarithmic transform as discussed by Casasent)[3] should perhaps be pursued. However, flexible use (again, a minimum number of multiplexed kinoforms) requires the origin of the r, θ system to vary from event to event (perhaps according to some scintillation counter input) and this problem has not yet been solved.

4. If some clustering criterion (optical or electronic) can be applied, so that light spread over adjacent output cells is recognized as a single signal then close to 100% efficiencies can be achieved, with < 10% extra signal generation for two particles, with circle center separation > 15 cell sizes. The extra signal generation rises to ∿ 20-30% for closer particle separations, and, of course, may be even worse with several close-lying particles, as would obtain in a jet. A typical particle angular separation may be ∿half the Cerenkov cone for particles in an ISABELLE jet (see Table 2). Thus, bin sizes of a few percent of the ring radius would be required to avoid generation of spurious extra signals.

Table 2

Some Parameters of a Rough Disk Cerenkov Design (from Ref. 4).

Particle Detector Plane	γ_{thres}	$p_{thres}(k)$	L	$\sin\theta_m$	Exp. Mom. Range	Expected Angular Particle Separation (0.35 = $p_\perp$)	R_{max}
C_1 2.5mx2.5m	15	7.5 GeV/c	∿1m	0.065	7.5-30 GeV/c	∿0.035 (p=10 GeV/c)	∿ 6.5 cm
C_2 7mx7m	35	17.5 GeV/c	∿5m	0.027	17-60 GeV/c	∿0.027 (20 GeV/c)	∿15 cm

Cell Size	No. of Cells
2.5 cm	∿10
7 cm	∿10

REFERENCES

1. W.E. Cleland, internal University of Pittsburg, Note OP-DOE-5. See also note by W.E. Cleland, elsewhere in these proceedings.
2. G.A. Thompson, internal University of Pittsburg, Note OP-DOE-5, gives more detail concerning the results summarized in this note.
3. Deformation Invariant, Space Variant Optical Pattern Recognition, D. Casasent and D. Psaltis, Progress in Optics, Vol. 16 (North Holland, 1978) pp. 289-356.
4. S. Aronson, et al., 1978 ISABELLE Workshop.

FIGURE CAPTIONS

Fig. 1. Schematic of the optical triggering device. At the input plane, logic signals from particles would trigger some individual light sources probably either LED's or solid state lasers. F is an optical filter, a kinoform in our conception, and the combination L1 (a lens which effectively performs a Fourier transform on the light input), F, and L2 (a second lens) can be treated as an optical black box which distributes the light on the output plane. At some predetermined point, if a pattern of interest is present in the input plane signals, a large amount of light will be detected by a light detector such as a pin divide plus amplifier. A signal above a preset threshold signals an event of interest.

Fig. 2. Superposition if input and output configurations for 5 photons on a circle.

Fig. 3. Efficiency of filter for Cerenkov light ring of different radius from that assumed for the filter.

Fig. 4a. For events with two particles incident upon the $\check{C}$ counter, the precentage of events for which the optical triggering device reports more than two found circles of the desired radius (particles of the desired velocity). The percentage of events with extra tracks is plotted as a function of the separation between the two tracks, expressed as a multiple of the light detector plane cell size. Monte Carlo statistical errors are shown.

Fig. 4b. For two particles incident upon the $\check{C}$ counter, the number of particles reported by the optical triggering device, as a function of the separation between the two tracks. Errors shown are Monte Carlo statistical errors.

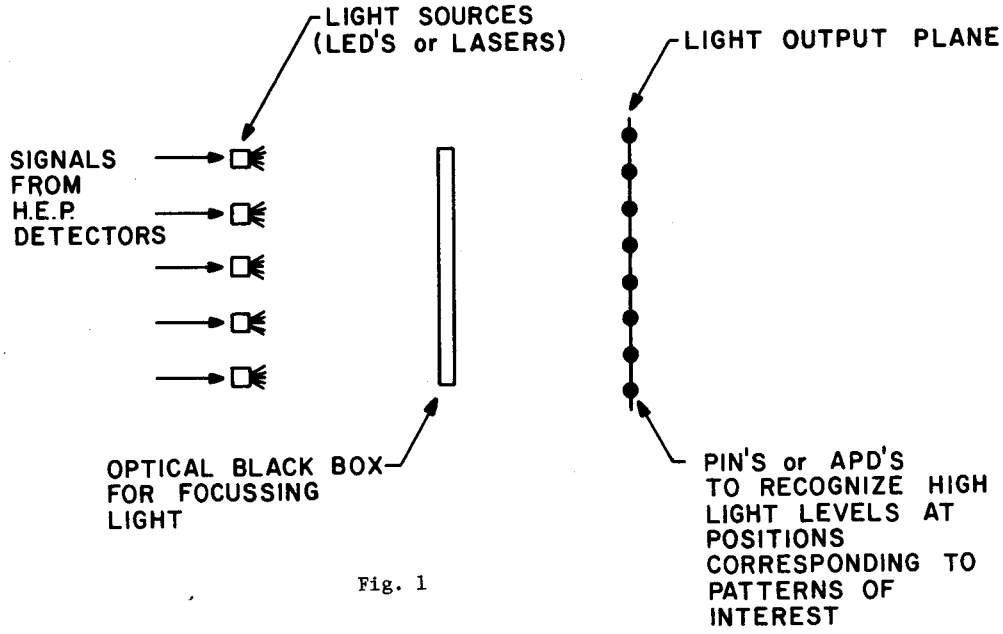
LIGHT SOURCES
(LED'S or LASERS)
LIGHT OUTPUT PLANE
SIGNALS
FROM
H.E.P.
DETECTORS
OPTICAL BLACK BOX
FOR FOCUSSING
LIGHT
PIN'S or APD'S
TO RECOGNIZE HIGH
LIGHT LEVELS AT
POSITIONS
CORRESPONDING TO
PATTERNS OF
INTEREST

Fig. 1

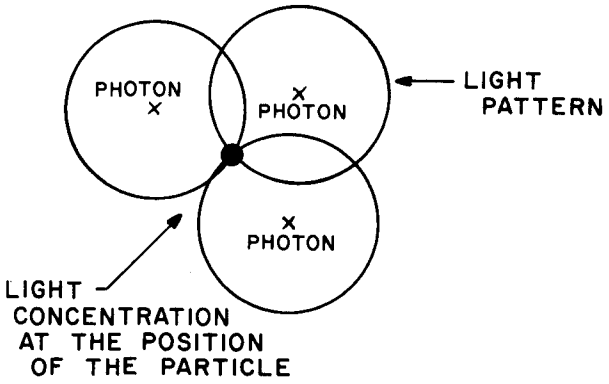
PHOTON
PHOTON
PHOTON
LIGHT
PATTERN
LIGHT
CONCENTRATION
AT THE POSITION
OF THE PARTICLE

Fig. 2

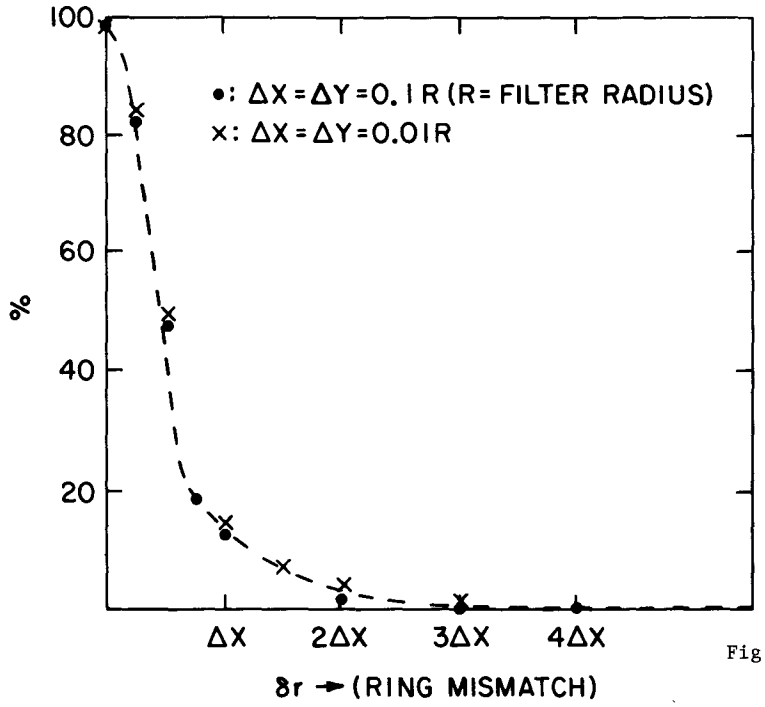
100
80
60
40
20
%
•: ΔX=ΔY=0.1R (R= FILTER RADIUS)
×: ΔX=ΔY=0.01R
ΔX
2ΔX
3ΔX
4ΔX
δr → (RING MISMATCH)

Fig. 3

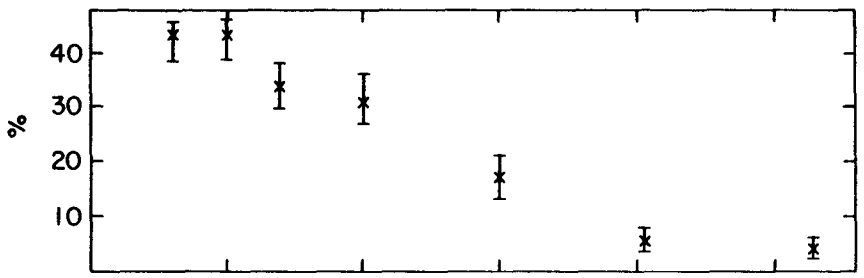
40
30
20
10
%

Fig. 4a

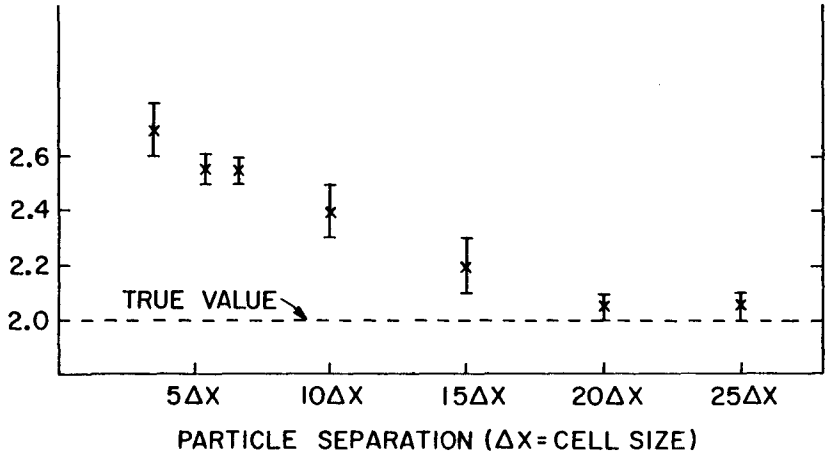
2.6
2.4
2.2
2.0
TRUE VALUE
5ΔX
10ΔX
15ΔX
20ΔX
25ΔX
PARTICLE SEPARATION (ΔX=CELL SIZE)

Fig. 4b

TRANSITION RADIATION

J. Thompson, University of Pittsburgh

An improvement in particle separation at low γ ($\sim 10^3$) and development of a "practical" transition radiation detector using a relatively simple electronic count of charge clusters has been described by Fabjan, Willis and collaborators. The count of charge clusters distinguishes rather well between the low number of clusters from ionization of the primary particle and the higher number from transition radiation quanta. The range of the detector is $\gamma \sim 10^3$-10^4. The detector is 10 x 10 cm^2 in cross section (MWPC to collect ionization) and 0.5-1.0 m long with 12-24 sets of radiators. The method requires 4 ADC's and a discriminator/radiator plane, to count the number of clusters with large amplitude collected at each plane. The speed of the device is set by the charge collection time, about 160 nanoseconds. The results are relatively stable over a wide range (2.5-4 KeV) for the cluster threshold energy, and both π/e and K/π separation is quite good. The π/e separation achieved is $\sim$ 0.2% pion contamination for 90% electron efficiency for 10-15 GeV/c π's and electrons, with 12 sets of Li foil radiators spaced over $\sim$ 0.5 m length. For π's and K's at 140 GeV/c, 24 planes of carbon fibers were used as radiators, spaced over a 1.3 m length. With that configuration they reduced the pion contamination to 1-2% for 90% kaon efficiency.

Thus, for applications where their granularity of 10 x 10 cm^2 is acceptable, the transition radiation technique appears to be quite satisfactory for electrons in the $\gtrsim$ 10 GeV/c range and π's and K's in the $\gtrsim$ 100 GeV/c range. The spatial resolution is set presently by the MWPC size but could perhaps be reduced by putting ADC's on individual groups of wires. Although generally transition radiation seems to be an excellent and relatively simple technique for electron identification there may be some specialized cases (e.g., identifying an electron within a jet) in which higher spatial resolution is required. In such cases, ring-imaging Cerenkov counters

may play a role. Of course, shower counters may also be used, placed behind the tracking chambers. However, patterns in these may be somewhat confused by the large number of particles expected in interesting events.

REFERENCES

1. C.W. Fabjan, et al., "Practical Prototypes of a Cluster-Counting Transition Radiation Detector", submitted to Nucl. Instrum. and Methods, October 1980.

ELECTRON IDENTIFICATION VIA SYNCHROTRON RADIATION

J. Kirz and A.H. Walenta

Detection of synchrotron radiation emitted by high energy electrons was successfully used for particle identification in the $\Lambda\beta$ decay experiment at FNAL. We describe the basic idea here as it could be used at Isabelle.

Total energy radiated, by an electron of energy E, in traversing length ℓ of field B is

$$\delta\, E(\mathrm{MeV}) \gtrsim 1.26 \times 10^{-5}\, E^2(\mathrm{GeV})\, B^2(\mathrm{kg})\, \ell(\mathrm{m})$$

The energy distribution follows a universal curve, whose half powerpoint is at

$$E_c(\mathrm{keV}) = 0.066 B E^2$$

For fixed B and ℓ, therefore, the increased energy comes from shifting the curve to higher energy.

Fig. 1 illustrates the spectrum: Here the number of photons emitted within a 10% energy band are shown as a function of photon energy for electrons traversing a 1.2 m long 13 K Gauss magnetic field region. Photon detectors sensitive in the 1-100 keV range will be particularly useful to detect the radiation from electrons in the 3-30 GeV interval.

Electrons are identified by the observation of x-rays within a restricted region of the detector, corresponding to the deflection of the particle in its bend-plane.

Rejection of other particles depends on keeping the spurious hits within this restricted area (typically 2 mm x $\ell^2/2R$, where ℓ is the field length and R is the orbit radius) low. With two or more detected x-rays, very high rejection ratios should be attainable.

To keep the loss of soft x-rays to a minimum, the path of the x-rays should be in helium or in a low-pressure chamber. The window of the x-ray detector must also be kept thin. To detect the harder x-rays with reasonable efficiency, a Xenon chamber of significant thickness appears to be most useful.

The overall detection efficiency of a system composed of 1.2 m He, 0.1 mil mylar entrance window and a 10 cm thick Xenon detector is shown on Fig. 2.

By combining the emission spectrum with this detection efficiency, we obtain the expected number of detected photons. Fig. 3 shows this quantity as a function of electron energy for a 1.2 m long magnet, and for B = 13 kG and 30 kG.

A possible detector arrangement is shown in Fig. 4. The track is measured in five concentric drift chambers. The outermost has a thickness of 10 cm and is filled with Xe to register most of the x-rays. The four inner chambers are built as thin as possible in order to be transparent to x-rays because the probability of separating the x-rays from the track signal improves with increased length of the track. Fortunately this effect is most pronounced for high electron momenta (stiff particles) where the x-ray spectrum is shifted to higher energies which penetrate these thin chambers and reach the outer chamber. For the reason of optimum double track resolution also the outer chamber is subdivided into 3 individual chambers, two filled with Xe and each 5 cm thick and a 1 cm chamber in front filled with C_3H_8 for detection of the soft x-rays.

FIGURE CAPTIONS

Fig. 1 Number of photons emitted within a 10% energy band. ℓ = 1.3 m, B = 13 kG.

Fig. 2 Detection efficiency for the end detector (10 cm Xe, 1 cm C_3H_8, .1 mil mylar window and 1.2 m He absorber).

Fig. 3 Number of detected x-rays as function of electron energy.

Fig. 4 Chamber arrangement for tracking and detection of synchrotron radiation.

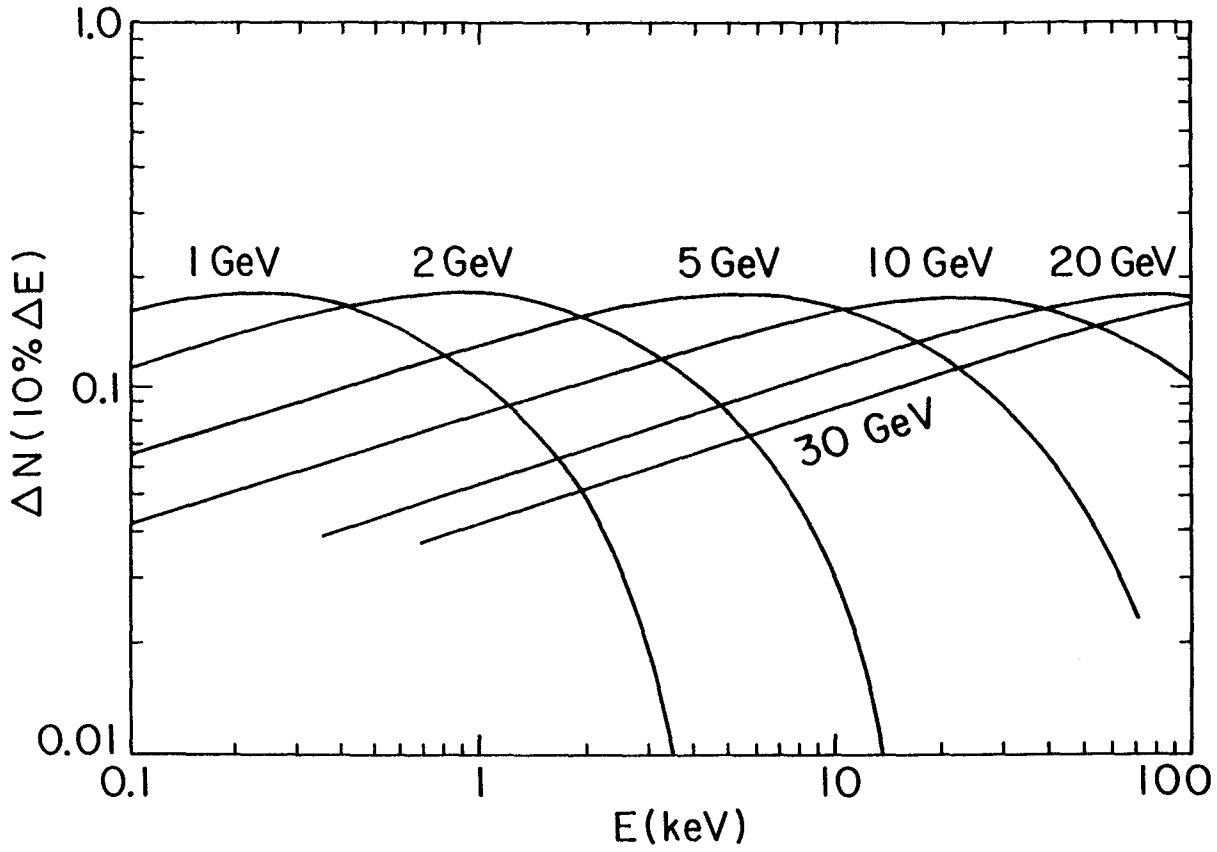
1.0
0.1
0.01
ΔN(10%ΔE)
1 GeV
2 GeV
5 GeV
10 GeV
20 GeV
30 GeV
0.1
1
10
100
E(keV)

Fig. 1

Fig. 2

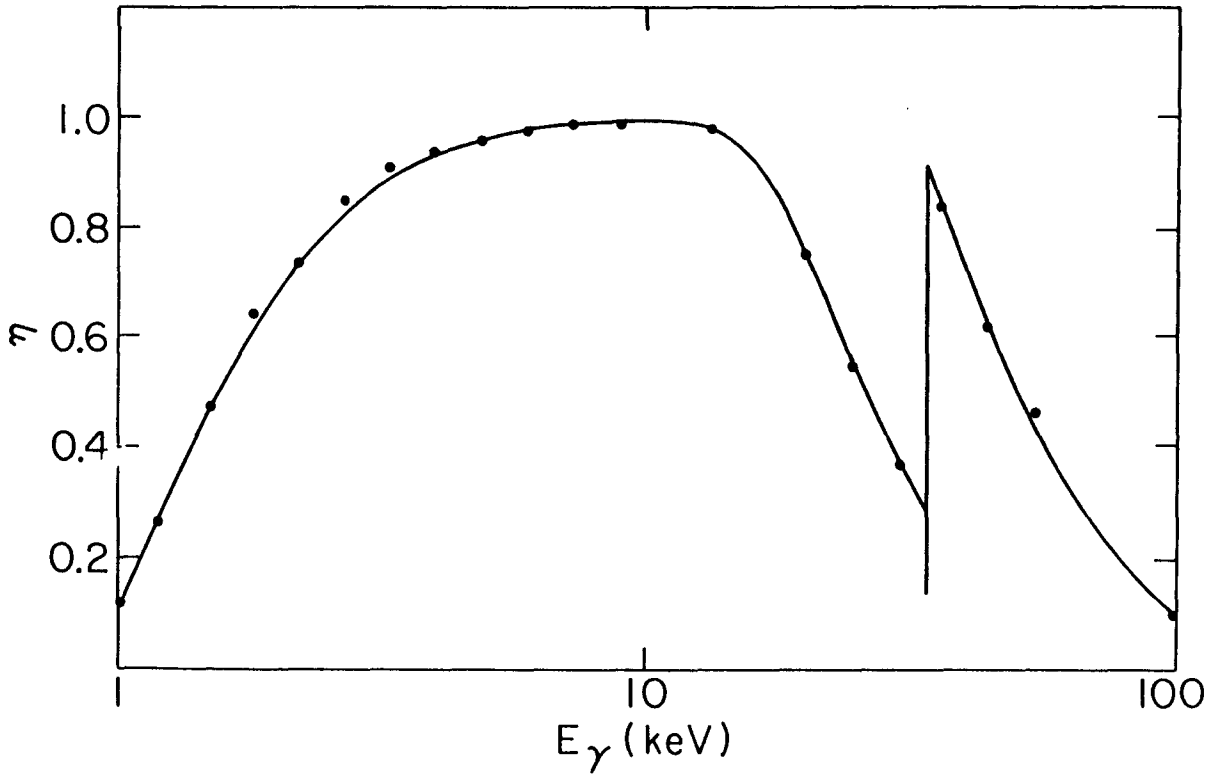

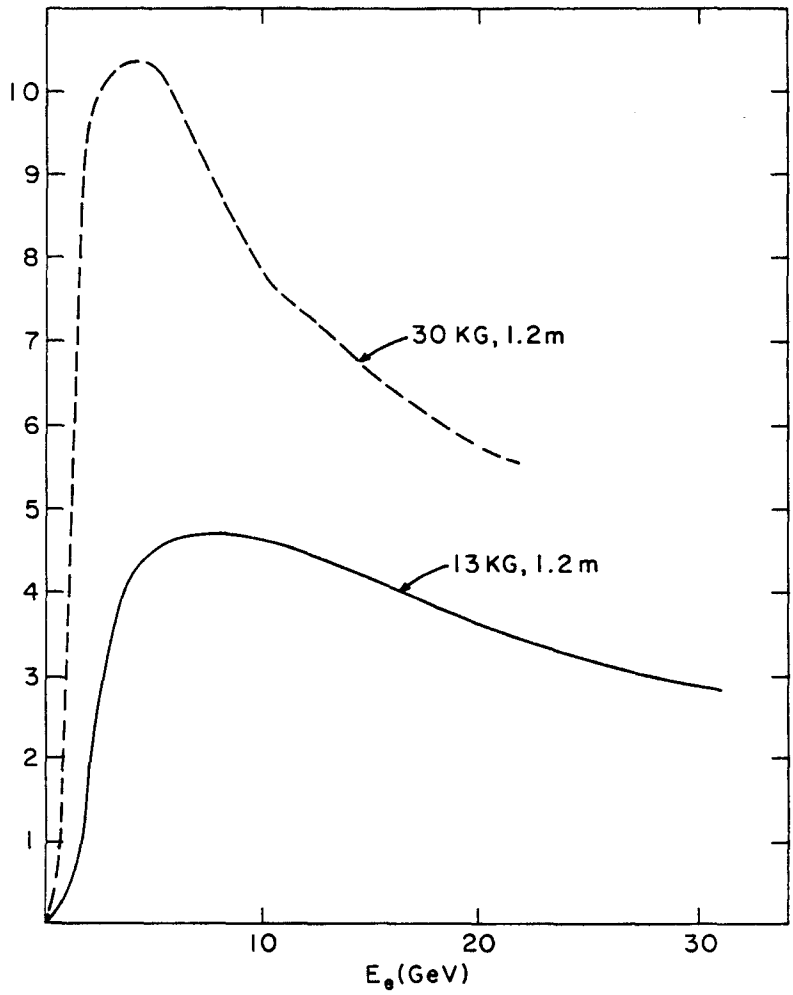

Fig. 3

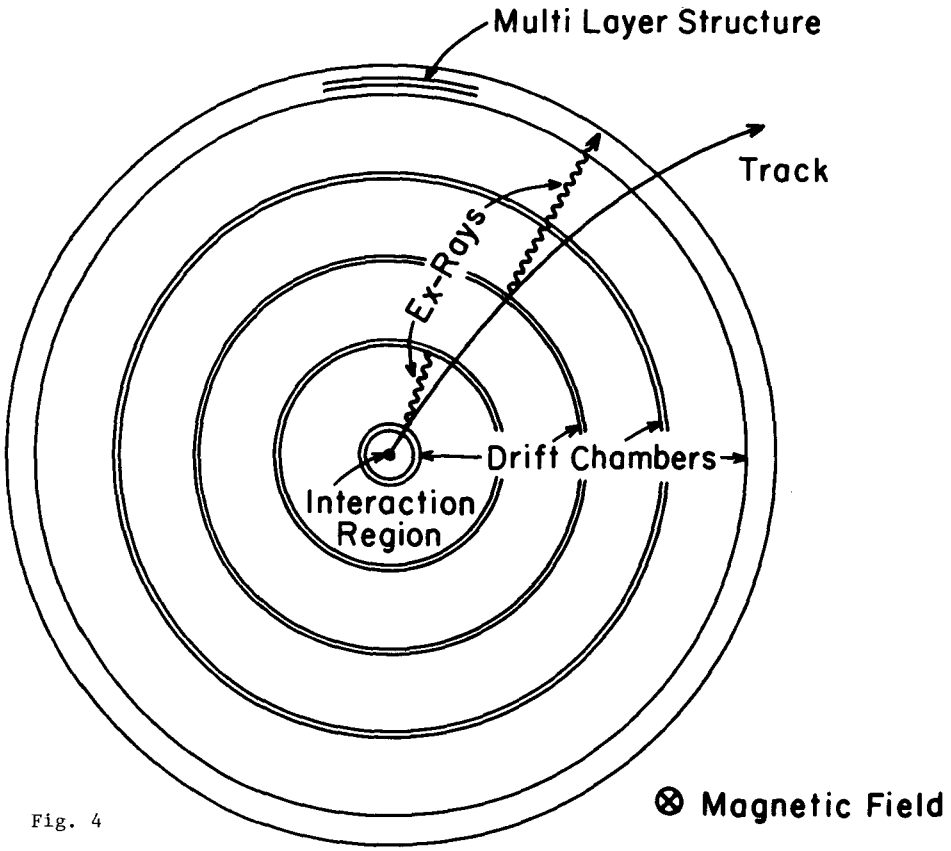
Multi Layer Structure
Track
Ex-Rays
Drift Chambers
Interaction Region
⊗ Magnetic Field

Fig. 4

NEW DIRECTIONS IN TRACK DETECTORS

R. Strand, Brookhaven National Laboratory

This is a summary report of a working group whose members are listed below.[1] Detailed write-ups of presentations made to the workshop will be found on the pages which follow.

While established detectors are adequate for most experiments at $10^{31}cm^{-2}sec^{-1}$, the high rates expected at $10^{33}cm^{-2}sec^{-1}$ exceed the capabilities of contemporary drift chambers that are close to the beam pipes. New varieties of scintillation counters and semiconductor detectors for use at the higher luminosities and a new PMT for use in magnetic fields were discussed. Fine detector elements have low counting rates and they also facilitate pattern recognition in adjacent drift chambers. Ultra-fine space resolution provides better momentum and secondary vertex resolution, which could serve a new class of experiments. However, fine detector elements escalate the number of readouts. The control of costs for readout is a challenge for which new directions are needed.

Millimeter-grained hodoscopes have been built from meter long scintillating optical fibers. One solid state avalanche photodiode per fiber is the preferred photodetector for barrel hodoscpes in magnetic fields. BNL has given a contract to RCA for the development of a small package wherein the scintillator light can be detected by an APD.

Semiconductor detectors with fine resolution strips for readout have been developed for areas of about 1 x 1 cm^2. Pat Skubic of the University of Oklahoma described detectors for use in an approved experiment at Fermilab. Achievable versions of these small sized detectors are ready for use in the forward direction at ISABELLE. Units of size 10 x 10 cm^2 are needed for use in barrel hodoscopes at ISABELLE. Two related aspects of this order of magnitude change of scale require further R&D. Larger units that can be manufactured and readout amplifier circuits need to be developed. Signal processing that interpolates between fine strips to 10 micron resolution is needed.

Solid-state physicist Darryl Coon, of the University of Pittsburgh described the discovery of frozen track images in silicon detectors that can be extracted by application of an electric field. At liquid helium temperatures the ionized electrons are efficiently captured in shallow traps. The working party was unable to find a specific ISABELLE experiment for this new detector, but stored high resolution track locations that are available for rapid extraction must be useful! Further R&D on this detector should be supported.

The microchannel plate electron amplifier has been improved by a 100 Angstrom layer of aluminum placed over the first surface. This prevents the back-streaming of positive ions from destroying the photocathode of PMT's using this position sensitive amplifier. The effective quantum efficiency is reduced from about 20% to about 10% by the ultrathin foil. Further R&D is needed to bring it back to at least 20%. If the distance between the photocathode and the MCP is small as in "proximity focusing" the PMT performs usefully in up to 10 kG magnetic fields. A MCP PMT with a segmented anode might be cost effective for detectors with fine segmentation.

Semiconductor detectors with fine resolution readouts are achievable for small angle tracks at ISABELLE. The other detectors that were discussed have demonstrated advantages that merit further R&D to achieve production units.

REFERENCES

1. R. Strand (Chairman), BNL; P. Braccini, PISA; S. Borenstein, BNL; C.P. Cheng, IHEP China; V. Radeka, BNL; H.W. Kraner, BNL; S.D. Smith, BNL; J. Fischer, BNL; C. Tang, IHEP China; P. Clarke, IHEP China; E.W. Anderson, BNL

TESTS OF PROTOTYPE SOLID STATE DETECTORS

P. Skubic, G. Kalbfleisch, J. Oostens, J. White
University of Oklahoma

M. Johnson and C. Nelson
Fermi National Accelerator Laboratory

J. Walton, Lawrence Berkeley Laboratory

J. Kalen, S. Kuramata, N. W. Reay, K. Reibal, R. Sidwell, N. R. Stanton
Ohio State University

B. J. Stacey and T.-S. Yoon
University of Toronto

ABSTRACT

Prototype position-sensitive semiconductor detectors with center-to-center strip spacing of 1 mm and approximately 300 microns thick have been tested with electrons from a Ru^{106} source and a 30 MeV linac. The average signal was 3.2 fc for minimum ionizing particles. A FET cascode charge sensitive amplifier gave an rms noise of 0.24 fc with the detector connected and the detector efficiency was measured to be $(97 \pm 2)\%$.

Prototyping of Solid State Detectors

Position-sensitive semiconductor detectors are being developed for use in a hybrid emulsion experiment at Fermilab (E653). The spectrometer design relies heavily on the excellent position resolution (<20 microns) and multiple track resolution which can be achieved with such detectors. They can also be operated in high vacuum, which may be useful for colliding beam experiments at machines such as ISABELLE.

The detectors are thin wafers of high resistivity silicon on which are deposited many narrow parallel strips which collect the ionization from charged particle tracks. The size of this signal is about 80 electron-hole pairs per micron of silicon, or 3.8 femtocoulombs for a fully-depleted wafer 0.3 mm thick. Analogue signals may be read out either from individual strips (as is necessary where the track density is high) or from taps every N strips, with the position being inferred from interpolation of the resistively-divided charge [1].

The latter method considerably reduces the instrumentation cost when relatively large areas of detector are needed, as is the case for E653, and maintains the same position resolution as the individual- strip readout in regions of lower track density. In this method strips are connected by constant inter-strip resistances R, as shown below:

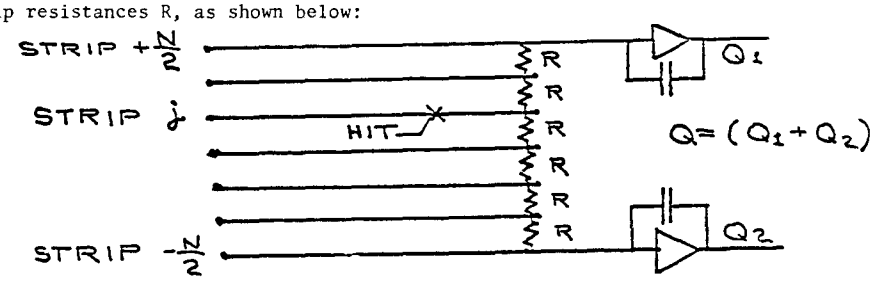

Since the charge-sensitive amplifiers act as virtual grounds, charge deposited by a track passing through strip j is divided according to path resistance onto only the amplifiers immediately adjacent to that strip. The struck strip

is then inferred from the divided charges Q_1 and Q_2:

$$j = \frac{N(Q_1 - Q_2)}{2(Q_1 + Q_2)}$$

For constant interstrip resistance R, the error in determining j is

$$\delta j = \frac{(Q_1^2 + Q_2^2)^{1/2}}{Q} N \frac{\delta Q}{Q}$$

where Q is the total deposited charge and δQ is the RMS uncertainty in each signal due to system noise. For N=10, Q=3.8 femtocoulombs (detector 0.3 mm thick), an RMS noise of δQ=0.15 femtocoulombs gives rise to a position uncertainty δj=0.38, comparable to the value of $(12)^{-1/2}$ expected for the case of individually-read strips without charge sharing between strips. There is also a contribution to δj from uncertainty in interstrip resistance which is roughly $(N)^{-1/2}\ \delta R/R$. Thus for N=10 the fractional error in R must be smaller than 10% RMS to maintain position accuracy. Though not demonstrated here, R must also be kept larger than 2000 ohms if δQ is not to be dominated by parallel resistance thermal input noise to the amplifier.

A. Construction of Position-Sensitive Silicon Detectors

Position-sensitive silicon detectors may be constructed using either surface barrier or diffused junction techniques. In surface barrier detectors the rectifying contact is at the surface between the silicon and the metal deposited on it. They are relatively easy to make by etching away an evaporated metal film to leave the desired pattern of strips. During the past year, several groups [2,3,4] have reported successful source or beam tests of surface barrier detectors with strip spacings of 600 microns down to 40 microns.

We have chosen to use the diffused junction technique in which the rectifying junction is buried below the surface, occurring between the silicon and an implanted impurity such as phosphorus on which the metal strips are laid (similar to the construction of commercial IC's). Although requiring specialized equipment, this

method has several advantages:

1) The buried junctions are more stable against deterioration and the resulting increase in noise, and the area between the strips is rendered inert by a layer of oxidized silicon. The resitance between the strips is high and stable, as required by the charge division readout. Achieving a uniform resistance for this application is much more difficult in surface barrier detectors.

2) Strip spacings smaller than 40 microns appear to be quite feasible with optical masking techniques, as witnessed by the few-micron line widths routine in IC fabrication.

3) The p-type semiconductor used in our diffused-junction device can easily handle the radiation in this experiment. No impairment of performance occurs for doses of minimum ionizing particles of $10^{14}/cm^2$. This feature is important for possible high-rate applications.

Prototype diffused junction detectors are being made for us by the Silicon Solid State Group at Lawrence Berkeley Laboratory. We are now in the second generation of prototypes. The first round of detectors, having 0.8 mm strips with 1.0 mm center-to-center spacing, were built mainly to gain experience in diffused junction strip technology; results of tests on these detectors are described below. Prototypes with strips on 40 micron centers have recently been fabricated, and at least 6 of these should be ready for testing this summer. The 9 mm x 9 mm active area of this 40 micron prototype and its printed circuit fanout board are shown in fig. 1.

B. Testing of Prototypes

The first generation of prototypes (1 mm spacing, 1 cm x 1 cm area) has been tested with Ru^{106} electrons (3.5 MeV endpoint) at Fermilab, the University

of Toronto, and the University of Oklahoma (OU), with the different groups trying different amplifier and readout schemes. Results from the Fermilab tests using a modified version of the Droege electronics (designed for liquid argon detectors) are shown in fig. 2. A very clean separation of signal and noise peaks is apparent.

A stack of three of these detectors is being tested both with the 3 MeV source and in the beam from a 30 MeV electron linac by the OU group. Four strips from each of the three wafers are read out of via FET-cascode amplifiers into standard ADC's. Typical pulse height spectra are shown in figure 3. A clear electron peak is observed at 3.2 fc average charge. Noise contributions were present from the amplifier alone (0.1 fc) and from the amplifier-detector combination (0.24 fc). These were increased to 0.4 fc by the noisy Rf environment of the linac.

The main questions to be addressed by this multi-detector test are: 1) How often does a particle give a signal in adjacent strips; 2) What is the overall efficiency; and 3) Is the space between metal strips alive or dead? Some preliminary results are available at this time. Correlations of hits between wafers are shown in figs. 4 a, b for both source and linac data. For perfectly aligned strips, no multiple scattering and no sharing between strips, only the diagonals of these correlation matrices would be populated. Although the multiple scattering from the source is approximately 1 mm, that from the 30 MeV linac beam is only 0.1 mm (comparable to the gaps between strips), and the angular divergence of the beam is much smaller than the mean multiple scattering angle. As is clear from fig. 4 b the 30 MeV data are in fact markedly more peaked at the diagonal. The small subdiagonal population implies a misalignment of about 1/7 strip spacing between planes. Both sets of data are in good

agreement with the monte carlo simulations in fig. 4 c,d which assume no signal sharing between adjacent strips. There is thus already evidence for clean 3-point trajectories.

An estimate of the inefficiency can be made by asking how often neither of the two central strips in the middle wafer failed to record tracks seen by the corresponding strips in both front and back wafers. Two misses were seen in 92 events, giving an efficiency (97$\pm$ 2)%. This high efficiency, together with the known misalignment of 1/7 strip, implies that the 0.2 mm gap between the 0.8 mm metal strips is essentially live. If it were dead (e.g. from increased collection time) one would expect an inefficiency of about 20%).

We are now preparing to test the second generation 40 micron prototypes at LAMPF, starting in August. four wafers with 30 instrumented strips each will be used in a closely spaced stack to study sharing between strips, position resolution, efficiency and amplifier performance. With a 550 MeV/c beam we will be able to measure the position resolution to 5-7 microns (standard deviation).

REFERENCES

1. V. Radeka and R.A. Boie, IEEE Trans. Nucl. Sci. 27, 351 (1980).

2. S.R. Amendolia et al., "A Multielectrode Silicon Detector for High Energy Physics Experiments," PISA 80-2 (1980); Nucl. Inst. and Meth. 176, 457 (1980).

3. E.H.M. Heijne et al., "A Silicon Surface Barrier Microstrip Detector Designed for High Energy Physics," CERN/EF/BEAM 80-6 (1980); Nucl. Instr. and Meth. 178, 331 (1980).

4 J.B.A. England et al., "Capacitative Charge Division Read-Out with a Silicon Strip Detector," CERN-EP/80-218 (1980).

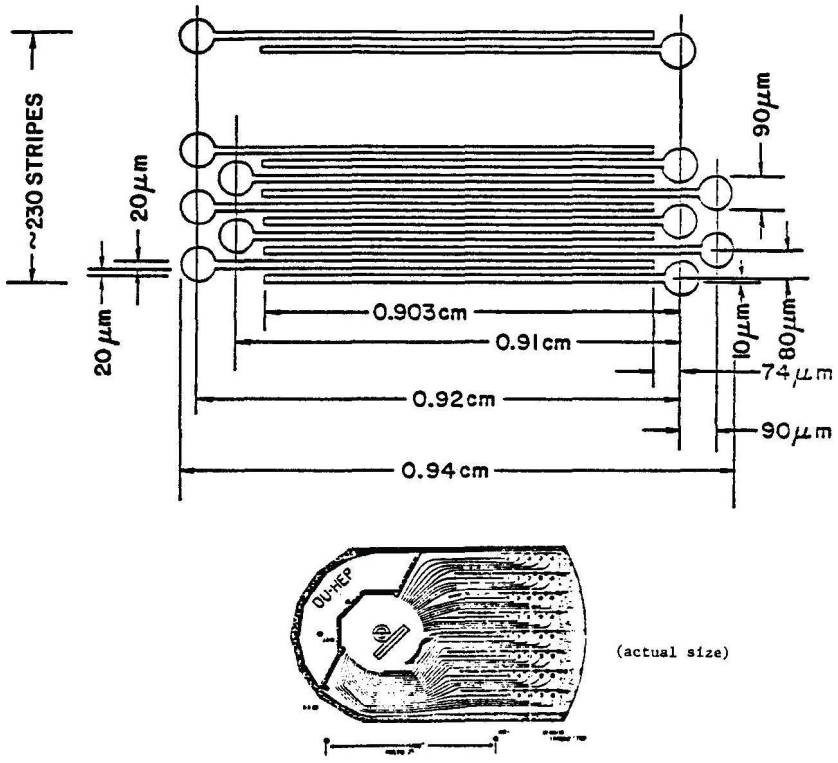

Figure 1. Layout of stripes and PC mounting board for 40 micron prototype.

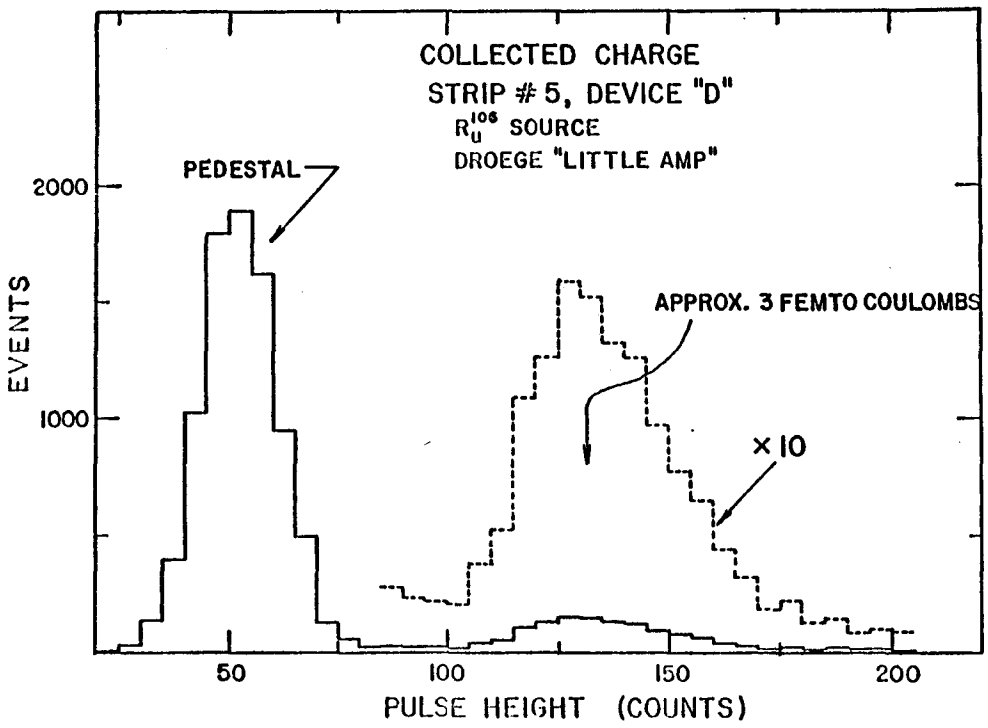

Figure 2. Pulse height spectrum for one mm prototype.

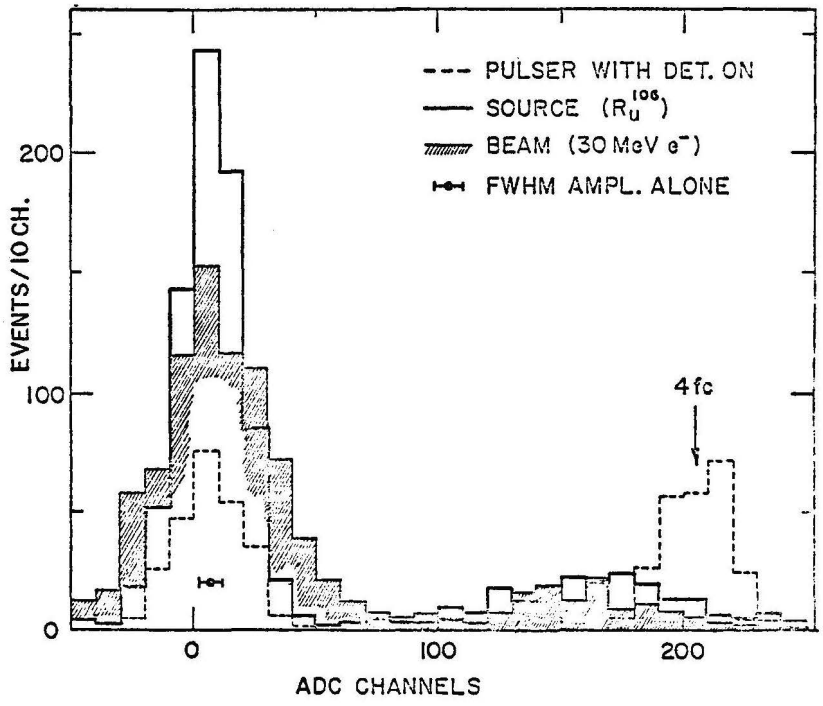

Figure 3. Pulse height spectrum for one mm prototype.

Figure 4

Stripe Hit Correlations

Matrix of correlated hits, first plane (1-4)→, second plane ↓ with last detector also hit.

	3 MeV Source						30 MeV Linac			
	a)					b)				
	58	10	0	3			80	2	4	0
	18	56	11	0			15	86	9	3
DATA	5	22	69	20			3	13	174	9
	0	0	6	42			6	4	22	116
				220	Diagonal	456				
				87	1 Off Diag.	70				
				8	> 1 Off	20				
				315		546				
	c)					d)				
	48	9	0	0			94	0	0	0
	14	54	12	1			20	149	0	0
MONTE CARLO	3	26	54	19			0	26	149	0
	0	7	26	42			0	0	17	91
				198	Diagonal	483				
				106	1 Off Diag.	63				
				11	> 1 Off	0				
				315		546				

SEMICONDUCTOR DETECTORS FOR HIGH ENERGY PHYSICS

P. Braccini,* H. W. Kraner,† P. Skubic,‡
T. Ludlam,† V. Radeka,† and D. D. Coon§

1. Introduction

Semiconductor detectors with position sensitivity have been rediscovered recently by high energy physicists in two dedicated conferences.[1,2] Although the reported technology of this kind of detector is not necessarily new,[3,4] the application to high energy physics has received recent impetus from the needs of storage ring machines such as ISABELLE. This report will include a brief introduction to the detectors themselves, their initial applications, further important applications attempting to suggest the scope of their usage, and a discussion of readouts and radiation damage.

In a sense, position sensitive detectors have already played a role in the CERN-SPS NA1 collaboration to determine the decay paths of charmed mesons. A stack of 400 μm thick silicon surface barrier detectors was used as an active target to register single or multiparticle energy losses. This application might be called "z-axis" position sensitivity, but is not specifically the lateral, spatial position sensitivity of main interest here.

Representative of the more conventional geometry of x-y position sensitive detectors that should be rapidly exploited in high energy physics is a "multielectrode" semiconductor detector (MESD) developed by the Pisa collaboration[5] which is shown in Fig. 1(a). Silicon surface barrier technology is employed[6] to form a p^+ gold junction in n-type silicon. The opposite side has ohmic n^+ aluminum evaporated through a mask to form position-sensitive strips, in this case with a pitch of 300 μm on a 400 μm thick wafer covering an area of ~ 1 cm^2. The detector is operated just above depletion where the

* INFN, Pisa, Italy
† Brookhaven National Laboratory, Upton, New York 11973
‡ University of Oklahoma, Norman, Oklahoma 73019
§ University of Pittsburgh, Pittsburgh, Pennsylvania 15260

impedance between strips approaches 1 MΩ. Connections to individual preamplifiers are shown in Fig. 1(b), and tests show that ≥ 95% of the ionization is collected on a single electrode for a direct "hit" with good linearity of charge division between electrodes as a function of interaction point between the electrodes. It is suggested that localization with the above detector may be possible to as low as 50 μm. Other workers have proposed similar detectors with narrower strip spacing and, consequently, higher spatial resolution to below 10 μm.[2]

A general review of properties of semiconductor junction detectors follows that may be helpful. In a semiconductor junction detector, a field is impressed over a region (depletion region), often up to 1 mm in thickness, by the reverse biasing of a diode structure. The surface barrier configuration involves the p^+ surface property of gold on n-type silicon, as described, although aluminum is also n^+ on a p-type substrate. Junctions can also be formed by diffusion or implantation of the opposite type impurity into either an n- or p-type substrate. Phosphorous diffusion into p-type silicon is often used. The active depth w in μm is given by

$$w = C \cdot (\rho V)^{\frac{1}{2}}$$

where C = 0.5 for n-type base material
= 0.3 for p-type base material
ρ is the material resistivity in Ω-cm
V is the applied bias in volts.

Both carriers created by the imaging event, electrons and holes, are mobile (having mobilities of 1400 and 500 cm^2/V-sec, respectively), and are collected. The current pulse during collision is, therefore, the sum of both holes and electron components and is sketched below. For a 1 mm thick device (achievable with readily available material resistivities and biases), charge collection is, essentially, complete within 100 nsec, indicating the pulse width and rate capabilities that may be expected. The relatively small energy required to create an ion pair, 3.6 eV and 2.9 eV in silicon and germanium, respectively, gives this kind of device better statistical resolution than most other types of detectors, gas or liquid. At an energy loss of ~ 460 eV/μm,

for minimum ionizing particles, detector thicknesses down to 100 μm may be considered, which will produce signals well above postulated ~ 30 keV noise levels.

At the present time, there are an increasing number of groups gathering detector expertise to develop and use semiconductor position sensitive detectors, silicon multielectrode silicon detectors in particular. An interesting overview of this activity can be obtained from the contents of an informal workshop held at CERN, 30 April 1981, which is reproduced as Fig. 2. The Saclay group (Borgeaud), the Pisa group as mentioned (Stefanini) and particularly the CERN group (Hiejne and Jarron) have already had extensive experience with MESD detectors of pitch ranging down to 50 μm. Other authors shown present serious proposals for future detectors. P. Skubic has reported at this Workshop on recent developments of strip detectors fabricated at Lawrence Berkeley Laboratory by J. Walton and co-workers. Diffused junction strips are made by a phosphorous diffusion through stripe "windows" in a thermally grown oxide created by photoresist processes. The p-type base material receives a p^+ contact on the opposite face by B ion implantation. The stripe pitch is 40 μm and tests of several such devices are to be carried out presently at LAMPF.

Brookhaven is also constructing test devices of conventional surface barrier technology with variable stripe pitch down to 20 μm. Tests will be carried out using the proton microprobe facility at the 3.5 MV Van de Graaff accelerator.

The general advantages to be gained from semiconductor position sensitive detectors may be summarized:

i) room-temperature, low voltage (< 200 V) operation

ii) compatibility with high vacuum environment

iii) insensitivity to magnetic fields

iv) true in-chamber operation with the collected charge proportional to the energy released by the traversing particles (energy loss for minimum ionizing particle is ~ 275 keV/mm in Si and ~ 700 keV/mm in Ge)

v) low ionization energy (Ge - 2.9 eV/ion pr., Si - 3.6 eV/ion pr., with correspondingly excellent energy resolution

vi) high rate capabilities determined by rapid carrier transect time (> 1 MHz); dead time is determined by pulse-shaping (typical ~ 100 μsec)

vii) ability to self trigger

viii) no dead area from interelectrode support structures.

2. Possible Applications to Colliding Beam Physics

i) Elastic Scattering

Present technology allows the construction of telescopes having areas of a few cm^2 silicon strip detectors (or MESD's) with a total number of electrodes ≤ 1000, which would provide spatial resolutions of ~ 50 μm. These telescopes are even now probably not excessively expensive (~ 50K$), and would be the natural substitutes for the high resolution drift chambers currently used inside "Roman-Pots" downstream from colliding beams used to measure elastic scattering.[7] Inside the Roman-Pots, the MESD's are shielded by the electromagnetic pulses induced by the circulating bunches. The absence of the gas required in drift chambers would make the operation easier and safer and the minimum accessible angle even smaller than that of drift chambers which require edge support.

ii) Forward Spectrometers

The projected excellent spatial and energy resolution, combined with the insensitivity to magnetic fields, suggests the possible use of MESD's inside small aperture, forward high momentum magnetic spectrometers. The improved spatial resolution improves, in turn, the momentum resolution which can ameliorate the field, size or cost requirements of the spectrometer.

iii) Total p-p Cross Section

At very high energies of ISABELLE, the fragmentation of the two beams will occur inside two very narrow cones ($\theta < 40$ mrad) around the direction of incidence. One could, therefore, envisage a detector system scaled down in size from that which was used at the ISR[8] for the total interaction rate measurement where the corresponding fragmentation cones were ~ 20° wide.

At ISABELLE, a series of circular MESD hodoscopes, a few centimeters in diameter with θ and ϕ granularity, spaced every few meters downstream from

the two beams inside the vacuum pipe, would mimic the Pisa-Stony Brook-ISR equipment, and permit comparable precision in the determination of the inelastic rate.

A small semiconductor detector of this sort, together with the elastic scattering apparatus described above, should allow the determination of the p-p cross section independently of any luminosity measurement to an accuracy of $\sim 1\%$. The CDF group at FNAL has proposed[9] the construction of this apparatus; Fig. 3 is a schematic view of the θ-ϕ hodoscopes they intend to build.

iv) High Resolution Central Vertex Detectors

More ambitious, but of great experimental interest, is the construction of a barrel made of several layers of MESD's immediately surrounding the intersection region. This detector would be expected to provide very accurate tracking of the particles before they enter the external spectrometer and yield some dE/dx information as well. This information, used in association with the external time-of-flight measurement, would be very effective for the identification of particles having $\beta < 1$.

However, the ultimate goal of such a detector would be the distinction of the secondary weak-decay vertices from the interaction star. A vertex resolution of ~ 30 μm would be sufficient to determine the decay path of a sizeable fraction of heavy flavour decays and to provide in this way a very clear signature for the otherwise elusive event configuration.

Two possible MESD central detectors have been proposed already. One at CERN for LEP has considered the problem of electromagnetic separation from the beam bunches and will be semi-integrated with the beam pipe itself. The CDF group[9] have also advanced the proposal of a realistic detector which conservatively stays in step with the present technology. It should easily provide the tracking of particles and dE/dx measurement and also permit the observation of a non-negligible fraction of the charm decay paths. The mini-detector for CDF is shown in Fig. 3; the solid angle coverage is 1/3 of 4π for a total number of (2112) readout channels which include the readout of the cathode pads transverse to the beam directions which are visible in the view A-A. It is of interest to report the estimate of costs made by the

authors which is ~ 90K$, out of which 78K$ are for the electronics (15$ for one preamplifier, 20$ for one ADC and 4000$ for the necessary power supplies).

3. Readout Considerations

Readout configurations are an integral part of the multielectrode position sensitive detectors of all sorts. The silicon devices considered so far are maintained thick enough (≥ 200 μm, with ~ 80 electrons/μm signal) to produce signals sufficient for detection by simple preamplifiers of modest energy resolution on each strip. Capacitance estimates (per strip) are consistent with this thickness constraint for strip widths as low as 10 μm. If a useful detector configuration surrounding a collision region of ISABELLE is considered, similar to that described by the CDF proposal,[9] one finds that a cylinder 20 cm long, 20 cm in diameter, has an area of 1200 cm^2. If individual strip detector segments are ~ 2 cm^2, 600 detector elements are required, each of which having (at ~ 10 μm spacing, or σ) as many as 2000 strips. Individual strip readouts, then, number 1.2 x 10^6 and a way must be found to reduce this number to a more manageable magnitude.

Analysis shows that position resolution of ~ 10 μm can be maintained on a detector of the scale mentioned with the individual signal outputs compressed by a factor of ~ 70 such that the number of signal outputs from the entire cylinder becomes ~ 2 x 10^4, which is large but imaginable. One means for this improvement is to connect the individual strips together via a resistive layer across the end of each strip which allows for resistive charge division between larger multiples of individual strips. This technique should be inherently more linear than capacitive charge division and is compatible with estimated signal levels. It should be mentioned that lateral diffusion of the charge during collection produces a spread of up to 30 μm (FWHM, gaussian) in a 1 mm thick silicon device, thus creating a natural interpolative situation, wherein strip pitch of less than ~ 10 μm is really unnecessary for very high spatial resolutions.

4. Radiation Damage

The vulnerability of semiconductor detectors to radiation damage was questioned early in the consideration of their usefulness and has only been

partially answered. An attempt has been made to apply the space and radiation effects literature to the radiation fields expected in both fixed target and colliding beam geometries and to better characterize the field expected at a colliding beam facility. Two representative silicon surface barrier detectors were exposed near an AGS production target and several deleterious effects were observed and compared with other estimations of response.

Two particular radiations are considered: minimum ionizing protons and fast (fission) neutrons through their effect on carrier lifetime (τ) degradation. van Lint[10] summarizes the effects of several radiations, including 20 MeV protons in terms of a damage constant K, finding that:

$$1/\tau = 1/\tau_o + K\phi$$

where ϕ is the radiation fluence. The drift length, $\ell = v_s \cdot \tau$ (v_s is the saturated carrier velocity), characterizes serious carrier happening when it is reduced to the dimensions of the device, d, when $\ell = v_s/K\phi \simeq d$. We can define a maximum fluence $\phi = v_s/kd$ in terms of the damage constant which is best estimated to be 5×10^{-6} cm^2/sec for 20 MeV protons and could be 5×10^{-7} cm^2/sec at minimum ionizing energy. With $v_s \cong 10^6$ cm/sec in silicon, we have $\phi_{max} = 2 \times 10^{14}/cm^2$. Ludlam[11] has estimated a maximum collider flux of $4 \times 10^5/cm^2$ sec which allows $\sim$ 16 years of operation before proton induced carrier trapping is a problem.

Srour[12] has also characterized the effects of fast neutrons on the increase in device leakage current through the degradation in carrier lifetime. The damage constant K_g in this case is the inverse of that defined by van Lint and is determined to be $7 \times 10^{+6}$ sec/cm^2. The change in leakage current is shown to be $\Delta J = q\, n_i\, d\, \phi/2K_g$, where q is the electronic charge, n_i = the intrinsic carrier concentration, $1.5 \times 10^{10}/cm^3$, d = device thickness, $\sim 10^{-2}$ cm. For a fluence of 10^{14}n/cm^2, we find $\Delta J = 170\ \mu a/cm^2$, which would severely affect the operation of a silicon detector. Heijne observed[2] an increase in leakage current for silicon detectors in a muon shield of $\Delta J/\phi = 0.5\ \mu a/1.2 \times 10^{11}/cm^2$, which makes $K_g = 2.5 \times 10^6$. The neutron fluence suggested above will prove to be an extreme upper limit, but comparable to that experienced by detectors near an AGS production target.

Two ORTEC standard transmission detectors, 50 mm^2, were placed near a production target in the test beam at the AGS[13] and were quickly observed to draw excessive leakage current (up to 85 μa at nominal bias). Neutrons were suspected and fast neutron fluence at this location was measured with $^{47}Ti(n, p)^{47}Sc$ threshold detectors to be 2.4 x 10^{14} n/cm^2 for an equal beam fluence. A hadron production calculation estimated 1.6 x 10^{14} n/cm^2 which also supports the damage constant estimate for the leakage current increase previously noted.

Sulphur and titanium threshold detectors were placed at 6 locations about the collision region at the ISR and registered fast neutron ($E \geq 1$ MeV) fluxes at representative conditions of 1-4 x 10^3 n/cm^2 sec, which does not seem to warrant excessive concern even when the relative machine luminosities are considered.

Other effects of the two exposed detectors included a change in base material type (to p-type, given the expected deep acceptor levels) and an observable radioactivity of the gold allowing the thermal fluence to be estimated at 10^{16} n/cm^2.

Further characterization of the radiation fields in configurations of interest at existing accelerators will be helpful and necessary for further estimates of radiation damage possibilities.

5. A Semiconductor Emulsion Detector

An interesting and potentially very exciting new technique is being developed at Pittsburgh.[14]

The trapping of charge produced by ionizing radiation in shallow impurity levels in semiconductors at cryogenic temperatures has been tested as a means of storing the information that energetic ionizing particles have passed through a lightly doped region (i-region) of a semiconductor device called a p-i-n diode. At low temperatures, trapping by ionized impurities is very efficient. A reverse bias pulse can be applied to the p-i-n structure which results in a high field in the i-region causing quantum mechanical field ionization of the impurities on which charge is trapped. The ejected charge is detected with a cryogenic FET preamplifier. By removing trapped charge,

field ionization also resets the detector to its initial state prior to exposure to radiation. Over an experimentally accessible range of fields, the field ionization rate can be varied between indefinitely long periods and times in the nanosecond to picosecond range. The capability of long term storage, together with rapid controlled release of charge and the possibility of preserving positional information along the track of the ionizing particle, has led us to the concept of this type of detector as a semiconductor "electronic emulsion".

Current work involves the design and fabrication of devices to test spatial resolutions beginning with a 3.5 μm resolution test device. Also planned are larger arrays which would cover a $(cm)^2$ area and which would involve readout of high resolution positional information from selected subarrays.

REFERENCES

1. Pisa Meeting on Miniaturization of Detectors for High Energy Physics, 18-21 September 1980; to be published in Plenum Press.

2. Workshop on Developments in Solid State Detectors for Elementary Particle Physics, CERN, 30 April 1981; CERN/EF/0439H/EH/ed., 5 May 1981.

3. W. K. Hofker, D. P. Oosthock, A.M.E. Hoeberechts, R. van Dantzig, K. Mulder, J.E.J. Oberski, L. A. ch. Koerts, J. H. Dieperink, E. Kok, and R. F. Rumphorst; IEEE Trans. Nuc. Sci. NS-13, 208 (1966).

4. E. Laegsgaard; Nucl. Inst. & Meth. 162, 73 (1978).

5. S. R. Amendolia et al.; Physica Scripta 23, 671 (1981); Nucl. Inst. & Meth. 176, 457 (1980).

6. c.f., G. Bertolini and A. Coche, Semiconductor Detectors, North Holland Pub. Co., Amsterdam (1968).

7. UA4 Collaboration - CERN - SPC/P114 and Add. 1,2.

8. Phys. Lett. 62B, 460 (1976).

9. FNAL - CDF Proposal.

10. V.A.J. van Lint, G. Gigas, and J. Barengoltz; IEEE Trans. Nuc. Sci. NS-22, 2663 (1975).

11. T. Ludlam; IEEE Trans. Nuc. Sci. NS-28, 549 (1981).

12. J. R. Srour, S. C. Chen, S. Othmer, and R. A. Hartmann; IEEE Trans. Nuc. Sci. NS-26, 4784 (1979).

13. H. W. Kraner, T. Ludlam, D. Kraus, and J. Renardy; BNL 28311 (1980); also in Ref. 1.

14. S. Chaudhuri, D. D. Coon, G. E. Derkits, E. Engels, P. F. Shepard (Univ. Pittsburgh), M. M. Sopira and R. N. Thomas (Westinghouse Research and Development Center, Pittsburgh); work in progress

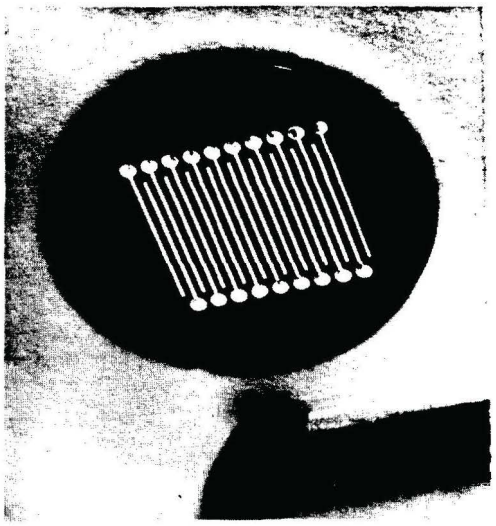

Fig. 1a

Fig. 1b

MEETING ON DEVELOPMENTS IN SOLID STATE DETECTORS

FOR ELEMENTARY PARTICLE PHYSICS

(Held at CERN on 30 April 1981)

L. Moroni (replacing G. Bellini)	Milano	Si detector telescopes
B. Borgeaud	Saclay	
G. Vegni	Milano	
A. Stefanini	Pisa	Si strip detectors
E. Heijne	CERN	CCD readout
C. Damerell	RHEL	CCD detectors
F. Krienen	CERN	SAW detectors
P. F. Manfredi	Pavia	Preamplifier electronics
A. Hrisoho	LAL, Orsay	
P. Musset	CERN	Use in experiments
E. Uggerhøj	Aarhus	Energy loss
B. Hyams	CERN	Charge division
R. Klanner	München	

Fig. 2

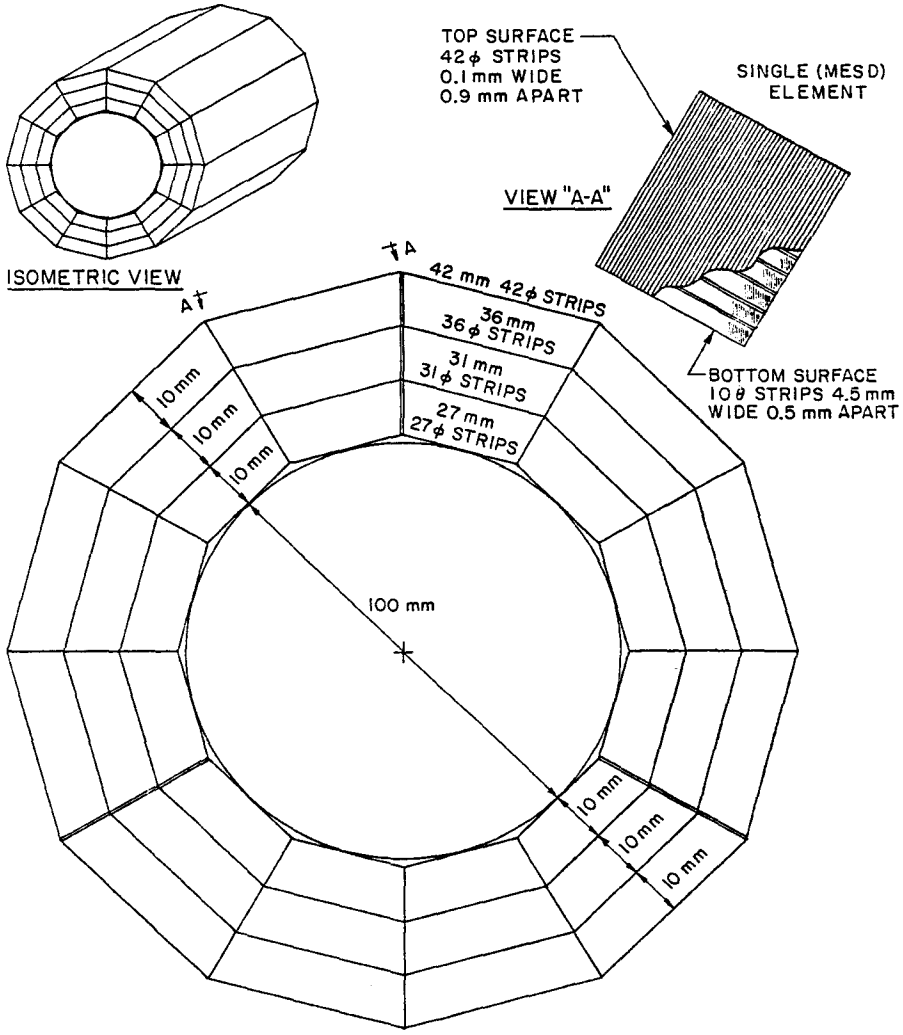
TOP SURFACE
42 ϕ STRIPS
0.1 mm WIDE
0.9 mm APART
SINGLE (MESD)
ELEMENT
VIEW "A-A"
ISOMETRIC VIEW
A
A
42 mm 42 ϕ STRIPS
36 mm
36 ϕ STRIPS
31 mm
31 ϕ STRIPS
27 mm
27 ϕ STRIPS
10 mm
10 mm
10 mm
100 mm
10 mm
10 mm
10 mm
BOTTOM SURFACE
10 ϕ STRIPS 4.5 mm
WIDE 0.5 mm APART

FIG. 3

FINE GRAINED HODOSCOPES BASED ON SCINTILLATING OPTICAL FIBERS

S.R. Borenstein, York College, CUNY

and

R.C. Strand, BNL

Abstract

In order to exploit the high event rates at ISABELLE, it will be necessary to have fast detection with fine spatial resolution. The authors are currently constructing a prototype fine-grained hodoscope, the elements of which are scintillating optical fibers. The fibers have been drawn from commercially available plastic scintillator which has been clad with a thin layer of silicone. So far it has been demonstrated with one mm diameter fibers, that with a photodetector at each end, the fibers are more than 99% efficient for lengths of about 60 cm. The readout will be accomplished either with small diameter photomultiplier tubes or avalanche photodiodes used either in the linear or Geiger mode. The program of fiber development and evaluation will be described. The status of the APD as a readout element will be discussed. Finally, an optical encoding readout scheme will be described for events of low multiplicity.

Introduction

During the 1978 summer study[1] it was decided that a research and development program should be undertaken to develop a fine grained scintillating hodoscope to cope with the high rates expected. Early attempts[2] to produce long bare scintillating filaments of one mm diameter yielded maximum useful lengths of about 15 cm, presumably due to cumulative losses at the scintillator to air interface.[3] In order to increase the useful length of the scintillating fiber, the experience and expertise of the fiber optics industry was used to draw a fiber from a heated preform of polished PVT scintillator, and to coat this with a cladding of lower refractive index. The principle is illustrated in Figure 1 where those rays of light making an angle, relative to the fiber axis, of less than the numerical aperture angle

of the fiber are trapped and guided to the end of the fiber where they are detected by a photodetector. A desirable candidate for the photodetector is the avalanche photodiode (APD) which has the virtue of small size and immunity from magnetic fields. It has a photon to electron quantum efficiency about 4 times greater than that of a photomultiplier tube; however, the probability that the photoelectron will propagate to a usable signal is correspondingly lower. Thus the sensitivity of the APD is comparable to that of the PMT.

I. HODOSCOPE DESCRIPTION

A section of a hodoscope constructed from such scintillating fibers is shown schematically as a bilayer of fibers imbedded in a protective isolating matrix. The centers of the fibers are offset by one radius from one layer to the next to assure that there are no cracks through which a particle might pass without penetrating a reasonable depth of scintillator.

II. FIBER EVALUATION PROCEDURE

Experimental Setup

In order to establish the feasibility of such a hodoscope, Brookhaven National Laboratory entered into a contract with Galileo Electro-Optical Corporation[4] to undertake an experimental program to draw and clad scintillating fibers. Various commercially available scintillators, several cladding materials, curing methods, temperatures, tensions, and draw speeds were tried. The scintillators NE102, NE110 and NE161, were obtained from Nuclear Enterprises. The cladding materials have been a proprietary ultraviolet cured acrylic and a heat cured silicone. The best results to date have been obtained with silicone coated NE161. The layout of the test facility[5] appears in Figure 2. An electron from Ruthenium 106 penetrates two small telescope counters T_1 and T_2 which sandwhich the fiber. Upon a coincidence from T_1T_2, the signal from S1 is detected by an RCA 8850 photomultiplier with single photoelectron resolution. From the resultant spectrum in Figure 2 we can calculate the mean number of photoelectrons (4 in the example shown).

A crucial feature of the test equipment is the use of a PMT with single photoelectron resolution. In this way all light yield and attenuation data

are obtained in terms of absolute number of photoelectrons. The distance from the pedestal to the first peak sets the scale in absolute photoelectrons regardless of the gain of the PMT and the associated electronics. In principle, the light yield for a given spectrum is obtained by determining the mean of the distribution. In practice, for low light levels it is found empirically that the light yield is more easily determined by measuring the ratio of the heights of the second, third and fourth peaks. For higher light levels the mean is almost the same as the peak of the distribution.

Test Results

The highlights of the results obtained so far are shown in the curves of Figure 3 and in the accompanying table where each fiber is characterized by an attenuation length and an effective photoelectron yield at the origin. The data were obtained from fibers whose diameter varied from .032" to .090" but the results have all been scaled to a diameter of .054" or 1.37 mm. The progression of curves 1 through 3 show a steady improvement due in part to choice of material, and in part to gradually improved technique. Curve No. 4 underscores the drastic attenuation suffered at the scintillator to air surface. By using coincidence techniques and setting discriminator thresholds below the single photoelectron level it is possible to construct hodoscope elements from fibers of about 1 mm diameter in lengths approaching 1 meter.

III. READOUT OPTIONS

Individual Fiber Readout

A useful hodoscope will ultimately consist of hundreds of such scintillating fibers and we must now address ourselves to the problem posed by the readout of so many channels.

Two types of photodetectors have been considered for the readout elements. PMT's and APD's. In the former case, the necessary technology is at hand and the solution consists of devising a scheme to couple the many fibers individually to small diameter, highly sensitive photomultipliers.

The disadvantages of this solution are:

1. The bulkiness of PMT's relative to the fiber diameter.
2. The cost of the PMT's which probably will not come down in the near future.
3. The inability of PMT's to function in magnetic fields.

In the case of the APD, the size of the device is well matched to the size of the fiber, and the device itelf is unaffected by magnetic fields. The cost is comparable to that of a PMT, but as seems to be the case with all silicon, one can anticipate drastic cost reduction as these devices start to be produced in much larger quantities.

The main disadvantage of this solution is that one is dealing with a new technology, and there is no experience to indicate that the device can be successfully operated in the Geiger or saturated mode. In theory, with the APD cooled to about -70°C and biased above the breakdown voltage, a photoelectron has a small (on the order of 20%) probability of causing a breakdown signal. This propbability is an increasing function of the overvoltage, but the signal size is independent of the number of photoelectrons that contributed to it so that the signal contains no analog information, and it occurs with a probability which depends upon the overvoltage as well as the number of photoelectrons. On the other hand, there is a dynamic dark count proportional to the true counting rate, which also increases with overvoltage. Thus, there is an optimum overvoltage obtained by trading off required photoelectron input versus acceptable dark count as shown in Figure 4 which shows required photoelectron input versus overvoltage for a detection efficiency of 99.9%. The other curve shows the total to input counting ratio as a function of the overvoltage, thus for an acceptable dynamic dark count of 20% the required input is 22 photoelectrons per pulse.

Referring back to Figure 3, for fibers of about 1 mm diameter and 50 cm length, the number of photoelectrons expected with perfect optical coupling between fiber and APD is about 30. (8 from Figure 3 multiplied by 4 for the higher quantum efficiency of the APD). Unfortunately the coupling between fiber and APD is far from perfect, and a means of packaging the APD silicon chip to optimize the light coupling is yet to be developed.

Optically Encoded Readout

Under most circumstances, the high event rates and large multiplicities for which the fiber hodoscope is being developed would preclude any multiplexing schemes to reduce the number of readout channels. However for specific applications of low multiplicity it might be possible to effect considerable economies in readout electronics by the use of optical encoding.

Let us consider one layer of the hodoscope which contains n elements. At the upper end, the fibers are grouped in n bundles, each consisting of $\sqrt{n}$ neighboring fibers. At the lower end the fibers are also grouped in $\sqrt{n}$ bundles, but the groupings are such that the first bundle consists of the first fiber of each bundle at the upper end, the second bundle consists of the second fiber of each bundle at the upoer end and so on. Thus a single fiber could be specified by a signal from one bundle at each end of the hodoscope. The number of readout channels has now been reduced from n to $2\sqrt{n}$. The problem with this scheme is that if more than one fiber is hit, the encoding is ambiguous. The level of ambiguity can be drastically reduced, by making use of the second layer of the hodoscope and arranging the bundles in groupings which are distinct from those already used. In practice this scheme is of interest when the number of elements is very large; for example 900 elements can be read out with just 60 photodetectors. However, for purposes of illustration we will describe a 2 x 25 element bilayer, as shown in Figure 5.

In this example, the simplest grouping is the ALPHA grouping, A,B,C,D,E each containing 5 successive fibers, at the lower end of the front layer. At the upper end of the front layer the first of each group of 5 goes to number 1 of the numerically grouped photodetectors. So far, a hit in the 9th fiber would give the signal B4. The rear layer is grouped as indicated by Greek letters at the upper end, and by Hebrew letters at the lower end. The four groupings can now be referred to as ALPHA, NUMERIC, GREEK and HEBREW. The same hit would now be characterized as B4ε℘.

In the examples shown, 3 hits in fibers, 2,9,20 would give rise to a 6-fold ambiguity if only one layer were available. The resolution of this amgiguity is illustrated by listing the expected signals for each ambiguous hypothesis as well as the number of absent signals and the number of extra signals for each hypothesis.

It is worth noting that with ALPHA and NUMERIC signals, the ambiguity is 6-fold, the addition of GREEK eliminates 4 of the ambiguities, and the final ambiguity is resolved only with the inclusion of the HEBREW group.

We also note that the ALPHA group can be used by itself as a hodoscope which is 5 times ($\sqrt{n}$) as coarse as the physical hodoscope.

Conclusion

So far we have demonstrated the feasibility of the scintillating fiber as a hodoscope element. To date the best results have been obtained with NE161 as the scintillating core and silicone as the cladding material. This combination is rather fragile and subject to deterioration with handling. To this end we are considering the application of a buffer coat, to protect the silicone cladding.

In addition we are studying several alternate cladding materials.

With regard to the optical readout, the preferred detector is the APD, and we are actively pursuing methods of both increasing the intrinsic sensitivity of the device, and improving the optical coupling between the fiber and the solid state chip.

This research was supported by the U.S. Department of Energy under contracts No. DE-AC02-76CH00016 and DE-AC02-81ER40035.

References

1. J. Marx and S. Ozaki, Topic I: Detectors and Experiments, Summary of Activity, Proc. 1977 ISABELLE Summer Workshop, BNL 50721, p. 4.
2. G.T. Reynolds and P.E. Condon, Rev. Sci. Instr. 28, No. 12, Dec. 1957; G.T. Reynolds, Nucleonics 16, No. 6, June 1958.
3. L. Reiffel and N.S. Kapany, Rev. Sci. Instr. 31, 1136-1142 (1960).
4. BNL Contract #463787-S with Galileo Electro-Optical Company.
5. S.R. Borenstein, R.B. Palmer and R.C. Strand, Optical Fibers and Avalanche Photodiodes for Scintillator Counters, presented at the International Conference on Experimentation at LEP, Uppsala, Sweden, 16-20 June, 1980: Physica Scripta, 23, No. 4:1, pp. 550-555 (April 1981) Ed: Tord Ekelof, Vol. 1-Invited Papers; Pub: Alden Press, Great Britain.

FIGURE CAPTIONS

Figure 1a. Sciltillating optical fiber, principle of operation;

b. Bilayer of fibers, encapsulated in isolating matrix.

Figure 2a. Fiber measurement setup: electron from source penetrates scintillators T_1 and T_2 as well as the fiber whose output signal S1 is analyzed;

b. Charge spectrum of fiber pulse using RCA 8850.

Figure 3. Attenuation curves for various fibers.

Figure 4. APD operation as a function of overvoltage.

Figure 5. Optical encoding and ambiguity resolution.

A schematic rendition of a 2 x 25 element bilayer ribbon. For ease of illustration, the fibers are drawn with a square cross section and the half-diameter shift from one layer to the next is not shown.

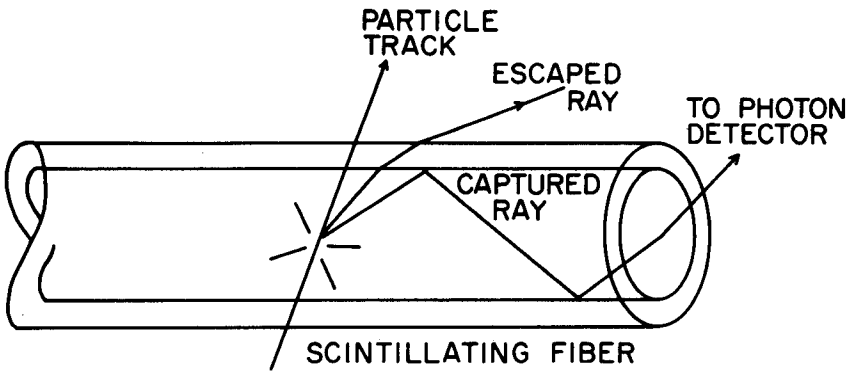
PARTICLE
TRACK
ESCAPED
RAY
TO PHOTON
DETECTOR
CAPTURED
RAY
SCINTILLATING FIBER

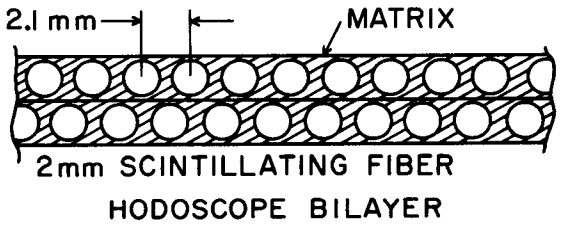
2.1 mm
MATRIX
2mm SCINTILLATING FIBER
HODOSCOPE BILAYER

Fig. 1

CHARGE SPECTRA OF SCINTILLATING FIBER
USING RCA 8850 PHOTOMULTIPLIER

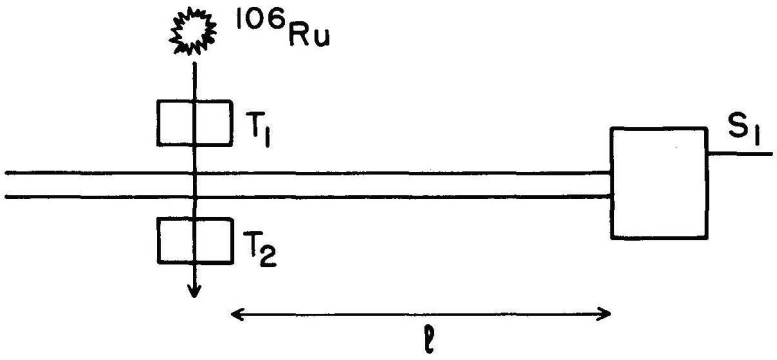

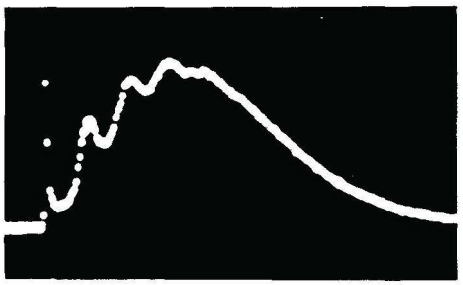

Fig. 2

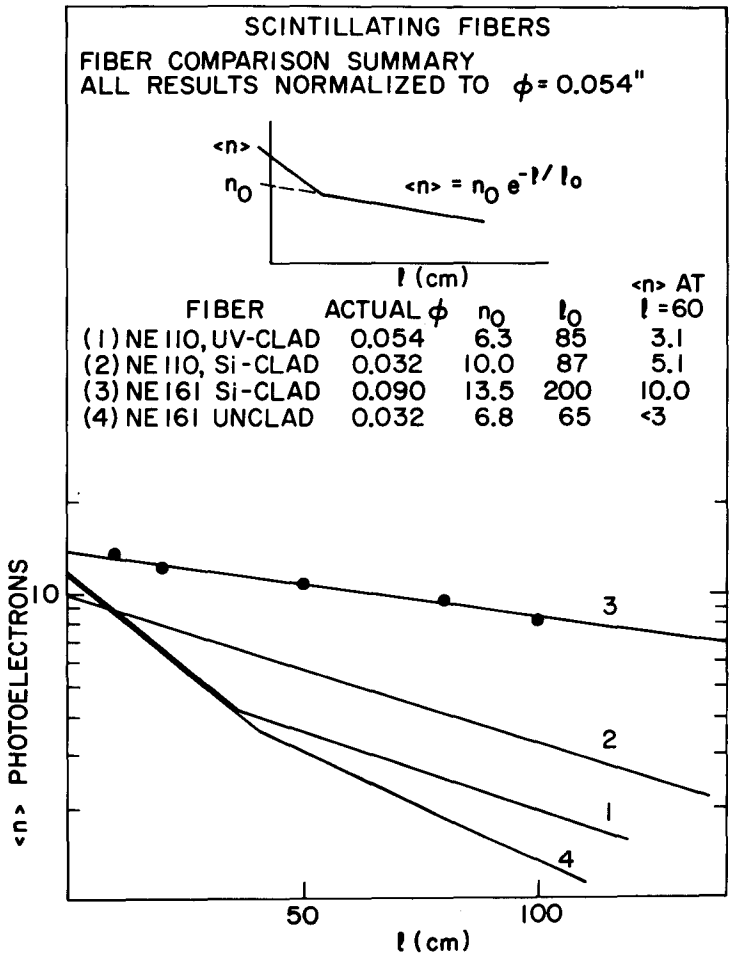
SCINTILLATING FIBERS
FIBER COMPARISON SUMMARY
ALL RESULTS NORMALIZED TO ϕ = 0.054"
<n>
n_0
<n> = $n_0 e^{-l/l_0}$
l (cm)
FIBER ACTUAL ϕ n_0 l_0 <n> AT l =60
(1) NE 110, UV-CLAD 0.054 6.3 85 3.1
(2) NE 110, Si-CLAD 0.032 10.0 87 5.1
(3) NE 161 Si-CLAD 0.090 13.5 200 10.0
(4) NE 161 UNCLAD 0.032 6.8 65 <3
<n> PHOTOELECTRONS
10
3
2
1
4
50
100
l (cm)

Fig. 3

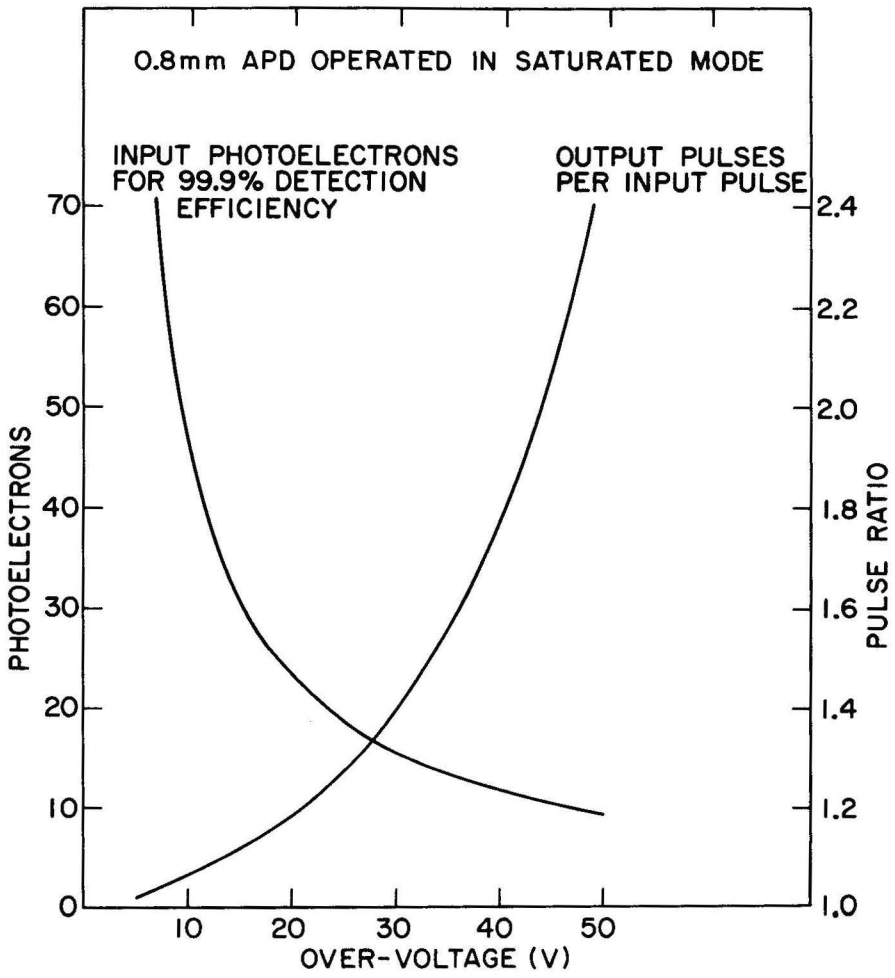
0.8mm APD OPERATED IN SATURATED MODE
INPUT PHOTOELECTRONS FOR 99.9% DETECTION EFFICIENCY
OUTPUT PULSES PER INPUT PULSE
PHOTOELECTRONS
PULSE RATIO
OVER-VOLTAGE (V)
0
10
20
30
40
50
60
70
1.0
1.2
1.4
1.6
1.8
2.0
2.2
2.4
10
20
30
40
50

Fig. 4

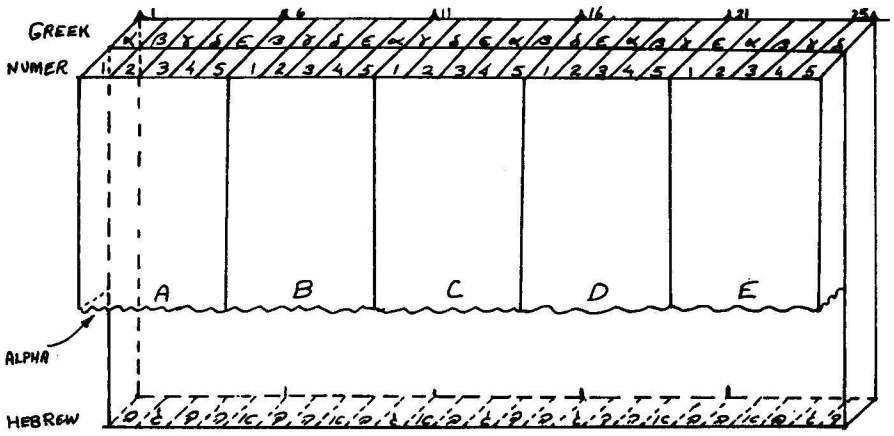

Elements hit: 2, 9, 20 = A2B4D5

Signal = ABD245βεγ ך ם

Hyp	Required	Signal	Absent	Extra
2, 9, 20	A2B4D5	β ε γ ך ם	0	0
2, 10, 19	A2B5D4	β α ך כ	2	3
4, 7, 20	A4B2D5	δ γ ן ם	2	3
4, 10, 17	A4B5D2	δ α ε ן ך ף	4	3
5, 7, 19	A5B2D4	ε γ β כ ן	2	2
5, 9, 17	A5B4D2	ε	כ ם ף	2	3

Figure 5. Optical Encoding and Ambiguity Resolution.

UPDATE ON MICRO-CHANNEL PLATES

S.D. Smith, BNL

The Proceedings of the 1977 Summer Workshop contain an excellent review by R. Majka of micro-channel plate detectors. The interested reader is strongly urged to peruse this thorough discussion of fabrication techniques, device characteristic and possible high energy physics applications. However, there has been some considerable work done in the intervening four years that I would like to outline here. During the nearly two year period beginning in late 1979, Brookhaven was fortunate to have Dr. Koichiro Oba, Director of Micro-channel Plate Development for the Hamamatsu TV Corporation as a full time visitor. He worked in collaboration with Dr. Pavel Rehak and occasionally myself. Publications detailing this work can be found in the IEEE Transactions on Nuclear Science for the 1979, 1980 and upcoming 1981 Nuclear Science Symposia. I will address only the issues of lifetime, quantum efficiency, and performance in a magnetic field.

I. LIFETIME

R. Majka's review suggested that in this respect the extant MCP photomultipliers were lacking. Studies of the timing distributions for after pulses following a scintillation induced initial pulse in a MCP photomultiplier showed four pronounced peaks. By studying the position of these peaks as a function of the voltage between the photocathode and the MCP, it was possible to identify each peak with one or more types of ions (H_2^+, H_2O^+, CO^+ and N_2^+, CO_2^+). These ions are liberated late in the cascade and are accelerated back, striking the photocathode, thus initiating the after pulse and damaging the photocathode. The time elapsed between the initial and after pulses is just the transit time of the positive ion. With the deposition of a thin (100 Å) aluminum film to the input surface of the MCP, these after pulses were observed to disappear completely. Figure 1 shows the results of lifetime test for two MCP photomultipliers - one with an Al film and one without. Note lifetime increase obtained with the Al film.

II. QUANTUM EFFICIENCY

The overall quantum efficiency of micro-channel plate photomultipliers is reduced compared to the standard photomultiplier by typically factors of 2 to 5. This arises because:

1. Photo-cathodes produced with MCP's were generally inferior and subject to damage.
2. Application of an Al film to improve item one can:
   a) cause photo-electrons to be lost due to straggling if the film is too thick.
   b) prevent secondary electrons, produced when the photo-electron strikes the closed area of the MCP, from initiating avalanches.
3. The probability that a photo-electron striking the micro-channel wall will produce no secondaries is not zero.

The first item on this list is overcome along with the problem described in 2a. The Galileo Electro-Optics Corporation has developed a technique for funneling the micro-channels on the input side, thus increasing the open area from the standard value of 60% to as much as 90%, thereby reducing the effect of 2b. Item 3 can be improved by increasing the secondary emission probability of the channel wall. This has been accomplished at Brookhaven with the application of CsI layers.

It would appear that MCP PM's can be made with quantum efficiencies of 80% of the standard photomultiplier value.

III. MAGNETIC FIELD

Oba and Rehak made detailed studies of the performance of MCP in magnetic fields of up to 7 kG for all angles of field orientation and several choices of channel bias angle. A bias angle of 15^{o} was found to be most insensitive to magnetic fields parallel to the MCP axis. A sample of this data is shown in Fig. 2. The biggest problem created by magnetic fields is with the transport of electrons from the photocathode to the MCP and from the MCP to the anode. Here field components parallel to the MCP surface are extremely detrimental unless the distances between the MCP, photocathode and anode are kept

small (mm). Unfortunately the processing of the photocathode in situ requires a large space (1 cm) between the PC and MCP. The solution of producing the photocathode prior to assembly (Transfer Technology) is expensive. Hamamatsu has developed the clever solution of assembling the tube with a bellows, allowing them to evacuate and seal the device with a large space between the PC and MCP. After the photocathode processing is done, the bellows is collapsed giving a PC-MCP spacing of $\sim$ 1 mm (see Fig. 3).

It would appear that all practical matters, apart from cost, limiting the application of MCP photomultipliers to high energy physics are in hand. Indeed multi-anode MCP-PM's are perhaps even cost effective. It would seem that now is the time for the physicists to repay this development effort by using the devices where appropriate in their experiments. Meanwhile, considerable development effort directed towards utilizing the fall 10μ image resolution continues apace.

FIGURE CAPTIONS

Fig. 1. Lifetime study of two MCP-PMT's. The factor of two deterioration observed in ZC-209 after 10^{-2} Coulombs/cm^2 represents a change in gain which apparently restabilized and not a loss in photocathode quantum efficiency.

Fig. 2. These are plots of the mean gain the the full width at half maximum of the single photoelectron response as a function of the magnetic field strength parallel to the axis. This MCP is 1 mm thick and has 15^{o} bias angle.

Fig. 3. A diagram of the Hamamatsu bellows technique for making photocathodes in situ for proximity focused MCP PMT's.

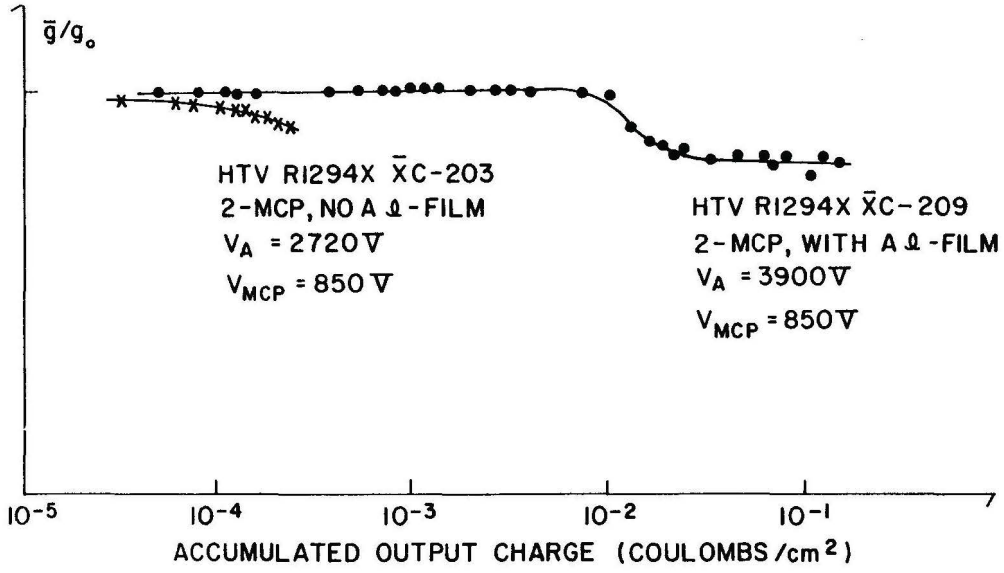
$\bar{g}/g_o$
HTV R1294X $\bar{X}$C-203
2-MCP, NO Al-FILM
V_A = 2720V
V_{MCP} = 850V
HTV R1294X $\bar{X}$C-209
2-MCP, WITH Al-FILM
V_A = 3900V
V_{MCP} = 850V
10^{-5}
10^{-4}
10^{-3}
10^{-2}
10^{-1}
ACCUMULATED OUTPUT CHARGE (COULOMBS/cm^2)

Fig. 1

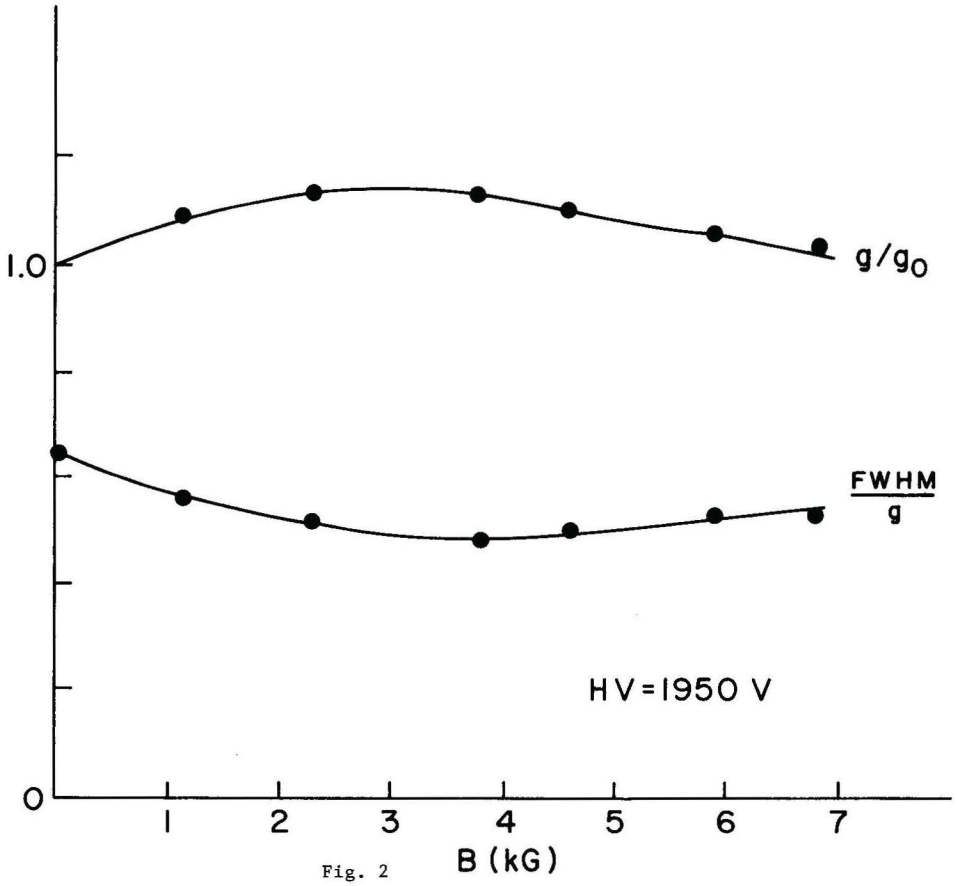

Fig. 2

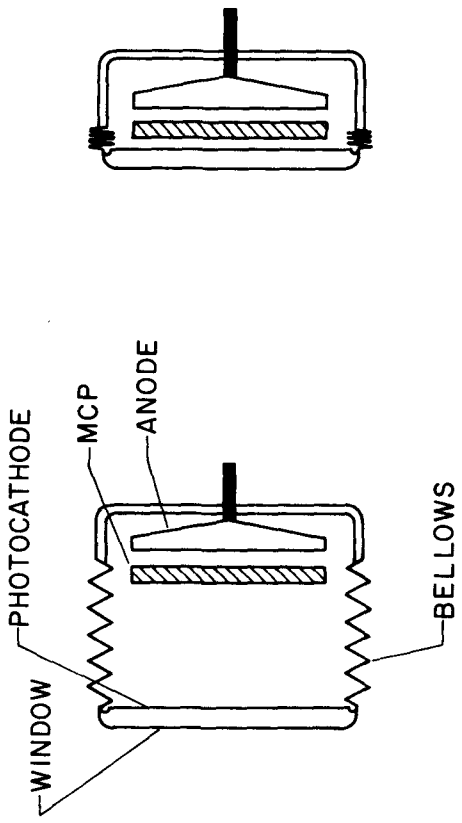

Fig. 3

SUMMARY OF THE ACTIVITIES OF THE SUBGROUP ON DATA ACQUISITION AND PROCESSING

P. L. CONNOLLY	B.N.L.
D. C. DOUGHTY	UNIV. OF PENNSYLVANIA
J. E. ELIAS	FERMILAB
B. GIBBARD	B.N.L.
J. W. HUMPHREY	B.N.L.
P. F. KUNZ	S.L.A.C.
L. LEIPUNER	B.N.L.
W. A. LOVE	B.N.L.
D. MAKOWIECKI	B.N.L.
M. J. MURTAGH	B.N.L.
J. NEIDERER	B.N.L.
E. D. PLATNER	B.N.L.
G. RABINOWITZ	B.N.L.
E. I. ROSENBERG	IOWA STATE UNIV.
M. SCHMIDT	YALE UNIV.
W. SIPPACH	NEVIS LAB.
E. J. SISKIND*	B.N.L.
J. SKELLY	B.N.L.

*Chairman

TABLE OF CONTENTS

I. INTRODUCTION

A data acquisition and handling subgroup consisting of approximately 20 members met during the 1981 ISABELLE summer study. Discussions were led by members of the BNL ISABELLE Data Acquistion Group (DAG) with lively participation from outside users. Particularly large contributions were made by representatives of BNL experiments 734, 735, and the MPS, as well as the Fermilab Colliding Detector Facility and the SLAC LASS Facility.

In contrast to the 1978 study, the subgroup did not divide its activities into investigations of various individual detectors, but instead attempted to review the current state-of-the-art in the data acquisition, trigger processing, and data handling fields. A series of meetings first reviewed individual pieces of the problem, including status of the Fastbus Project, the Nevis trigger processor, the SLAC 168/E and 3081/E emulators, and efforts within DAG. Additional meetings dealt with the questions involving specifying and building complete data acquisition systems.

For any given problem, a series of possible solutions was proposed by the members of the subgroup. In general, any given solution had both advantages and disadvantages, and there was never any consensus on which approach was best. However, there was agreement that certain problems could only be handled by systems of a given power or greater. What will be given here is a review of various solutions with associated powers, costs, advantages, and disadvantages.

This report makes frequent references to processing capabilities in various units. Table I includes approximate estimates of the capabilities and costs of various standard processors in use in high energy physics.

II. CURRENT HARDWARE TECHNIQUES

We begin by considering digital processing hardware currently in use in the field, and the approximate computing power, cost effectiveness, one-time and per-use research and development costs, and scale of problems associated with each. The numbers quoted are approximate, and are only intended to give a feeling for the ranges involved. We note that in applying a given technique to a range of problems, the costs include a term that is independent of the problem, a term which is proportional to the size of the event under

consideration (e.g. length of data memory), and a term which is proportional to the size of the algorithm employed (e.g. length of program memory).

The units used in the discussion below are machine "instructions" - for reference we note that the complete reduction of a typical event from a large ISABELLE detector is expected to use of order 10^7 of these, and a reasonable trigger algorithm can be expected to use of order a few times 10^4 to 10^5 (e.g. several operations per channel on a 5000 channel calorimeter).

As a point of reference we consider current off-the-shelf medium to large mainframe computers. The cost effectiveness of the processors in such systems is in the range 2-10 instructions per second per dollar. Such machines range in power from around 10^6 instructions per second (IPS) for $\$10^5$ for a VAX and around $1.5x10^6$ IPS for $\$2.5x10^5$ for an IBM 4341 to of order 10^7 IPS for several million dollars for CDC 7600 and IBM 3081 class machines. Typical machines are equipped with an initial memory space sufficiently large to handle any event and algorithm size currently in use (with the exception of older machines such as the CDC 7600 which may require overlaying or use of large core memory to fit large offline production codes). Memory for current machines is approaching the $5000 per megabyte cost range. The advantage of such machines lies in their existence - no R&D is necessary to build a system, and everyone knows how to use them. The disadvantage is in the large scale and correspondingly high price of the peripherals required to support them.

The use of a cluster of commercial microprocessors (1,2) programmed in a high level language such as Fortran has been proposed by a number of groups including both the BNL multi-particle spectrometer and the DAG. Some of the current 16 bit micros (e.g. M68000, Z8000) are not equipped with floating point instruction sets, while others (e.g. 8086/7, LSI-11) have floating point addons implemented either as firmware or additional hardware. Even with these additions, the ratio of floating point to integer execution time is higher than that obtained with typical commercial mainframes. A new generation of floating point chips not designed for any particular processor may correct this, but is not yet generally available. A possible advantage has been the ability of the user to tailor the memory size to the current application. Current scales are single board processors with minimal on-board memory of power in the range $1-2x10^5$ IPS for $500-$1000, while additional memory runs

$5000 per megabyte. The address space of most micros now runs to at least 4-16 megabytes. The user has the choice of programming in machine language or Fortran, with all of the trade-offs between speed and program development ease that this choice normally entails. In general, the available Fortran compilers do not perform heavy optimization, and while commercial compilers for development systems or cross-compilation do exist, there is a large possibility that the user will have to support an R&D effort of order a man-year to produce a minimal cross compiler to support either the latest hardware release, for which a commercial offering does not yet exist, or a hybrid system containing an integer micro plus floating point from another vendor. However, if a microprocessor were to implement the same fixed and floating point instruction set as an existing "large" system (e.g. LSI-11, rumored LSI-VAX), then the optimizing compiler and debugger already available on such a system could be utilized. The advantages of a system using some number of microprocessors include the possibility of easy programming in a high level language and the relative ease of moving an application which has been developed on an off-the-shelf system to the micros, as well as the fact that the major costs of hardware R&D and debugging have been borne by the chip manufacturer. The disadvantage lies in the number of units it may require to handle large problems, and the corresponding duplication of memory that this would entail. Typical R&D efforts include the development of interfaces to multi-processor busses, cross-compiler generation, and run-time support system creation, each of which is of order a man-year. Once a system is in place, a new program can typically be introduced to the micro system in of order several minutes to an hour.

Emulators of commercial machine instruction sets (3,4,5) are now a fact of life in high energy physics, with more than 50 168/E's in use or under construction. The SLAC LASS group is currently using 4 of them in a single array, and will shortly increase that number to 9, with an estimated effective power of 8.9 processors, in an application involving offline production code. The 168/E has an effective power of 1.5×10^6 IPS at a cost of $3000 plus memory at $15000 per megabyte. The floating point unit has the same performance relative to the integer unit as a typical mainframe, and implements real *4 format with results which are identical bit for bit with those obtained via

IBM execution, as well as real*6 operations which yield results which are statistically indistinguishable from IBM real*8 results for reconstruction codes. The maximum memory size is 128 kilobytes of data and 32 kilowords of program in 24 bit microcode (which corresponds to about 4000 lines of typical Fortran code). Codes which will not fit in this space rquire the use of overlaying from a solid state drum implemented using commercial PDP-11/70 semiconductor memory cards. A run-time system using a PDP-11/04 connected to an IBM channel has been implemented at SLAC. A proposed new version (the 3081/E) will be a more heavily pipelined processor, with a pipeline generated at the time the IBM program image is translated into the microcode executed by the emulator. This effectively makes the machine as efficient in the use of its execution units as an array processor is. The 3081/E will also implement the full IBM real*8 precision, and will address a memory of 16 megawords of program and 2 gigabytes of data. Power is estimated at 3.3×10^6 IPS at a processor cost of $6000. The R&D estimate for the 168/E is 4 man-years for the processor and microcode translator, 3 man-years for the solid state drum and associated "Bermuda Triangle" interface plus software support, and 3 man-years for the PDP-11/04 run-time support system with IBM channel interface and support. Much of this effort will be reused for the 3081/E. The major advantages of such systems are again the ease of programming and debugging using existing optimizing Fortran compilers and their associated run-time library routines, plus the presence of strong floating point hardware support. Once the hardware and run-time support at a particular installation are in place, new applications move into the processor in times of order a day, unless overlay preparation for large codes in the 168/E is required (this occurs when programs exceed the memory addressing capacity, which is .8 that of small core in a 7600). In this case, the current worst case effort required of order a man-month to prepare overlays for an application involving around 10 man-years of programming. The disadvantages of the system include the relative lack of run-time debugging aids for programs already running in the emulator, the requirement of a host processor having the corresponding instruction set on which to develop and compile code, and the possibility of I/O bottlenecks in applications requiring a large ratio of I/O to compute

power (these exist in any processor or processors for which I/O is performed by a support computer with insufficient I/O bandwidth).

Array processors were not discussed very much, possibly because their principal proponents in high energy physics (Wilson et al. (6) of Cornell) were not represented. Their experience is with an AP-190 connected to an IBM system at the computing center. A Fortran compiler ("Aptran") and run-time support system were developed by the group, but programming in machine code is required to take full advantage of the pipeline capabilities of the hardware. When this is done, it is estimated that an average of two of the execution units can be kept occupied in each cycle (in applications involving theoretical calculations for lattice gauge theories). A new hardware release, the AP-164, comes complete with a disk-based operating system and Fortran compiler. Current costs are in the range of $\$10^5$ for machines with 6 MHz clocks (i.e. 6×10^6 IPS per execution unit) with memory in the $40000 per megabyte range. Advantages of this solution again include the choice of Fortran or machine language programming, while difficulties include the relatively small (but increasing) size of program memories and the apparent difficulty of debugging code, especially that programmed in machine language. With the appearance of the AP-164, R&D costs are decreasing to the scale of off-the-shelf systems.

Another class of processor which received minimal discussion because of lack of proponents was the custom microprogrammed processor (7-10). Typical examples of this type of machine are the FNAL M7 and the CERN ESOP. These can range from simple bit-slice processors to fully pipelined machines with multiple execution units and microarchitectures optimized for specific calculations (e.g. the M7 is optimized to perform one 2-vector dot product per instruction). Typical examples of such machines now are equipped with meta-assemblers for the microcode, but rather minimal debugging tools. Typical ECL machines have a power of a few times 10^7 to 10^8 IPS for a price of order a few times $\$10^4$, while corresponding TTL machines may have both speed and price smaller by a factor of 4-10. Typical program memories contain several thousand machine instructions, and since (to our knowledge) no efforts have been made to overlay memory, large offline production codes have not been executed in this fashion. R&D efforts are typically of order one to a few

man-years to produce the first machine, while programming times of several man-months are required to implement small trigger algorithms (several hundred lines of program). Advantages of this approach center around the relatively large quantum of computing power available in a single piece of hardware and the cost effectiveness of the solution, while disadvantages include the difficulty of writing and debugging code required to achieve this effectiveness and power, and the relative scarcity of people within an experiment with the capability to understand and change the code.

The final class of trigger system discussed was the modular trigger processor under development at Nevis Labs (11), and in use in a less ambitious guise at FNAL (12). This processor design is motivated by noting that any given algorithm can be recast from the usual description as a sequential instruction stream, into a number of operations performed on a data stream (this is what computer scientists call a "data driven computer"). Such an engine is constructed by cabling together a series of basic execution modules each of which is capable of performing only a single type of operation. The programming of such a machine lies in the selection of the identities of the execution modules and in their interconnections. A prototype of such a Nevis machine will shortly be installed in a dimuon experiment at FNAL - a more ambitious effort is part of an experiment scheduled to run at the AGS in 1982 and at FNAL sometime thereafter. An unusual characteristic of this type of processor is that there is no natural scale to such a machine. In particular, if an algorithm requires the summing of an array of numbers, it can be implemented in one execution unit in one unit of time, two execution units in one-half unit of time, and so on. In fact, the designer is free to trade number of execution units for execution time up to a limit which is determined by the log of the number of channels (i.e. the number of stages required to combine the results of independent execution units goes as the log of the number of such units). Although it is certainly not true that one line of Fortran in a conventional processor necessitates a corresponding execution unit in the algorithm, it is generally conceded that it would be difficult to program large offline production codes in such an environment. In particular, the approach seems to require careful thought about a problem in order to reduce it to an elegant and somewhat symmetric formulation (e.g. although

there certainly is a mechanism for making cuts, the consideration of all straight line tracks between hits in two chambers except those that pass through some oddly shaped piece of material between them, which could be handled trivially although not elegantly in conventional Fortran, would seem to involve the proliferation of special purpose and therefore rarely used units). Current costs are of order a few hundred dollars for execution units which can produce 4×10^7 results per second if kept fully occupied. Research and development efforts are estimated at 3-6 man-years to produce an initial system, including cable formats and standard board layouts, as well as simulation tools, while program effort is estimated at one to several man-years to implement a trigger algorithm for a large experiment. These estimates are hard to make at this point, as expertise in this technique resides in a very few individuals. Advantages of the system are the possibility of handling very large data rates in machines containing many execution units and the cost effectiveness of such a processor if the algorithm is constructed to make maximum use of each execution unit, while disadvantages stem from the lack of programming experience, and the programming difficulty encountered in casting algorithms into a form which makes such use of the execution unit, as well as the inability of the approach to tolerate "large" algorithms which contain one-of-a-kind non-symmetries.

III. DIGITAL TRIGGER PROCESSING

We now proceed to a discussion of the applicability of these hardware techniques to trigger processing. None should be thought of as replacements for conventional fast logic triggers, or for analog triggering schemes involving clever energy sums or comparators, etc. For discussion purposes we lump the analog and fast logic portion of the solution into "the pretrigger" and then proceed with calculations to determine what pretrigger rate a digital trigger processor can accommodate.

The implementation of a trigger algorithm in Fortran was estimated at of order 10^4 to 10^5 machine instructions per event. A particular calorimeter trigger suggested by the workshop organizers and involving computing angular moments about jet axes in a calorimeter of 5000 channels was analyzed and estimated at 3×10^4 machine operations. Actual performance of one-half of the

algorithm was measured at 2.25 milliseconds on the CDC 7600, and thus corresponds to 2.25×10^4 operations for this half. For a typical scale we estimate 10^5 operations on a data stream involving 1 KHz input rate from the pretrigger. This involves 10^8 IPS of performance requirement, or a facility of order 10 7600 equivalents. The processing power requirement is of course independent of the actual rejection power achieved by the algorithm.

The use of a microprocessor for a simple programmable trigger algorithm involves the need for a memory of order 100 kilobytes in order to handle a single complete event (estimated to be of order 40 kilobytes) as well as associated program and processed data. This involves a memory of order $500, which is on the same scale as the processor cost. If the algorithm can be implemented without floating point operations, then the micro is not burdened with unnecessary hardware. If not, it might be at a disadvantage. Again, the possibility of programming in both machine code and Fortran, or possibly a mix of both, is attractive. Using current machines of power of order 10^5 IPS would require the management of an array of order 10^3 processor to achieve large scale performance. Careful use of machine code programming and lookup tables could reduce this number substantially.

The use of an existing emulator such as the 168/E would typically not involve the use of an overlaying scheme and associated overheads. The proposed 3081/E is so carefully optimized for floating point performance in a pipeline that it might prove optimal to build a stream data converter from integer to floating point format to take advantage of the increased performance. As yet, there exist no programming tools to program this machine in microcode, but given the optimization performed implicitly in the pipeline generation during microcode generation, the advantage of this is not so apparent. The unit quantum of performance is such that management of an array of perhaps 30 processors of 3081/E scale would be necessary to achieve 10^8 IPS of performance.

Array processor memory size is such that a trigger algorithm and data should fit comfortably. Again, the use of a steam data converter might be necessary. The quantum size is such that large data rates might be processed with of order 10 processors programmed in machine code. The possible use of

a mix of Fortran and machine coded programming might again be advantageous, but one would pay a penalty for lack of Fortran optimization.

The use of custom microcoded processors and the Sippach et al. data driven modular processor in trigger processing was the reason for the development of these techniques. The current scales of these machines are optimized for the types of problems that trigger processing presents, and in the case of machines like the M7, so are the internal microarchitectures. The advantages and disadvantages of these processors in triggering are thus as described in the preceeding section.

In summary, trigger processng by programmable filters seems to have a number of roughly comparable alternatives using commercial microprocessors, emulators, or array processors. Given numbers like 10^4 to 10^5 instructions per event and a capital budget of $\$10^5$ to $\$10^6$, it seems likely that such a filter could accept input events at a rate something like 10^2 to 10^3 Hz. The best hope for a general purpose digital filter to handle input trigger rates orders of magnitude higher than this is the modular data driven trigger processor. Using such a device containing a few hundred to a thousand execution units, it does not appear impossible to handle pretrigger rates in the 10^4 to 10^5 Hz range.

IV. INTERACTION REGION COMPUTING SYSTEMS

A standard picture of an interaction region computer system was proposed by DAG and generally accepted. This system consisted of a real-time data acquisition arm, an interactive computing system body, and a CPU enhancer brain. The physicist at the interaction region basically sees the interactive system, and through that controls and monitors the entire system. The data acquisition system performs essentially all of the real-time computing, including digital filtering and tape writing. This system is capable of furnishing data streams at any level (e.g., both before and after the programmable filter) to the interactive system, and is controlled by the interactive system. Program development for the data acquisition occurs in the interactive host.

A desirable addition to the data acquisition arm is referred to by the FNAL collider group as a 'Human Interface Computer' (HIC). This is an

interactive computer imbedded in the acquisition system in such a way that during the development of the detector, all data in a detector sub-system can be routed to the HIC, and that during operation of the integrated detector the HIC can still 'spy' on the data stream. This concept basically exists in modern large detectors (e.g., UA1, UA2, and several PEP detectors), but the degree of transparency of operation between the setup and operation phases, as well as the human interface (i.e., command language and graphics facilities on the HIC as compared to that on the main interactive computer) vary widely. It is hoped that program development for the HIC would occur in the main interactive computer once the detector subsystem for which a HIC is responsible is integrated into the whole detector.

The interactive computer is responsible for code development for all computers in the interaction region, as well as database management for the entire detector. It is also responsible for directing, but not performing, whatever online analysis is necessary to ensure continued calibration of the detector.

The actual online analysis is performed in the CPU enhancer. This analysis consists of full reconstruction of a few percent of all acquired events in order to calculate efficiencies and resolutions of detector elements, as well as to generate new calibration constants for placement in the data tape and in the data acquisition database. The methods currently available for building such an enhancer are essentially the cluster of microprocessors, emulators, or array processors described above.

It is assumed that the interaction region computing system will be built out of modular components in order to tailor the size of the system at any interaction region to the requirements of the experiment installed there. Therefore, we can now make only rough estimates of the approximate sizes of components. In the previous section, the computing power of the programmable filter was estimated at 10^3 Hz of events requiring 10^4 to 10^5 instructions of processing, for a total of 10^7 to 10^8 IPS power. The size of the interactive system is estimated by assuming that during periods of intense system debugging, experiment construction, and machine down periods, approximately 20-25 percent of the physicists on the experiment will be logged on. This leads us to suggest that the interactive system for a small ISABELLE

experiment be capable of supporting around 10 interactive users, while that for a large experiment be capable of supporting around 20 users. Finally, the CPU enhancer should be capable of reconstructing a few percent of a data stream of 10^1 Hz events, each requiring of the order 10^7 instructions of processing. This corresponds to 10^6 to 10^7 IPS of total power.

The question of whether the architecture of the intersection region computing system, especially its interactive and CPU enhancer sections, should be basically IBM compatible or DEC compatible was discussed at some length and with great spirit. The conversation was limited to these two alternatives only because 'Experts' on these architectures were present, and there was no intent to suggest that these were in fact the only possibilities. At one point, a list of about 30 criteria by which such a selection should be made was displayed, with each side feeling that the criteria in which its offering was superior were the more pressing ones. Although no conclusion of which was a superior architecture was reached (none was expected), this in itself marks quite a change in the state of affairs, since in the past high energy physics online computing has been the province of DEC and similar minicomputer manufacturers. The absence of IBM had been due to high initial entry cost, poor cost/performance ratio, lack of interactive support, and difficulty in interfacing to user equipment for good real-time performance. The scale of ISABELLE experiments has probably now exceeded the entry cost barrier, while the separation of real-time and interactive functions has essentially reduced the user interfacing requirements to a single port to the experiment (presumably Fastbus) without tremendous bandwidth requirements. The advent of the 4341 class processors has brought the cost/performance ratio to within at least a factor of two of the minicomputer manufacturers, with the possibility of future improvements due to competition with Japanese plug-compatible manufacturers. Finally, the appearance of the interactive features of the VM/CMS interactive operating/monitor system means that a small but growing group of high energy physicists (currently primarily at SLAC and several east coast universities) will have experience with IBM interactive computing.

In summary, the subgroup concluded that the interaction region computing system should most likely be centered around an interactive computing system which for the larger ISABELLE experiments should be around twice the size of

the current VAX-11/780, and that this be supplemented by a real-time data acquisition system interfaced to the interactive system at a single point, and by a CPU enhancer at the approximate level of a CDC 7600 for online analysis. It was pointed out that the same techniques used for creating a programmable filter for the data acquisition system of roughly 10 times this power could be used for such a enhancer but there were members of the subgroup who felt that compatibility for use as a CPU enhancer should not necessarily be forced on the design of the filter. Finally, it was realized that with the introduction of the model 4341 processor, as IBM based solution should be seriously considered.

V. DATA PROCESSING

The subgroup considered the problems of data processing, although this was not specifically in its charge, because it was felt to be an associated problem which was not under consideration elsewhere at the summer study, and because it arose naturally out of the discussion of technique. The subgroup was concerned with the scale of both the data storage capacity and the processing capacity required to support ISABELLE.

The assumption in these discussion was that some clever triggering scheme had taken the raw interaction rate of 1-5 MHz at phase I or 50 MHz at phase II, reduced this to a pretrigger rate in the 10^4 to 10^5 Hz range, pushed this through a modular trigger processor to achieve something like two orders of magnitude reduction, and finally through a programmable filter to achieve a rate of 10 Hz. We therefore assume a 10 Hz event rate or 400 kilobyte/second data rate. A further assumption is that a good year of ISABELLE running produces in the range of 1-3 months of actual data recording, and thus $3\text{-}10\times10^7$ events and $1\text{-}3\times10^{12}$ bytes of data.

The worry about data storage is where to store 1000-3000 gigabytes of data per experiment per year. A 6250 BPI magtape holds 10^8 bytes, and so this is $1\text{-}3\times10^4$ tapes (i.e., a good sized tape library). Actually, this is not such an insoluble problem as long as it isn't allowed to propagate. What needs to be pointed out is that the first stage data reduction had best be a true reduction in volume, and not an expansion in volume. As an interesting comparison, it is widely assumed by the paranoids among us that the federal

government (in the guise of either the IRS or the Census Bureau, probably the former) has possesion of a database describing the citizenry of this country. A reasonable guess would be that a few kilobytes of data per person would suffice. The size of such a database is thus of order 10^{12} bytes or 10^4 6250 BPI magtapes, i.e. around one running month of data from a large ISABELLE detector. The subgroup noted the differentiation between the actual volume of data and the physical volume and number of media required to store the data. The latter problem is subject to future technology developments such as optical disks, while the former is not.

The question of how much processing capacity is required to handle ISABELLE data was discussed at some length. It was suggested that it is useful to split this capacity into a portion proportional to the number of physicists and a portion proportional to the number of events. The first portion is essentially interactive computing required to develop and debug code and test algorithms, as well as to analyze data summary tapes. The second portion is production computing used to create summary tapes and to generate and analyze monte carlo events.

There was general agreement that the amount of interactive and support computing required was in the neighborhood of .1-.2 VAX equivalents (or .01-.02 7600 equivalents) per physicist. This comes from observation of the number of people supported both at HEP computing centers at universities (typically a VAX or IBM 4341) and at accelerator centers (the FNAL CYBER system and the SLAC 3081). Much of this computing power can actually be provided by the home institutions of the ISABELLE users. However, BNL should be prepared to provide interactive computing for BNL participants on ISABELLE experiments, and for graduate students and postdocs from outside institutions in residence at ISABELLE. An estimate of the interactive power required is thus 100-200 physicists in residence at .01-.02 7600's each, or 1-4 7600's worth of interactive computing. This is essentially a long-winded way of saying the obvious, namely that BNL needs an interactive center on the scale of FNAL or SLAC.

The amount of production capacity required is estimated at around one 7600 second per event for reconstruction. At the data rates mentioned above, this corresponds to about 5 7600's per large experiment running all year long

to process the data acquired during that year. These estimates, which are based on current reconstruction figures from R807 at the ISR and from plans for the FNAL collider, and are matched quite well with current rumors about plans for CESR-II, especially when one folds in the possibility of generating and reconstructing one monte carlo event per data event acquired. Kunz of LASS pointed out that these are not especially large numbers, given the fact that SLAC Group B will have a 7600 worth of production capacity in 168/E's by the end of the summer, with plans to expand at a later date.

The DAG and the FNAL collider representative went to great lengths to point out that processing power in a programmable trigger filter was of the right size to address this problem during the period that no data is being taken. In particular, a trigger filter capable of reducing the data rate from 1 kHz to 10 Hz by running events through an algorithm which requires 1 percent of the processing power of the full offline could also run the full offline on the 10 Hz data rate. Certainly, if ISABELLE were to run 4 months of the year, the other 8 months use of the trigger filter could be turned over to production work, provided that sufficient resources existed to manage such a use, and an operator were provided to mount tapes. This would be true regardless of whether the filter were realized in commercial microprocessors, emulators, or array processors. The subgroup agreed that this was a possibility, but refused to come to a consensus on the advisability of such a procedure, and again, as in the case of the use of the programmable filter as the CPU enhancer for online analysis, did not wish to constrain the design of the filter so that it would be useable as an offline engine.

In summary, the subgroup concluded that a 10 Hz trigger rate during several months of the year required the use of the equivalent of tens of thousands of 6250 BPI magnetic tapes for storage of a year's data, and certainly more than 10 7600 equivalents of production capacity to reduce the data (probably implemented in special purpose hardware rather than off the shelf systems), as well as an interactive facility at the level of a few 7600 equivalents to support 100-200 physicists in residence. If data storage and production capacity of this scale are not available at BNL, the only rational alternative would be to further increase the selectivity of the trigger. In the minds of some subgroup members, this corresponds to the progression from

a standard bubble chamber experiment, in which all events are available for subsequent analysis, to a triggered bubble chamber, an option not to be explored until after an initial survey experiment. To others, it was not clear why the reduction in rate from 10 Hz should be considered as "triggering," while that from 1-50 MHz to 10 Hz was considered "standard." However, regardless of trigger rate, it is important to understand that the need for interactive computing remains large.

VI. STANDARDS

The subgroup discussed standards, especially the Fastbus, on several occasions. The majority opinion was that standards are necessary, but only where they are useful.

The question of where to standardize in high energy physics data acquisition is a purely fiscal and political one. As a potential user of a standard, one uses it if it costs less to use an existing standard (or to modify it to one's use) than to construct something equal or better. As a potential inventor of a standard, one invests the time and effort only if one believes that in the end one will make back one's investment.

In high energy physics data acquistion a representative standard product is PDP-11/CAMAC MULTI. FNAL required around 3-5 man-years to take an existing program (which itself took several man-years to develop) and turn it into a standard. Every time a new experiment uses MULTI, that experiment saves itself at least 2 man-years of development. The $100K or so that this represents far outweighs the $10K or so required to purchase the requisite CAMAC hardware, and the time delay is hardware delivery time, not uncertain software production time.

It was assumed that ISABELLE experiments are so big that real standards must exist within each experiment. It is no harder to generate a standard for one experiment than for 6, and thus it pays to standardize for all of ISABELLE. A rough estimate from FNAL MULTI, which is borne out in the ISABELLE controls system, is that half of the actual labor involved in producing such a system is independent of the experiment being performed or the device being controlled. A further estimate is that a complete data acquisition system for a large ISABELLE detector, including data collection,

trigger processing, human interface computing (HIC), downline loading, calibration and online monitoring hardware and software, will require around 50 man-years to produce. The potential benefits from a standard experiment independent ISABELLE data acquisition system will thus run to around 25 man-years for each experiment past the first to use it.

The subgroup considered some of the characteristics that such a system should contain. These included a standard hardware interface (assumably the Fastbus), a standard way to obtain a data buffer containing an event in an interactive program running either on a HIC or on the interaction region interactive computer, a standard way to talk to the console and associated display devices, and a standard command language to use at any console.

The emerging standard interface between high energy physics hardware and computers is the Fastbus, under which there are currently two systems being implemented. The trigroup version is in the advanced design stage, and is anticipated as the standard for the FNAL colliding detector facility. A single crate implementation of BNL-Yale version has been in use for a year at AGS E-735, with a multiple crate version under construction for use in an experiment this winter. If a standard is to be adopted at ISABELLE, it will be needed at an early stage so that detectors being planned can utilize it for tests and debugging. If no standard is adopted, each experiment will develop its own system, and in the long run there will be much wasted effort in such uninteresting but time consuming areas such as backplanes, power supplies, cooling and ventilation, and so on.

VII. RESEARCH AND DEVELOPMENT

The ISABELLE data acquisition group described its current efforts to the subgroup. These included: (1) investigation of current commercial network products for file transfer; (2) development of software to manage multiple microprocessors or emulators for use in programmable trigger filters or CPU enhancers for online processing; (3) possible development of an emulator for the VAX architecture; (4) design of a Fastbus host interface for the VAX-11/780 (with the PEP Mark II and TPC experiments); and (5) participation in the design of the data acquistion system for the FNAL colliding detector

facility in order to gain experience with systems on the scale of those required for ISABELLE detectors.

The subgroup suggested the addition of the following topics: (6) investigation of the control of experiments (e.g., high voltages, gas systems, etc.), possibly through use of standard modules developed for the ISABELLE controls system; and (7) development of guidelines for data acquisition system integration, i.e. providing means such that systems software developed for use during the construction and debugging phases of detector development could be re-used during the actual running of the detector.

In addition, the subgroup expressed its desire for both the standard data acquisition system described in the preceeding section, and for a standard modular data driven trigger processor, provided that upcoming experiments at the AGS and FNAL validate the basic principles of that design. The subgroup did not however, explicitly commend these projects to the attention of the DAG.

VIII. SUMMARY

The subgroup on data acquisition and processing considered a number of computing-related topics during a series of very lively and not particularly highly directed meetings. The major topics and "conclusions" are listed here.

Digital Trigger Processing: A number of possible approaches exist to the problem of providing standard Fortran programmable trigger filters at the level of 10^4 to 10^5 machine instructions on several hundred Hz to 1 KHz event rate. A most promising hardware technique to extend our capabilities beyond this level is the modular data driven trigger processor under development by Sippach et al. at Nevis Labs. It is important to recognize that the triggering problem for an experiment which is to run somewhat continously for several years is solved not when the event rate is reduced to one at which data can be stored for later offline analysis, but rather when that rate is such that the existing analysis capacity can process the data at a rate equal to that at which it accumulates.

Interaction Region Computing Systems: The computing configuration should be built from an interactive host, a real-time data acquisition system, and a CPU enhancer. At a large experiment, the host should be capable of supporting

around 20 users, while the CPU enhancer should have processing power in the range of CDC 7600, but be built out of more cost effective hardware. With the advent of the 4341 class processors, and the VM/CMS interactive operating/monitor system, the use of an IBM compatible architecture merits serious consideration.

Data Processing: The volume of data written on tape or other mass storage is of order 1000 gigabytes, which corresponds to 10,000 6250 BPI tapes (but will hopefully be in more dense media), per large experiment per year at a 10 Hz logging rate. Efforts should be made to reduce the voulme of this data (in the literal sense) at the earliest opportunity as such a data rate corresponds to 6250 BPI tape drive turning at approximately full speed. For such an accumulation rate, the amount of production capacity required to create data summary tapes and generate and reconstruct monte carlo events is at least of the order of 5 CDC 7600's per experiment. This is sufficient to process the data from a year's running during that year. Although it is unlikely that computing on such a scale can be provided with off-the-shelf commercial systems, we believe that there exist techniques which promise an order of magnitude improvement over such a solution. However, regardless of this capacity, experiments should strive to reduce ther trigger rates to match the then available processing capability. In addition to this production capacity, an interactive computing facility of order 1-2 CDC 7600's is required at BNL per 100 physicists in residence at ISABELLE in order to support code generation and debugging as well as physics results preparation by analysis of data summary tapes.

Standard Data Acquistion and the Fastbus: The construction of a standard data acquisition system based on the Fastbus is likely to require of order 50 man-years of hardware and software labor, approximately half of which is experiment independent. The effort required to produce the experiment independent portion as a standard product would be well justified, but will be wasted unless the system will obviously (to the satisfication of experiments) be available for use in time for the first experiment to use it during its debugging phase.

REFERENCES

1. H. Bernstein et al., Preprint BNL 29509, (1981)
2. L.O. Hertzberger, Preprint NIKHEF-H/81-3, (1981)
3. P.F. Kunz et al., IEEE Trans. Nucl. Sc. NS-27, 582, (1980)
4. C. Halatsis et al., Preprint CERN DD/79/7, (1979)
5. R. Grishman, Preprint New York Univ. Puma System, (1978)
6. K.G. Wilson, Preprint Cornell CLNS-81/477, (1981)
7. T.F. Droege et al., IEEE Trans. Nucl. Sc. NS-25, 692, (1978)
8. T. Lingjaerde, Preprint CERN/DD/75-17, (1975)
9. G. Franke, Preprint DESY 80/109, (1980)
10. P. Waloschek, Preprint DESY 80/114, (1980)
11. W. Sippach et al., IEEE Trans. Nucl. Sc. NS-27, 578, (1980)
12. E. Barsotti et al., Preprint Fermilab FN-312, (1978)

TABLE I

System	Processing Power (MIPS)	Processor Cost ($1000)	Year of Introduction
CDC 7600	10	4000	1971
CDC CYBER 175	5	2500	1978
IBM 3081	15	4000	1981
IBM 370/168	3.3	2000	1972
IBM 4341	1.5	250	1978
SLAC 168/E	1.5	10 (Parts only)	1980
DEC VAX-11/780	1.0	100	1977

Summary of processing power and CPU cost for systems in common use for high energy physics data reduction (production). All numbers are approximate to within a factor of two. Costs are for central processor and memory only, and are not intended to indicate cost for a complete computer center based on the indicated processor. Processing power is in "million instructions per second," and is intended to indicate relative performance for a typical floating point instruction content in a system used primarily for production.

OPTICAL COMPUTING - AN ALTERNATE APPROACH TO TRIGGER PROCESSING

W.E. Cleland
University of Pittsburgh

The enormous rate reduction factors required by most ISABELLE experiments suggests that we should examine every conceivable approach to trigger processing. One approach that has not received much attention by high energy physicists is optical data processing. The past few years have seen rapid advances in optoelectronic technology, stimulated mainly by the military and the communications industry. An intriguing question is whether one can utilize this technology together with the optical computing techniques that have been developed over the past two decades to develop a rapid trigger processor for high energy physics experiments.

Optical data processing is a method for performing a few very specialized operations on data which is inherently two dimensional. Typical operations are the formation of convolution or correlation integrals between the input data and information stored in the processor in the form of an optical filter. Optical processors are classed as coherent or incoherent, according to the spatial coherence of the input wavefront. Typically, in a coherent processor a laser beam is modulated with a photographic transparency which represents the input data. In an incoherent processor, the input may be an incoherently illuminated transparency, but self-luminous objects, such as an oscilloscope trace, have also been used. We consider here an incoherent processor in which the input data is converted into an optical wavefront through the excitation of an array of point sources - either light emitting diodes or injection lasers.

A schematic diagram of the processor is shown in Fig. 1. It consists of an input plane of the type mentioned above, two lenses L1 and L2, a filter F, and a photodetector PD. The function of the lenses is to perform Fourier transformations of the optical wavefront. (The two conjugate variables in this transformation are the spatial position x and the spatial frequency cos θ/λ. As an example, recall that a lens of large aperture transforms light from a point source located in its focal plane into a plane wave with a

definite angle, or spatial frequency, but with wide spatial extent.) The input wavefront, transformed by L1, interacts with the filter F which contains the information stored in the system. In many coherent optical processors, F is a hologram, which can be generated either naturally or synthetically, by means of a computer. In incoherent systems, F may also be a hologram, but there are technical advantages in using a device called a kinoform, which can only be generated synthetically. This is a type of hologram which modulates the phase rather than the amplitude of the incident wavefront. The advantage of a kinoform over an amplitude hologram is that essentially all of the light can be diffracted into one order, resulting in increased intensity at the desired points in the detector plane and decreased light "noise" in either zero order or in the conjugate order, both of which are strongly present in amplitude holograms.

In order to see how the input data can be combined with the information contained in the filter, let the amplitude of the input signal be described by a function $O(x_1,y_1)$, in which x_1 and y_1 are the coordinates in the input plane. We can think of the light sources as points in this plane, so this function is of the form

$$O(x_1,y_1) = \sum_i A_i \ \delta(x_i-x_1,y_i-y_1),$$

in which A_i represents the intensity of the source located at the position (x_i,y_i). The intensity at the position (x_2y_2) in the detector plane is given by

$$I(x_2,y_2) = \iint O(x_1,y_1)F(x_2-x_1,y_2-y_1)dx_1dy_1$$

in which F is the point spread function (PSF) of the system. The PSF, determined in our case by the filter, is that intensity distribution $F(x_2,y_2)$ which is obtained by placing a point source of unit intensity at the origin (optical axis) of the input plane. If the unit point source is shifted to a point (a,b) in the input plane, the intensity appearing at the detector plane will be the same function, but shifted:

$$I(x_2,y_2) = F(x_2-a,\ y_2-b).$$

Thus a number of incoherent point sources located at different points in the input plane will be imaged into the detector plane as the sum of as many shifted PSFs. By constructing the filter F to give the appropriate PSF, it is possible to either search for patterns present in the data or to carry out analogue calculations.

We consider two examples of a possible optical trigger processor. Another example is described in a note by J. Thompson elsewhere in these proceedings.

Example I. Digital Bit Pattern Recognition

Consider the case where digital data are represented as a two dimensional array in which one wishes to search for a particular pattern of bits. In the digital case $A_i = 0$ or 1. To be definite, we consider the 4x4 array shown in Fig. 2. In Fig. 2a, we represent the desired bit pattern, and in Fig. 2b, the corresponding PSF. Note that the PSF is the mirror image of the desired pattern (which means that F is a matched filter). By replicating and shifting the PSF for each source which is illuminated in the input array containing the desired pattern, we obtain the intensity pattern shown in Fig. 2c, in which there are four units of intensity at the origin. This is the autocorrelation integral of the input bit pattern. A photodetector placed at the origin followed by a threshold discriminator would sense the presence of the desired pattern, independently of the presence of other bits. Note that if the input pattern obtained by shifting the original one by $(\Delta x,\Delta y) = (a,b)$ is also of interest, it can be simultaneously detected by placing a photodetector at the point (a,b) in the detector plane. This feature of space invariance may be very useful in certain situations; in cases in which it is unimportant, it can be traded for rotational or scale invariance, by making an appropriate transformation on the coordinates of the input data plane.[1]

Example II. Analogue Calculations

Consider the case of a processor in which the A_i are allowed to take on values representative of the data, such as the pulse height of a cell in a

calorimeter. The PSF for the system can in this case perform a weighting function, combining for example pulse height data with geometrical data. If we wish to create a processor to study jets, we need to form summations over the data weighted with geometrical quantities which depend on the assumed jet axis. We therefore let the coordinates (x_2,y_2) of the detector plane represent the intersection of the jet axis with the face of the calorimeter. To find the thrust, we need to form the sum

$$T = \frac{\Sigma E_i |\cos \theta_i|}{\Sigma E_i} ,$$

which means that each input pulse needs to be weighted with cos θ, in which θ is the angle between the cell that was hit and the assumed jet axis. This implies that the PSF should have the form:

$$F(x_2,y_2) \propto \cos\theta = \frac{1}{\sqrt{1+(x_2^2/d)^2 + (y_2^2/d)^2}}$$

in which d is the spacing between the origin of the events and the calorimeter face. In order to locate the axis of the jet, one would have to search the detector plane for an intensity maximum. A processor to calculate sphericity could be fabricated in a similar way, only in that case, the light intensity would be made proportional to the square of the pulse height, and one would search for a minimum in the sum

$$S = \frac{\Sigma E_i^2 \sin^2 \theta_i}{\Sigma E_i^2} .$$

An exercise that was considered at this workshop was to estimate the processing power required to calculate the moments

$$e_n = \Sigma E_i \theta_i^n | \Sigma E_i .$$

This problem could be done rapidly in an optical processor, but of course not with the precision or dynamic range possible in a digital processor.

In cases like the above, where multiple operations are to be performed on the same input data, it should be possible to place several filters in the plane between the lenses, each with its own set of photodetectors. This is shown schematically in Fig. 3 and demonstrates one of the advantages of placing the filter in the Fourier transform plane. Since each input source is turned into a plane wave, the information present in the input data is spread over the entire plane where the filters are located. The number of filters which can be accomodated will be limited by intensity and signal/noise considerations.

Clearly, a number of technical details need to be considered to establish the feasibility of producing a practical trigger processor of this type. There exists many examples in the literature of optical processors which have been built for pattern recognition,[2] most of which use coherent light. In recent years, however, there has been a renewed interest in incoherent optical processors, due to their better noise characteristics and reduced sensitivity to mechanical alignment. An interesting example[3] is an incoherent processor which has been developed to perform the analogue multiplication of an input vector by a constant matrix. In this processor, the sources are light emitting diodes, and the matrix is represented as a gray scale on a photographic plate.

At the University of Pittsburgh, we are developing the capability to produce kinoforms, which should allow us to create an incoherent optical system with an arbitrary PSF. The process begins by specifying the desired PSF as the input to a computer program.[4] A calculation is then performed, whose output is a magnetic tape containing instructions for a computer-controlled photographic recorder. In this recorder, a glass-backed emulsion is exposed by an LED while it is being transported on a microstage driven by stepping motors. The emulsion is then developed and bleached. In the bleaching process, variations in the opacity of the emulsion are converted into variations in the index of refraction, producing a phase profile. Each step in the process has been successfully performed, but mechanical imperfections in the motion of the stage must be corrected before we can create a usable filter.

An important element in the discussion of any processor is its cost. In the case of an optical processor of the type we are considering here, the dominating factor in the cost for a system with a large (>100) number of input sources and/or detectors will be in the optoelectronic elements themselves and the associated electronics. These costs will depend on the number of channels and speed required. Injection lasers can be switched in less than 1 ns, but they presently cost about $200 each. Light emitting diodes are cheaper by a factor of 10 to 100, but they are slower (10-20 ns), and they emit light over a broader wavelength and therefore limit the size of an input array. (The number of sources along either axis in the input plane cannot exceed $\lambda/\Delta\lambda$. For an LED, this number is typically 10-15, placing a limit of about 100 on the number of input channels. For an injection laser $\lambda/\Delta\lambda \simeq 100$.) The detector array could consist of individual PIN photodiodes at about $10 each, plus amplifiers and discrimators, and since the photocurrents are typically microamps, one could envision using electronics similar to that on MWPCs, at the cost of approximately $20 per detector channel. Alternatively, photodiode arrays, such as CCDs or CIDs could be used if sufficient time exists for their contents to be scanned. An accurate cost estimate can be made only once the detailed requirements for the processor are known. The cost for the optics and the mechanical mounts should not exceed a few thousand dollars.

REFERENCES

1. D. Casasent and D. Psaltis, Progress in Optics XVI, 289 (1978).
2. D. Casasent, ed. Optical Data Processing, Topics in Applied Physics, Vol. 23 (Springer-Verlag, 1978).
3. J.W. Goodman, A.R. Dias, and L.M. Woody, Opt. Lett 2, 1 (1978); D. Psaltis, D. Casasent, and M. Carlotto, Opt. Lett. 4, 348 (1979).
4. This is a modified version of a program developed by a group at the Université de Haute Alsace, France. This group, with which we are collaborating in the development of a processor, has been previously interested in optical computing for high energy physics. See M. Perrin and G. Metzger, Nuclear Inst. and Methods 126, 509 (1975), for a discussion of an approach to the track recognition problem using a coherent optical processor.

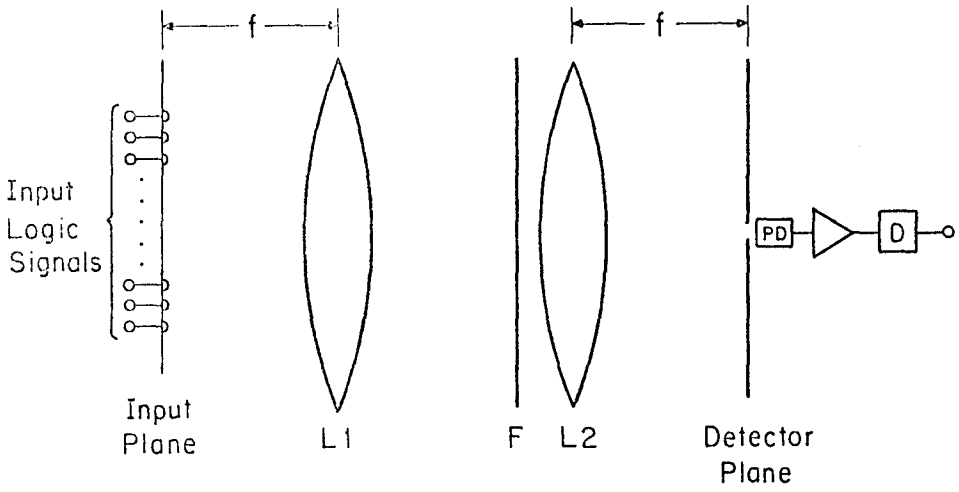

Fig. 1 Optical Processor with a Single Filter F

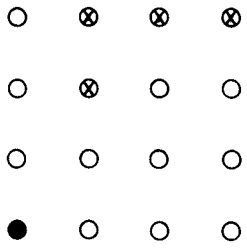

Fig. 2a BIT PATTERN TO BE RECONIZED IN A 4 x 4 ARRAY. THE X's REPRESENT LOGICAL ONES. THE DARK CIRCLE REPRESENTS THE ORIGIN (OPTICAL AXIS).

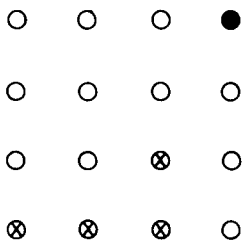

Fig. 2b PSF OF THE PROCESSOR FOR RECOGNITION OF THE PATTERN SHOWN IN Fig. 1a THIS IS THE PATTERN APPEARING AT THE DETECTOR PLANE WHEN THE SOURCE AT THE ORIGIN OF THE INPUT PLANE IS ILLUMINATED.

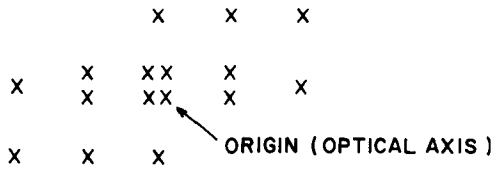

Fig. 2c DISTRIBUTION OF LIGHT INTENSITY IN THE DETECTOR PLANE WHEN THE INPUT PLANE IS ILLUMINATED WITH THE DESIRED BIT PATTERN. THE NUMBER OF X's IS PROPORTIONAL TO THE LIGHT INTENSITY AT EACH POINT.

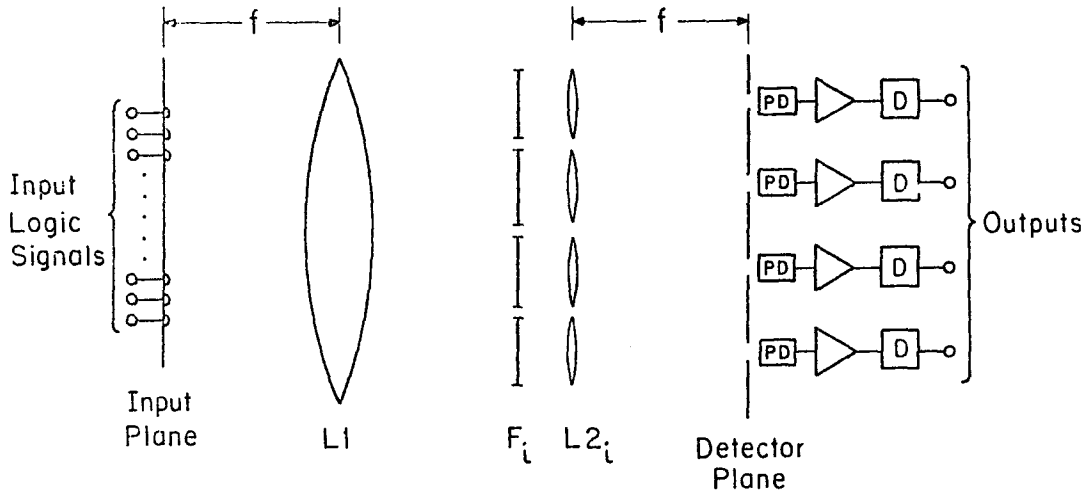

Fig. 3 Optical Processor with Multiple Filters and Detector Arrays

ON PLANAR, QUASI-PLANAR, AND SELECTIVELY BLIND TRACKING DETECTOR FOR VERY HIGH MULTIPLICITY EVENTS

W. Willis, CERN

No one has measured the upper tail of charged particle multiplicity at the ISR, though it might contain interesting physics. The reason is that it takes a rather special electronic detector to measure, say, 100 prong events.

Consideration of nucleus-nucleus collisions, or even rare p-p events at ISABELLE energies, sharpens this problem. Here I mention some possible approaches to this problem, aside from the simplest one of sampling the high multiplicity event in a well-chosen particle acceptance.

The tracking of particles of a wide range of momentum in a magnetic field is a mess largely because it is an essentially three-dimensional problem. L on p_T tracks cross over many other tracks, in the projection along B which contains the momentum information. The pattern recognition then is a global probem, with correlations between distant tracks and distant parts of the chamber. If it could be turned into a local problem, one could forsee the use of very different techniques, such as local pattern recognition processing of data before passage to the central "brain" as done in the eye.

This would be the case if the information collection were limited to a surface surrounding the source. (Let us assume the interaction vertex point is known, since it is always easy to provide enough tracking to locate it, on events of very high multiplicity.) A simple system is illustrated in Fig. 1, as an approximation to this. A cylindrical tracking chamber of small radial depth is an approximation to a surface, a "quasi-planar" detector. This is sufficient to determine a vector for each track, sufficient to determine its sign and momentum if the point of origin and magnetic field are known. Several objections and answers may be noted.

1. The measurement of high p_T tracks is unreliable because the segment observed may be a decay track, etc.
- True, it is assumed that we are trying to measure many low p_T tracks, and that occasional mistakes of this sort don't bother us.

2. Can't measure V^o's.

- True. Sad. Can't have everything, and this objection is intrinsic to all such methods, since V^o's are quintessentially a 3-D problem.

On the other hand, this is easy, cheap, and computation would be very fast, and could be locally done sector by sector if desired.

A truly planar detector is a ring imaging Cerenkov detector. It can provide more assurance that the track is legitimate and give the mass as well, though doesn't help on V^o's.

This detector is also selectively blind, by virtue of the Cerenkov threshold. This can give us the possibility of blanking out all the low p_T tracks, though that may not be desirable for the physics of true events.

One selection which is likely to be desirable is to see all the electrons in an event, but not the many hadrons. Transition radiation is ideal for this purpose, since it is also a threshold device. In practice, a gas Cerenkov ring imaging device might be sufficiently selective for this purpose. The cost is probably higher than that of a transition radiation detector, but it gives information on high p_T hadrons as well as electrons.

SUPERCONDUCTING ELECTRONICS AT ISABELLE

J.M. Shpiz, City College of New York

The expected high event rate at ISABELLE due to the exceptionally high luminosity is expected to reach the limit of the speed of present state-of-the-art electronics. Present computers are limited in their memory storage and retrieval speed by I^2R heating which limits the size of the integrated circuits. It is suggested here that the massive refrigerated areas will provide a ready environment for superconducting memory and computing arrays.

Possible superconducting logic circuits have been explored elsewhere using the superconducting to normal transition in a Josephson junction as the switching device, and on the switching from one vortex mode to another in Josephson junctions.[1]

Thus, while it may seem that present computer technology limits the usefulness of the high luminosity expected from ISABELLE, one expects cryogenic computers to be available in time for the first experiments, and to be fully available and to make maximal use of the extraordinary large amounts of data expected. Finally, we note that the expected increase in computing power for cryogenic logic and data storage provides further arguments for the orignal design specifications of ISABELLE.

REFERENCES

1. Superconducting Quantum Interference Devices and Their Applications, Proc. of International Conf., 1976, edited by H.D. Hahlbohm and H. Lubbig.

AUTHOR INDEX

Volume 1 contains pages 1-402 + δ
Volume 2 contains pages 403-804
Volume 3 contains pages 805-1134
Volume 4 contains pages 1135-1488

U.S. GOVERNMENT PRINTING OFFICE: 714-037#17